Imperial College London

Department of Civil and Environmental Engineering

Structural Behaviour and Design of Stainless Steel I-sections in Fire

Zhe Xing

25th October 2020

Submitted in part fulfilment of the requirements for the degree of Doctor of Philosophy in Civil and Environmental Engineering of Imperial College London and the Diploma of Imperial College London

Declaration of Originality

I confirm that this thesis is my own work and that any material from published or unpublished work from others is appropriately referenced.

Copyright declaration

The copyright of this thesis rests with the author and is made available under a Creative Commons Attribution Non-Commercial No Derivatives licence. Researchers are free to copy, distribute or transmit the thesis on the condition that they attribute it, that they do not use it for commercial purposes and that they do not alter, transform or build upon it. For any reuse or redistribution, researchers must make clear to others the licence terms of this work.

Abstract

Recent years have witnessed substantial research into the behaviour and design of stainless steel structures, enabling the development and expansion of, among others, the European structural stainless steel design standard EN 1993-1-4. However, despite considerable progress in the establishment of room temperature design guidance, design rules for elevated temperatures are far less developed. The fire design provisions set out in EN 1993-1-2 for stainless steel structural components are largely based on those originally developed for carbon steel, as well as the room temperature stainless steel design rules given in EN 1993-1-4; as a result, there is significant scope for improvement.

To this end, a comprehensive study has been carried out into the structural behaviour of stainless steel I-sections in fire. At the cross-section level, finite element models of stainless steel plates and I-sections, capable of mimicking their response in fire, were first created and validated against experimental results from the literature; the validated models were then employed to generate extensive structural performance data. A new cross-section classification approach and new effective width equations that are able to reflect the variation in strength and stiffness of stainless steel at different temperature levels were put forward. At the member level, eight column fire tests and six beam-column fire tests were conducted, the results of which were replicated numerically. Extensive parametric studies were then performed on stainless steel I-section columns and beam-columns at elevated temperatures. For the purpose of establishing an accurate and practical means of designing stainless steel columns and beam-columns in fire, new design rules were also proposed. The fire design provisions proposed in this research are due to be incorporated into

the upcoming version of EN 1993-1-2.

Acknowledgements

My deepest gratitude goes to my supervisor, Professor Leroy Gardner, who throughout both my Master's and PhD studies at Imperial College London has always been available to help and guide my progress. His profound knowledge and meticulous scholarship are very impressive and inspiring. I would like to express my sincerest appreciation for his patience, advice and encouragement. I am also extremely grateful for all the support of my second supervisors, Dr Merih Kucukler and Dr Ou Zhao. The successful development of my doctoral studies would not have been possible without their help.

The excellent contribution of the technicians and contractors in the Nanyang Technological University and Imperial College London, especially Kenny Lim, Toh Yau Meng, Cheng Weng Kong, Li Fali, Choi Siew Pheng, Lim Yong Cheng and Gordon Herbert, to the experimental work conducted in this research is greatly acknowledged.

I would also like to thank my friends and colleagues at Imperial College London and Nanyang Technological University, including, but not limited to: Luis Munoz Heinen, Behnam Behzadi Sofiani, Luke Lapira, Fiona Walport, Sophie Day, Wing Wan, Oluwole Kunle Fajuyitan, Yukai Zhong, Yao Sun, Lulu Zhang and Andi Su, for making my research time a pleasurable experience.

A special thanks to my parents Jintao Hu and Shulin Xing, my little sister Chao Xing and my boyfriend Kaidong Wu. They encourage and support me forever. Their love and company motivated me to face any challenges bravely throughout the three-year PhD life.

Last but not least, this thesis was made possible with the financial support provided by the China Scholarship Council, which is also gratefully acknowledged.

Contents

List of figures **14**

List of tables **24**

Notations **28**

1 Introduction **32**

1.1 Background 32

1.2 Chemical composition 33

1.3 Structural applications 33

1.4 Fire design 35

1.5 Research objectives 36

1.6 Thesis outline 36

2 Literature Review **39**

2.1 Introduction 39

2.2 Material behaviour 39

2.3 Fire tests 43

2.3.1 Cross-section behaviour 46

2.3.2 Member behaviour 47

2.4 Numerical studies 51

2.4.1 Numerical modelling 52

2.4.2 Cross-section behaviour 53

2.4.3 Member behaviour 55

2.5 European fire design standard 56

2.5.1 Development of EN 1993-1-2 56

2.5.2 Design rules for local buckling 57

2.5.3 Design rules for global instability 58

2.6 Conclusions 58

3 Local buckling of plates **59**

3.1 Introduction 59

3.2 Finite element modelling 60

3.2.1 Development of finite element models 60

3.2.2 Validation of numerical models 66

3.2.3 Parametric studies 69

3.3 Current EN 1993-1-2 design method for stainless steel in fire 70

3.3.1 Cross-section classification 70

3.3.2 Effective width method 71

3.3.3 Cross-section resistance 73

3.3.4 Assessment of EN 1993-1-2 provisions for the design of stainless steel plates in fire 74

3.4 New cross-section classification rules and effective width equations for stainless steel elements in fire 75

3.4.1 Classification of stainless steel cross-sections in fire 78

3.4.2 New effective width method for stainless steel plates in fire 78

3.4.3 Cross-section resistance of stainless steel structural elements in fire . . . 80

3.5 Comparison between EN 1993-1-2 and new effective width method 83

3.5.1 Accuracy assessment 83

3.5.2 Reliability assessment 89

3.6 Conclusions 90

4 Cross-section behaviour of I-sections **92**

4.1 Introduction 92

4.2 Finite element modelling 93

4.2.1 Development of finite element models 93

4.2.2 Validation of numerical models 97

4.2.3 Parametric studies 100

4.3 Assessment of EN 1993-1-2 provisions for the cross-section design of stainless steel I-sections in fire 103

4.4 Assessment of the design method of Chapter 3 for stainless steel I-sections in fire 104

4.5 Extension of the plastic effective width method of Bambach & Rasmussen (2004) to the design of stainless steel I-sections under minor axis bending in fire 111

4.6 Comparison of design methods and reliability assessment 112

4.6.1 Accuracy assessment 114

4.6.2 Reliability assessment 116

4.7 Conclusions 116

5 Testing of I-section columns **118**

5.1 Introduction 118

5.2 Material properties 119

5.3 Geometry and imperfection measurements 126

5.4 Column tests at room temperature 130

5.4.1 Test setup and testing procedures 131

5.4.2 Test results . . . 133

5.5 Column fire tests . . . 135

5.5.1 Test setup . . . 135

5.5.2 Testing procedure . . . 140

5.5.3 Test results . . . 141

5.6 Conclusions . . . 146

6 FE modelling and design of I-section columns 148

6.1 Introduction . . . 148

6.2 Finite element modelling . . . 149

6.2.1 Development of finite element models . . . 149

6.2.2 Validation of finite element models . . . 151

6.3 EN 1993-1-2 rules for flexural buckling assessment of stainless steel columns in fire . . . 152

6.4 Development of new flexural buckling rules for stainless steel columns in fire . . . 155

6.4.1 New proposal for the definition of the generalised imperfection factor η_θ 157

6.4.2 New design rules for flexural buckling assessment of stainless steel columns in fire . . . 161

6.4.3 Calibration of the proposed design rules . . . 162

6.4.4 Assessment of the accuracy and reliability of new proposals . . . 165

6.5 Conclusions 170

7 Testing of I-section beam-columns 172

7.1 Introduction 172

7.2 Geometry and imperfection measurements 173

7.3 Beam-column tests at room temperature 175

7.4 Beam-column fire tests 176

7.5 Conclusions 183

8 FE modelling and design of I-section beam-columns 184

8.1 Introduction 184

8.2 Finite element modelling 185

8.2.1 Development of finite element models 185

8.2.2 Validation of finite element models 187

8.2.3 Parametric studies 187

8.3 Assessment of existing EN 1993-1-2 design rules for stainless steel beam-columns in fire 192

8.4 Development of new proposals for the design of stainless steel beam-columns in fire 201

8.4.1 New proposals for the design of stainless steel beam-columns in fire . . . 201

8.4.2 Assessment of accuracy and reliability of new proposals 210

8.5 Conclusions 214

9 Conclusions and suggestions for future research 216

9.1 Conclusions 216

9.2 Suggestions for future research 219

References 221

List of figures

1.1 Sanomatalo building, Helsinki 34

1.2 Helix bridge, Singapore 34

1.3 World Trade Center attack in 2001 35

1.4 Laser welding technique 37

2.1 Typical stress-strain curves for stainless steel and carbon steel at room temperature 40

2.2 Comparison of strength ($k_{2,\theta}$, $k_{p0.2,\theta}$) and stiffness ($k_{E,\theta}$) reduction factors for different stainless steel grades considered in this thesis and carbon steel at elevated temperatures 42

2.3 Thermal conductivity for stainless steel and carbon steel at elevated temperatures 43

2.4 Stress-strain response of different stainless steel grades considered in this thesis and carbon steel at elevated temperatures 44

2.5 Standard heating curve (ISO-834, 1999) 45

2.6 Stub column test setup at elevated temperatures (Uppfeldt *et al.*, 2008) 46

2.7 Beam test setup at elevated temperatures (Gardner & Baddoo, 2006) 51

2.8 Illustration of cross-section resistances in EN 1993-1-2 (CEN, 2005) 57

3.1 Two-stage elevated temperature Ramberg-Osgood material model adopted in FE models 62

3.2 Boundary conditions applied to the FE models of stainless steel internal elements and outstand flanges 64

3.3 Lowest eigenmodes for internal elements (left) and outstand flanges (right) used to apply geometrical imperfections in subsequent nonlinear analyses 65

3.4 Typical failure modes of compressed internal elements (left) and outstand flanges (right) in fire 65

3.5 Definition of plate dimensions used in validation of numerical plate FE models against experiments performed by Uppfeldt *et al.* (2008) on stainless steel SHS in fire 67

3.6 Variation of $\sqrt{k_{E,\theta}/k_{2,\theta}}$ for austenitic, duplex and ferritic stainless steel and carbon steel at different elevated temperature levels 71

3.7 Axial post-buckling stress distribution in a simply-supported plate and effective width method 72

3.8 Assessment of EN 1993-1-2 (CEN, 2005) against FE results for the local buckling strength predictions of hot-rolled stainless steel plates subjected to axial compression 76

3.9 Assessment of EN 1993-1-2 (CEN, 2005) against FE results for the local buckling strength predictions of hot-rolled stainless steel plates subjected to bending . 77

3.10 Cross-sectional resistances in new design method 82

3.11 Assessment of new design method based on $f_{2,\theta}$ against FE results for the local buckling strength predictions of hot-rolled stainless steel plates 85

3.12 Assessment of new design method based on $f_{2,\theta}$ against FE results for the local buckling strength predictions of cold-formed stainless steel plates 86

3.13 Assessment of new design method based on $f_{2,\theta}$ against FE results for the local buckling strength predictions of hot-rolled stainless steel plates subjected to bending 87

3.14 Assessment of EN 1993-1-2 (CEN, 2005) and new proposal against FE results for all stainless steel plates 88

4.1 Boundary conditions applied to the finite element models 95

4.2 Local imperfections applied to the finite element models 96

4.3 Residual stress patterns applied to the finite element models 96

4.4 Comparison between load versus end shortening curves obtained from experiments (Pauli, 2012) and finite element models for carbon steel I-section stub columns in fire 99

4.5 Typical failure modes of stainless steel I-sections under different loading conditions 102

4.6 Assessment of EN 1993-1-2 (CEN, 2005) against FE results for austenitic stainless steel I-sections 105

4.7 Assessment of EN 1993-1-2 (CEN, 2005) against FE results for duplex stainless steel I-sections 106

4.8 Assessment of EN 1993-1-2 (CEN, 2005) against FE results for ferritic stainless steel I-sections 107

4.9 Assessment of design method of Chapter 3 against FE results for austenitic stainless steel I-sections 108

4.10 Assessment of design method of Chapter 3 against FE results for duplex stainless steel I-sections 109

4.11 Assessment of design method of Chapter 3 against FE results for ferritic stainless steel I-sections 110

4.12 Strain and stress distributions in I-sections under minor axis bending based on plastic effective width method proposed by Bambach & Rasmussen (2004), with tensile stresses indicated as positive 112

4.13 Assessment of plastic effective width method of Bambach & Rasmussen (2004) with plate slenderness $\bar{\lambda}_{\mathrm{p},\theta}$ defined in eq. (3.22) against FE results for stainless steel I-sections under minor axis bending 113

4.14 Assessment of EN 1993-1-2 (CEN, 2005) and design methods of Chapter 3 and Bambach & Rasmussen (2004), referred to as the proposed design methods in this figure, against FE results for all stainless steel I-sections 115

5.1 Cross-section labelling system and locations of tensile coupons 120

5.2 Dimensions of tensile coupon (dimensions in mm) 120

5.3 Tensile coupon test setup 121

5.4 Tensile coupon test results at room temperature 122

5.5 Strength ($k_{\mathrm{p0.2},\theta}$, $k_{2,\theta}$), stiffness ($k_{E,\theta}$) and ductility ($k_{\varepsilon_{\mathrm{u},\theta}}$) reduction factors of grade 1.4301 austenitic stainless steel at elevated temperatures from SCI (2017) . 125

5.6 Stress-strain response of stainless steel at elevated temperatures determined using eqs. (3.1) and (3.2), based on the measured room temperature material properties and the elevated temperature reduction factors from SCI (2017), shown, as an example, for the 8 mm thick material 125

5.7 Column test setup at room temperature 127

5.8 Imperfection measurement setup 128

5.9 Imperfection measurement locations 128

5.10 Typical measured local imperfection distributions; shown for the top flange of specimen LC2-20C 129

5.11 Typical measured initial global imperfection distributions; shown for specimen LC2-20C 130

5.12 Details of loading system at column head 131

5.13 Positioning of specimens and end-plates 132

5.14 Strain gauge arrangement adopted at the mid-height of the specimens 133

5.15 Typical failure mode from room temperature tests, showing flexural buckling about the minor axis, illustrated for specimen LC2-20C 134

5.16 Load-mid-height lateral deflection curves for column tests at room temperature . 134

5.17 Column test setup at elevated temperature 136

5.18 Inside of furnace used in fire tests 137

5.19 Furnace temperature measured by two thermocouples 137

5.20 Thermocouple embedded in furnace wall 138

5.21 Locations of seven thermocouples on column specimens (dimensions in mm) . . 139

5.22 LVDT covered by heat resistant fabric used to measure mid-height lateral deflection of columns 140

5.23 Typical minor flexural buckling failure modes of specimens LC2-0.6, LC2-0.5, LC2-0.4, LC2-0.3 from top to bottom 142

5.24 Comparison of measured furnace temperature-time relationship with ISO-834 (1999) standard fire curve 143

5.25 Temperature rise of column surface, shown for LC2-0.3 143

5.26 Average measured column surface temperature-time relationships for eight fire test specimens 144

5.27 Axial deformation versus column temperature paths obtained from eight fire tests, with positive deformations corresponding to expansion of the columns . . . 145

5.28 Mid-height lateral deflection versus column temperature paths obtained from eight column fire tests, with positive lateral deflections corresponding to downward deflections of the columns 146

6.1 Global imperfections applied to the finite element models 150

6.2 Finite element model of a typical stainless steel column 150

6.3 Comparison between the load versus end-shortening paths obtained from experiments (Pauli *et al.*, 2012) and finite element models for carbon steel I-section columns undergoing flexural buckling in fire 153

6.4 Accuracy of strength predictions from EN 1993-1-2 and the new design proposal relative to FE results for the flexural buckling of stainless steel columns in fire . . 156

6.5 Imperfect pin-ended column used in the derivation of column buckling equations in EN 1993-1-2 (CEN, 2005) following the Perry-Robertson concept 157

6.6 Equivalent imperfections $\overline{e}_0$ relative to column lengths L (i.e. $\overline{e}_0/L$) for austenitic stainless steel and carbon steel columns at different temperatures as adopted in EN 1993-1-2 (CEN, 2005) 159

6.7 Variation of the square root of the elevated temperature strength-to-stiffness ratio factor ξ_θ with temperature for different steel types 160

6.8 Calibration of generalised imperfection factors $\eta_{\theta*}$ for austenitic stainless steel columns buckling about the major axis in fire 163

6.9 Accuracy of the new design proposals for the major axis flexural buckling assessment of stainless steel columns in fire 166

6.10 Accuracy of the new design proposals for the minor axis flexural buckling assessment of stainless steel columns in fire 167

6.11 Comparison of the accuracy of the new proposal against EN 1993-1-2 (CEN, 2005) and the method of Lopes *et al.* (2010a) for all stainless steel columns considered in this study 169

7.1 Typical measured imperfection distributions; shown for specimen BC-Z10-20C . 174

7.2 Positioning of specimens and end-plates 175

7.3 Typical failure mode from room temperature tests, showing flexural buckling about the minor axis, illustrated for specimen BC-Z30-20C 176

7.4 Load-lateral deflection curves for beam-column tests at room temperature 177

7.5 Failure modes of the beam-column fire test specimens with the 10 mm nominal eccentricity 178

7.6 Comparison of the measured furnace temperature-time relationships with the ISO-834 standard fire curve 179

7.7 Specimen surface temperature versus time paths measured by thermocouples along specimen length, shown for BC-Z10-0.4 180

7.8 Average measured specimen surface temperature-time paths for six fire test specimens 180

7.9 Axial deformation versus specimen temperature paths obtained from six fire tests, with positive deformations corresponding to expansion of the specimens . . 182

7.10 Lateral deflection versus specimen temperature paths obtained from six beam-column fire tests 182

8.1 Boundary conditions applied to beam-column finite element models 186

8.2 Experimental and numerical failure modes for specimen BC-Z10-0.4 188

8.3 Definition of radial angle ϕ on axial load-moment interaction curve 190

8.4 Typical failure modes of stainless steel beam-columns under different loading conditions 191

8.5 Assessment of EN 1993-1-2 (CEN, 2005) and new proposals for austenitic stainless steel beam-columns under major axis bending plus axial compression 195

8.6 Assessment of EN 1993-1-2 (CEN, 2005) and new proposals for duplex stainless steel beam-columns under major axis bending plus axial compression 196

8.7 Assessment of EN 1993-1-2 (CEN, 2005) and new proposals for ferritic stainless steel beam-columns under major axis bending plus axial compression 197

8.8 Assessment of EN 1993-1-2 (CEN, 2005) and new proposals for austenitic stainless steel beam-columns under minor axis bending plus axial compression 198

8.9 Assessment of EN 1993-1-2 (CEN, 2005) and new proposals for duplex stainless steel beam-columns under minor axis bending plus axial compression 199

8.10 Assessment of EN 1993-1-2 (CEN, 2005) and new proposals for ferritic stainless steel beam-columns under minor axis bending plus axial compression 200

8.11 Calibration of interaction factors k_{yy} for austenitic stainless steel beam-columns in fire 204

8.12 Calibration of interaction factors k_{zz} for austenitic stainless steel beam-columns in fire 205

8.13 Calibration of interaction factors k_{yy} for duplex stainless steel beam-columns in fire 206

8.14 Calibration of interaction factors k_{zz} for duplex stainless steel beam-columns in fire 207

8.15 Calibration of interaction factors k_{yy} for ferritic stainless steel beam-columns in fire 208

8.16 Calibration of interaction factors k_{zz} for ferritic stainless steel beam-columns in fire 209

8.17 Comparison of accuracy of new proposals against FE results relative to EN 1993-1-2 (CEN, 2005) for stainless steel beam-columns under major axis bending plus axial compression in fire 211

8.18 Comparison of accuracy of new proposals against FE results relative to EN 1993-1-2 (CEN, 2005) for stainless steel beam-columns under minor axis bending plus axial compression in fire 212

List of tables

1.1 Chemical compositions for selected stainless steel grades studied in this thesis . . 33

2.1 Stainless steel stub column tests in fire (Uppfeldt *et al.*, 2008) 47

2.2 Summary of stainless steel beam tests in fire 47

2.3 Summary of stainless steel column tests in fire: Part 1 48

2.4 Summary of stainless steel column tests in fire: Part 2 49

2.5 Summary of stainless steel beam-column tests in fire 50

3.1 Summary of room temperature material properties for austenitic, duplex and ferritic stainless steel grades used in this study 63

3.2 Comparison of ultimate strengths of stainless steel plates obtained from physical experiments by Uppfeldt *et al.* (2008) and from FE analyses in this study 68

3.3 Comparison of ultimate bending moments of stainless steel beams obtained from physical experiments by Gardner & Baddoo (2006) and from FE analyses in this study 69

3.4 Width-to-thickness limits for plate classification at room temperature 70

3.5 Determination of cross-sectional resistances in EN 1992-1-2 (CEN, 2005) 74

3.6 Definition of cross-sectional resistances in new design method 81

3.7 Accuracy assessment of new design proposals 87

3.8 Accuracy assessment of EN 1993-1-2 (CEN, 2005) 89

3.9 Reliability assessment of new design proposals 90

3.10 Reliability assessment of EN 1993-1-2 (CEN, 2005) 91

4.1 Comparison between the load-carrying capacities obtained from stainless steel RHS stub column tests in fire conducted by Uppfeldt *et al.* (2008) and those determined through finite element modelling 98

4.2 Comparison between the load-carrying capacities obtained from beam tests on stainless steel I-sections in fire (Gardner & Baddoo, 2006; Xing *et al.*, 2020) and those determined through finite element modelling 100

4.3 Local plate slenderness values considered in parametric studies 103

4.4 Accuracy assessment of EN 1993-1-2 (CEN, 2005) and design methods of Chapter 3 and Bambach & Rasmussen (2004), referred to as the proposed design methods in this table, against numerical results for all stainless steel I-sections 114

4.5 Reliability assessment of EN 1993-1-2 (CEN, 2005) and design methods of Chapter 3 and Bambach & Rasmussen (2004), referred to as the proposed design methods in this table, against numerical results for all stainless steel I-sections. Values are given as percentages 116

5.1 Chemical compositions in mill certificates 119

5.2 Material properties in mill certificates 119

5.3 Key material properties obtained from tensile coupon tests 123

5.4 Geometric properties of tested stainless steel I-section column specimens 126

5.5 Geometric imperfections of tested stainless steel I-section column specimens . . 129

5.6 Key experimental results of column tests at room temperature 133

5.7 Measured imperfections, pre-applied axial loads and load ratios of columns subjected to fire testing 141

5.8 Measured fire resistances from column tests 145

6.1 Comparison of ultimate load carrying capacities $N_{u,test}$ of simply-supported stainless steel columns in fire determined from the tests reported in Chapter 5 and finite element models $N_{u,FE}$ created in this chapter 152

6.2 Comparison of ultimate load carrying capacities $N_{u,test}$ of simply-supported HEA 100 carbon steel columns in fire determined by Pauli *et al.* (2012) and finite element models $N_{u,FE}$ created in this chapter 153

6.3 Range of the proportions of the cross-sections considered in the calibration . . . 164

6.4 Calibrated values of imperfection factor α and auxiliary coefficient β for the new proposal 164

6.5 Accuracy of the new proposals, EN 1993-1-2 (CEN, 2005) and Lopes *et al.* (2010a) relative to the FE results for the flexural buckling assessment of stainless steel columns in fire 168

6.6 Assessment of the reliability of the new proposal, EN 1993-1-2 (CEN, 2005) and Lopes *et al.* (2010a) on the basis of the three reliability criteria set out by Kruppa (1999). Note that the numbers denoted by * violates the corresponding criterion. . 170

7.1 Geometric properties and imperfections of tested stainless steel I-section beam-column specimens 173

7.2 Key experimental results of beam-column tests performed at room temperature . 175

7.3 Pre-applied loads and load ratios of specimens under compression and bending about the minor axis subjected to fire testing 177

7.4 Measured fire resistances from beam-column tests 181

8.1 Comparison of ultimate capacities of stainless steel beam-columns obtained from physical experiments reported in Chapter 7 and from FE analyses 188

8.2 Summary of parameters considered in numerical parametric studies carried out in this chapter 190

8.3 Proposed values of auxiliary coefficients D_y and D_z 205

8.4 Assessment of new proposals against FE results relative to EN 1993-1-2 (CEN, 2005) for stainless steel beam-columns in fire 213

8.5 Reliability assessment of new proposals against FE results relative to EN 1993-1-2 (CEN, 2005) for stainless steel beam-columns in fire 214

Notation

Latin upper case letters

A	cross-section area
A_{corner}	area of corner region
A_{flat}	area of flat region
$E_{\text{p0.2}}$, $E_{\text{p0.2},\theta}$	tangent modulus at the 0.2% proof stress at room temperature and elevated temperature θ respectively
L	length
L_{c}	length of column
$M_{\text{fi,t,Rd}}$	design bending moment resistance in fire at time t
$M_{\text{u,EC3}}$	ultimate bending moment resistance determined using EN 1993-1-2
$M_{\text{u,prop}}$	ultimate bending moment resistance determined using proposed method
N_{u}	ultimate load capacity
N_{cr}	elastic critical buckling load
$N_{\text{fi,t,Rd}}$	design axial force resistance in fire at time t
$N_{\text{u,EC3}}$	ultimate axial force resistance determined using EN 1993-1-2

$N_{u,prop}$ ultimate axial force resistance determined using proposed method

$N_{u,FE}$ ultimate load capacity obtained from finite element model

$N_{u,test}$ ultimate load capacity obtained from test

S_0 cross-sectional area of coupon

T average furnace temperature in degrees Celsius

W_{eff} effective section modulus

W_{el} elastic section modulus

W_{pl} plastic section modulus

Latin lower case letters

b width of plate or width of I-section

b_{eff} effective width of plate

e_0 additional introduced loading eccentricity

$f_{2.0}$, $f_{2,\theta}$ stress at 2% total strain at room temperature and elevated temperature θ respectively

$f_{p1.0}$ 1% proof stress

f_u, $f_{u,\theta}$ ultimate stress at room temperature and elevated temperature θ respectively

f_y, $f_{p0.2,\theta}$ 0.2% proof stress at room temperature and elevated temperature θ respectively

h depth of I-section

$k_{2,\theta}$ reduction factor for stress at 2% total strain at elevated temperature θ relative to 0.2% proof stress at room temperature

$k_{p0.2,\theta}$ 0.2% proof stress reduction factor at elevated temperature θ

k_σ	buckling coefficient
$k_{\varepsilon_{\mathrm{u},\theta}}$	ultimate strain reduction factor at elevated temperature θ
$k_{E,\theta}$	Young's modulus reduction factor at elevated temperature θ
m_{u}, m_θ	exponent for stage 2 of compound Ramberg-Osgood (R-O) formulation at room temperature and elevated temperature θ respectively
n, n_θ	Ramberg-Osgood (R-O) exponent at room temperature and elevated temperature θ respectively
n_{r}	load ratio
t	time in minutes or thickness
t_{f}	flange thickness of I-section
t_{w}	web thickness of I-section
$t_{\mathrm{fi,test}}$	time duration for which the test specimen is able to resist the pre-applied load in fire test
v_0	measured global geometric imperfection magnitude
w_0	measured local geometric imperfection magnitude
w_{f}	measured flange local imperfection magnitude
w_{w}	measured web local imperfection magnitude

Greek lower case letters

α	imperfection factor
$\bar{\lambda}$	non-dimensional slenderness
$\bar{\lambda}_0$	plateau length of column buckling curve

$\bar{\lambda}_{\mathrm{p0}}$, $\bar{\lambda}_{\mathrm{p0},\theta}$	plateau length of plate buckling curve at room temperature and elevated temperature θ respectively
$\bar{\lambda}_{\mathrm{p}}$, $\bar{\lambda}_{\mathrm{p},\theta}$	non-dimensional plate slenderness at room temperature and elevated temperature θ respectively
$\bar{\lambda}_{\theta}$	non-dimensional slenderness at elevated temperature θ
β	auxiliary coefficient
χ_{fi}	buckling reduction factor in fire
$\gamma_{M,\mathrm{fi}}$	partial factor for fire design
ν	Poisson's ratio
ρ	plate buckling reduction factor
σ	stress
σ_{cr}	elastic buckling stress
θ	temperature
θ_{cr}	critical failure temperature
ε	material factor at room temperature or strain
$\varepsilon_{\mathrm{p0.2}}$, $\varepsilon_{\mathrm{p0.2},\theta}$	total strain at the 0.2% proof stress at room temperature and elevated temperature θ
ε_{u}, $\varepsilon_{\mathrm{u},\theta}$	strain at ultimate stress at room temperature and elevated temperature θ respectively
ε_{θ}	material factor at elevated temperature θ
ξ_{θ}	temperature dependent factor

Chapter 1

Introduction

1.1 Background

Fire is considered as one of the most serious hazards in structural engineering since the loss of strength and stiffness of structural components at high temperature reduces their load-bearing capacity and can even lead to collapse of the entire building structure. Fire design is therefore an integral part of structural design. Over the years, there have been significant developments in the testing, simulation and design of carbon steel structures subjected to fire. However, the response of stainless steel structures at elevated temperatures has received significantly less attention, although stainless steel has been increasingly utilised in structural and offshore applications owing to its aesthetic appearance, high corrosion resistance and favourable material properties (Gardner, 2019; Wang & Han, 2019). This is particularly the case for stainless steel I-section components, which are being increasingly utilised to fulfil higher load-carrying capacity requirements in stainless steel structures. The research study presented in this thesis focuses primarily on the structural behaviour and design of stainless steel I-sections in fire.

1.2 Chemical composition

Stainless steel is an alloy of iron with a minimum of 10.5% chromium and a maximum of 1.2% carbon by mass, together with nickel, manganese, silicon, phosphorus and other alloying elements. The corrosion resistance of stainless steel stems from its chromium content, whereby the chromium produces a very thin chromium rich oxide layer on the surface of the material, known as 'passive layer', which effectively prevents corrosion and staining; moreover, the thin layer is able to reform when the surface of the stainless steel is scratched. Stainless steel is commonly classified into four main types: austenitic, ferritic, duplex and martensitic, of which the first three types are most commonly used in the construction industry. Table 1.1 shows the chemical compositions for the three grades of stainless steel studied in this research, namely austenitic grade 1.4301, duplex grade 1.4462 and ferritic grade 1.4003 stainless steel.

Table 1.1: Chemical compositions for selected stainless steel grades studied in this thesis

Grade	Content of alloying element by mass (%)				
	C	Cr	Ni	Mo	Others
1.4301	0.07	17.5 – 19.5	8.0 – 10.5	-	-
1.4462	0.03	21.0 – 23.0	4.5 – 6.5	2.5 – 3.5	N: 0.1 – 0.22
1.4003	0.03	10.5 – 12.5	0.3 – 1.0	-	-

1.3 Structural applications

Reviews of structural applications of stainless steel have been presented in (Baddoo *et al.*, 1997; Gardner, 2005, 2008; Gedge, 2008; Baddoo, 2013). Early landmark applications can be traced back to St Paul's Cathedral (London) in 1925 and the Chrysler Building (New York) in 1929, followed by the Pompidou Centre (Paris) in 1977 and the Lloyds Building (London) in 1981. More recently, the number of stainless steel buildings and bridges, such as the Sanomatalo building in Helsinki (Fig. 1.1) and the Helix bridge in Singapore (Fig. 1.2), is increasing as a result of the need for structural sustainability and the increase in awareness of whole-life costs.

Figure 1.1: Sanomatalo building, Helsinki
(http://roopeahonen.weebly.com/visit-in-sanomatalo)

Figure 1.2: Helix bridge, Singapore
(https://www.coxarchitecture.com.au/project/the-helix-bridge)

1.4 Fire design

Steel structures are more vulnerable to fire than reinforced concrete and timber structures owing to the rapid temperature development in the steel structures. There have been a number of notable fire incidents in steel structures, such as the World Trade Center (WTC) attack in 2001 (Fig. 1.3) where the twin towers WTC 1 and WTC 2 collapsed within merely 102 minutes and 56 minutes, respectively, after being exposed to fire and damage. Therefore, to reduce the possibility of building collapse and fatalities owing to fire, steel structures should be carefully designed, ensuring adequate load-bearing capacity for a required duration at elevated temperatures.

Figure 1.3: World Trade Center attack in 2001
(https://buglefeed.com/10-times-final-destination-happened-in-real-life)

The fire design of stainless steel structures requires a good understanding of their behaviour at elevated temperatures. Since the chemical composition of stainless steel differs from that of carbon steel, the physical and thermal properties also differ and there are different strength and stiffness retention at elevated temperatures. Determination of the fire resistance of structural components is a complex process owing to the many factors involved, such as the fire growth and the temperature development in the elements. The standard fire test offers a relatively simple

method to determine the idealised fire resistances of components in fire and enables comparisons to be made between elements on an even basis. However, experimental results are often limited since fire testing is expensive and time-consuming; this has promoted the widespread use of the numerical modelling to generate extensive structural performance data. The finite element analysis software ABAQUS (2014), which has been shown to be able to replicate the nonlinear behaviour of stainless steel components in fire, is employed throughout this study.

1.5 Research objectives

To investigate the structural behaviour of stainless steel I-sections in fire, an experimental programme is carried out in this study, in which all the tested stainless steel I-sections are fabricated through the laser-welding of stainless steel plates. Laser-welding is a recently introduced fabrication method; as can be seen in Fig. 1.4, lasers are utilized to locally melt and fuse individual plates into an I-section. Compared to conventional arc welding, laser-welding is more precise and generates a lower level of residual stresses (Gardner *et al.*, 2016b). Numerical investigations and analyses of stainless steel I-sections in fire are also carried out herein. Based upon the findings from the experimental and numerical analyses, revised design rules for stainless steel I-sections in fire are proposed in order to further develop the European fire design standard EN 1993-1-2 (CEN, 2005).

1.6 Thesis outline

This chapter provides a brief introduction of stainless steel structures and their fire design. The objectives of this research study and the outline of this thesis are also presented. In Chapter 2, a comprehensive literature review relevant to this thesis is reported with the aim of giving an overview of important topics. More detailed appraisals of the key literature are given within each

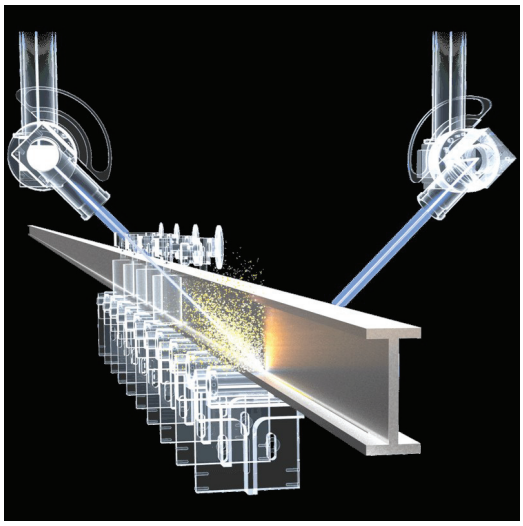

Figure 1.4: Laser welding technique
(https://www.montanstahl.com/about/production-technologies/laser-welding)

individual chapter.

Chapter 3 presents numerical parametric studies of the local buckling behaviour of stainless steel plates at elevated temperatures. On the basis of the obtained numerical results, new effective width-based design methods are proposed to determine the local buckling strengths of stainless steel plates subjected to fire. The cross-section behaviour of stainless steel I-sections in fire is then investigated in Chapter 4. Finite element (FE) models able to replicate the cross-section behaviour of stainless steel I-sections at elevated temperatures are created and validated; the results are then utilized to assess the current codified rules and the new design proposals from Chapter 3.

The stability of stainless steel I-section columns subjected to fire is studied using both experimental and numerical methods. The results of eight full-scale anisothermal fire tests on grade 1.4301 austenitic stainless steel laser-welded I-section columns are reported in Chapter 5. Complementary initial local and global geometric imperfection measurements, room temperature tensile coupon tests and room temperature column buckling tests are also described. In Chapter 6, finite element models of structural stainless steel columns in fire are created and validated

against the test data reported in Chapter 5; the validated models are then utilised to carry out extensive numerical parametric studies. A new design approach, compatible with existing design rules in EN 1993-1-2 (CEN, 2005), is proposed for the purpose of establishing an accurate and practical means of designing stainless steel columns in fire.

Similarly, the stability of stainless steel I-section beam-columns in fire is also studied by experimental and numerical means. A total of six full-scale anisothermal fire tests on grade 1.4301 austenitic stainless steel laser-welded I-section beam-columns are reported in Chapter 7. Parametric studies are then performed, as presented in Chapter 8. Based upon the findings from the fire tests and numerical parametric studies, new design provisions for stainless steel beam-columns in fire are proposed and compared with the existing design methods in EN 1993-1-2 (CEN, 2005).

Finally, in Chapter 9, a summary of the key findings of this research study and suggestions for further work are provided.

Chapter 2

Literature Review

2.1 Introduction

This chapter provides a comprehensive review of previous literature pertinent to this thesis. Previous research studies on the stainless steel components at elevated temperatures are presented, together with the corresponding codified design rules and proposals for revised design rules. Key research findings from the experimental and numerical studies are collated and summarised in this chapter. Additionally, the European fire design standard EN 1993-1-2 (CEN, 2005) is briefly introduced since the primary purpose of this research study is to develop improved design provisions for stainless steel structures in fire, suitable for inclusion in the upcoming version of EN 1993-1-2.

2.2 Material behaviour

The material response of stainless steel differs from that of carbon steel at room temperature. Fig. 2.1 shows typical stress-strain curves up to 1.5% strain for stainless steel and carbon steel at room

temperature (Afshan, 2013), where it can be seen that, relative to carbon steel, stainless steel has a more rounded stress-strain response and no clear yield point; stainless steel also generally has a higher ratio of ultimate-to-yield stress and greater ductility (Rasmussen, 2003; Gardner, 2005; Hradil *et al.*, 2013; Gardner, 2019; Afshan *et al.*, 2019).

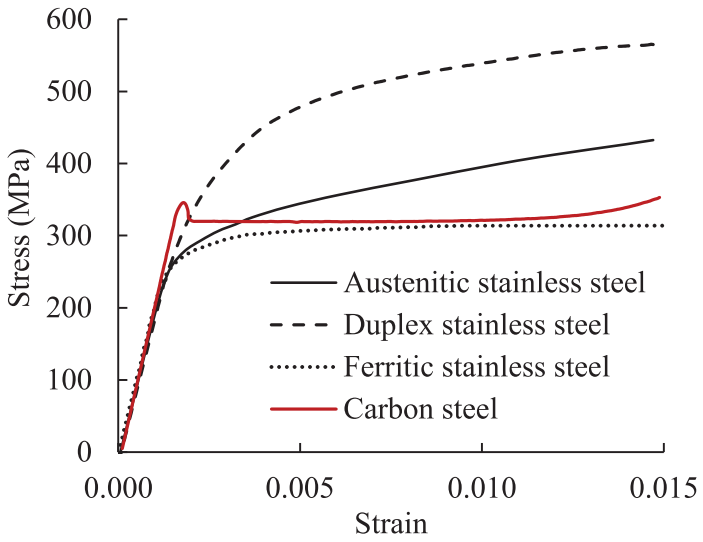

Figure 2.1: Typical stress-strain curves for stainless steel and carbon steel at room temperature (Afshan, 2013)

At elevated temperatures, stainless steel also displays different physical and thermal properties compared to carbon steel owing to the high alloying elements of stainless steel. Previous studies on the elevated temperature material properties of stainless steel (Gardner & Ng, 2006; Chen & Young, 2006; Gardner *et al.*, 2010; Huang & Young, 2014b; Gardner *et al.*, 2016a) have found that stainless steel displays better retention of strength and stiffness than carbon steel. The elevated temperature strength ($k_{p0.2,\theta}$, $k_{2,\theta}$) and stiffness ($k_{E,\theta}$) reduction factors, which are taken from Design Manual for Structural Stainless Steel (SCI, 2017), are shown in Fig. 2.2 for the (a) austenitic, (b) duplex and (c) ferritic stainless steel grades considered in this thesis; those for carbon steel (CEN, 2005) are also shown for comparison in Fig. 2.2 (d). Fig. 2.3 shows the thermal conductivity of stainless steel and carbon steel, where it can be seen that the thermal conductivity of stainless steel is generally lower than that of carbon steel, increasing steadily

with temperature from 15W/mK at room temperature to the vicinity of 30 W/mK at 1200 °C for austenitic and duplex stainless steel while increasing from 21W/mK at room temperature to 29W/mK at 750 °C and then decreasing to 25 W/mK at 1200 °C for ferritic stainless steel. (Gardner & Ng, 2006; Gardner, 2007; Gardner *et al.*, 2010).

The elevated temperature material stress-strain response of stainless steel also has been investigated by many researchers (Chen & Young, 2006; Abdella, 2009; Gardner *et al.*, 2010; Liang *et al.*, 2019; Fan *et al.*, 2020). Chen & Young (2006) proposed a series of equations for determining the yield strength, elastic modulus, ultimate tensile strength and ultimate strain of stainless steel at elevated temperatures. Additionally, a stress-strain model for stainless steel at elevated temperatures was also developed by Chen & Young (2006) based on the basic Ramberg–Osgood material models (Ramberg & Osgood, 1943; Mirambell & Real, 2000). Gardner *et al.* (2010) determined strength and stiffness reduction factors of stainless steel at elevated temperatures and also proposed a material model for the continuous prediction of the stress-strain response by means of modified compound Ramberg-Osgood equations. Liang *et al.* (2019) then utilised the Ramberg–Osgood material model developed in (Gardner *et al.*, 2010) to represent the elevated temperature stress-strain response of stainless steel, together with a new expression of m_θ to ensure that the second stage of the Ramberg-Osgood material model passes through the elevated temperature strength at 2% total strain $f_{2,\theta}$ at 2% total strain. Adopting the Ramberg-Osgood material model presented in (Liang *et al.*, 2019) in conjunction with the elevated temperature material property reduction factors provided in Design Manual for Structural Stainless Steel (SCI, 2017), the material stress-strain curves for the typical stainless steel grades considered in this thesis for different temperature levels are shown in Fig. 2.4, in addition to those of carbon steel. Note that the carbon steel stress-strain curves were determined on the basis of the reduction factors and stress-strain model provided in EN 1993-1-2 (CEN, 2005). As can be seen from Fig. 2.4, the elevated temperature stress-strain response of stainless steel is significantly different from that of carbon steel, and there is significant variation between different types of stainless steel.

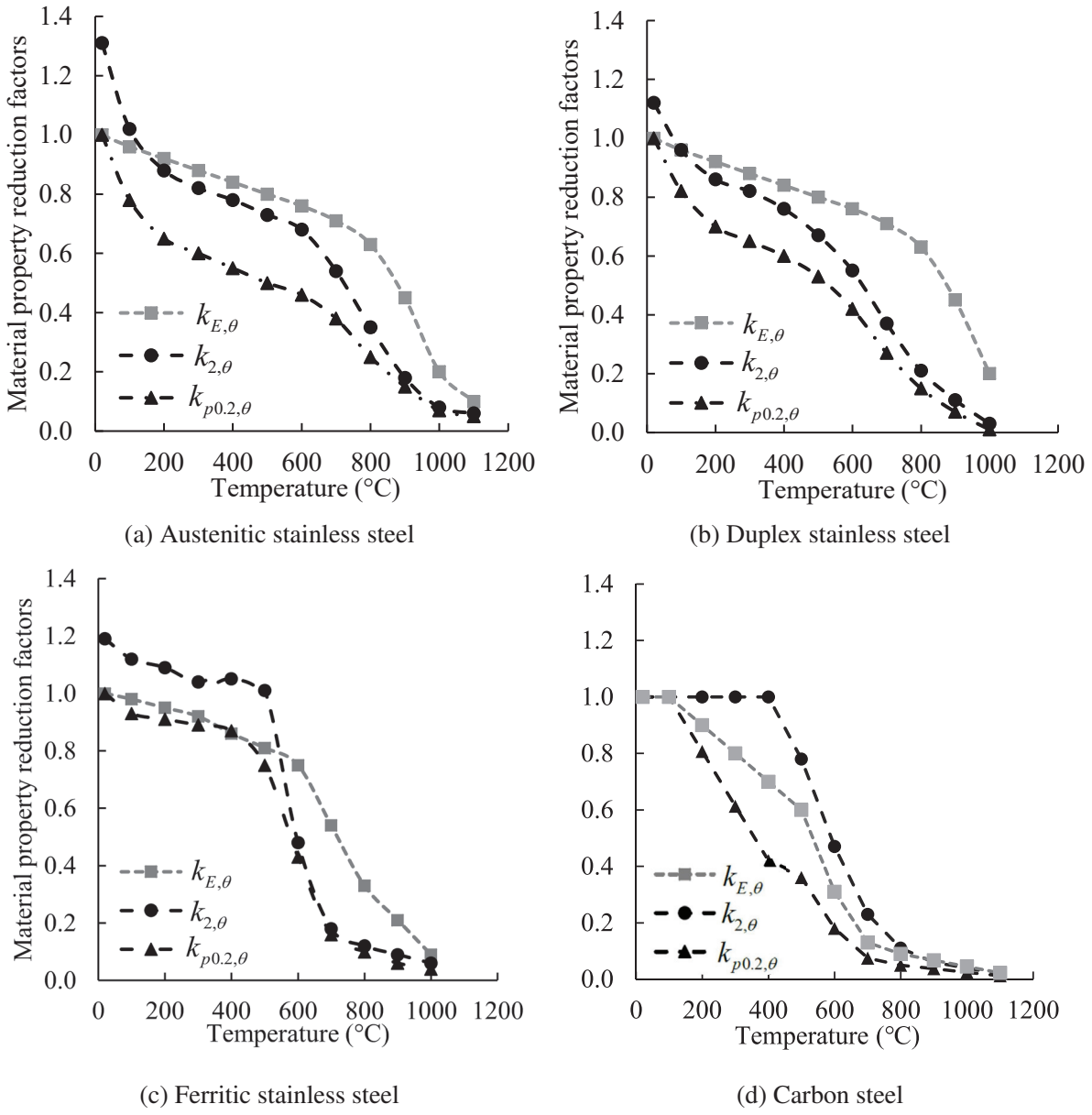

(a) Austenitic stainless steel

(b) Duplex stainless steel

(c) Ferritic stainless steel

(d) Carbon steel

Figure 2.2: Comparison of strength ($k_{2,\theta}$, $k_{p0.2,\theta}$) and stiffness ($k_{E,\theta}$) reduction factors for different stainless steel grades considered in this thesis and carbon steel at elevated temperatures

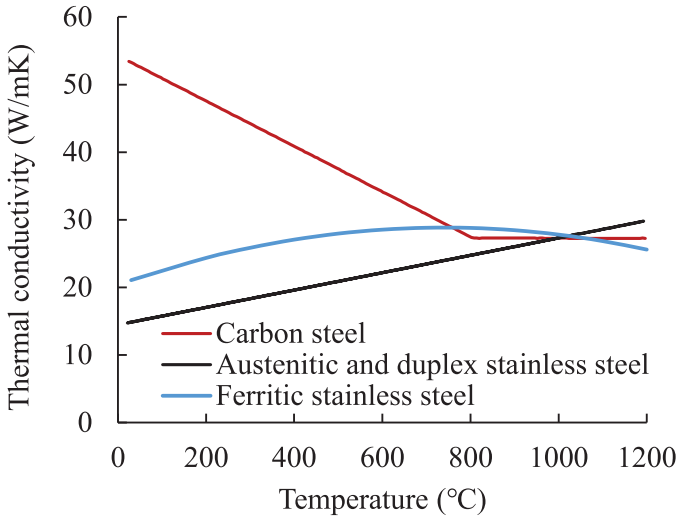

Figure 2.3: Thermal conductivity for stainless steel and carbon steel at elevated temperatures

2.3 Fire tests

Standard fire testing of simple building components is the most common method for demonstrating the structural performance of buildings in fire. In recent years, there have been a wide range of standard fire tests on columns (Feng *et al.*, 2003; Han *et al.*, 2003; Tan *et al.*, 2007; Li *et al.*, 2010; Maraveas *et al.*, 2016), beams (Liu *et al.*, 2002; Ding & Wang, 2007; Li & Guo, 2008; Bihina *et al.*, 2013; Ukomski *et al.*, 2017), beam-columns (Han, 2001; Tao & Han, 2007; Dwaikat *et al.*, 2011) and connections (Wang *et al.*, 2010b; Cai & Young, 2014; Ozyurt *et al.*, 2014; Cai & Young, 2016; Lan *et al.*, 2018). In addition to the standard fire tests, extensive post-fire tests of simple building components have also been carried out to study their structural behaviour after exposure to elevated temperatures (Han *et al.*, 2005; Wang *et al.*, 2010a; Liu *et al.*, 2014; He *et al.*, 2019; Cai & Young, 2019; He *et al.*, 2020). Previous fire tests on stainless steel structural components at the cross-section and member levels are reviewed in this section.

There are two commonly adopted testing methods to evaluate the response of steel structures at elevated temperatures, which are known as isothermal and anisothermal testing methods. In

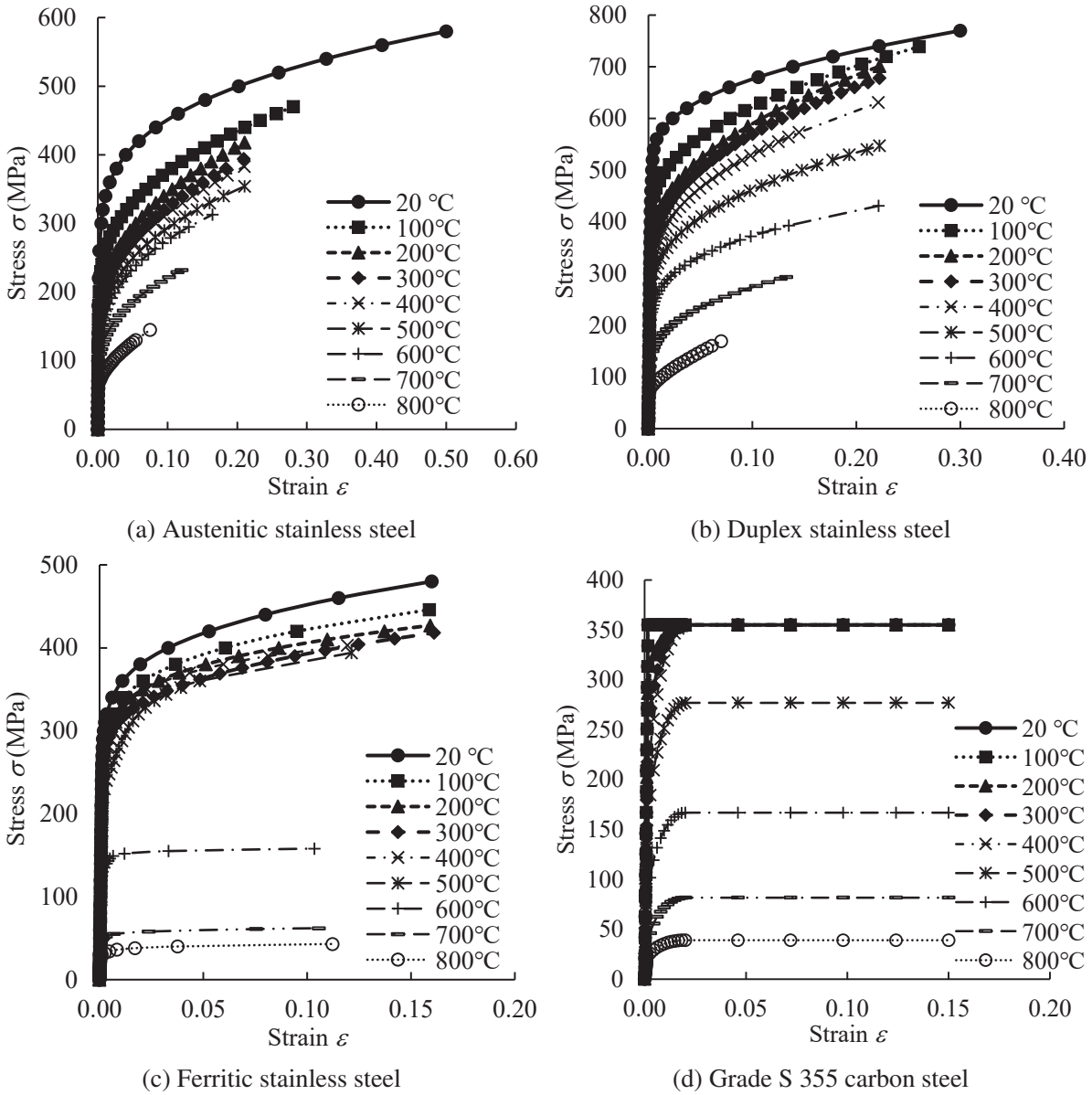

(a) Austenitic stainless steel

(b) Duplex stainless steel

(c) Ferritic stainless steel

(d) Grade S 355 carbon steel

Figure 2.4: Stress-strain response of different stainless steel grades considered in this thesis and carbon steel at elevated temperatures

the isothermal testing method, a test specimen is heated up to a certain temperature, and then a mechanical load is applied to the specimen until failure. The obtained ultimate load during testing is taken as the ultimate resistance of the test specimen at this temperature. Conversely, in the anisothermal testing method, the mechanical load is first applied to the test specimen and then the specimen is heated until failure. ISO-834 (1999) gives the standard heating curve for anisothermal fire tests, in which the average furnace temperature is controlled such that it follows the relationship:

$$T = 345log_{10}(8t + 1) + 20, \tag{2.1}$$

where T is the average furnace temperature in degrees Celsius and t is the time in minutes (see Fig. 2.5).

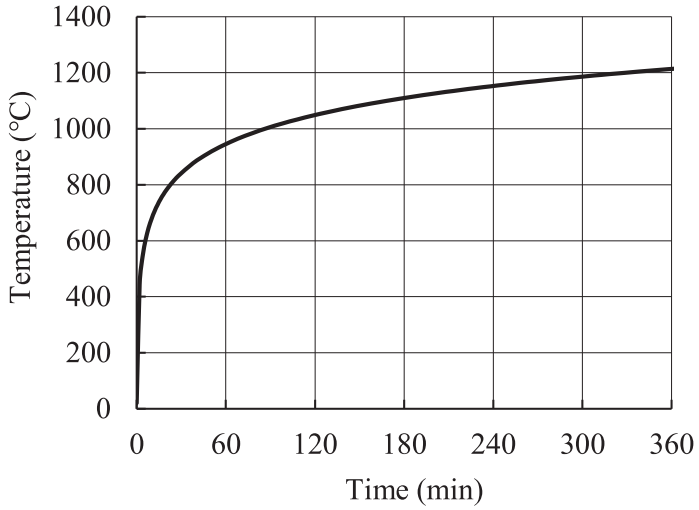

Figure 2.5: Standard heating curve (ISO-834, 1999)

In anisothermal testing, the fire resistance of a test specimen, therefore, is expressed in terms of critical temperature θ_{cr} for which the specimen no longer resist the pre-applied load. All the fire tests summarised in this section adopted the anisothermal testing method since it is more representative of a real fire situation than the isothermal testing method (Gardner & Baddoo, 2006; Wang *et al.*, 2012).

2.3.1 Cross-section behaviour

A series of fire tests have been performed to investigate the cross-section behaviour of stainless steel components at elevated temperatures, which included stub column tests (Uppfeldt *et al.*, 2008) and beam tests (Zhao & Blanguernon, 2004; Gardner & Baddoo, 2006). As reported by Uppfeldt *et al.* (2008), six stub column tests were carried out at elevated temperatures with the test setup of Fig. 2.6, whose experimental results are summarised in Table 2.1, where L is the column length and N_{Ed} is the pre-applied axial load.

Figure 2.6: Stub column test setup at elevated temperatures (Uppfeldt *et al.*, 2008)

The basic information and key results of the beam tests in fire are summarised in Table 2.2, where M_{Ed} is the pre-applied moment. As can be seen from this table, the seven beam fire tests include three top-hat sections, one rectangular hollow section made up of two channel sections welded tip-to-tip, one I-section made up of two channel sections welded back-to-back and two conventional I-sections. All the tested beams reported by Gardner & Baddoo (2006) supported a concrete slab with the purpose of achieving full lateral restraint as shown in Fig. 2.7.

Table 2.1: Stainless steel stub column tests in fire (Uppfeldt *et al.*, 2008)

Stainless steel grade	Cross-section	L (mm)	N_{Ed} (kN)	θ_{cr} (°C)
Austenitic (1.4301)	RHS 150×150×3	900	203	676
	RHS 150×150×3	900	165	720
	RHS 150×150×3	900	248	588
	RHS 200×200×5	900	694	609
	RHS 200×200×5	900	567	685
	RHS 200×200×5	900	463	764

Further details, including the load configurations and test setup, have been described by Zhao & Blanguernon (2004) and Gardner & Baddoo (2006).

Table 2.2: Summary of stainless steel beam tests in fire

Reported by	Stainless steel grade	Cross-section	M_{Ed} (kNm)	θ_{cr} (°C)
Zhao & Blanguernon (2004)	Austenitic (1.4318)	Top hat H100×100×2	2.38	880
		Top hat H100×100×2	4.37	765
		Top hat H100×100×2	5.46	805
Gardner & Baddoo (2006)	Austenitic (1.4301)	RHS 200×125× 6	27.8	884
		][200×150×6	17.2	944
		I 20×64	15.2	650
		I 20×64	8.9	840

2.3.2 Member behaviour

There have been a number of experimental studies on the response of stainless steel members exposed to fire. Fire tests on a total of 39 columns (Ala-Outinen & Oksanen, 1997; Zhao & Blanguernon, 2004; Gardner & Baddoo, 2006; Tondini *et al.*, 2013; Fan *et al.*, 2016; Liu *et al.*, 2019) and 9 beam-columns (Fan *et al.*, 2016, 2018) have been reported. The materials, nominal cross-section sizes, end conditions, specimen length L and the key experimental results for these fire tests are summarised in Table 2.3, Table 2.4 and Table 2.5, where e in Table 2.5 refers to the loading eccentricity in the beam-column tests. As can be seen from these tables, of the 48 member tests in fire, merely eight were performed on I-sections, while the remainder were mainly performed on square and rectangular hollow sections.

Table 2.3: Summary of stainless steel column tests in fire: Part 1

Reported by	Stainless steel grade	Cross-section	End conditions	L (mm)	N_{Ed} (kN)	θ_{cr} (°C)
Ala-Outinen & Oksanen (1997)	Austenitic (1.4301)	RHS 40×40×4	Pinned	888	44.6	872.7
		RHS 40×40×4	Pinned	888	129.4	579.0
		RHS 40×40×4	Pinned	888	114.4	648.7
		RHS 40×40×4	Pinned	888	94.6	709.9
		RHS 40×40×4	Pinned	888	54.8	831.7
		RHS 40×40×4	Pinned	888	74.7	766.4
Ala-Outinen (1999)	Austenitic (1.4571)	RHS 40×40×4	Pinned	888	102	720
		RHS 40×40×4	Pinned	888	73	834
		RHS 40×40×4	Pinned	888	63	873
	Austenitic (1.4301)	RHS 30×30×3	Pinned	888	41	610
		RHS 30×30×3	Pinned	888	33	693
		RHS 30×30×3	Pinned	888	21	810
		CHS 33.7×2	Pinned	888	26	668
		CHS 33.7×2	Pinned	888	12	850
		CHS 33.7×2	Pinned	888	20	716
Zhao & Blanguernon (2004)	Austenitic (1.4318)	RHS 100×100×3	Pinned	3615	52	880
		RHS 100×100×3	Pinned	3615	52	835
Gardner & Baddoo (2006)	Austenitic (1.4301)	RHS 150×100×6	Fixed	3400	268	801
		RHS 150×75×6	Fixed	3400	140	883
		RHS 100×75×6	Fixed	3400	156	806
		I 200×150×6	Fixed	3400	413	571
		SHS 100×100×4	Pinned	3990	80	835
		SHS 200×200×4	Pinned	3990	230	820
Tondini *et al.* (2013)	Ferritic (1.4003)	SHS 80×80×3	Fixed	3000	72	709
		SHS 80×80×4	Fixed	2500	78	708
		RHS 120×80×3	Fixed	2500	100	705

Table 2.4: Summary of stainless steel column tests in fire: Part 2

Reported by	Stainless steel grade	Cross-section	End conditions	L (mm)	N_{Ed} (kN)	θ_{cr} (°C)
Fan *et al.* (2016)	Austenitic (1.4301)	SHS 100×4	Pinned	3300	85	>742.0
		SHS 100×4	Pinned	3300	120	720.8
		SHS 100×4	Pinned	3300	152	642.4
		SHS 120×4	Pinned	3300	132	793.0
		SHS 120×4	Pinned	3300	184	723.0
		SHS 120×4	Pinned	3300	236	593.0
Liu *et al.* (2019)	Austenitic (1.4301)	I 120×120×6×8	Pinned	2800	55.7	520
		I 120×120×6×8	Pinned	2800	83.6	579
		I 150×125×6×8	Pinned	2800	131.6	515
		I 150×125×6×8	Pinned	2800	98.7	583
		I 150×125×6×8	Pinned	2800	79.2	639
		I 120×120×6×6	Fixed	3150	127.2	578
		I 120×120×6×6	Fixed	3150	105.9	622

Table 2.5: Summary of stainless steel beam-column tests in fire

Reported by	Stainless steel grade	Cross-section	End conditions	L (mm)	e (mm)	N_{Ed} (kN)	θ_{cr} (°C)
Fan *et al.* (2016)	Austenitic (1.4301)	SHS 120×4	Pinned	3300	13.2	700.8	160
		SHS 120×4	Pinned	3300	23.8	655.0	140
Fan *et al.* (2018)	Austenitic (1.4301)	RHS 120×120×5	Pinned	3300	20	495	94
		RHS 140×120×5	Pinned	3300	20	575	83
		RHS 140×120×5	Pinned	3300	20	509	116
		RHS 140×120×5	Pinned	3300	20	583	133
		RHS 140×120×5	Pinned	3300	30	630	104
		RHS 140×120×5	Pinned	3300	40	560	94
		RHS 160×120×5	Pinned	3300	20	593	138

Figure 2.7: Beam test setup at elevated temperatures (Gardner & Baddoo, 2006)

2.4 Numerical studies

A number of numerical studies have been performed to provide a further insight into the structural response of stainless steel components at elevated temperatures. The finite element software ABAQUS (2014) has been successfully adopted in many previous studies to simulate the non-linear response of carbon steel components in fire (Feng *et al.*, 2004; Chen & Young, 2007; Knobloch *et al.*, 2008; Wang *et al.*, 2010a; Young & Ellobody, 2011; Albrifkani & Wang, 2020) and stainless steel components in fire (Ng & Gardner, 2007; Uppfeldt *et al.*, 2008; Afshan *et al.*, 2013; Liu *et al.*, 2018; Cai & Young, 2018; Ding *et al.*, 2019; Mohammed & Afshan, 2019; Pournaghshband *et al.*, 2019b). SAFIR is another finite element package that has been successfully used to mimic the behaviour of stainless steel components subjected to fire (Lopes *et al.*, 2010a,b, 2012, 2019). This section summarises the modelling assumptions relevant to the FE analysis in the thesis, as well as previous numerical studies into the behaviour of stainless steel structures in fire.

2.4.1 Numerical modelling

The software ABAQUS (2014) is used in the numerical studies carried out in this thesis. Relevant assumptions adopted in these numerical studies, including element type, material modelling, geometric imperfections and analysis technique, are discussed herein.

Element type

There are a wide range of finite elements in the ABAQUS (2014) element library for different modelling purposes, of which shell elements are often adopted to simulate thin-walled structures so as to decrease the computational time without compromising the accuracy of the numerical results, relative to solid elements. The S4R element – a four-noded reduced integration general purpose shell finite element – is used to create all the finite element models in this thesis; this is in line with similar previous numerical studies on the response of stainless steel structures at room temperature (Zhou & Young, 2007; Theofanous *et al.*, 2009; Huang & Young, 2012; Saliba & Gardner, 2013; Zhao *et al.*, 2015b) and elevated temperatures (Ng & Gardner, 2007; Tao *et al.*, 2016; Mohammed & Afshan, 2019; Pournaghshband *et al.*, 2019a).

Material modelling

In ABAQUS (2014), the material properties are required to be defined in the format of true stress-log plastic strain for the chosen element type. Therefore, the engineering stress-strain curves obtained from tensile coupon tests or predictive material models, normally represented by the two-stage compound Ramberg–Osgood material model, should be converted into true-stress-log plastic strain by:

$$\sigma_{\text{true}} = \sigma_{\text{nom}}\left(1+\varepsilon_{\text{nom}}\right), \tag{2.2}$$

$$\varepsilon_{\text{ln}}^{\text{pl}} = ln\left(1+\varepsilon_{\text{nom}}\right) - \frac{\sigma_{\text{true}}}{E}, \tag{2.3}$$

before being inputted into ABAQUS (2014), where σ_{true} is the true stress, ε_{ln}^{pl} is the log plastic strain, σ_{nom} is the engineering stress and ε_{nom} is the engineering strain.

Geometric imperfections

Both local and global geometric imperfections have an inevitable influence on the stability of structural members and should generally be incorporated into finite element models. Since the shape of geometric imperfections are typically unknown in practice, eigenmode-affine imperfection shapes are generally utilized to represent the least favourable imperfection pattern (Gardner & Nethercot, 2004; Ashraf *et al.*, 2006). The amplitude of the geometric imperfections is normally taken as the measured values during the validation of finite element models, and as predicted or tolerance-related values in parametric studies. Further details about the local and global geometric imperfections adopted in this thesis are given in the later chapters.

Analysis techniques

The finite element models in this thesis are analysed isothermally where initially a uniform temperature increase to a predefined temperature θ is assumed, which is represented by the modification of the material response, and then the loading is applied at the predefined elevated temperature θ. The modified Riks analysis is employed to perform the Geometrically and Materially Nonlinear Analyses with Imperfections (GMNIA) to trace the full load-displacement response of the structural members.

2.4.2 Cross-section behaviour

Gardner (2007) performed a numerical study into the local buckling response of stainless steel rectangular hollow sections, whose results were then utilised to develop a new approach to classify cross-sections and treat local buckling. In the new cross-section classification approach of

Gardner (2007), the material factor at elevated temperatures ε_θ was taken as:

$$\varepsilon_\theta = \left[\frac{k_{E,\theta}}{k_{2,\theta}}\right]^{0.5} \varepsilon \quad \text{for Class 1 and 2 sections,} \tag{2.4}$$

$$\varepsilon_\theta = \left[\frac{k_{E,\theta}}{k_{\mathrm{p0.2},\theta}}\right]^{0.5} \varepsilon \quad \text{for Class 3 and 4 sections,} \tag{2.5}$$

where $k_{E,\theta}$ is the stiffness reduction factor at elevated temperatures, $k_{2,\theta}$ and $k_{\mathrm{p0.2},\theta}$ are the strength reduction factors at elevated temperatures and ε is the material factor at room temperature, noting that cross-sections initially classified at room temperature should be re-classified utilizing the ε_θ defined in eqs. (2.4) and (2.5). When determining the cross-section resistances of stainless steel components in fire, the strength reduction factor was based on $k_{2,\theta}$ for Class 1 and 2 sections and $k_{\mathrm{p0.2},\theta}$ for Class 3 and 4 sections. The proposed methods of Gardner (2007) were shown to yield significant improvements in the prediction of cross-section resistances of stainless steel components in fire. More details of these proposed methods were provided by Ng & Gardner (2007). The cross-section classification approach of Gardner (2007) was also assessed and supported by Uppfeldt *et al.* (2008) on the basis of their findings from parametric numerical studies of stainless steel columns at elevated temperatures.

Since the previous numerical studies into the cross-section behaviour of stainless steel structures in fire are rather limited in number, relevant studies on carbon steel are also summarised herein so as to provide benchmark references for the fire design of stainless steel cross-sections. Based on a numerical parametric study, Ranby (1998) showed that while use of the elevated temperature strength at 2% total strain $f_{2,\theta}$ as the reference strength leads to accurate ultimate cross-section strength predictions for Class 1, 2 and 3 cross-sections owing to the attainment of high strains levels in structural elements in fire, adoption of the elevated temperature 0.2% proof strength $f_{\mathrm{p0.2},\theta}$ is generally more appropriate for Class 4 cross-sections since local buckling precludes the attainment of high strain levels. The recommendations of Ranby (1998) were adopted in EN 1993-1-2 (CEN, 2005). However, recently, Couto *et al.* (2014) highlighted shortcomings of this approach, particularly at the transition between Class 3 and Class 4 cross-sections where a discontinuity in strength predictions exists due to the adoption of the different reference strengths

(i.e. $f_{2,\theta}$ and $f_{\mathrm{p0.2},\theta}$). To eliminate this discontinuity, the use of the elevated temperature strength at 2% total strain $f_{2,\theta}$ for the ultimate cross-section strength predictions of all cross-sections regardless of their class was proposed, in conjunction with a new set of effective width formulations for the local buckling assessment of carbon steel plates in fire.

2.4.3 Member behaviour

The behaviour of stainless steel members subjected to fire has been investigated in a number of numerical studies. Ng & Gardner (2007) utilised the physical tests reported by Gardner & Baddoo (2006) to validate their numerical models; the validated models were then employed to assess the accuracy of the design provisions provided in EN 1993-1-2 (CEN, 2005). A revised buckling curve with the plateau length $\bar{\lambda}_0$ of 0.2 and the imperfection factor α of 0.55 was also proposed by Ng & Gardner (2007). Uppfeldt *et al.* (2008) carried out a series of numerical simulations of stainless steel columns at elevated temperatures, and recommended the use of the room temperature buckling curve with the temperature-dependent plateau length $\bar{\lambda}_{0,\theta}$ calculated as:

$$\bar{\lambda}_{0,\theta} = \bar{\lambda}_0 \left[\frac{k_{\mathrm{p0.2},\theta}}{k_{E,\theta}} \right]^{0.5} \tag{2.6}$$

for the fire design of stainless steel members with Class 4 cross-sections. Lopes *et al.* (2010a) performed numerical studies into the flexural buckling response of welded stainless steel I-section columns at elevated temperatures, observing some limitations in the current design methods provided in EN 1993-1-2 (CEN, 2005). Afshan *et al.* (2013) created numerical models able to mimic the response of ferritic stainless steel SHS and RHS columns subjected to fire; comprehensive structural performance data were then generated to compare with the buckling curves provided in EN 1993-1-2 (CEN, 2005) and its modified versions proposed by Ng & Gardner (2007) and Uppfeldt *et al.* (2008). Liu *et al.* (2018) conducted extensive numerical studies into the structural behaviour of stainless steel RHS beam-columns at elevated temperatures. Ding *et al.* (2019) performed numerical simulations of stainless steel I-section columns subjected to fire. Lopes *et al.* (2019) carried out numerical parametric studies on stainless steel beam-columns

in fire, also, along with (Mohammed & Afshan, 2019), assessing the accuracy of current design provisions given in EN 1993-1-2 (CEN, 2005). However, although drawbacks to the current design provisions were highlighted, a comprehensive approach to the design of stainless steel members in fire has yet to be established and the full range of contributing parameters has yet to be systematically explored.

2.5 European fire design standard

EN 1993-1-2 (CEN, 2005) is the European design standard covering the fire design of stainless steel structures. Since this research study is performed with the primary purpose of providing revised design rules for the upcoming version of EN 1993-1-2, the development of EN 1993-1-2 (CEN, 2005) and the current fire design provisions for stainless steel structures in this standard are introduced in this section.

2.5.1 Development of EN 1993-1-2

The European pre-standard ENV 1993-1-2 (ENV, 1995) was drafted by the European Committee for Standardization (CEN) in 1995. A National Application Document (NAD) was then incorporated into ENV 1993-1-2 (ENV, 1995) to enable this ENV to be utilized in the fire design of buildings constructed in the UK, which was known as the draft for development (DD) of ENV 1993-1-2 (ENV, 2001). However, although the DD ENV 1993-1-2 (ENV, 2001) stated that the performance of stainless steel structures in fire was usually significantly better than that of carbon steel, it still merely directed the designers to the methods of carbon steel to determine the resistances of stainless steel structures subjected to fire. Four years later, the full European fire design standard EN 1993-1-2 (CEN, 2005) was published to replace the DD ENV 1993-1-2 (ENV, 2001) version and is still in use today.

2.5.2 Design rules for local buckling

The current EN 1993-1-2 (CEN, 2005) directs designers to the methods presented in EN 1993-1-4 (CEN, 2015) for the local buckling assessment of stainless steel cross-sections in fire, despite the significantly varying material response of stainless steel at elevated temperatures. However, the design methods in EN 1993-1-4 (CEN, 2015) were developed considering the room temperature local buckling response of stainless steel cross-sections, thus typically failing to accurately represent the local buckling behaviour of stainless steel cross-sections in fire. Fig. 2.8 shows the cross-section resistance determined by EN 1993-1-2 (CEN, 2005) for stainless steel structural elements in fire, where A is the gross cross-section area, W_{pl} and W_{el} refer to the plastic and elastic section modulus, respectively, $f_{2,\theta}$ is the elevated temperature strength at 2% total strain and $f_{\mathrm{p0.2},\theta}$ is the elevated temperature 0.2% proof strength, $\bar{\lambda}_{\mathrm{p}}$ is the normalised plate slenderness and $\bar{\lambda}_{\mathrm{p0}}$ is the plateau length defining the transition between Class 3 and 4 sections. Since the elevated temperature strength at 2% total strain $f_{2,\theta}$ is utilized for Class 1–3 sections but the elevated temperature 0.2% proof strength $f_{\mathrm{p0.2},\theta}$ is utilized for Class 4 sections, there exists an abrupt step in the cross-section resistance at the transition between Class 3 and 4 sections, as shown in Fig. 2.8 (a) and (b), as well as between Class 2 and 3 sections owing to the use of the plastic and elastic resistances respectively, as shown in Fig. 2.8 (b).

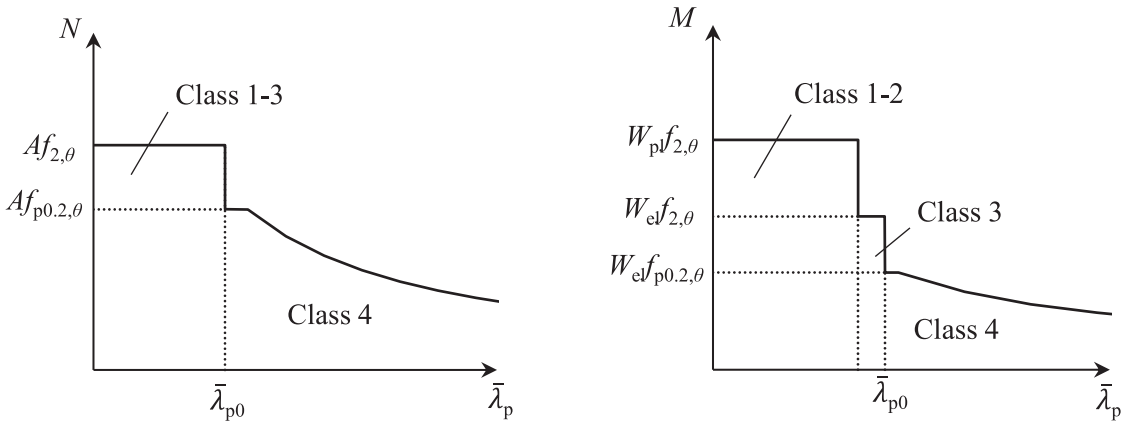

(a) Stainless steel cross-sections in compression (b) Stainless steel cross-sections in bending

Figure 2.8: Illustration of cross-section resistances in EN 1993-1-2 (CEN, 2005)

2.5.3 Design rules for global instability

The fire design rules for stainless steel members in the current EN 1993-1-2 (CEN, 2005) largely follow those for carbon steel, with the main difference being the material properties at elevated temperatures. The elevated temperature material properties of stainless steel have been incorporated into Annex C of EN 1993-1-2 (CEN, 2005) such that the scope of this standard extends to the fire design of stainless steel structures. However, owing to the intrinsically different material response of stainless steel relative to carbon steel at elevated temperatures, stainless steel structural elements exhibit a significantly different response in fire relative to their carbon steel counterparts (Lopes *et al.*, 2010a; Mohammed & Afshan, 2019). The design provisions given in the current EN 1993-1-2 (CEN, 2005) for stainless steel structural members in fire lead to, in some areas, an inconsistent design treatment relative to their actual behaviour at elevated temperatures.

2.6 Conclusions

An overview of the previous literature on stainless steel structures in fire relevant to this thesis has been presented in this chapter. In general, the previous experimental and numerical studies of stainless steel components in fire are rather limited and, moreover, the existing fire design rules for stainless steel structures have significant scope for improvement. This is particularly the case for stainless steel I-section components in fire. Therefore, experimental and numerical analysis of structural stainless steel I-section components subjected to fire and revising the existing fire design rules are the subject of this thesis.

Chapter 3

Local buckling of plates

3.1 Introduction

The local buckling response of stainless steel plates at elevated temperatures is investigated in this chapter. Finite element models of stainless steel plates are first created to replicate their behaviour in fire, and then validated against a series of experimental results from the literature. Shortcomings of the existing design provisions in EN 1993-1-2 (CEN, 2005) for the local buckling assessment of stainless steel plates in fire are illustrated through comparisons with the results from the validated finite element models. A new effective width-based design method, utilising the strength at 2% total strain $f_{2,\theta}$ as the reference strength, is proposed to determine the local buckling strength of stainless steel plates at elevated temperatures. The accuracy and reliability of the proposed method are thoroughly verified against the results from the nonlinear finite element modelling, considering various elevated temperature levels, stainless steel grades and plate slendernesses.

3.2 Finite element modelling

The development and validation of finite element models able to replicate the response of stainless steel plates in fire are presented in this section. The finite element models are used in Section 3.3 for the assessment of the current EN 1993-1-2 (CEN, 2005) design provisions and in Section 3.4 for the establishment and verification of the new proposals.

3.2.1 Development of finite element models

The finite element analysis software ABAQUS (2014) was used for all the numerical simulations carried out in the current study. Two categories of stainless steel plates were considered: (i) a 1600 mm $\times$ 400 mm plate with both longitudinal edges simply-supported, mimicking the response of the internal elements of stainless steel cross-sections and (ii) a 4000 mm $\times$ 400 mm plate with one longitudinal edge simply-supported and the other longitudinal edge free, replicating the response of outstand flanges of open stainless steel sections. Note that the dimensions of the internal stainless steel plate elements were selected in accordance with those adopted by Couto *et al.* (2014), while the dimensions of the outstand plate elements, which show no elastic buckling minimum and are more sensitive to length effects were modified to obtain elastic buckling stress values in closer agreement with analytical results for long plates (Trahair *et al.*, 2007; Gardner *et al.*, 2019; Fieber *et al.*, 2019). Finite element models of both hot-rolled and cold-formed stainless steel plates were created. The four-noded reduced integration general purpose shell finite element S4R (ABAQUS, 2014) was used to create all the finite element models. The element size was taken as 20 mm by 20 mm (i.e. 20 elements across the 400 mm plate width) for all plates. This mesh size was chosen on the basis of a prior mesh sensitivity study. It should be noted that in this study, grade 1.4301 austenitic, grade 1.4462 duplex and grade 1.4003 ferritic stainless steel were considered to generally represent the common grades of austenitic, duplex and ferritic stainless steel respectively.

To represent the elevated temperature stress-strain (σ-ε) response of stainless steel, the two-stage compound Ramberg–Osgood material model (Arrayago *et al.*, 2015; Mirambell & Real, 2000; Rasmussen, 2003) was utilised as given by eqs. (3.1) and (3.2):

$$\varepsilon = \frac{\sigma}{E_\theta} + 0.002\left(\frac{\sigma}{f_{\text{p0.2},\theta}}\right)^{n_\theta} \quad \text{for} \quad \sigma \leq f_{\text{p0.2},\theta} \tag{3.1}$$

$$\varepsilon = \frac{\sigma - f_{\text{p0.2},\theta}}{E_{\text{p0.2},\theta}} + \left(\varepsilon_{\text{u},\theta} - \varepsilon_{\text{p0.2},\theta} - \frac{f_{\text{u},\theta} - f_{\text{p0.2},\theta}}{E_{\text{p0.2},\theta}}\right)\left(\frac{\sigma - f_{\text{p0.2},\theta}}{f_{\text{u},\theta} - f_{\text{p0.2},\theta}}\right)^{m_\theta} + \varepsilon_{\text{p0.2},\theta} \quad \text{for} \quad f_{\text{p0.2},\theta} < \sigma \leq f_{\text{u},\theta}, \tag{3.2}$$

where n_θ and m_θ are strain hardening exponents, E_θ is the modulus of elasticity at temperature θ, and $E_{\text{p0.2},\theta}$ and $\varepsilon_{\text{p0.2},\theta}$ are the tangent modulus and total strain respectively corresponding to $f_{\text{p0.2},\theta}$ and $f_{\text{u},\theta}$ and $\varepsilon_{\text{u},\theta}$ are the ultimate tensile strength and strain at temperature θ. It was ensured that the second stage of the Ramberg-Osgood material model passed through $f_{2,\theta}$ and $f_{\text{u},\theta}$ exactly at 2% total strain and the ultimate strain $\varepsilon_{\text{u},\theta}$ respectively by adopting m_θ values calculated from:

$$m_\theta = \frac{\ln\left(\dfrac{0.02 - \varepsilon_{\text{p0.2},\theta} - \dfrac{f_{2,\theta} - f_{\text{p0.2},\theta}}{E_{\text{p0.2},\theta}}}{\varepsilon_{\text{u},\theta} - \varepsilon_{\text{p0.2},\theta} - \dfrac{f_{\text{u},\theta} - f_{\text{p0.2},\theta}}{E_{\text{p0.2},\theta}}}\right)}{\ln\left(\dfrac{f_{2,\theta} - f_{\text{p0.2},\theta}}{f_{\text{u},\theta} - f_{\text{p0.2},\theta}}\right)} \tag{3.3}$$

as illustrated in Fig. 3.1. The elevated temperature material properties (i.e. $f_{\text{p0.2},\theta}$, $f_{2,\theta}$, $f_{\text{u},\theta}$, $\varepsilon_{\text{u},\theta}$ and E_θ) utilised in the Ramberg-Osgood material model given in eqs. (3.1) and (3.2) were determined by multiplying the standardised room temperature material properties set out in (Afshan *et al.*, 2019) by the corresponding strength ($k_{\text{p0.2},\theta}$, $k_{2,\theta}$), stiffness ($k_{\text{E},\theta}$) and ductility ($k_{\varepsilon_{\text{u},\theta}}$) reduction factors given in the SCI Structural Stainless Steel Design Manual (SCI, 2017), which are based on the results from extensive elevated temperature material testing (Gardner *et al.*, 2010, 2016a; Chen & Young, 2006; Ala-Outinen & Oksanen, 1997), i.e. $f_{\text{p0.2},\theta} = k_{\text{p0.2},\theta} f_{\text{y}}$,

$f_{2,\theta} = k_{2,\theta} f_y$, $E_\theta = k_{E,\theta} E$, $f_{u,\theta} = k_{u,\theta} f_u$ and $\varepsilon_{u,\theta} = k_{\varepsilon_{u,\theta}} \varepsilon_u$. The standardised room temperature material properties (Afshan *et al.*, 2019) of hot-rolled and cold-formed austenitic, duplex and ferritic stainless steel plates used to determine $f_{p0.2,\theta}$, $f_{2,\theta}$, $f_{u,\theta}$, $\varepsilon_{u,\theta}$ and E_θ are given in Table 3.1, where f_y is the 0.2% proof stress, f_u is the ultimate tensile strength, ε_u is the ultimate tensile strain and n is the Ramberg-Osgood exponent used to define the first stage of the stress-strain response. In accordance with the recommendations made in SCI (2017), the elevated temperature Ramberg-Osgood exponents n_θ used in eqs. (3.1) and (3.2) were taken equal to the room temperature values n given by Afshan *et al.* (2019), which are shown in Table 3.1.

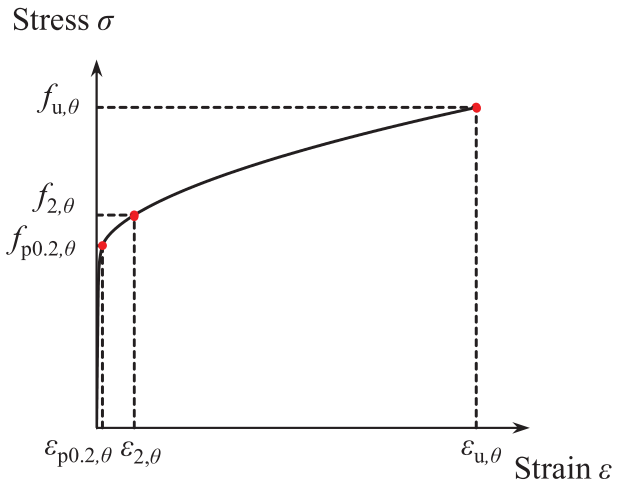

Figure 3.1: Two-stage elevated temperature Ramberg-Osgood material model adopted in FE models

The boundary conditions applied to the finite element models of the internal and outstand stainless steel plates are illustrated in Fig. 3.2. As can be seen from the figure, to simulate simply-supported restraint conditions along the longitudinal edges, only the vertical translations were restrained (i.e. $U3 = 0$). For the loaded edges, the vertical translations were also restrained (i.e. $U3 = 0$) in addition to the horizontal translations (i.e. $U2 = 0$) at the mid-width nodes. Finally, the mid-width node of one of the loaded edges were restrained along the longitudinal direction ($U1 = 0$). Loading was applied as point forces and/or bending moments to reference points constrained to the loaded edges as shown in Fig. 3.2. Elastic buckling stresses obtained from the

Table 3.1: Summary of room temperature material properties for austenitic, duplex and ferritic stainless steel grades used in this study

Material properties used for hot-rolled plates					
Material grade	E (GPa)	f_y (MPa)	f_u (MPa)	ε_u	$n_\theta (= n)$
Austenitic	200	280	580	0.50	9.1
Duplex	200	530	770	0.30	9.3
Ferritic	200	320	480	0.16	17.2
Material properties used for cold-formed plates					
Material grade	E (GPa)	f_y (MPa)	f_u (MPa)	ε_u	$n_\theta (= n)$
Austenitic	200	460	700	0.20	7.1
Duplex	200	630	780	0.13	7.5
Ferritic	200	430	490	0.06	11.5

Linear Buckling Analyses (LBA) of the developed finite element plate models were compared against elastic buckling stresses calculated using the formulae provided in (Timoshenko & Gere, 1961); excellent agreement was observed between the numerically and analytically determined elastic buckling stress values, verifying the appropriateness of the boundary and loading conditions applied to the finite element models.

The lowest eigenmode-affine imperfection shapes obtained from Linear Buckling Analyses (LBA) of the modelled plates, as shown in Fig. 3.3, were used to define the shapes of local geometrical imperfections in the finite element simulations; these imperfection shapes were scaled to 1/200 of the plate widths for the internal elements and 1/50 of the plate widths for the outstand flanges in accordance with the recommendations made in EN 1993-1-5 (CEN, 2006). Considering their negligible effect on the ultimate resistances of steel plates at elevated temperatures, as shown in (Couto *et al.*, 2014), residual stresses were not explicitly taken into account in the finite element models created herein, though their influence does inherently feature in the stress-strain properties of the cold-formed material (Jandera *et al.*, 2008). Typical failure modes from the finite element models of the internal and outstand stainless steel plates under compression are illustrated in Fig. 3.4.

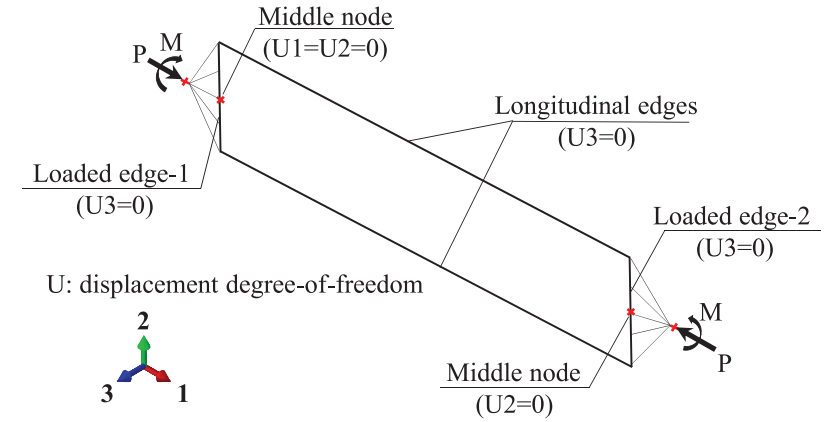

(a) Internal element

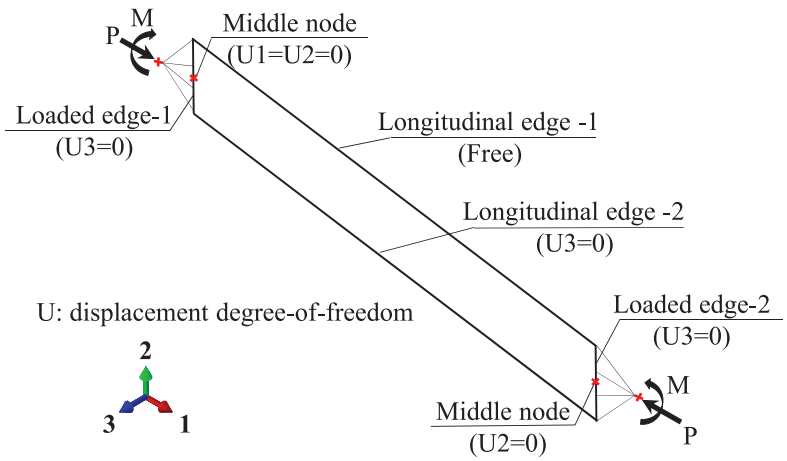

(b) Outstand flange

Figure 3.2: Boundary conditions applied to the FE models of stainless steel internal elements and outstand flanges

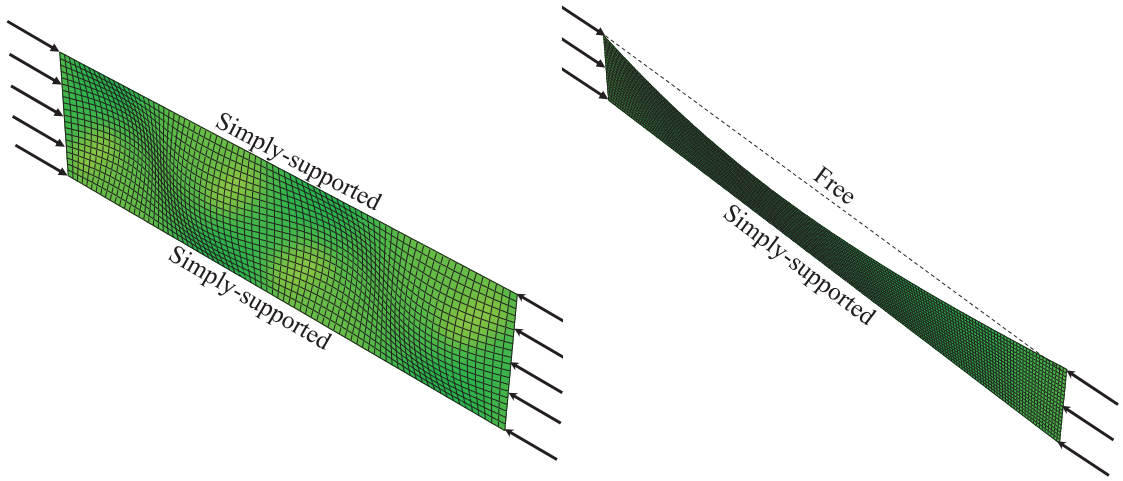

Figure 3.3: Lowest eigenmodes for internal elements (left) and outstand flanges (right) used to apply geometrical imperfections in subsequent nonlinear analyses

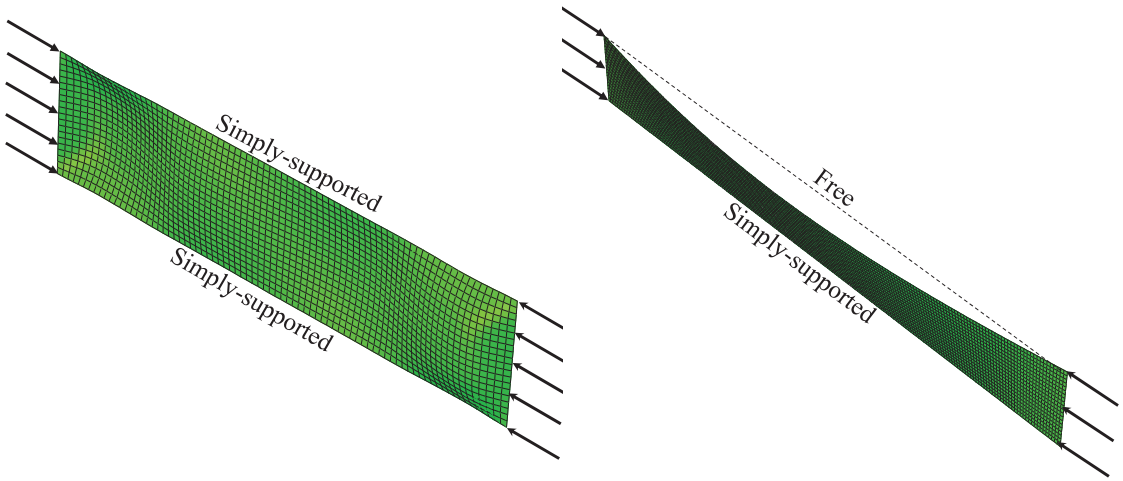

Figure 3.4: Typical failure modes of compressed internal elements (left) and outstand flanges (right) in fire

3.2.2 Validation of numerical models

The adopted finite element modelling approach has been validated (i) through comparisons of the FE results with the results obtained from fire experiments carried out on stainless steel hollow section stub columns by Uppfeldt *et al.* (2008) and on stainless steel beams by Gardner & Baddoo (2006) and (ii) by reference to the existing study (Couto *et al.*, 2014) where the same simulation strategy has been employed.

Uppfeldt *et al.* (2008) tests

The finite element modelling approach adopted in this study for stainless steel plates in compression was validated using the experimental results of Uppfeldt *et al.* (2008), where six stainless steel square hollow section (SHS) stub columns were tested in fire. On the basis of the stub column failure loads reported in (Uppfeldt *et al.*, 2008), the experimental failure loads of the plates constituting the stub columns were calculated considering their corresponding areas and compared against the numerical failure loads of the plates. In the finite element models of the plates, the plate sizes were determined considering the flat parts and corner regions of the stub columns of Uppfeldt *et al.* (2008) as shown in Fig. 3.5, taking the thicknesses of the plates equal to the thicknesses of the stub columns t and the widths of the plates equal to the centreline widths of the stub column cross-sections $(h-t)$. Twenty elements were defined across the width of the modelled stainless steel plates and an element aspect ratio of unity (i.e. square elements) was maintained throughout. The two-stage compound Ramberg-Osgood material model given by eqs. (3.1) and (3.2) was used to define the material response of the specimens in fire, using the elevated temperature material properties determined by multiplying the strength and stiffness reduction factors given in SCI (2017) by the corresponding room temperature material properties of the specimens obtained from a series of tensile coupon tests reported by Uppfeldt *et al.* (2008). The enhanced strengths of the corner regions owing to cold-working were allowed for in the material properties of the plates by using the following expression to determine their weighted-

average room temperature 0.2% proof strengths:

$$f_{\mathrm{y}} = \frac{f_{\mathrm{y,flat}} A_{\mathrm{flat}} + f_{\mathrm{y,corner}} A_{\mathrm{corner}}}{A_{\mathrm{flat}} + A_{\mathrm{corner}}}, \tag{3.4}$$

where $f_{\mathrm{y,flat}}$ and $f_{\mathrm{y,corner}}$ are the 0.2% proof strengths of the flat and corner regions and A_{flat} and A_{corner} are the areas of the flat and corner regions, respectively. The local geometric imperfection amplitudes in the finite element models were taken as the measured values reported in (Uppfeldt *et al.*, 2008).

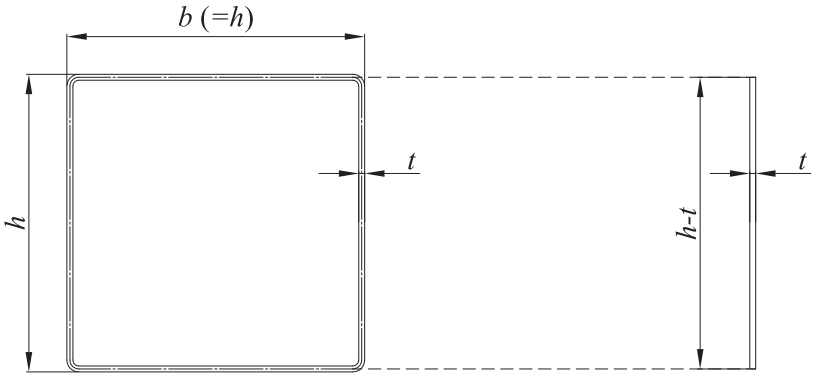

Figure 3.5: Definition of plate dimensions used in validation of numerical plate FE models against experiments performed by Uppfeldt *et al.* (2008) on stainless steel SHS in fire

Table 3.2 summarizes the failure loads of the plates determined from the tests $N_{\mathrm{u,test}}$ and those obtained from the finite element models $N_{\mathrm{u,FE}}$. As can be seen from the table, the $N_{\mathrm{u,FE}}$/ $N_{\mathrm{u,test}}$ values are generally close to unity with reasonable scatter, indicating that the finite element models are able to provide accurate estimations of the ultimate resistances of compressed stainless steel internal plate elements in fire.

Gardner & Baddoo (2006) tests

The finite element modelling approach adopted in this study for stainless steel internal plate elements in bending and outstand flanges in compression was validated using the results from three anisothermal tests performed on stainless steel beams at elevated temperatures reported in (Gard-

Table 3.2: Comparison of ultimate strengths of stainless steel plates obtained from physical experiments by Uppfeldt *et al.* (2008) and from FE analyses in this study

Section	f_y (20 °C) (MPa)	Temp. (°C)	$N_{u,test}$ (kN)	$N_{u,FE}$ (kN)	$N_{u,FE}/N_{u,test}$
SHS 200×200×5	360	609	176	169	0.96
SHS 200×200×5	360	685	144	145	1.01
SHS 200×200×5	360	764	118	115	0.98
SHS 150×150×3	405	676	51	57	1.11
SHS 150×150×3	405	720	42	48	1.16
SHS 150×150×3	405	588	63	62	0.99

ner & Baddoo, 2006), where one stainless steel rectangular hollow section (RHS) beam and two stainless steel I-section beams were tested in fire. Since the determination of the failure forces and moments of the isolated web and flange plates of the beams is not straightforward owing to the varying level of support afforded by the flange plates to the web plates and vice versa, the full beam cross-sections were modelled instead of the individual plates. The FE failure moments $M_{u,FE}$ were then compared against those obtained from the experiments $M_{u,test}$. Note that for the SHS stub columns considered in the previous section, all four internal plate elements have the same elastic local buckling stress and half-wavelength; the plates therefore buckle simultanously and mirror the response of isolated plates with simply-supoorted boundary conditions along the adjoined edges (Gardner *et al.*, 2019; Fieber *et al.*, 2019). In the full beam finite element models created herein, the element type and mesh size (i.e. 20 elements across the width of each plates and an element aspect raitos of unity) were taken to be the same as those employed in the finite element models of the individual plates. The measured material properties were taken as those measured in the corresponding experiments. The test and FE results are compared in Table 3.3, where it can be seen that there is close agreement between the two. Thus, further to the validation for stainless steel internal plate elements in compression presented in Section 3.2, the adopted finite element modelling approach is also considered to be appropriate for the simulation of stainless steel internal plate elements in bending and outstand flange elements in compression.

Table 3.3: Comparison of ultimate bending moments of stainless steel beams obtained from physical experiments by Gardner & Baddoo (2006) and from FE analyses in this study

Cross-section	f_y (20 °C) (MPa)	Temp. (°C)	$M_{u,test}$ (kNm)	$M_{u,FE}$ (kNm)	$M_{u,FE}/M_{u,test}$
RHS-200×125×6	262	884	27.8	26.4	0.95
I-200×150×6	262	944	17.2	17.4	1.01
I-120×64	275	650	15.2	14.4	0.95

3.2.3 Parametric studies

Upon validation of the numerical models, parametric studies were conducted to generate comprehensive structural performance data, taking into consideration different stainless steel grades (austenitic, duplex and ferritic), elevated temperature levels, plate thicknesses and loading conditions. In total, four temperature levels were considered: 200 °C, 400 °C, 600 °C and 800 °C. The plate thicknesses were varied to investigate the response of stainless steel plates with a spectrum of local plate slendernesses $\bar{\lambda}_p$ (see Section 3.3.2) ranging between 0.15 and 2.0. Thus, plate thicknesses ranging between about 2 mm and 80 mm were considered in the numerical parametric studies of the internal elements, while the thicknesses of the outstand elements were varied between about 12 mm and 200 mm. Note that, since relatively wide plates were considered (particularly for the outstand flanges), rather large plate thicknesses were needed to achieve low plate slenderness values. Stainless steel plates under compression, bending and combined compression and bending were considered. Combined compression and bending was applied such that the ratios ψ of the stresses applied at the edges of the plates (σ_1 and σ_2) were equal to 0.5, 0 and -0.5 (i.e. $\psi = \sigma_1/\sigma_2 = 0.5, 0, -0.5$).

3.3 Current EN 1993-1-2 design method for stainless steel in fire

The EN 1993-1-2 (CEN, 2005) cross-section classification and effective width-based design rules for determining the local buckling strengths of stainless steel plates in fire are briefly described in this section; their accuracy is then assessed against the results obtained from nonlinear finite element modelling.

3.3.1 Cross-section classification

For the classification of stainless steel cross-sections in fire, EN 1993-1-2 (CEN, 2005) directs the designer to EN 1993-1-4 (CEN, 2015) but with a reduced value for material factor ε_θ, where stainless steel cross-sections are grouped into four classes; the class of a cross-section is taken as the highest class of its constituent plates. Specific limiting width-to-thickness ratios, summarised in Table 3.4, are given for the constituent internal and outstand plates of stainless steel sections in EN 1993-1-4 (CEN, 2015) to determine their classes.

Table 3.4: Width-to-thickness limits for plate classification at room temperature

Element	Class 1	Class 2	Class 3
Internal element subjected to compression	33ε	35ε	37ε
Internal element subjected to bending	72ε	76ε	90ε
Outstand flanges subjected to compression	9ε	10ε	14ε

At elevated temperatures, the material factor ε_θ is calculated as:

$$\varepsilon_\theta = 0.85\varepsilon = 0.85\left[\frac{235}{f_y}\frac{E}{210000}\right]^{0.5} \quad \text{with } f_y \text{ and } E \text{ in MPa,} \tag{3.5}$$

where ε is the room temperature material factor given in EN 1993-1-4 (CEN, 2015); note that the definition of ε is due to be simplified to $\varepsilon = (235/f_y)^{0.5}$ in the upcoming version of the code. While this classification approach leads to the straightforward determination of the class

of a stainless steel cross-section in fire, it disregards the differential erosion of the strength and stiffness of stainless steel at different temperature levels, which is shown in Fig. 3.6. In fact, the 0.85 factor was originally derived considering the lowest value of the square root of the ratios of the stiffness reduction factors to the yield strength reduction factors $\sqrt{k_{E,\theta}/k_{2,\theta}}$ for carbon steel and is somewhat inappropriate for stainless steel, as shown in Fig. 3.6. Thus, despite its practicality, the cross-section classification approach provided in EN 1993-1-2 (CEN, 2005) does not provide a sound basis for assessing the response of stainless steel cross-sections at elevated temperatures.

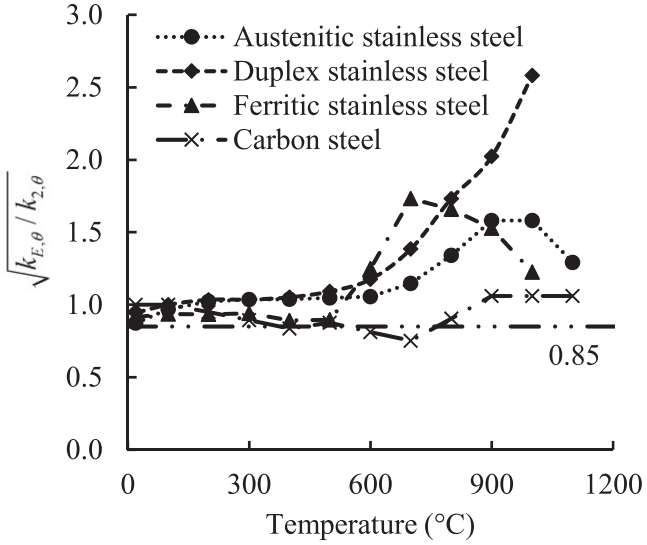

Figure 3.6: Variation of $\sqrt{k_{E,\theta}/k_{2,\theta}}$ for austenitic, duplex and ferritic stainless steel and carbon steel at different elevated temperature levels

3.3.2 Effective width method

Thin plates subjected to in-plane compressive loading exhibit a stable post-buckling response, enabling load-carrying capacities beyond the critical buckling load to be sustained. After buckling occurs, the stress distribution across the plate width becomes non-uniform. In the effective width method, this non-uniform stress distribution is simplified into two uniform stress blocks

with a width of $b_{\text{eff}}/2$ as shown in Fig. 3.7 and the effective widths of stainless steel plates are calculated using the following expression (Gardner & Theofanous, 2008):

$$b_{\text{eff}} = \rho b, \tag{3.6}$$

where ρ is the plate buckling reduction factor.

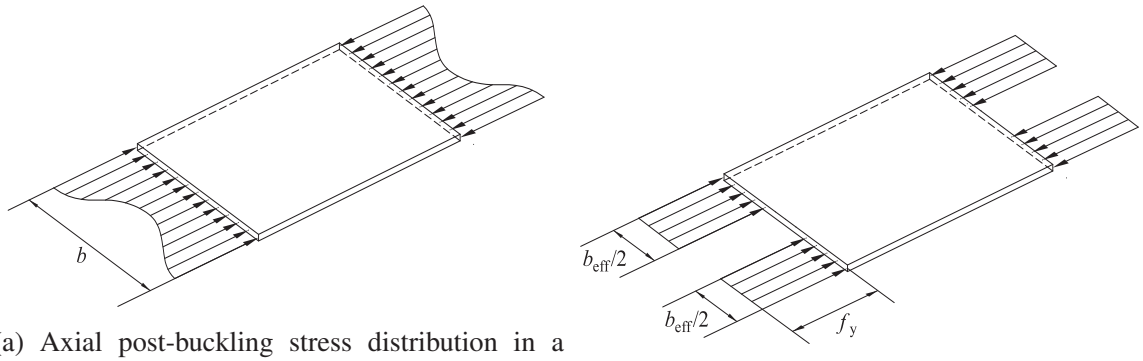

(a) Axial post-buckling stress distribution in a simply-supported plate

(b) Effective width method

Figure 3.7: Axial post-buckling stress distribution in a simply-supported plate and effective width method

EN 1993-1-2 (CEN, 2005) also directs the designer to EN 1993-1-4 (CEN, 2015) for the determination of the plate buckling reduction factor ρ based on room temperature material properties. For internal elements, ρ is calculated as:

$$\rho = \frac{0.772}{\bar{\lambda}_{\text{p}}} - \frac{0.079}{\bar{\lambda}_{\text{p}}^{\,2}} \quad \text{but} \quad \rho \leq 1.0, \tag{3.7}$$

while for the outstand flanges, ρ is determined from:

$$\rho = \frac{1}{\bar{\lambda}_{\text{p}}} - \frac{0.188}{\bar{\lambda}_{\text{p}}^{\,2}} \quad \text{but} \quad \rho \leq 1.0, \tag{3.8}$$

in which $\bar{\lambda}_{\text{p}}$ is the non-dimensional plate slenderness, calculated as:

$$\bar{\lambda}_{\text{p}} = \sqrt{\frac{f_{\text{y}}}{\sigma_{\text{cr}}}} = \frac{b/t}{28.4\varepsilon\sqrt{k_\sigma}}, \tag{3.9}$$

where σ_{cr} is the elastic buckling stress of the plate, t is the plate thickness and k_σ is the buckling coefficient determined on the basis of the stress distribution and edge boundary conditions of the plate as described in EN 1993-1-5 (CEN, 2006). Note that an alternative approach to treating local buckling on an element by element basis is to consider the elastic buckling stress of the full cross-section, as described in (Gardner *et al.*, 2019).

It is worth noting that while EN 1993-1-2 (CEN, 2005) requires the use of the elevated temperature material factor $\varepsilon_\theta = 0.85\varepsilon$ for the classification of stainless steel cross-sections in fire, it recommends the use of room temperature material properties for the determination of the effective cross-section areas and effective section moduli of Class 4 stainless steel cross-sections at elevated temperatures. This represents an inconsistency in the consideration of the structural response of stainless steel cross-sections in fire in that even though the influence of changes in the material properties at elevated temperatures on the cross-section response is considered in the cross-section classification (albeit somewhat inappropriately), it is disregarded in the calculations of effective section properties used to determine the ultimate resistances of Class 4 stainless steel cross-sections in fire.

3.3.3 Cross-section resistance

The cross-section resistance of stainless steel structural elements in fire is defined in EN 1993-1-2 (CEN, 2005) on the basis of the classification of the section, as summarised in Table 3.5, where $N_{fi,t,Rd}$ and $M_{fi,t,Rd}$ are the axial and bending design cross-section resistances in fire at time t, respectively, A_{eff} is the effective cross-sectional area, W_{eff} is the effective section modulus and $\gamma_{M,fi}$ is the partial factor for fire design. The calculation of cross-sectional resistances of stainless steel structural elements in fire can be seen to be similar to their determination at room temperature except for the use of the elevated temperature strength at 2% strain $f_{2,\theta}$ for Class 1, 2 and 3 sections and the elevated temperature 0.2% proof strength $f_{p0.2,\theta}$ for Class 4 sections.

Table 3.5: Determination of cross-sectional resistances in EN 1992-1-2 (CEN, 2005)

Cross-section classification	Design resistance in compression	Design resistance in bending
Class 1 and 2	$N_{\mathrm{fi,t,Rd}} = A f_{2,\theta}/\gamma_{\mathrm{M,fi}}$	$M_{\mathrm{fi,t,Rd}} = W_{\mathrm{pl}} f_{2,\theta}/\gamma_{\mathrm{M,fi}}$
Class 3	$N_{\mathrm{fi,t,Rd}} = A f_{2,\theta}/\gamma_{\mathrm{M,fi}}$	$M_{\mathrm{fi,t,Rd}} = W_{\mathrm{el}} f_{2,\theta}/\gamma_{\mathrm{M,fi}}$
Class 4	$N_{\mathrm{fi,t,Rd}} = A_{\mathrm{eff}} f_{\mathrm{p0.2},\theta}/\gamma_{\mathrm{M,fi}}$	$M_{\mathrm{fi,t,Rd}} = W_{\mathrm{eff}} f_{\mathrm{p0.2},\theta}/\gamma_{\mathrm{M,fi}}$

3.3.4 Assessment of EN 1993-1-2 provisions for the design of stainless steel plates in fire

The accuracy of the EN 1993-1-2 (CEN, 2005) provisions for the design of stainless steel internal and outstand plates in fire is assessed against results from nonlinear shell finite element modelling considering different elevated temperature levels and room temperature non-dimensional plate slendernesses $\overline{\lambda}_{\mathrm{p}}$. Assessment of the EN 1993-1-2 (CEN, 2005) compression and bending resistance functions are shown in Fig. 3.8 and Fig. 3.9 for the case of hot-rolled stainless steel plates in fire. Further comparisons are shown in Section 3.5. As can be seen from the figures, EN 1993-1-2 (CEN, 2005) provides a single plate buckling curve to predict the ultimate axial compression and bending moment resistances of stainless steel plates at different elevated temperature levels; the ordinates of the plateaus of the plate buckling curves vary due to the different ratios of $f_{2,\theta}$ to $f_{\mathrm{p0.2},\theta}$ (i.e. $f_{2,\theta}/f_{\mathrm{p0.2},\theta}$) at different temperature levels and the use of the plastic and elastic section moduli to determine the bending moment resistances of stainless steel plates falling into the Class 1 and 2 and Class 3 categories, respectively. Since EN 1993-1-2 (CEN, 2005) utilises the elevated temperature strength at 2% strain $f_{2,\theta}$ for Class 1, 2 and 3 sections and the elevated temperature 0.2% proof strength for Class 4 sections, there is an abrupt step in local capacity at the plateau slenderness $\overline{\lambda}_{\mathrm{p},0}$, which corresponds to the transition between Class 3 and Class 4 sections according to the classification limits provided in Table 3.4. Fig. 3.8 shows that the plate buckling curve of EN 1993-1-2 (CEN, 2005) yields inaccurate and rather conservative ultimate strength predictions for slender stainless steel plates under axial compression at high temperatures, particularly for the duplex and ferritic stainless steel grades. Moreover, the plateau lengths of the plate buckling curves $\overline{\lambda}_{\mathrm{p},0}$ determined on the basis of the Class 3 classi-

fication limits given in Table 3.4 lead to significant overpredictions of the ultimate strengths of moderately slender austenitic stainless steel plates subjected to axial compression, indicating that shorter plateau lengths $\overline{\lambda}_{p,0}$ are necessary.

3.4 New cross-section classification rules and effective width equations for stainless steel elements in fire

To enable accurate and safe ultimate strength predictions for stainless steel plates at elevated temperatures, new cross-section classification rules and effective width equations are presented. In line with the effective width approach put forward by Couto *et al.* (2014) for carbon steel plates in fire, the elevated temperature material strength at 2% strain $f_{2,\theta}$ is adopted as the sole reference strength for the determination of the ultimate strengths of stainless steel plates at elevated temperatures. A new system of cross-section classification is introduced whereby the four classes defined at room temperature are replaced with two classes – (i) non-slender and (ii) slender – at elevated temperature on the basis of whether or not $f_{2,\theta}$ can be reached. This simplifies design and is justified considering (i) a distinction between Class 1 and Class 2 sections, used to assess the applicability of the plastic design at room temperature, is not necessary in the fire design of steel structures and (ii) a much lower number cross-sections with practical proportions fall into the traditional Class 1, 2 and 3 categories than at room temperature owing to the use of the elevated temperature strength at 2% total strain $f_{2,\theta} = k_{2,\theta} f_y$. Note that, despite the differences in the adopted standardised material properties used to reflect hot-rolled and cold-formed stainless steel plates (see Table 3.1), the resulting structural behaviour was sufficiently similar that it was deemed that no distinction between the two is necessary for design purposes. This is in line with the current plate buckling design treatment for both carbon steel and stainless steel in Eurocode 3. In Section 3.5, the accuracy and reliability of the proposed effective method are verified and compared against the existing plate buckling assessment provisions set out in EN 1993-1-2 (CEN, 2005), taking into account various elevated temperature levels, stainless steel

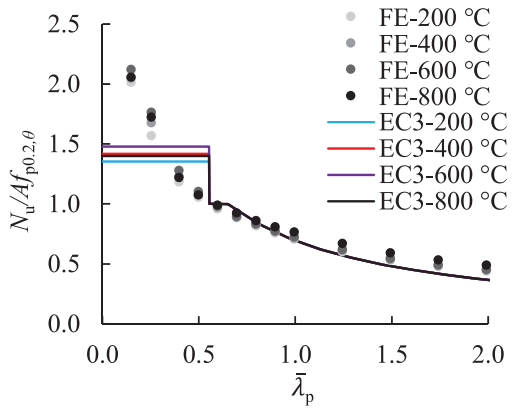

(a) Internal elements in compression (Austenitic)

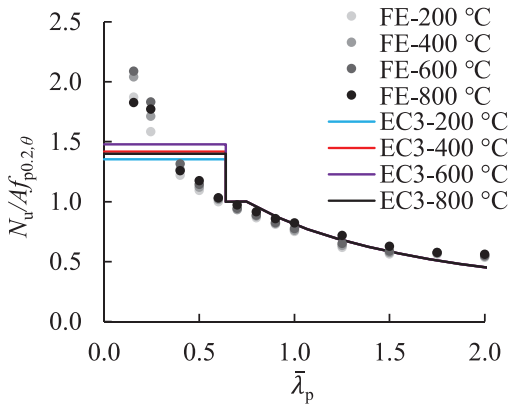

(b) Outstand flanges in compression (Austenitic)

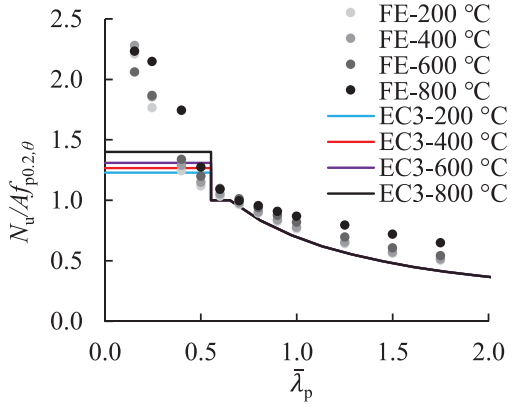

(c) Internal elements in compression (Duplex)

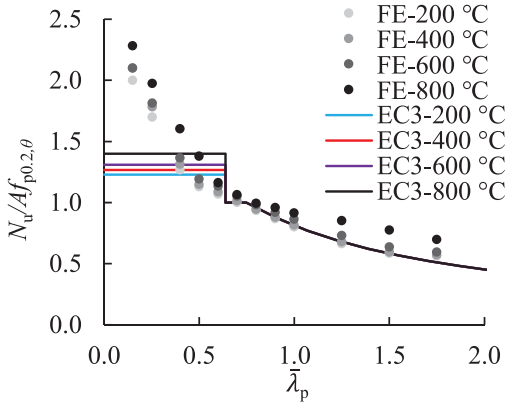

(d) Outstand flanges in compression (Duplex)

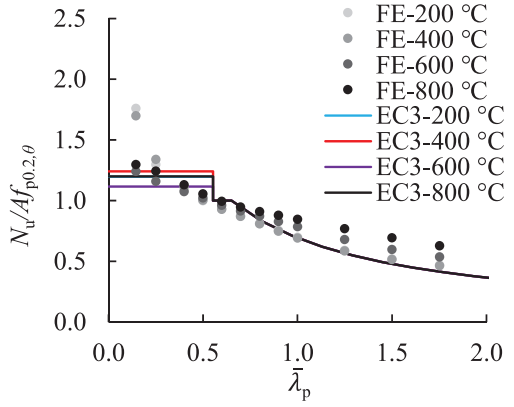

(e) Internal elements in compression (Ferritic)

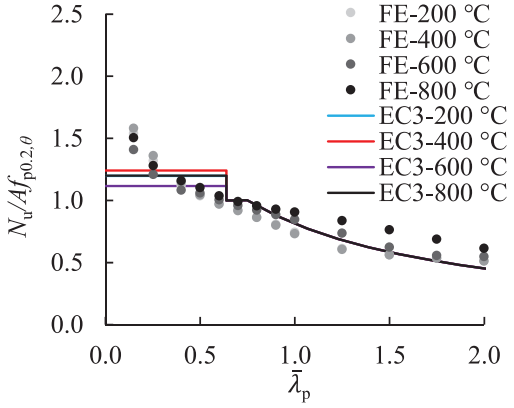

(f) Outstand flanges in compression (Ferritic)

Figure 3.8: Assessment of EN 1993-1-2 (CEN, 2005) against FE results for the local buckling strength predictions of hot-rolled stainless steel plates subjected to axial compression

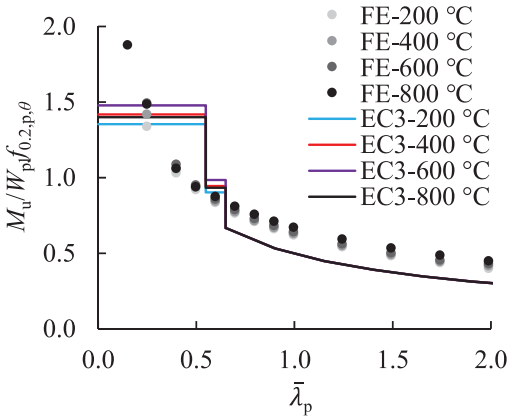

(a) Internal elements in bending (Austenitic)

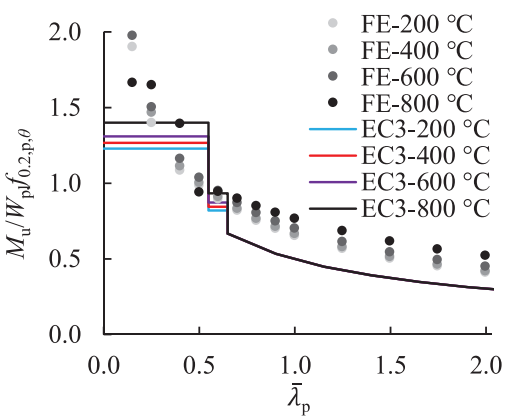

(b) Internal elements in bending (Duplex)

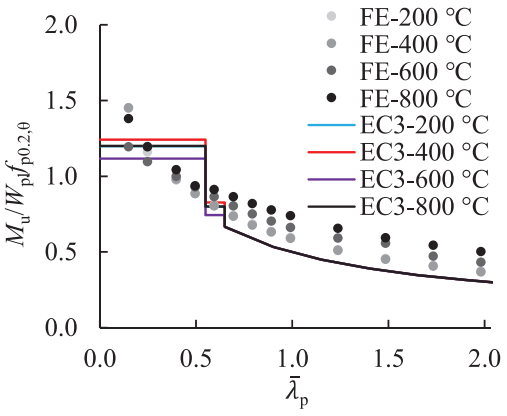

(c) Internal elements in bending (Ferritic)

Figure 3.9: Assessment of EN 1993-1-2 (CEN, 2005) against FE results for the local buckling strength predictions of hot-rolled stainless steel plates subjected to bending

grades and plate slendernesses.

3.4.1 Classification of stainless steel cross-sections in fire

A new classification approach for stainless steel cross-sections in fire is introduced. In the new cross-section classification approach, the class of a cross-section is determined on the basis of the classes of its constituent plates. A cross-section is classified as 'non-slender' only if all of its constituent plates are classified as 'non-slender'. When one or more plates constituting a cross-section are classified as 'slender', the cross-section is classified as 'slender'. For the classification of the individual stainless steel plates constituting a cross-section, the plateau slendernesses $\bar{\lambda}_{\mathrm{p0},\theta}$ given in eq. (3.12) and eq. (3.18) are used for austenitic stainless steel internal and outstand plates, while the plateu slendernesses $\bar{\lambda}_{\mathrm{p0},\theta}$ provided in eq. (3.15) and eq. (3.21) apply for duplex and ferritic stainless steel internal and outstand plates, respectively. If the elevated temperature slenderness $\bar{\lambda}_{\mathrm{p},\theta}$ of a plate determined using eq. (3.22) is less than the corresponding plateau slenderness $\bar{\lambda}_{\mathrm{p0},\theta}$, the plate is classified as 'non-slender', while if the plate slenderness $\bar{\lambda}_{\mathrm{p},\theta}$ is greater than the plateau slenderness $\bar{\lambda}_{\mathrm{p0},\theta}$, the plate is classified as 'slender'.

3.4.2 New effective width method for stainless steel plates in fire

To retain consistency between the room temperature and fire design of stainless steel cross-sections, the new effective width formulae proposed in this study follow a similar format to the existing effective width formulae in EN 1993-1-4 (CEN, 2015), but using the elevated temperature plate slenderness $\bar{\lambda}_{\mathrm{p},\theta}$ in lieu of room temperature plate buckling slenderness $\overline{\lambda}_{\mathrm{p}}$ to reflect the different variations in strength and stiffness of stainless steel at elevated temperatures. The use of elevated temperature slenderness for local buckling is also consistent with the approach for member buckling.

For internal compression elements, the proposed reduction factors for the local buckling ρ of

austenitic stainless steel plates are as follows:

$$\rho = 1 \qquad \text{for} \quad \bar{\lambda}_{\mathrm{p},\theta} \leq \bar{\lambda}_{\mathrm{p0},\theta}, \tag{3.10}$$

$$\rho = \frac{0.54}{\left(\bar{\lambda}_{\mathrm{p},\theta} \Big/ \sqrt{\xi_\theta}\right)^{0.75}} - \frac{0.015\,(3+\psi)}{\left(\bar{\lambda}_{\mathrm{p},\theta} \Big/ \sqrt{\xi_\theta}\right)^{1.5}} \quad \text{for} \quad \bar{\lambda}_{\mathrm{p},\theta} > \bar{\lambda}_{\mathrm{p0},\theta} \tag{3.11}$$

with

$$\bar{\lambda}_{\mathrm{p0},\theta} = \left(0.27 + \sqrt{0.0279 - 0.015\psi}\right)^{1.33} \sqrt{\xi_\theta}. \tag{3.12}$$

For duplex and ferritic stainless steel internal plates, the proposed local buckling reduction factors ρ are:

$$\rho = 1 \qquad \text{for} \quad \bar{\lambda}_{\mathrm{p},\theta} \leq \bar{\lambda}_{\mathrm{p0},\theta}, \tag{3.13}$$

$$\rho = \frac{0.6}{\left(\bar{\lambda}_{\mathrm{p},\theta} \Big/ \sqrt{\xi_\theta}\right)^{0.75}} - \frac{0.015\,(3+\psi)}{\left(\bar{\lambda}_{\mathrm{p},\theta} \Big/ \sqrt{\xi_\theta}\right)^{1.5}} \quad \text{for} \quad \bar{\lambda}_{\mathrm{p},\theta} > \bar{\lambda}_{\mathrm{p0},\theta} \tag{3.14}$$

with

$$\bar{\lambda}_{\mathrm{p0},\theta} = \left(0.3 + \sqrt{0.045 - 0.015\psi}\right)^{1.33} \sqrt{\xi_\theta}. \tag{3.15}$$

For outstand flanges, the proposed plate buckling reduction factors ρ for austenitic stainless steel are:

$$\rho = 1 \qquad \text{for} \quad \bar{\lambda}_{\mathrm{p},\theta} \leq \bar{\lambda}_{\mathrm{p0},\theta}, \tag{3.16}$$

$$\rho = \frac{0.6}{\left(\bar{\lambda}_{\mathrm{p},\theta} \Big/ \sqrt{\xi_\theta}\right)^{0.6}} - \frac{0.075}{\left(\bar{\lambda}_{\mathrm{p},\theta} \Big/ \sqrt{\xi_\theta}\right)^{1.2}} \quad \text{for} \quad \bar{\lambda}_{\mathrm{p},\theta} > \bar{\lambda}_{\mathrm{p0},\theta} \tag{3.17}$$

with

$$\bar{\lambda}_{\mathrm{p0},\theta} = 0.237\sqrt{\xi_\theta}. \tag{3.18}$$

For duplex and ferritic stainless steel outstand plates, it is proposed that ρ is calculated as follows:

$$\rho = 1 \qquad \text{for} \quad \bar{\lambda}_{\mathrm{p},\theta} \leq \bar{\lambda}_{\mathrm{p0},\theta}, \tag{3.19}$$

$$\rho = \frac{0.67}{\left(\bar{\lambda}_{\mathrm{p},\theta} \Big/ \sqrt{\xi_\theta}\right)^{0.6}} - \frac{0.075}{\left(\bar{\lambda}_{\mathrm{p},\theta} \Big/ \sqrt{\xi_\theta}\right)^{1.2}} \quad \text{for} \quad \bar{\lambda}_{\mathrm{p},\theta} > \bar{\lambda}_{\mathrm{p0},\theta} \tag{3.20}$$

with

$$\bar{\lambda}_{\mathrm{p0},\theta} = 0.344\sqrt{\xi_\theta}. \tag{3.21}$$

In eqs. (3.10)–(3.21), ψ is the ratio between the stresses at the edges of the plate as described in EN 1993-1-5 (CEN, 2006), $\overline{\lambda}_{\mathrm{p0},\theta}$ is the threshold plate slenderness below which $\rho = 1.0$ and $\bar{\lambda}_{\mathrm{p},\theta}$ is the elevated temperature plate slenderness calculated as:

$$\bar{\lambda}_{\mathrm{p},\theta} = \xi_\theta \sqrt{\frac{f_\mathrm{y}}{\sigma_\mathrm{cr}}} \quad \text{with} \quad \xi_\theta = \sqrt{\frac{k_{2,\theta}}{k_{E,\theta}}}, \tag{3.22}$$

where f_y is the room temperature 0.2% proof strength and σ_cr is the elastic critical buckling stress of the plate at room temperature, calculated as follows:

$$\sigma_\mathrm{cr} = k_\sigma \frac{\pi^2 E}{12(1-\nu^2)} \left(\frac{t}{b}\right)^2, \tag{3.23}$$

in which k_σ is the buckling coefficient determined for the corresponding stress distribution and boundary conditions of the plate (CEN, 2006), ν is the Poisson's ratio and b and t are the plate width and thickness, respectively.

3.4.3 Cross-section resistance of stainless steel structural elements in fire

Table 3.6 and Fig. 3.10 show the calculation of cross-sectional resistances for cross-sections falling into the non-slender and slender classes. As can be seen from the table and figure, in the

determination of the axial force and bending moment resistances of stainless steel cross-sections falling into the non-slender class, use of the full cross-section areas A and the plastic section moduli W_{pl} is recommended, while use of the effective cross-section areas A_{eff} and the effective section moduli W_{eff} is recommended for slender sections. The effective section properties A_{eff} and W_{eff} are determined considering the effective widths of the plates constituting the cross-section determined using eqs. (3.10)–(3.21) on the basis of the procedure set out in EN 1993-1-5 (CEN, 2006). It is worth noting that in line with the proposals made herein, the adoption of two section classes using the full and effective cross-section properties was also recommended in (Couto *et al.*, 2014).

Table 3.6: Definition of cross-sectional resistances in new design method

Cross-section classification	Design resistance in compression	Design resistance in bending
Non-slender	$N_{\text{fi,t,Rd}} = A f_{2,\theta}/\gamma_{\text{M,fi}}$	$M_{\text{fi,t,Rd}} = W_{\text{pl}} f_{2,\theta}/\gamma_{\text{M,fi}}$
Slender	$N_{\text{fi,t,Rd}} = A_{\text{eff}} f_{2,\theta}/\gamma_{\text{M,fi}}$	$M_{\text{fi,t,Rd}} = W_{\text{eff}} f_{2,\theta}/\gamma_{\text{M,fi}}$

It should be noted that unlike the provisions of the current version of EN 1993-1-2 (CEN, 2005), the proposed cross-section design approach and effective width method utilise the elevated temperature strength and stiffness in the definition of slenderness, which introduces an additional level of complexity. However, consideration of the differential rates of erosion of strength and stiffness in fire leads to more accurate predictions of cross-section capacities, as shown in Section 3.5. Moreover, this additional complexity can be conservatively avoided by using the maximum value of $\xi_\theta = \sqrt{k_{2,\theta}/k_{E,\theta}}$ for austenitic, duplex and ferritic stainless steel, as given by the expression below, in the predictions of cross-section capacities in the proposed effective width equations given in Section 3.4.2.

$$\xi_{\theta,max} = \max\left(\sqrt{k_{2,\theta}/k_{E,\theta}}\right) = 1.15. \tag{3.24}$$

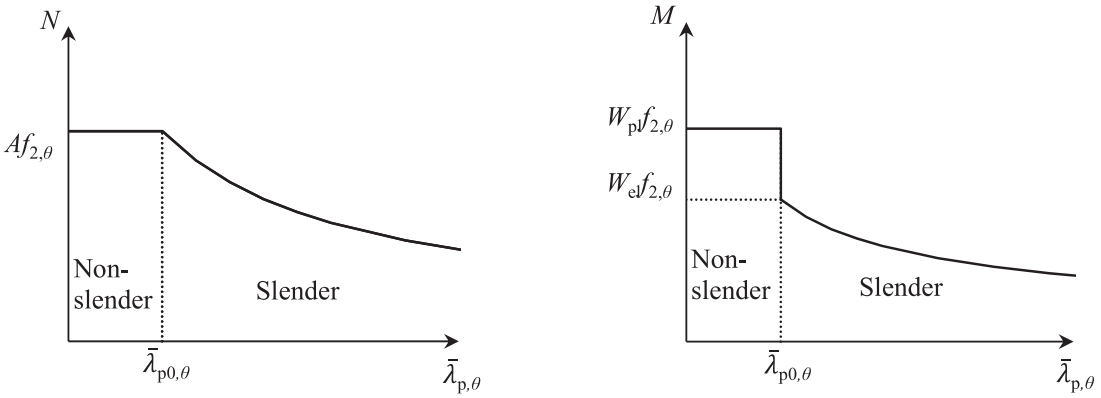

(a) Plates in compression

(b) Plates in bending

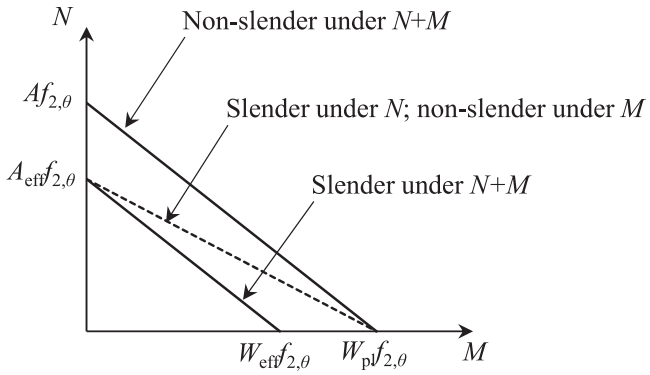

(c) Plates under combined compression and bending

Figure 3.10: Cross-sectional resistances in new design method

3.5 Comparison between EN 1993-1-2 and new effective width method

The accuracy and reliability of the new effective width method for the ultimate strength predictions of stainless steel plates in fire are compared against those of the existing provisions of EN 1993-1-2 (CEN, 2005) in this section, using a large number of results obtained from finite element simulations of stainless steel plates with different edge boundary conditions, elevated temperature levels, stainless steel grades and plate slendernesses. Comparisons are also made against the test results of Uppfeldt *et al.* (2008).

3.5.1 Accuracy assessment

The accuracy of the new effective width method for the prediction of the ultimate resistance of stainless steel plates subjected to axial compression in fire is illustrated in Fig. 3.11 for hot-rolled stainless steel plates and Fig. 3.12 for cold-formed stainless steel plates. As can be seen from the figures, the proposed effective width method leads to accurate axial strength predictions for different elevated temperature levels owing to the consideration of the influence of the differential variations in the strength and stiffness at elevated temperatures on the response through the use of the non-dimensional elevated temperature plate buckling slenderness $\overline{\lambda}_{\mathrm{p},\theta}$ in its formulations (see eq. (3.22)). Unlike the effective method of EN 1993-1-2 (CEN, 2005), the new effective method leads to multiple plate buckling curves which results from the use of $\xi_\theta = \sqrt{k_{2,\theta}/k_{E,\theta}}$ in the expression of the plate buckling reduction factors ρ in eqs. (3.10)–(3.21), thereby representing the behaviour of stainless steel plates more accurately at different elevated temperature levels. Resistance predictions obtained through the new effective method are compared against those determined through nonlinear finite element modelling in Fig. 3.13 for hot-rolled stainless steel plates subjected to bending in fire. As can be seen from the figure, although it is less accurate for the prediction of bending moment capacities relative to axial compression resistances, the

proposed approach leads to an improved level of accuracy relative to EN 1993-1-2 (CEN, 2005) for the estimations of the ultimate resistances of stainless steel plates in bending.

The accuracy of the new effective width method and EN 1993-1-2 (CEN, 2005) is also compared in Fig. 3.14 for all stainless steel plates. The results presented in the figure are for internal and outstand stainless steel plates subjected to both pure axial compression and combined bending and axial compression (with the ratios between the edge stresses ψ being equal to 0.5, 0 and -0.5 (i.e. $\psi = 0.5, 0, -0.5$) in the latter loading case), as well as internal plates under pure bending. In Fig. 3.14, $N_{\mathrm{u,FE}}$ and $M_{\mathrm{u,FE}}$ are the ultimate axial force and bending moment resistances of the stainless steel plates determined using the finite element models, $N_{\mathrm{u,prop}}$ and $M_{\mathrm{u,prop}}$ are the ultimate axial force and bending moment resistances determined using the proposed effective width method and $N_{\mathrm{u,EC3}}$ and $M_{\mathrm{u,EC3}}$ are the ultimate axial force and bending moment resistances predicted using EN 1993-1-2 (CEN, 2005). As can be seen from Fig. 3.14, the new effective width method leads to considerably more accurate ultimate strength predictions with a much lower level of scatter for all the internal and outstand plates of different stainless steel grades and with different elevated temperature levels, loading conditions and plate slendernesses $\overline{\lambda}_{\mathrm{p},\theta}$.

The accuracy of the new effective width method and EN 1993-1-2(CEN, 2005) is also assessed in Table 3.7 and Table 3.8 by taking into account the mean and the coefficient of variation (COV) of the ratios of the ultimate strength predictions obtained from nonlinear finite element modelling to those determined through the new effective width method and EN 1993-1-2. As can be seen from the tables, the mean values of the ratios between the ultimate resistances obtained through the finite element models and the proposed effective width method (i.e. $N_{\mathrm{u,FE}}/N_{\mathrm{u,prop}}$, $M_{\mathrm{u,FE}}/M_{\mathrm{u,prop}}$ and $N_{\mathrm{u,FE}}/N_{\mathrm{u,prop}} + M_{\mathrm{u,FE}}/M_{\mathrm{u,prop}}$) are closer to 1.0 relative to the corresponding mean values of the ratios determined using the EN 1993-1-2 (CEN, 2005) strength predictions (i.e. $N_{\mathrm{u,FE}}/N_{\mathrm{u,EC3}}$, $M_{\mathrm{u,FE}}/M_{\mathrm{u,EC3}}$ and $N_{\mathrm{u,FE}}/N_{\mathrm{u,EC3}} + M_{\mathrm{u,FE}}/M_{\mathrm{u,EC3}}$) with lower COV values, indicating that the proposed effective width method is able to more accurately predict the ultimate resistances of stainless steel plates in fire relative to EN 1993-1-2 (CEN, 2005).

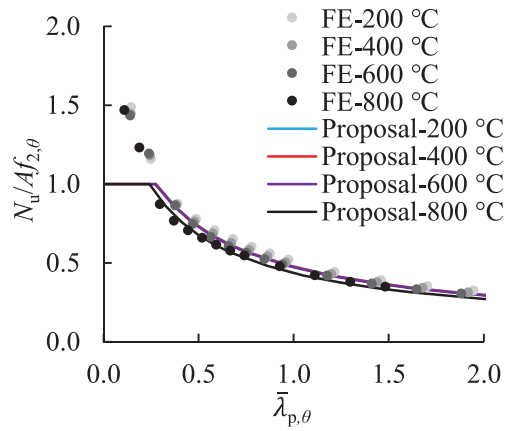

(a) Internal elements in compression (Austenitic)

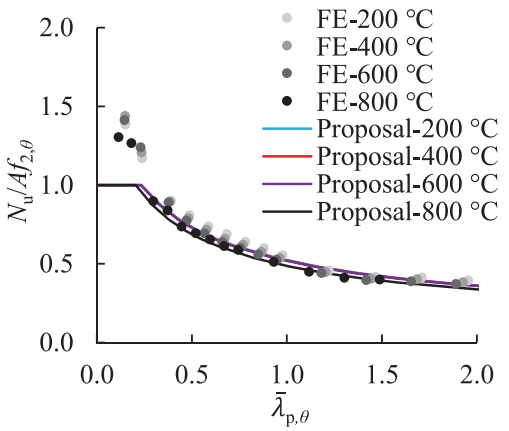

(b) Outstand flanges in compression (Austenitic)

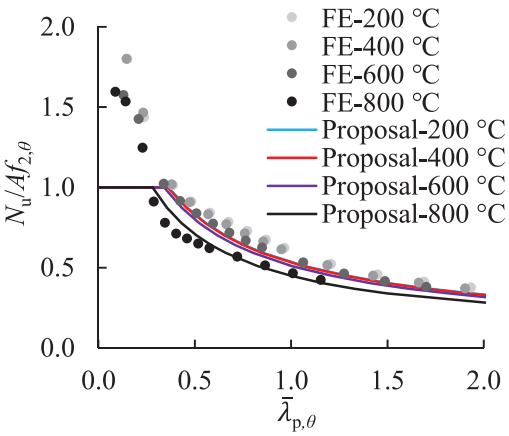

(c) Internal elements in compression (Duplex)

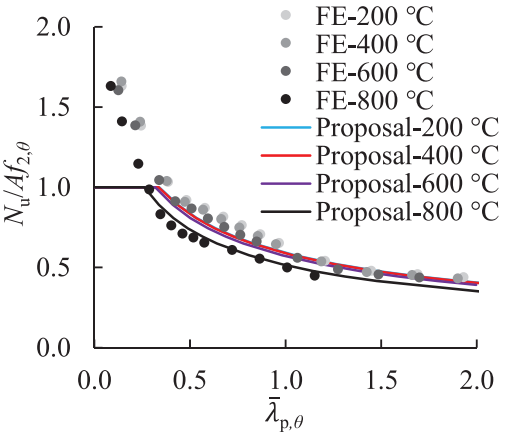

(d) Outstand flanges in compression (Duplex)

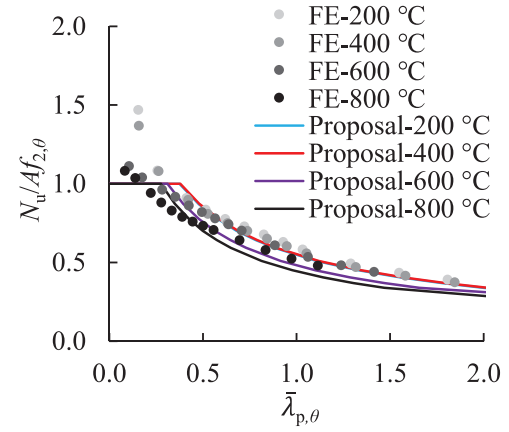

(e) Internal elements in compression (Ferritic)

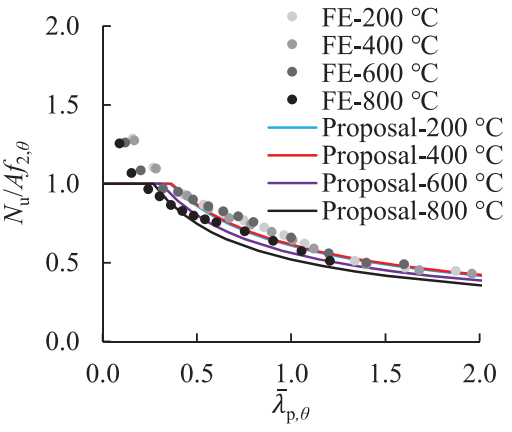

(f) Outstand flanges in compression (Ferritic)

Figure 3.11: Assessment of new design method based on $f_{2,\theta}$ against FE results for the local buckling strength predictions of hot-rolled stainless steel plates

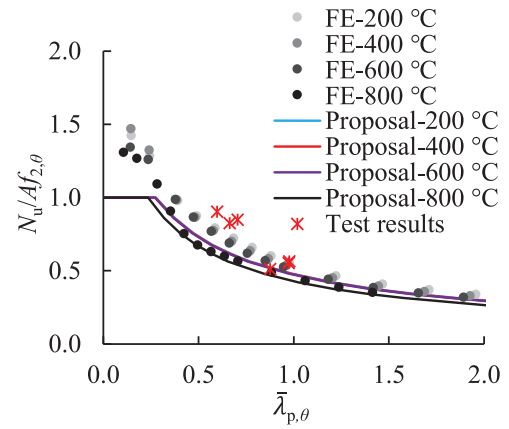

(a) Internal elements in compression (Austenitic)

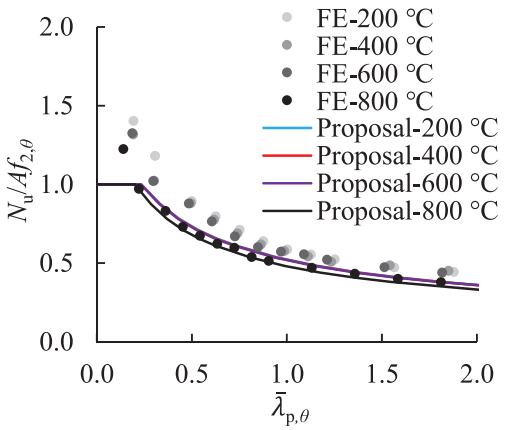

(b) Outstand flanges in compression (Austenitic)

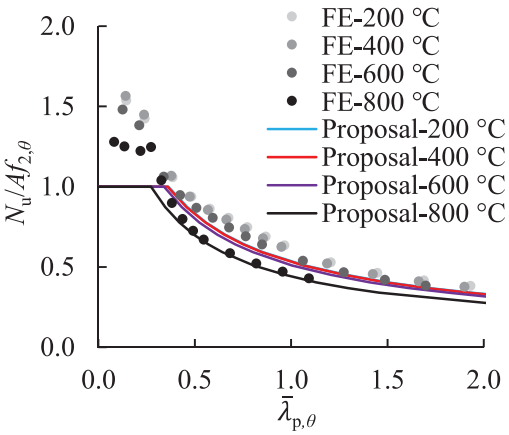

(c) Internal elements in compression (Duplex)

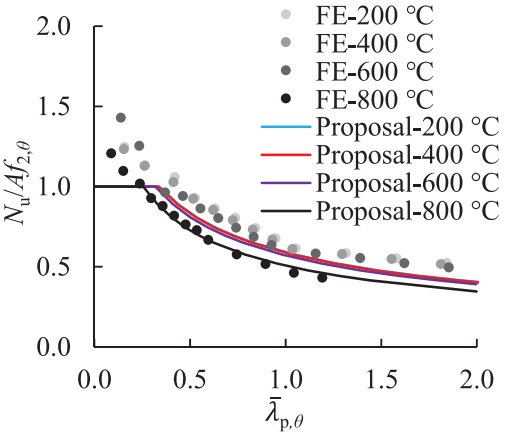

(d) Outstand flanges in compression (Duplex)

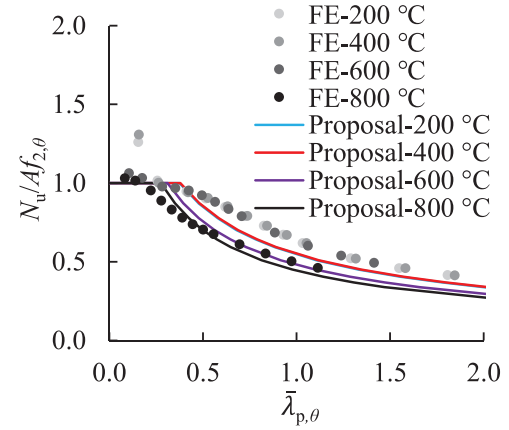

(e) Internal elements in compression (Ferritic)

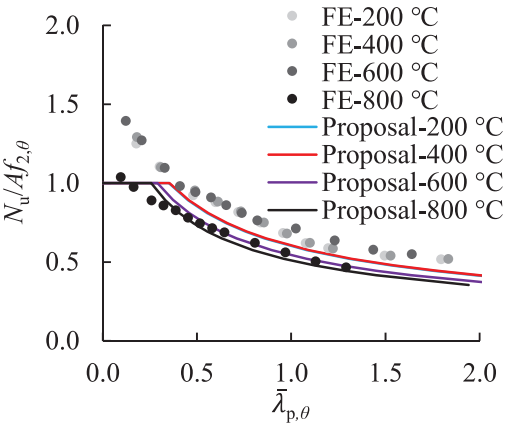

(f) Outstand flanges in compression (Ferritic)

Figure 3.12: Assessment of new design method based on $f_{2,\theta}$ against FE results for the local buckling strength predictions of cold-formed stainless steel plates

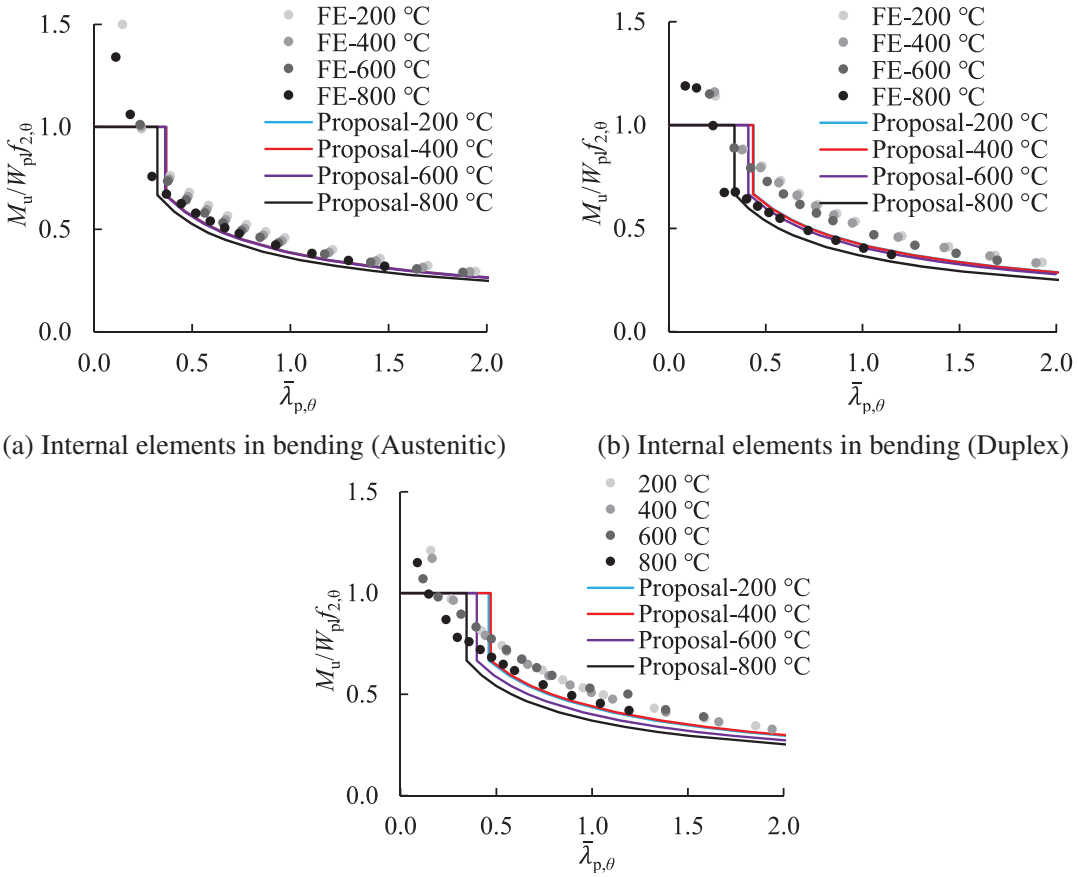

(a) Internal elements in bending (Austenitic)

(b) Internal elements in bending (Duplex)

(c) Internal elements in bending (Ferritic)

Figure 3.13: Assessment of new design method based on $f_{2,\theta}$ against FE results for the local buckling strength predictions of hot-rolled stainless steel plates subjected to bending

Table 3.7: Accuracy assessment of new design proposals

Plates in compression			
$N_{u,FE}/N_{u,prop}$	Austenitic	Duplex	Ferritic
Mean	1.100	1.146	1.101
COV	0.105	0.154	0.096
Plates in bending			
$M_{u,FE}/M_{u,prop}$	Austenitic	Duplex	Ferritic
Mean	1.182	1.183	1.198
COV	0.080	0.094	0.150
Plates in combined axial compression and bending			
$N_{u,FE}/N_{u,prop} + M_{u,FE}/M_{u,prop}$	Austenitic	Duplex	Ferritic
Mean	1.297	1.293	1.294
COV	0.095	0.085	0.120

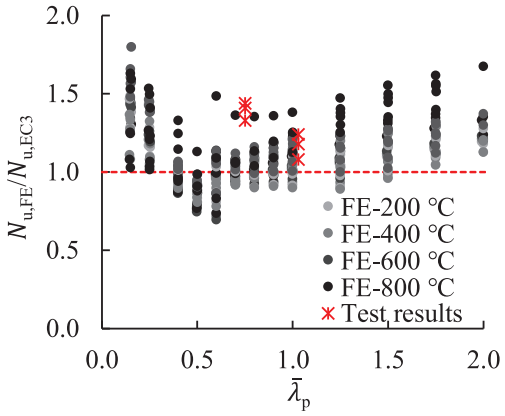

(a) Assessment of EN 1993-1-2 for stainless steel plates in compression

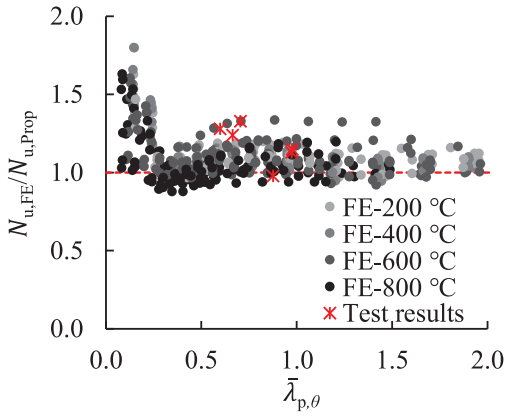

(b) Assessment of new proposal for stainless steel plates in compression

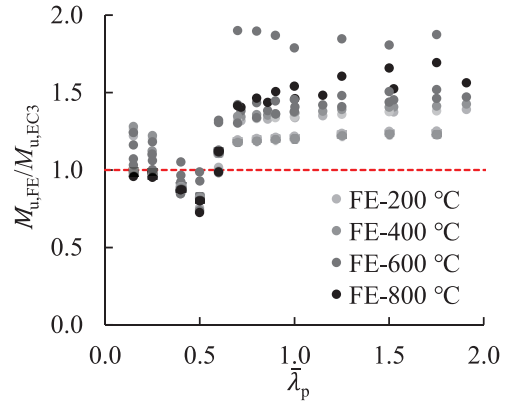

(c) Assessment of EN 1993-1-2 for stainless steel plates in bending

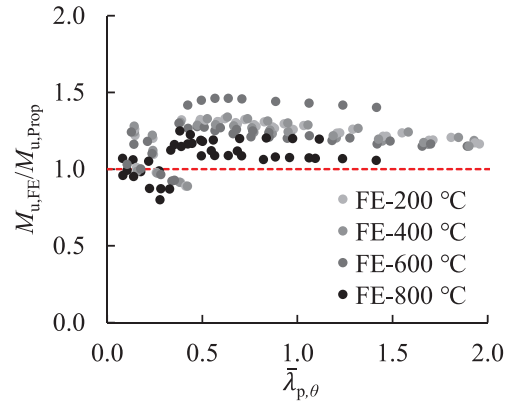

(d) Assessment of new proposal for stainless steel plates in bending

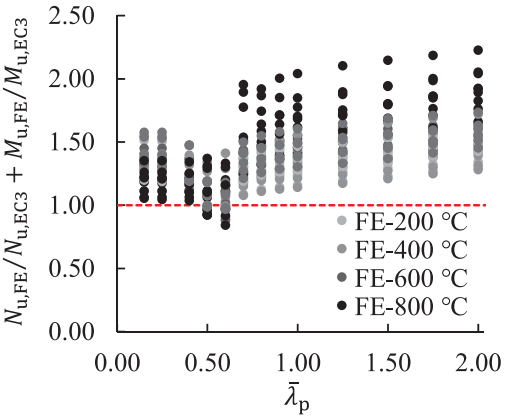

(e) Assessment of EN 1993-1-2 for stainless steel plates under combined axial compression and bending

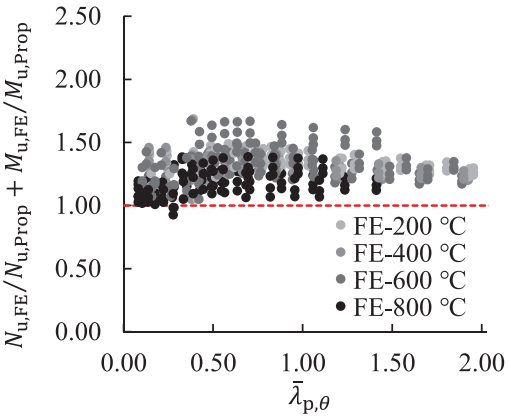

(f) Assessment of new proposal for stainless steel plates under combined axial compression and bending

Figure 3.14: Assessment of EN 1993-1-2 (CEN, 2005) and new proposal against FE results for all stainless steel plates

Table 3.8: Accuracy assessment of EN 1993-1-2 (CEN, 2005)

Plates in compression			
$N_{u,FE}/N_{u,EC3}$	Austenitic	Duplex	Ferritic
Mean	1.069	1.181	1.057
COV	0.162	0.173	0.155
Plates in bending			
$M_{u,FE}/M_{u,EC3}$	Austenitic	Duplex	Ferritic
Mean	1.250	1.346	1.207
COV	0.205	0.216	0.196
Plates in combined axial compression and bending			
$N_{u,FE}/N_{u,EC3}+M_{u,FE}/M_{u,EC3}$	Austenitic	Duplex	Ferritic
Mean	1.315	1.412	1.297
COV	0.154	0.177	0.161

3.5.2 Reliability assessment

The reliability of the new effective width method is assessed in Table 3.9 considering the three reliability criteria put forward by Kruppa (1999) for the design of structural steel elements in fire. According to Criterion 1 of Kruppa (1999), none of the strength predictions obtained using the considered design approach should exceed the FE results by more than 15%, while Criterion 2 of Kruppa (1999) states that less than 20% of the design predictions should be on the unsafe side. Finally, Criterion 3 of Kruppa (1999) states that the design predictions should be safe-sided on average. In Table 3.9, the percentage of the plates for which the overpredictions of resistance exceeded 15% of those obtained from the finite element (FE) models is shown under Criterion 1, the percentage of the plates whose ultimate strengths were overpredicted is shown under Criterion 2 and the average percentage of the differences between the design and FE ultimate strengths is shown under Criterion 3. The violated criteria are highlighted with '*'. As shown in Table 3.9, the new proposal satisfies all three criteria of Kruppa (1999) with the exception of Criterion 2 for the ferritic stainless steel plates in bending, but this is deemed to be acceptable since the reliability criterion is only violated by a very small margin (1.92%) for only one case. The reliability of the existing design provisions of EN 1993-1-2 (CEN, 2005) is also assessed considering the three reliability criteria of Kruppa (1999) in Table 3.10. As can be seen

Table 3.9: Reliability assessment of new design proposals

Plates in compression			
$N_{u,FE}/N_{u,prop}$	Austenitic	Duplex	Ferritic
Criterion 1	0.00	0.00	0.00
Criterion 2	11.49	8.91	15.38
Criterion 3	-8.25	-11.01	-8.43
Plates in bending			
$M_{u,FE}/M_{u,prop}$	Austenitic	Duplex	Ferritic
Criterion 1	0.00	0.00	1.92*
Criterion 2	5.77	9.62	20.00
Criterion 3	-14.80	-14.61	-14.47
Plates in combined axial compression and bending			
$N_{u,FE}/N_{u,prop} + M_{u,FE}/M_{u,prop}$	Austenitic	Duplex	Ferritic
Criterion 1	0.00	0.00	0.00
Criterion 2	0.52	0.00	0.93
Criterion 3	-29.66	-29.31	-29.25

from the table, EN 1993-1-2 (CEN, 2005) violates the reliability criteria of Kruppa (1999) for a high number of cases, indicating that the proposed design method provides significantly more reliable ultimate strength predictions for stainless steel plates in fire.

3.6 Conclusions

The current provisions of the European structural steel fire design standard EN 1993-1-2 (CEN, 2005) directs the designer to EN 1993-1-4 (CEN, 2015) for the local buckling assessment of stainless steel plates in fire. However, since the plate buckling design rules of EN 1993-1-4 (CEN, 2015) were originally developed considering the room temperature response of stainless steel plates, they lead to inaccurate predictions of ultimate strength in fire due to (i) failure to reflect the material stress-strain response of stainless steel in fire and (ii) the neglect of the different rates of strength and stiffness erosion of stainless steel at elevated temperatures.

To enable accurate predictions of the response of stainless steel plates at elevated temperatures, a new effective width method is proposed in this chapter. Unlike the current provisions of EN

Table 3.10: Reliability assessment of EN 1993-1-2 (CEN, 2005)

Plates in compression			
$N_{u,FE}/N_{u,EC3}$	Austenitic	Duplex	Ferritic
Criterion 1	8.91*	1.72*	5.70*
Criterion 2	35.34*	12.93*	45.30*
Criterion 3	-3.98	-13.01	-3.32
Plates in bending			
$M_{u,FE}/M_{u,EC3}$	Austenitic	Duplex	Ferritic
Criterion 1	13.46*	5.77*	5.77*
Criterion 2	25.00*	13.46	25.00*
Criterion 3	-15.75	-22.06	-13.89
Plates in combined axial compression and bending			
$N_{u,FE}/N_{u,EC3} + M_{u,FE}/M_{u,EC3}$	Austenitic	Duplex	Ferritic
Criterion 1	0.52*	0.00	0.51*
Criterion 2	9.90	3.08	6.67
Criterion 3	-31.54	-41.15	-29.15

1993-1-2 (CEN, 2005), in the new effective width method, temperature-dependent plate slenderness $\bar{\lambda}_{p,\theta}$ is employed in conjunction with new plate buckling curves to determine the effective widths of stainless steel plates in fire. It was shown that the new effective width method leads to more accurate and reliable ultimate strength predictions relative to the current design rules of EN 1993-1-2 (CEN, 2005) as assessed against results obtained from nonlinear finite element modelling of stainless steel plates of different grades for a range of elevated temperature levels, loading conditions, boundary conditions and local slendernesses. In conjunction with the new effective width method, new cross-section classification rules were also introduced for stainless steel cross-sections in fire, adopting two distinct classes, referred to as 'non-slender' and 'slender', whose ultimate cross-section resistances are determined using the full and effective cross-section properties, respectively. The proposed method for the treatment of local buckling of stainless steel plates in fire based on the elevated temperature strength at 2% strain $f_{2,\theta}$ described in Section 3.4 is due to be incorporated into the upcoming version of EN 1993-1-2.

Chapter 4

Cross-section behaviour of I-sections

4.1 Introduction

A comprehensive numerical study focusing on the cross-section behaviour of stainless steel I-sections in fire is first carried out in this chapter. Finite element models that are able to capture the cross-section response of stainless steel I-section members are created and validated against a series of experimental results from the literature. Parametric studies are then carried out to generate extensive fundamental structural performance data, covering a wide range of stainless steel grades, elevated temperature levels, cross-section geometries and loading conditions. Assessment of the design provisions in the current European structural steel fire design standard EN 1993-1-2 (CEN, 2005) and those proposed in Chapter 3 is subsequently carried out through comparisons against the obtained numerical data. For stainless steel I-sections subjected to minor axis bending in fire, the plastic effective width method of Bambach & Rasmussen (2004), originally developed to determine the room temperature minor axis bending moment resistances of carbon steel sections, is also evaluated and shown to provide accurate results. Finally, a reliability assessment is presented.

4.2 Finite element modelling

In this section, finite element models that are able to replicate the cross-section behaviour of stainless steel I-section members at elevated temperatures are developed and validated against a series of experimental results from the literature. The validated finite element models are used to assess the accuracy of the current design provisions given in EN 1993-1-2 (CEN, 2005), as well as the design proposals of Chapter 3 and Bambach & Rasmussen (2004).

4.2.1 Development of finite element models

The numerical simulations were carried out using the finite element analysis software ABAQUS (2014). The S4R element was adopted in the finite element modelling. To accurately capture the cross-section behaviour of stainless steel I-sections in fire, twenty elements were employed across each web and flange plate; the number of the elements along the length of the members was selected such that the aspect ratios of the elements were equal to unity. Note that the member length L to cross-section depth h ratios L/h were equal to 3.0 (i.e. $L/h = 3.0$) and the cross-section depth h to width b aspect ratios h/b were equal to 1.0 ($h/b = 1.0$) for all the created models; thus, sixty elements were used along the length of the members. The two-stage compound Ramberg-Osgood material model presented in Section 3.2.1 was utilised in the finite element modelling of the stainless steel I-sections in this chapter, in which the elevated temperature material properties were determined by multiplying the standardised room temperature material properties set out for hot-rolled austenitic, duplex and ferritic stainless steel plates (Afshan *et al.*, 2019) (see Table 3.1) by the corresponding reduction factors given in SCI (2017).

The boundary conditions adopted in the numerical models are illustrated in Fig. 4.1. As can be seen in Fig. 4.1 (a), to simulate the structural response of stainless steel I-sections subjected to compression, the displacements and rotations of the end cross-sections were linked to two concentric reference points (i.e. reference point 1 and reference point 2) through rigid body kin-

ematic coupling constraints; all degrees of freedoms of the two reference points were restrained except for the longitudinal translation (U1) of the reference point 1. The compressive loading was applied as a point force to reference point 1. Similar boundary conditions as those for the models under compression were also adopted in the models of I-sections under bending but with two differences: (i) the rotations about axis 2 (UR2) at the two reference points for major axis bending (see Fig. 4.1 (b)) and the rotations about axes 2 and 3 (UR2 and UR3) at the two reference points for minor axis bending (see Fig. 4.1 (c)) were released to ensure that the models were free to rotate about their respective axis of bending and (ii) the longitudinal translation (U1) of the node at the centre of the web at the mid-span section was restrained instead of the longitudinal translation (U1) of reference point 2. Bending moments were applied at the two reference points in the beam models.

Local geometric imperfections were taken into consideration in the finite element models as shown in Fig. 4.2, in accordance with EN 1993-1-5 (CEN, 2006), where local imperfections with sinusoidal half-wavelengths equal to the plate widths b were applied to the models. The local imperfection magnitude of the plate with lower elastic buckling stress was first determined in accordance with EN 1993-1-5 (CEN, 2006) – the flange imperfection $e_{0,\mathrm{f}}$ was scaled to 1/50 of the half flange width (i.e. $e_{0,\mathrm{f}} = b_{\mathrm{f}}/50$) when the elastic buckling stress of the flanges was lower than that of the web (i.e. $\sigma_{\mathrm{cr,f}} < \sigma_{\mathrm{cr,w}}$), while the web imperfection $e_{0,\mathrm{w}}$ was scaled to 1/200 of the web height (i.e. $e_{0,\mathrm{w}} = b_{\mathrm{w}}/200$) when the elastic buckling stress of the web was lower than that of the flanges (i.e. $\sigma_{\mathrm{cr,w}} < \sigma_{\mathrm{cr,f}}$). The local imperfection magnitude of the plate with the higher elastic buckling stress was determined such that the angle of the web-flange junction remained at 90°.

Residual stresses were incorporated into the finite element models by adopting the residual stress pattern proposed by Yuan *et al.* (2014) for arc-welded stainless steel I-sections. As can be seen in Fig. 4.3, the peak tensile residual stresses in the flanges (σ_{ft}) and web (σ_{wt}) were taken as 80% of the room temperature yield strength f_{y} for the austenitic stainless steel I-sections (i.e. $\sigma_{\mathrm{ft}} = \sigma_{\mathrm{wt}} = 0.8 f_{\mathrm{y}}$), while the peak tensile residual stresses in the flanges and web were taken as

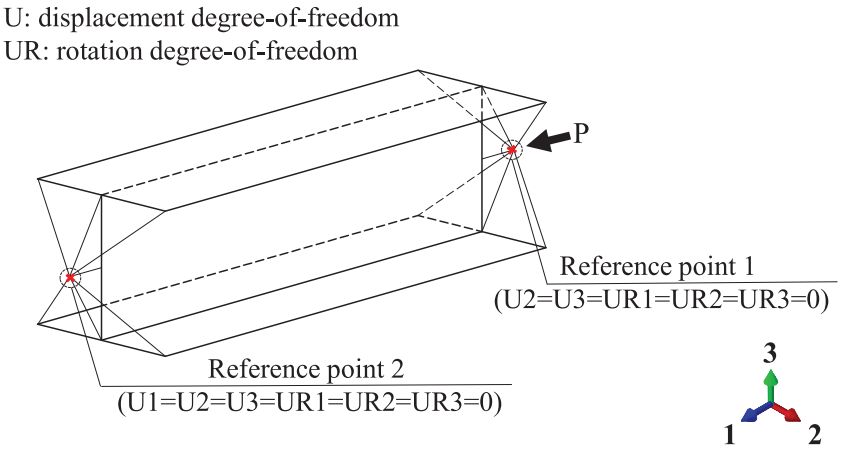

(a) I-sections in compression

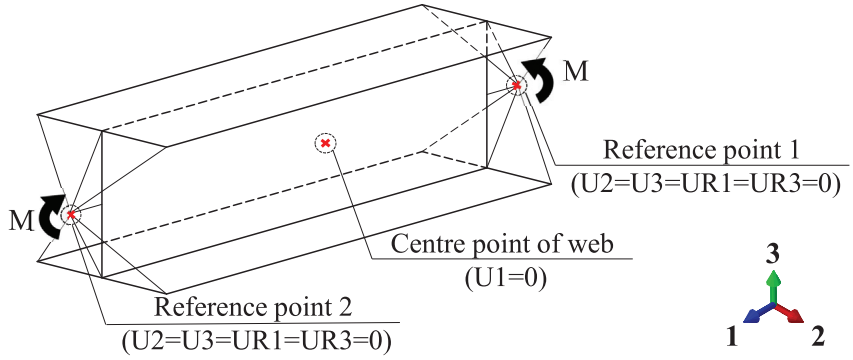

(b) I-sections in bending about the major axis

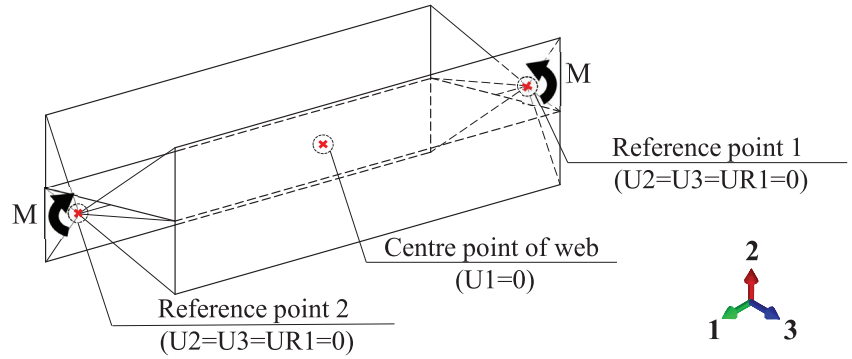

(c) I-sections in bending about the minor axis

Figure 4.1: Boundary conditions applied to the finite element models

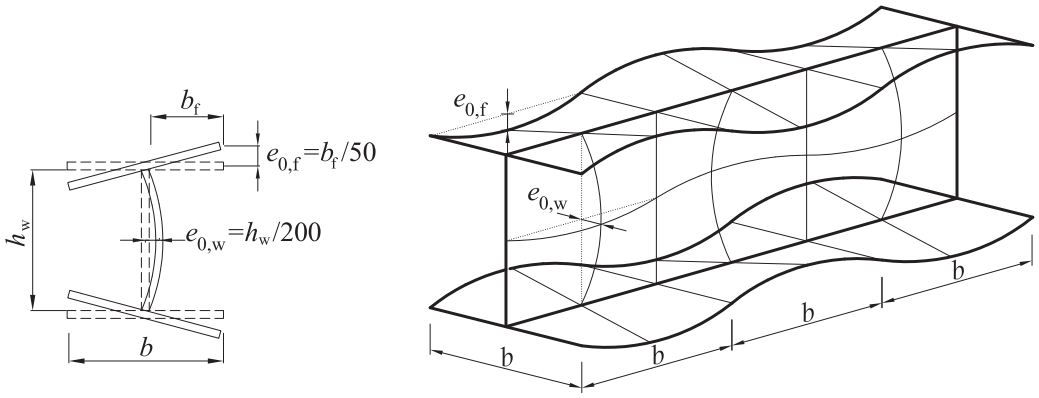

Figure 4.2: Local imperfections applied to the finite element models

60% of the room temperature yield strength f_y for the duplex and ferritic stainless steel I-sections (i.e. $\sigma_{ft} = \sigma_{wt} = 0.6f_y$). The peak compressive residual stresses in the flanges (σ_{fc}) and web (σ_{wc}) were then calculated by considering the cross-section axial force equilibrium, as recommended by Yuan *et al.* (2014). The residual stresses were incorporated into the FE models by defining stress values at the element integration points at room temperature; when the temperature of the FE models was increased, the residual stresses decreased with the development of thermal strains.

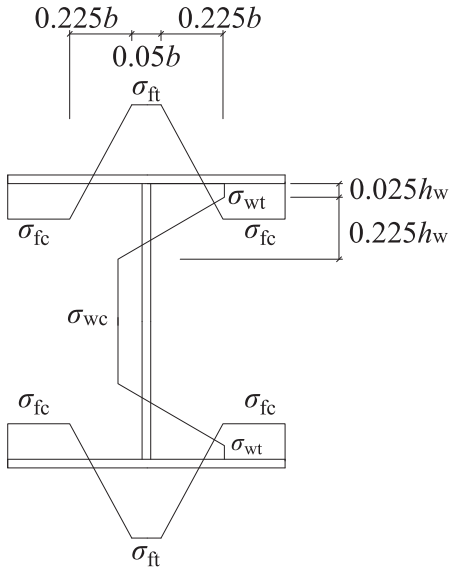

Figure 4.3: Residual stress patterns applied to the finite element models

The finite element models were analysed isothermally by adopting the three steps. The first step,

performed using a *STATIC, General analysis, was the application of the residual stresses in conjunction with the residual plastic strains $\varepsilon_{\mathrm{res,pl}}$, where the residual plastic strains $\varepsilon_{\mathrm{res,pl}}$ were calculated considering the Ramberg–Osgood material model defined in eq. (3.1), where σ_{res} is the value of the applied residual stress at each location, as recommended by Jandera *et al.* (2008):

$$\varepsilon_{\mathrm{res,pl}} = 0.002 \left(\frac{\sigma_{\mathrm{res}}}{f_{\mathrm{y}}} \right)^{n}. \tag{4.1}$$

After reaching self-equilibrium in the first step, the temperature of the model was uniformly increased to the target temperature θ in the second step, performed using a *STATIC, General analysis, during which the development of thermal strains was allowed. Finally, the loading was applied in the third step, where the modified Riks analysis was utilised to trace the full load-deformation response of the stainless steel I-sections at the designated elevated temperature level θ; the peak load obtained in this step was taken as the ultimate cross-section resistance of the I-sections at the designated elevated temperature value θ.

4.2.2 Validation of numerical models

The finite element models for stainless steel I-sections in compression were validated against the results of the fire tests performed on stainless steel box section stub columns (Uppfeldt *et al.*, 2008) and carbon steel I-section stub columns (Pauli, 2012) due to the absence of fire tests on stainless steel I-section stub columns in the literature. Validation of the finite element models for stainless steel I-sections in bending was carried out against the results obtained from the fire tests on I-sections under major axis bending conducted by Gardner & Baddoo (2006) and under minor axis bending by Xing *et al.* (2020).

Stainless steel I-sections in compression

A total of six fire tests on stainless steel square hollow section (SHS) stub columns carried out by Uppfeldt *et al.* (2008) were utilised to validate the finite element modelling approach adopted in this study. The geometric properties and local imperfections of the six stub columns reported by Uppfeldt *et al.* (2008) were included in the finite element models created herein. Twenty elements were employed for each face of the SHS profiles; the element number along the member length was then determined to achieve an element aspect ratio of unity. The two-stage Ramberg-Osgood material model given in Section 3.2.1 was utilised to define the material response of the specimens at elevated temperatures, using the elevated temperature material properties determined by multiplying the strength and stiffness reduction factors given by SCI (2017) by the room temperature material properties obtained from the tensile coupon tests performed by Uppfeldt *et al.* (2008). The analysis steps described in Section 8.2.1 were adopted in the validation of the finite element models with the target temperature θ taken equal to the critical temperature θ_{cr} in the fire tests. The numerically determined failure loads $N_{u,FE}$ are compared against those obtained from the tests $N_{u,test}$ in Table 4.1, where it can be seen that the ratios of the numerically determined failure loads $N_{u,FE}$ to those observed in the experiments $N_{u,test}$ (i.e. $N_{u,FE}/N_{u,test}$) are generally close to unity, indicating that the finite element models created in this study can replicate the local buckling response of stainless steel cross-sections in fire.

Table 4.1: Comparison between the load-carrying capacities obtained from stainless steel RHS stub column tests in fire conducted by Uppfeldt *et al.* (2008) and those determined through finite element modelling

Section	θ_{cr} (°C)	$N_{u,test}$ (kN)	$N_{u,FE}$ (kN)	$N_{u,FE}/N_{u,test}$
RHS 200×200×5	609	694	653	0.94
RHS 200×200×5	685	567	549	0.97
RHS 200×200×5	764	463	425	0.92
RHS 150×150×3	676	203	216	1.06
RHS 150×150×3	720	165	185	1.12
RHS 150×150×3	588	248	244	0.98

Additionally, three fire tests on carbon steel I-section stub columns performed by Pauli (2012),

which were conducted isothermally at three different elevated temperature levels (400 °C, 550 °C and 700 °C), were also used to validate the finite element models created in this study. The measured geometric properties and elevated temperature material properties of the tested specimens were included in the finite element models. Fig. 4.4 shows a comparison of the load versus end shortening curves determined from the experiments and those obtained from the FE models created in this study. As can be seen from the figure, there is a good correlation between the experimental and numerical load versus end shortening paths, which verifies the accuracy and suitability of the finite element modelling approach adopted in this study for simulating the fire behaviour of cross-sections in compression.

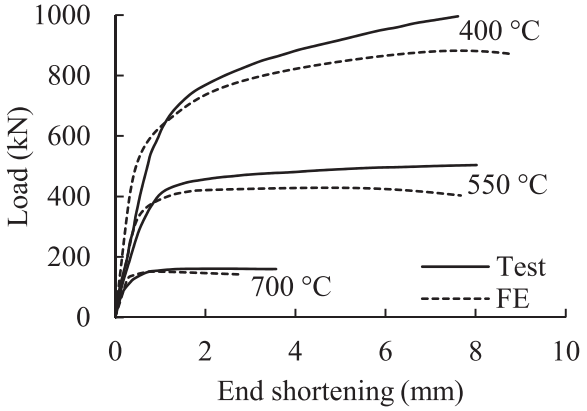

Figure 4.4: Comparison between load versus end shortening curves obtained from experiments (Pauli, 2012) and finite element models for carbon steel I-section stub columns in fire

Stainless steel I-sections in bending

Experimental data from the two major axis bending fire tests performed by Gardner & Baddoo (2006) and the four minor axis bending fire tests performed by Xing *et al.* (2020) on stainless steel I-sections were utilised to validate the adopted finite element modelling approach for stainless steel I-sections in bending. In the validation studies, only the parts of the beams under constant bending moments were modelled, with the bending moments applied at the two end cross-sections; this was consistent with the finite element models used in the parametric studies.

The full elevated temperature stress-strain curves obtained from a series of isothermal elevated temperature tensile coupon tests (Gardner & Baddoo, 2006) were employed to model the elevated temperature material behaviour for the beam tests reported by Gardner & Baddoo (2006), while the two-stage Ramberg-Osgood material model given in Section 3.2.1, using the elevated temperature material properties determined by multiplying the strength and stiffness reduction factors given in SCI (2017) by the room temperature material properties obtained from tensile coupon tests (Xing *et al.*, 2020), was employed for the beam tests reported by Xing *et al.* (2020). Table 4.2 summarises the ultimate bending moment resistances obtained from the finite element analyses $M_{\mathrm{u,FE}}$ and those from the fire tests $M_{\mathrm{u,test}}$, where it can be seen that the numerical results are in a good agreement with the test results, thus verifying that the finite element modelling approach adopted in this study is also able to accurately capture the structural response of stainless steel I-sections in bending at elevated temperatures.

Table 4.2: Comparison between the load-carrying capacities obtained from beam tests on stainless steel I-sections in fire (Gardner & Baddoo, 2006; Xing *et al.*, 2020) and those determined through finite element modelling

Reported by	Cross-section	θ_{cr} (°C)	$M_{\mathrm{u,test}}$ (kNm)	$M_{\mathrm{u,FE}}$ (kNm)	$M_{\mathrm{u,FE}}/M_{\mathrm{u,test}}$
Gardner & Baddoo (2006)	I 200×150×6	944	17.2	17.4	1.01
	I 120×64	650	15.2	14.4	0.95
Xing *et al.* (2020)	I 248×249×8×13	300	87.25	85.85	0.98
	I 248×249×8×13	400	84.77	84.52	1.00
	I 248×249×8×13	500	82.43	81.82	0.99
	I 248×249×8×13	600	69.56	73.58	1.06

4.2.3 Parametric studies

Upon validation of the finite element models, comprehensive structural performance data on stainless steel I-sections at elevated temperatures were generated by means of extensive numerical parametric studies, considering different stainless steel grades (austenitic, duplex and ferritic), elevated temperature levels (200 °C, 400 °C, 600 °C and 800 °C), loading conditions and cross-section geometries. Three loading conditions, namely axial compression, major axis bend-

ing and minor axis bending, were considered. All the simulated cross-sections had cross-section depths h and widths b equal to 100 mm (i.e. $h = b = 100$ mm), while various thicknesses were employed for the flange and web plates to generate a wide range of plate slenderness values for the web $\overline{\lambda}_{\mathrm{p,w}}$ and flange $\overline{\lambda}_{\mathrm{p,f}}$ plates. Note that the web $\overline{\lambda}_{\mathrm{p,w}}$ and flange $\overline{\lambda}_{\mathrm{p,f}}$ plate slendernesses were calculated using:

$$\overline{\lambda}_{\mathrm{p,w}} = \sqrt{\frac{f_y}{\sigma_{\mathrm{cr,w}}}}, \tag{4.2}$$

$$\overline{\lambda}_{\mathrm{p,f}} = \sqrt{\frac{f_y}{\sigma_{\mathrm{cr,f}}}}, \tag{4.3}$$

where $\sigma_{\mathrm{cr,w}}$ and $\sigma_{\mathrm{cr,f}}$ are the local buckling stresses of the individual web and flange plates, respectively. The considered web $\overline{\lambda}_{\mathrm{p,w}}$ and flange $\overline{\lambda}_{\mathrm{p,f}}$ plate slenderness values are provided in Table 4.3, where it can be seen that I-sections with the web $\overline{\lambda}_{\mathrm{p,w}}$ and flange $\overline{\lambda}_{\mathrm{p,f}}$ plate slendernesses ranging from 0.15 to 2.0 were modelled. To expand the numerical data pool, in addition to the basic I-sections with the same web plate $\overline{\lambda}_{\mathrm{p,w}}$ and flange plate $\overline{\lambda}_{\mathrm{p,f}}$ slendernesses (i.e. $\overline{\lambda}_{\mathrm{p,w}} = \overline{\lambda}_{\mathrm{p,f}}$), two additional cases were also considered: (i) stainless steel I-sections with the web plate slendernesses $\overline{\lambda}_{\mathrm{p,w}}$ less than the flange plate slendernesses $\overline{\lambda}_{\mathrm{p,f}}$ (i.e. $\overline{\lambda}_{\mathrm{p,w}} < \overline{\lambda}_{\mathrm{p,f}}$) and (ii) stainless steel I-sections with the web plate slendernesses $\overline{\lambda}_{\mathrm{p,w}}$ greater than the flange plate slendernesses $\overline{\lambda}_{\mathrm{p,f}}$ (i.e. $\overline{\lambda}_{\mathrm{p,w}} > \overline{\lambda}_{\mathrm{p,f}}$). The web thicknesses were varied from 0.5 mm to 10 mm and the flange thickness were varied between 1.5 mm and 25 mm.

Typical failure modes from the FE models under different loading conditions are shown in Fig. 4.5. As can be seen from Fig. 4.5 (a), there is local buckling in both web and two flanges of the I-sections under axial compression, while, as expected, for the I-sections in bending (see Figs. 4.5 (b) and (c)), local buckling is largely restricted to the portions of cross-sections under compressive stresses.

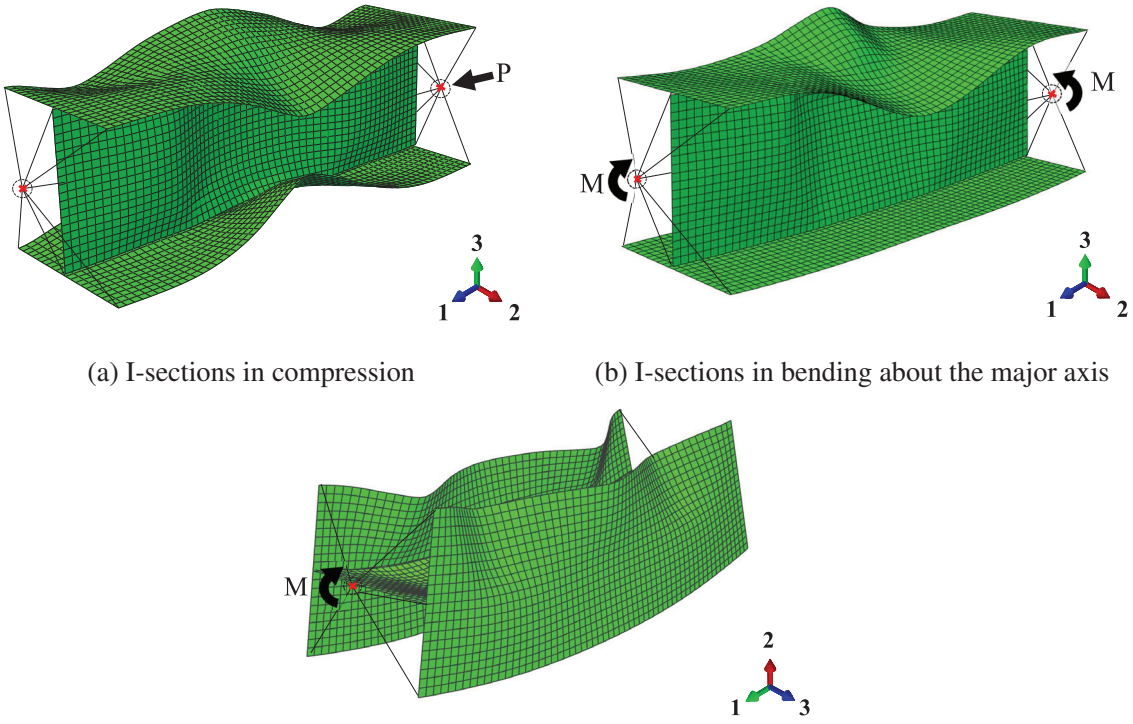

(a) I-sections in compression

(b) I-sections in bending about the major axis

(c) I-sections in bending about the minor axis

Figure 4.5: Typical failure modes of stainless steel I-sections under different loading conditions

Table 4.3: Local plate slenderness values considered in parametric studies

Loading condition	Web slenderness $\overline{\lambda}_{p,w}$	Flange slenderness $\overline{\lambda}_{p,f}$
Compression	0.15, 0.35, 0.55, 0.75, 0.95, 1.15, 1.35, 1.55, 1.75, 2.00	$\overline{\lambda}_{p,f} = \overline{\lambda}_{p,w}$
	0.25	0.35, 0.55, 0.75, 0.95, 1.15, 1.35, 1.55, 1.75, 2.00
	0.35, 0.55, 0.75, 0.95, 1.15, 1.35, 1.55, 1.75, 2.00	0.25
Major axis bending	0.15, 0.35, 0.55, 0.75, 0.95, 1.15, 1.35, 1.55, 1.75, 2.00	$\overline{\lambda}_{p,f} = \overline{\lambda}_{p,w}$
	0.25	0.35, 0.55, 0.75, 0.95, 1.15, 1.35, 1.55, 1.75, 2.00
	0.55, 0.75, 0.95, 1.15, 1.35, 1.55, 1.75, 2.00	0.40
Minor axis bending	0.15, 0.35, 0.55, 0.75, 0.95, 1.15, 1.35, 1.55, 1.75, 2.00	$\overline{\lambda}_{p,f} = \overline{\lambda}_{p,w}$
	0.25	0.35, 0.55, 0.75, 0.95, 1.15, 1.35, 1.55, 1.75, 2.00
	0.35, 0.55, 0.75, 0.95, 1.15, 1.35, 1.55, 1.75, 2.00	0.25

4.3 Assessment of EN 1993-1-2 provisions for the cross-section design of stainless steel I-sections in fire

The description of the current EN 1993-1-2 (CEN, 2005) design provisions for the determination of the cross-section resistance of stainless steel members in fire has been presented in Section 3.3. In this section, the accuracy of the EN 1993-1-2 (CEN, 2005) design provisions is assessed against the nonlinear shell finite element model results generated in Section 4.2.3. The assessment is presented in Fig. 4.6 for the austenitic stainless steel I-sections, in Fig. 4.7 for the duplex stainless steel I-sections and in Fig. 4.8 for the ferritic stainless steel I-sections. In these figures, $N_{u,FE}$ and $M_{u,FE}$ are the cross-section compression and bending moment resistances obtained from the FE simulations, while $N_{fi,Rd,EC3}$ and $M_{fi,Rd,EC3}$ are the cross-section compression and bending moment resistances predicted using EN 1993-1-2 (CEN, 2005). As can be seen from the figures, EN 1993-1-2 (CEN, 2005) provides somewhat conservative ultimate resistance

predictions for stainless steel I-sections under compression and major axis bending when the slendernesses of the constituent plates are high, while the predictions lie on the unsafe side in the intermediate slenderness range. For stainless steel I-sections in minor axis bending, the EN 1993-1-2 (CEN, 2005) resistance predictions become increasingly conservative with increasing slenderness and become very conservative in the slender range. This is because although the minor axis bending resistance of slender I-sections is determined on the basis of a linear elastic stress distribution acting over an effective cross-section, in reality significant inelastic behaviour, resulting in higher bending capacity, is observed. Note that, for clarity, the results shown in Figs. 4.6, 4.7 and 4.8 are for the I-sections with the same web $\overline{\lambda}_{\mathrm{p,w}}$ and flange $\overline{\lambda}_{\mathrm{p,f}}$ plate slendernesses (i.e. $\overline{\lambda}_{\mathrm{p,w}} = \overline{\lambda}_{\mathrm{p,f}}$); the full set of results are presented in Section 4.6.

4.4 Assessment of the design method of Chapter 3 for stainless steel I-sections in fire

The accuracy of the design method developed in Chapter 3 for the prediction of the cross-section response of stainless steel I-sections in fire is investigated in this section. Comparisons between the FE results and design predictions are presented in Figs. 4.9–4.11 for austenitic, duplex and ferritic stainless steel I-sections, respectively, where $N_{\mathrm{fi,Rd,prop}}$ and $M_{\mathrm{fi,Rd,prop}}$ are the elevated temperature cross-section compression and bending moment resistances predicted using the design method of Chapter 3. As can be seen from the figures, relative to EN 1993-1-2 (CEN, 2005), the design method of Chapter 3 provides more consistent resistance predictions for the cases of axial compression and major axis bending, with no results on the unsafe side. This is because the influence of the variation of strength and stiffness at different elevated temperature levels is appropriately captured. However, for the case of stainless steel I-sections under minor axis bending, similar to EN 1993-1-2 (CEN, 2005), the predictions of the design method of Chapter 3 are overly conservative; again, this results from the neglect of the inelastic behaviour of outstand flanges under stress gradients. To address this overconservatism, the plastic effective

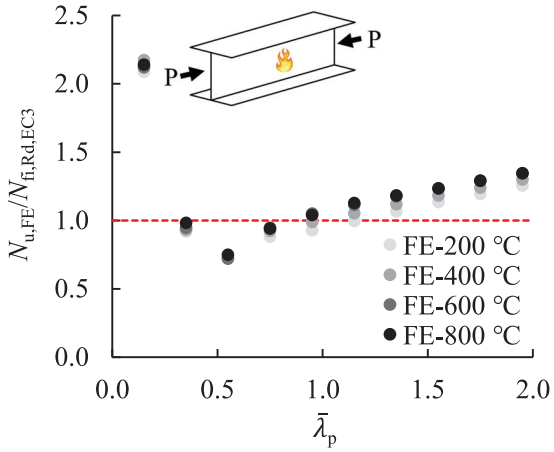

(a) I-sections in compression

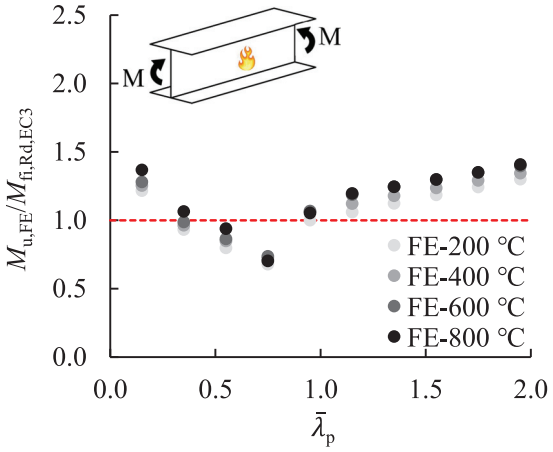

(b) I-sections in bending about the major axis

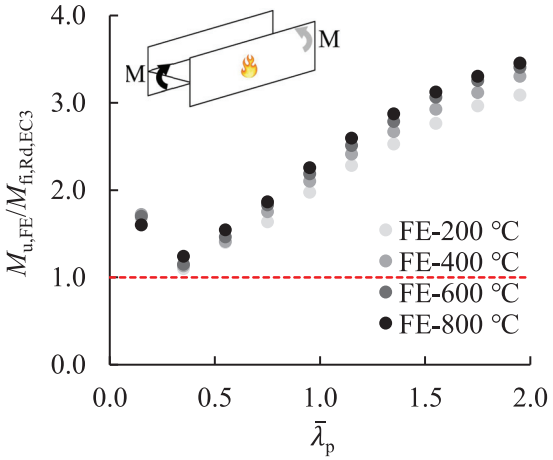

(c) I-sections in bending about the minor axis

Figure 4.6: Assessment of EN 1993-1-2 (CEN, 2005) against FE results for austenitic stainless steel I-sections

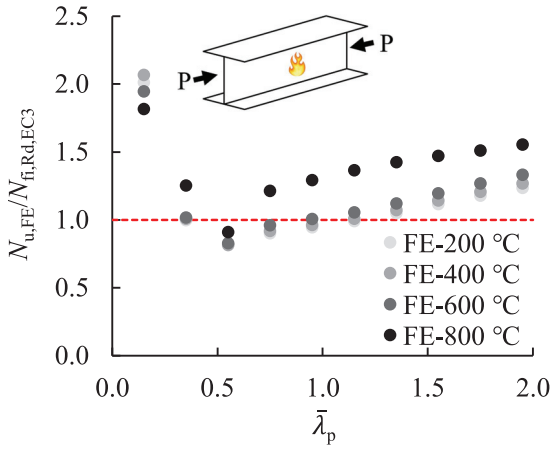

(a) I-sections in compression

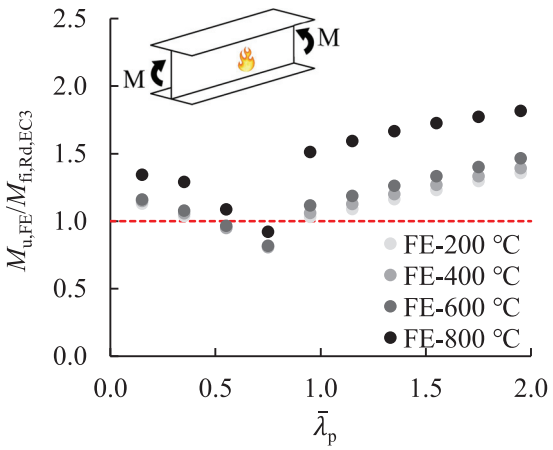

(b) I-sections in bending about the major axis

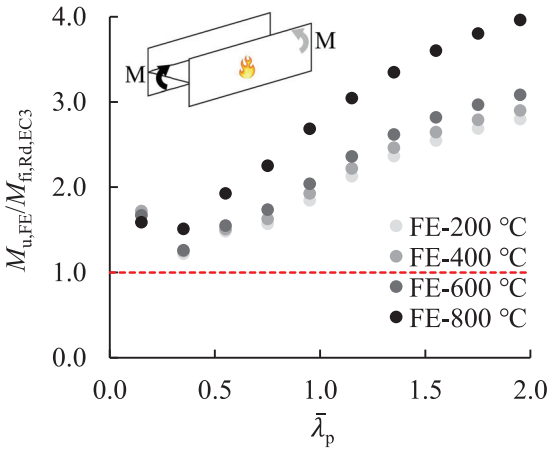

(c) I-sections in bending about the minor axis

Figure 4.7: Assessment of EN 1993-1-2 (CEN, 2005) against FE results for duplex stainless steel I-sections

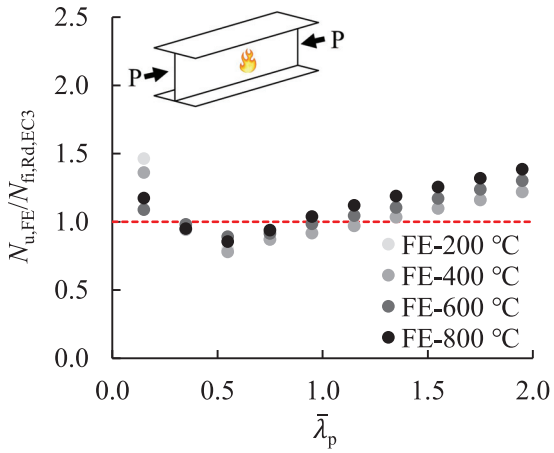

(a) I-sections in compression

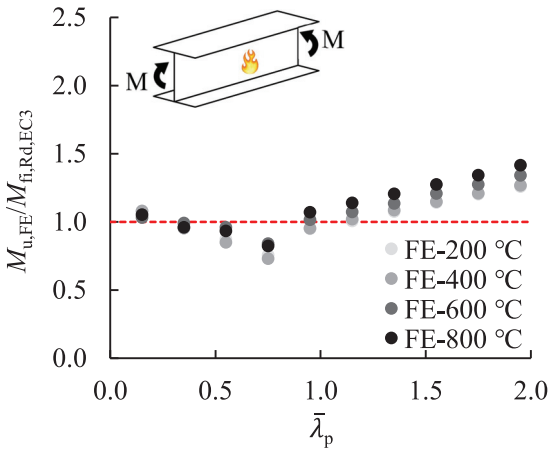

(b) I-sections in bending about the major axis

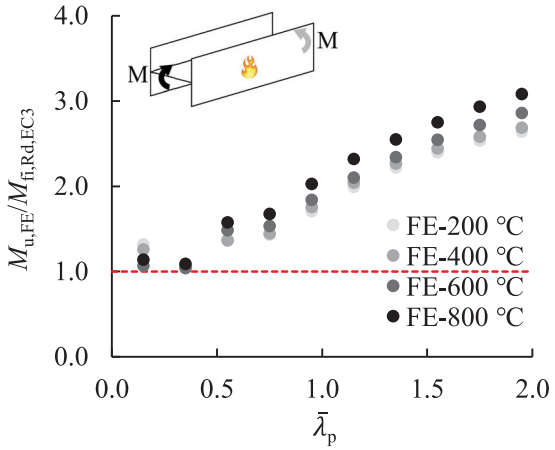

(c) I-sections in bending about the minor axis

Figure 4.8: Assessment of EN 1993-1-2 (CEN, 2005) against FE results for ferritic stainless steel I-sections

width method of Bambach & Rasmussen (2004), which was originally developed to reflect the room temperature inelastic behaviour of outstand flanges under stress gradients within carbon steel I-sections, is extended herein to the prediction of the minor axis bending moment resistance of stainless steel I-sections at elevated temperatures, as presented in the following section.

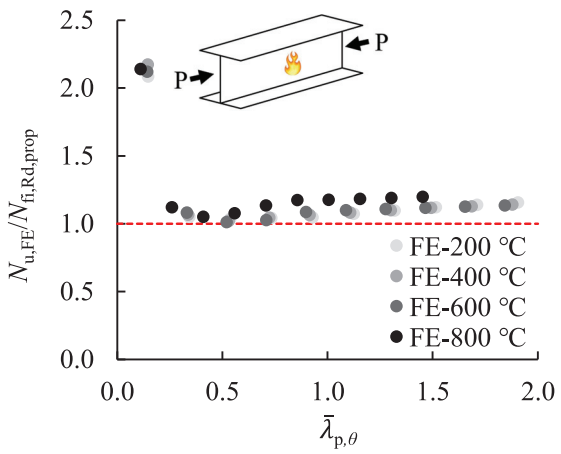

(a) I-sections in compression

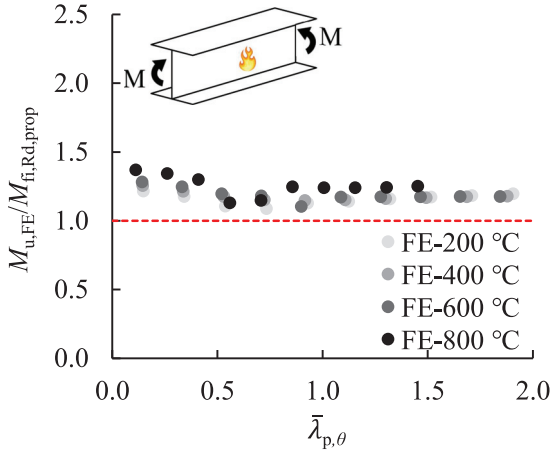

(b) I-sections in bending about the major axis

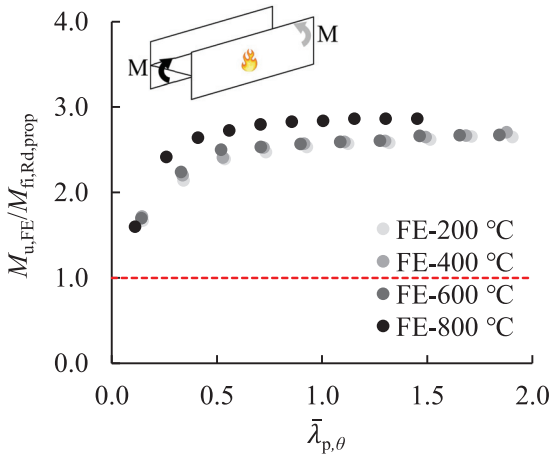

(c) I-sections in bending about the minor axis

Figure 4.9: Assessment of design method of Chapter 3 against FE results for austenitic stainless steel I-sections

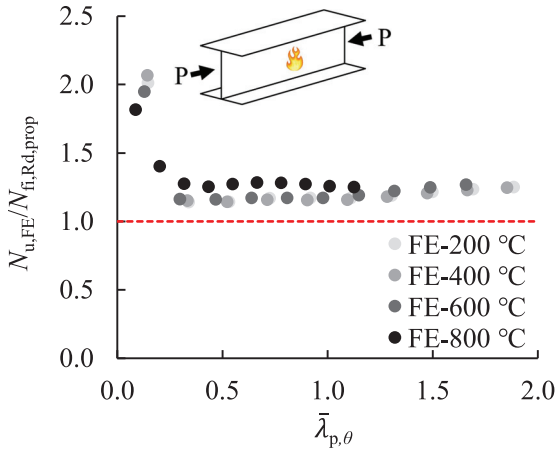

(a) I-sections in compression

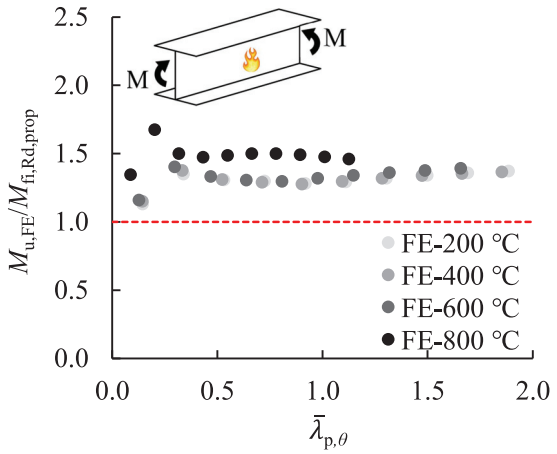

(b) I-sections in bending about the major axis

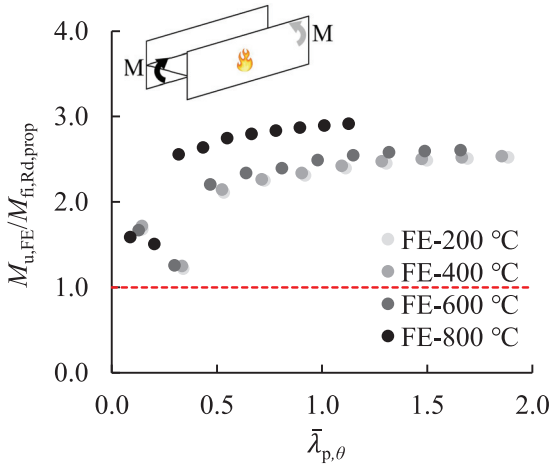

(c) I-sections in bending about the minor axis

Figure 4.10: Assessment of design method of Chapter 3 against FE results for duplex stainless steel I-sections

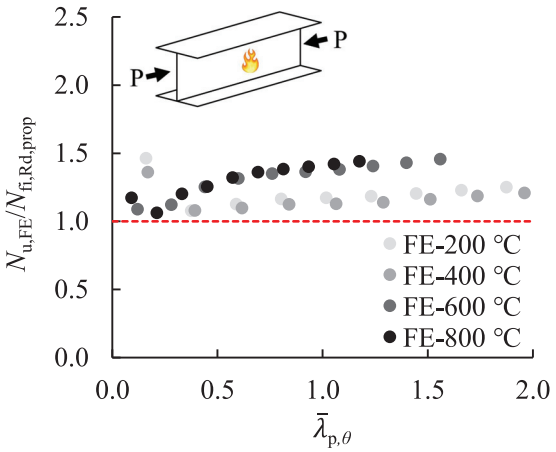

(a) I-sections in compression

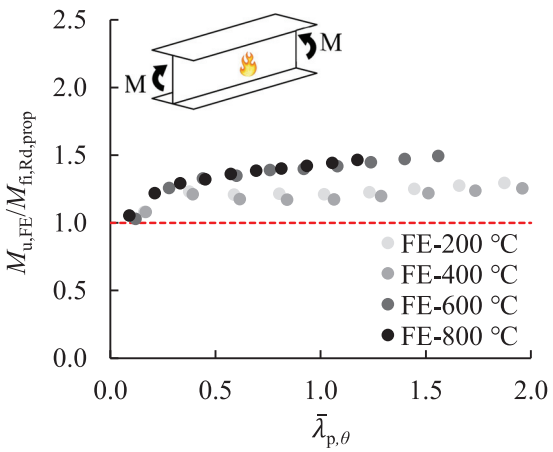

(b) I-sections in bending about the major axis

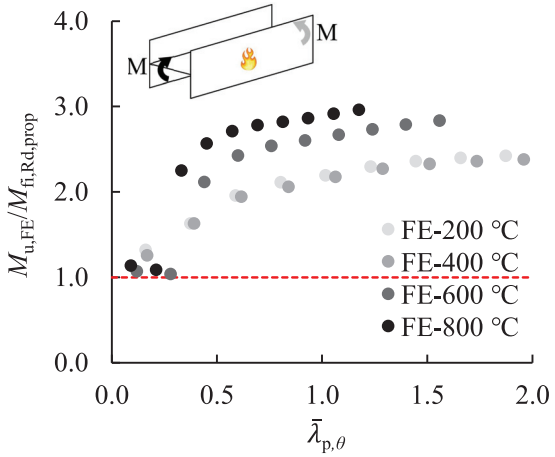

(c) I-sections in bending about the minor axis

Figure 4.11: Assessment of design method of Chapter 3 against FE results for ferritic stainless steel I-sections

4.5 Extension of the plastic effective width method of Bambach & Rasmussen (2004) to the design of stainless steel I-sections under minor axis bending in fire

In the plastic effective width method of Bambach & Rasmussen (2004), the effective width of outstand flanges under stress gradients is assumed to be located at an eccentricity relative to the supported edge and hence two variables – effective width b_{eff} and eccentricity e_1 – are utilised as shown in Fig. 4.12. Adopting the elevated temperature plate buckling slenderness $\overline{\lambda}_{\text{p},\theta}$ defined in eq. (3.22), the effective width b_{eff} of the flanges of I-sections subjected to minor axis bending can be calculated by Bambach & Rasmussen (2004):

$$\frac{b_{\text{eff}}}{b} = 0.4(1+\psi)\overline{\lambda}_{\text{p},\theta}{}^{-\frac{3}{4}} \leq 1 \tag{4.4}$$

and eccentricity e_1 is calculated by Bambach & Rasmussen (2004):

$$e_1 = 0.45b(1-\psi) \leq 1 - \frac{b_{\text{eff}}}{b} \quad \text{for } 0 \leq \psi \leq 1, \tag{4.5}$$

where ψ is the ratio of the stresses at the plate edges. Once b_{eff} and e_1 have been calculated, the strain distribution can be determined on the assumption that the maximum allowable strain in the effective section is equal to three times the yield strain (i.e. $\varepsilon_{\text{max}} = 3\varepsilon_{\text{y}}$), as illustrated in Fig. 4.12 (a); the corresponding stress distribution, where the stress σ is equal to f_{y} ($\sigma = f_{\text{y}}$) when the strain is greater than or equal to ε_{y} ($\varepsilon \geq \varepsilon_{\text{y}}$) while the stress σ is equal to εE_θ when the strain is less than ε_{y} ($\varepsilon < \varepsilon_{\text{y}}$), is shown in Fig. 4.12 (b). The moment capacity of the cross-section is then determined based on the resulting stress distribution. The accuracy of the plastic effective width method of Bambach & Rasmussen (2004), with the plate slenderness defined in eq. (3.22), is assessed in Fig. 4.13, where it can be seen that the ratios of the minor axis bending moment resistances to those obtained from the shell finite element models are generally close to unity, demonstrating the suitability of the plastic effective width method for the design of stainless steel

I-sections under minor axis bending at elevated temperatures.

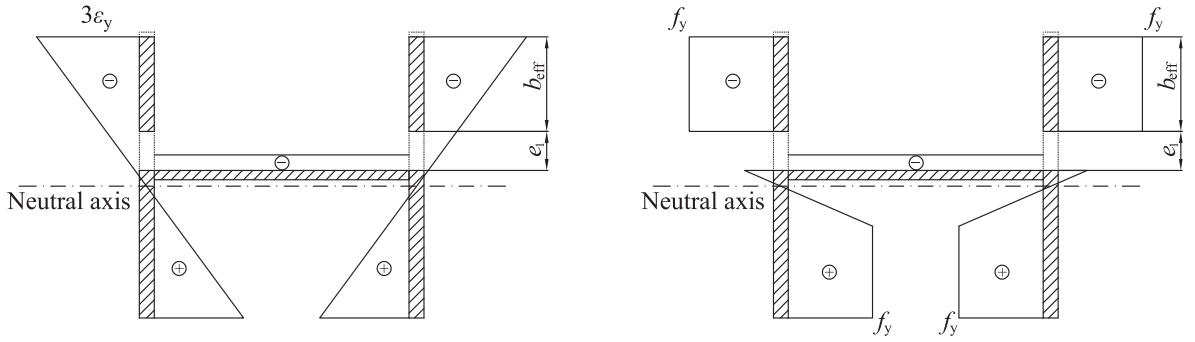

(a) Strain distribution (b) Stress distribution

Figure 4.12: Strain and stress distributions in I-sections under minor axis bending based on plastic effective width method proposed by Bambach & Rasmussen (2004), with tensile stresses indicated as positive

4.6 Comparison of design methods and reliability assessment

In this section, the accuracy and reliability of the design methods of Chapter 3 and Bambach & Rasmussen (2004), as well as EN 1993-1-2 (CEN, 2005), for determining the cross-section resistance of stainless steel I-sections in fire are assessed. Comparisons are made against a total of over 1000 shell FE results covering different stainless steel grades, elevated temperature levels, loading conditions and cross-section geometries against those of the existing design rules in EN 1993-1-2 (CEN, 2005). For design using the methods set out in Chapter 3 and (Bambach & Rasmussen, 2004), the expressions proposed in Chapter 3 alone were used for the cases of axial compression and major axis bending, while the Bambach & Rasmussen (2004) expressions, with the plate slenderness defined in eq. (3.22) were used for minor axis bending.

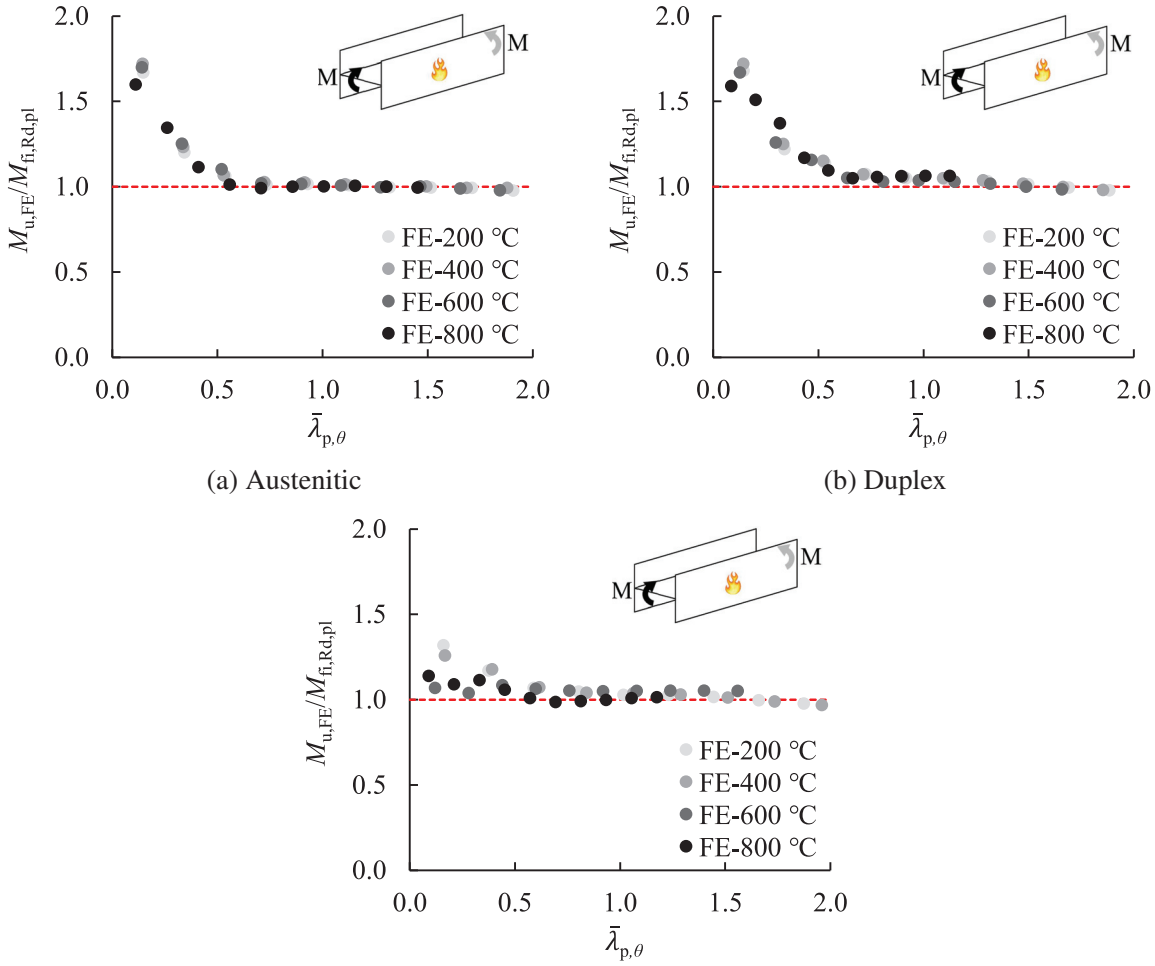

(a) Austenitic

(b) Duplex

(c) Ferritic

Figure 4.13: Assessment of plastic effective width method of Bambach & Rasmussen (2004) with plate slenderness $\bar{\lambda}_{p,\theta}$ defined in eq. (3.22) against FE results for stainless steel I-sections under minor axis bending

4.6.1 Accuracy assessment

The accuracy of the design methods of Chapter 3 and Bambach & Rasmussen (2004) is visually illustrated against that of the existing design rules of EN 1993-1-2 (CEN, 2005) in Fig. 4.14. Four different elevated temperature levels ranging from 200 °C to 800 °C in increments of 200 °C and the range of local plate slenderness values listed in Table 4.3 were considered. As can be seen from the figure, the design methods of Chapter 3 and Bambach & Rasmussen (2004) lead to more accurate and consistent cross-section resistance predictions relative to the existing design rules of EN 1993-1-2 (CEN, 2005), particularly for I-sections subjected to minor axis bending. In Table 4.4, the accuracy of the design methods of Chapter 3 and Bambach & Rasmussen (2004) is assessed in terms of the mean value and the coefficient of variation (COV) of the ratios of the cross-section resistances obtained from the numerical simulations to the corresponding predictions determined using the design methods of Chapter 3 and Bambach & Rasmussen (2004) (i.e. $\varepsilon = N_{\mathrm{u,FE}}/N_{\mathrm{fi,Rd,prop}}$). As can be seen from Table 4.4, relative to EN 1993-1-2 (CEN, 2005), the design methods of Chapter 3 and Bambach & Rasmussen (2004) provide more accurate and safe-sided cross-section resistance predictions with a lower level of scatter, indicating the better suitability of these methods for the design of stainless steel I-sections in fire.

Table 4.4: Accuracy assessment of EN 1993-1-2 (CEN, 2005) and design methods of Chapter 3 and Bambach & Rasmussen (2004), referred to as the proposed design methods in this table, against numerical results for all stainless steel I-sections

Loading condition	Grade	EN 1993-1-2		Proposed design methods	
		$\varepsilon_{\mathrm{mean}}$	$\varepsilon_{\mathrm{COV}}$	$\varepsilon_{\mathrm{mean}}$	$\varepsilon_{\mathrm{COV}}$
Compression	Austenitic	1.37	0.231	1.13	0.133
	Duplex	1.42	0.253	1.24	0.122
	Ferritic	1.16	0.141	1.14	0.097
Major axis bending	Austenitic	0.98	0.178	1.22	0.074
	Duplex	1.03	0.187	1.28	0.101
	Ferritic	0.97	0.131	1.24	0.081
Minor axis bending	Austenitic	2.49	0.348	1.32	0.168
	Duplex	2.45	0.334	1.35	0.169
	Ferritic	1.91	0.306	1.13	0.087

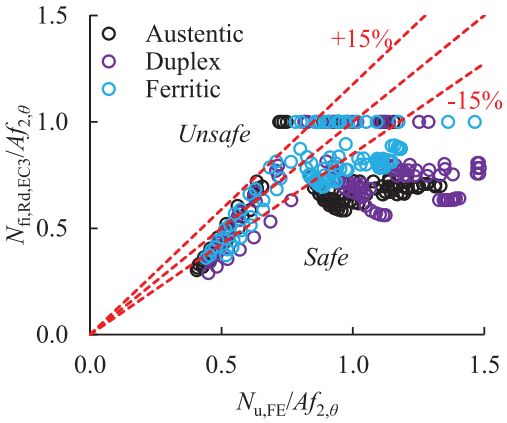

(a) Assessment of EN 1993-1-2 (CEN, 2005) for I-sections in compression

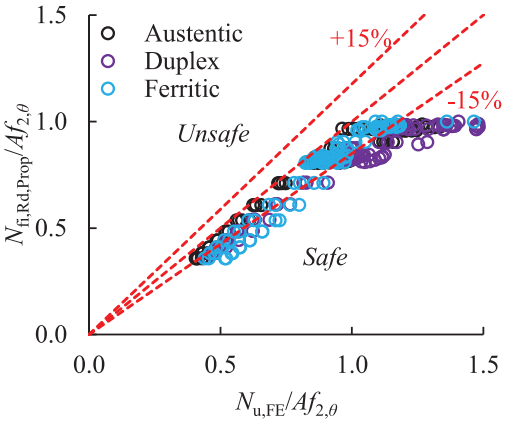

(b) Assessment of proposed design methods for I-sections in compression

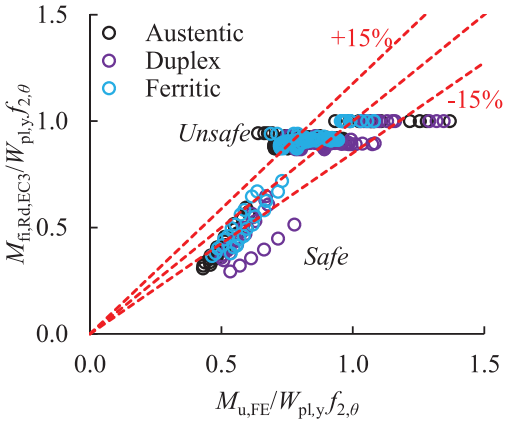

(c) Assessment of EN 1993-1-2 (CEN, 2005) for I-sections in bending about the major axis

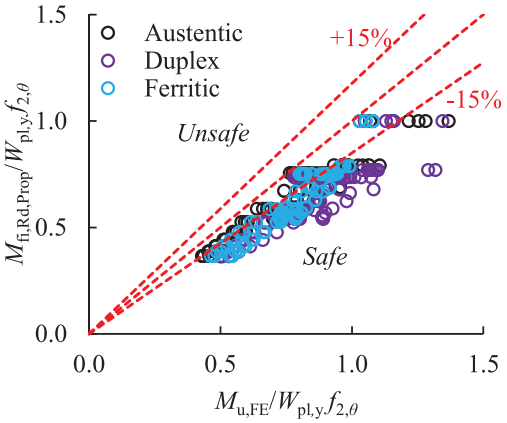

(d) Assessment of proposed design methods for I-sections in bending about the major axis

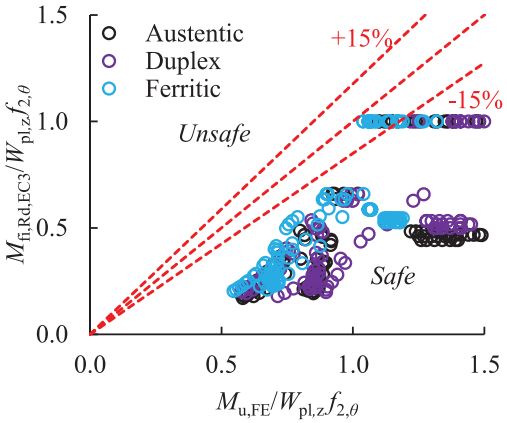

(e) Assessment of EN 1993-1-2 (CEN, 2005) for I-sections in bending about the minor axis

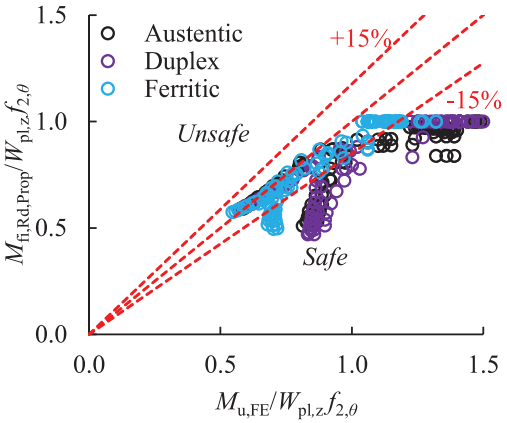

(f) Assessment of proposed design methods for I-sections in bending about the minor axis

Figure 4.14: Assessment of EN 1993-1-2 (CEN, 2005) and design methods of Chapter 3 and Bambach & Rasmussen (2004), referred to as the proposed design methods in this figure, against FE results for all stainless steel I-sections

4.6.2 Reliability assessment

The reliability of the methods provided in EN 1993-1-2 (CEN, 2005) and Chapter 3 and Bambach & Rasmussen (2004) for the cross-section design of stainless steel I-sections in fire is assessed by considering the three reliability criteria proposed by Kruppa (1999) in this subsection. The assessment results of these design methods are summarised in Table 4.5. As can be seen from the table, EN 1993-1-2 (CEN, 2005) frequently violates the reliability criteria of Kruppa (1999), while the design methods of Chapter 3 and Bambach & Rasmussen (2004) satisfy all the criteria of Kruppa (1999), indicating their suitability for the design of stainless steel I-sections in fire.

Table 4.5: Reliability assessment of EN 1993-1-2 (CEN, 2005) and design methods of Chapter 3 and Bambach & Rasmussen (2004), referred to as the proposed design methods in this table, against numerical results for all stainless steel I-sections. Values are given as percentages

Loading condition	Grade	EN 1993-1-2			Proposed design methods		
		Crit. 1	Crit. 2	Crit. 3	Crit. 1	Crit. 2	Crit. 3
Compression	Austenitic	4.5*	17.1	-23.1	0.0	0.0	-13.6
	Duplex	2.7*	12.6	-26.1	0.0	0.0	-21.0
	Ferritic	2.7*	22.5*	-12.1	0.0	0.0	-12.5
Major axis bending	Austenitic	22.2*	48.6*	4.4*	0.0	0.0	-17.3
	Duplex	3.0*	27.9*	-4.1	0.0	0.0	-23.2
	Ferritic	15.3*	42.9*	3.4*	0.0	0.0	-18.8
Minor axis bending	Austenitic	0.0	0.0	-53.6	0.0	9.2	-21.7
	Duplex	0.0	0.0	-53.8	0.0	4.2	-24.0
	Ferritic	0.0	0.0	-42.0	0.0	7.5	-10.7

*Reliability criterion of Kruppa (1999) not satisfied.

4.7 Conclusions

The cross-section behaviour and design of stainless steel I-sections in fire have been investigated in this chapter. To simulate the response of stainless steel I-sections at elevated temperatures, shell finite element models were created and validated against a series of experimental results from the literature. Parametric studies were then carried out, in which different cross-section

geometries, stainless steel grades, elevated temperature levels and loading conditions were considered. The design methods provided in the current version of EN 1993-1-2 (CEN, 2005) and Chapter 3 were subsequently assessed against the numerical results from the parametric studies, where shortcomings of the existing rules in EN 1993-1-2 (CEN, 2005) for the design of stainless steel I-sections in fire have been highlighted. Unlike EN 1993-1-2 (CEN, 2005), the design guidance of Chapter 3 was shown to provide accurate predictions of the response of stainless steel I-sections under compression and major axis bending in fire owing to the adoption of a new cross-section classification approach in conjunction with the temperature-dependent local buckling curves. Moreover, to consider the inelastic behaviour of slender outstand flanges under stress gradients, which was observed for stainless steel I-sections under minor axis bending, the plastic effective width method of Bambach & Rasmussen (2004), originally developed for the room temperature design of carbon steel I-sections, was extended to the design of stainless steel I-sections under minor axis bending in fire. The research findings in this chapter demonstrated the accuracy and reliability of the design methods of Chapter 3 and Bambach & Rasmussen (2004) for stainless steel I-sections in fire, and confirmed the suitability of the design method of Chapter 3 for inclusion into the upcoming version of 1993-1-2 (CEN, 2005).

Chapter 5

Testing of I-section columns

5.1 Introduction

Eight full-scale fire tests have been performed on grade 1.4301 austenitic stainless steel laser-welded I-section columns and are presented in this chapter. In addition to the fire tests, two room temperature tests on columns with the same geometric properties and from the same batch of material as those of the specimens subjected to fire testing have also been conducted. In the fire tests carried out in this study, the critical temperatures of the specimens ranged between approximately 300 °C and 800 °C, thereby covering the full practical range of fire design temperatures. The anisothermal testing method was adopted in the experiments to mimic a real fire situation. In this method, axial compression is first applied to the test specimen, and then the specimen is heated at a predefined heating rate until failure. The experimental results for the ten austenitic stainless steel columns, covering two cross-sections and four different axial load levels, are reported in addition to tensile coupon tests at room temperature and initial geometric imperfection measurements made on the specimens.

5.2 Material properties

The tested I-section members were fabricated through the laser-welding of hot-rolled grade 1.4301 austenitic stainless steel plates; the laser-welding was carried out to Class B quality level for weld imperfections according to EN ISO 13919-1 (CEN, 1997). The chemical compositions and material properties of the tested I-section members, as provided in the manufacturer's mill certificates, are summarised in Tables 5.1 and 5.2 respectively, where $f_{y,mill}$ is the 0.2% proof stress, $f_{p1.0,mill}$ is the 1% proof stress, $f_{u,mill}$ is the ultimate tensile stress and $\varepsilon_{f,mill}$ is the strain at fracture measured over the gauge length of $5.65\sqrt{S_0}$, where S_0 is the cross-sectional area of the coupon extracted. Two cross-section sizes were employed for the column test specimens for: I-198×99×4.5×7 and I-248×124×5×8. The labelling system of the cross-sections in Table 5.2 is based on the cross-section dimensions shown in Fig. 5.1 - i.e. I-198×99×4.5×7 indicates an I-section with a cross-section nominal depth h of 198 mm, flange width b of 99 mm, web thickness t_w of 4.5 mm and flange thickness t_f of 7 mm.

Table 5.1: Chemical compositions in mill certificates

Specimen	Grade	C (%)	Si (%)	Mn (%)	P (%)	S (%)	Ni (%)	Cr (%)	N (%)
I-198×99×4.5×7	1.4301	0.026	0.41	1.37	0.032	0.001	8.00	18.01	0.070
		0.024	0.40	1.38	0.031	0.002	8.05	18.05	0.069
I-248×124×5×8	1.4301	0.026	0.41	1.37	0.032	0.001	8.00	18.01	0.070
		0.021	0.22	1.77	0.038	0.003	8.08	18.32	-

Table 5.2: Material properties in mill certificates

Specimen	$f_{y,mill}$ (N/mm^2)	$f_{p1.0,mill}$ (N/mm^2)	$f_{u,mill}$ (N/mm^2)	$\varepsilon_{f,mill}$ (%)
I-198×99×4.5×7	312	349	630	51
	313	348	625	52
I-248×124×5×8	312	349	630	51
	329	-	612	52

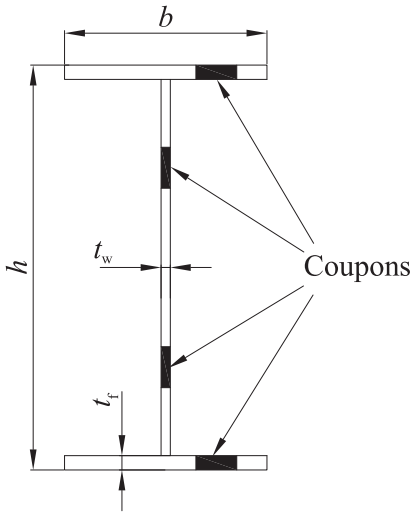

Figure 5.1: Cross-section labelling system and locations of tensile coupons

A total of eight tensile coupons were extracted from the two tested cross-section shapes. As shown in Fig. 5.1, two tensile coupons were cut from the top and bottom flanges and the other two were cut from the web of each cross-section. Fig. 5.2 shows the dimensions of the tensile coupons, which are in accordance with the recommendations of Huang & Young (2014a).

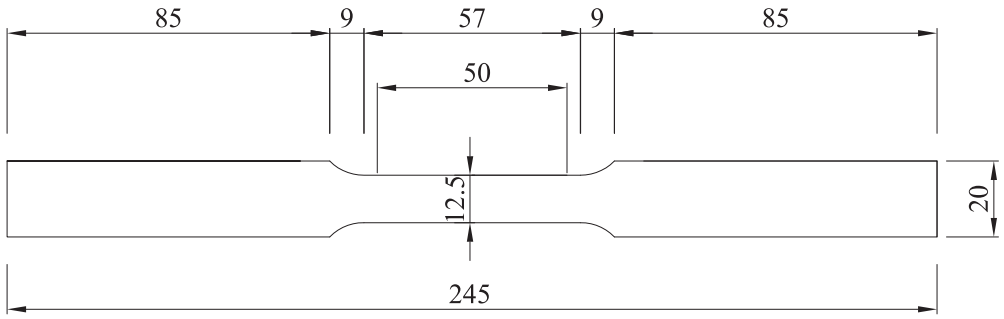

Figure 5.2: Dimensions of tensile coupon (dimensions in mm)

All of the coupon tests were performed using a 250 kN hydraulic testing machine under a displacement-controlled loading scheme; the initial loading rate was 0.05 mm/min, and once the nominal yield stress had been reached, the loading rate was increased to 0.8 mm/min until

the fracture. The tensile coupon test setup is illustrated in Fig. 5.3, where it can be seen that an extensometer was mounted onto the middle of the coupons and two strain gauges were adhered to the mid-height of the two sides of the coupons.

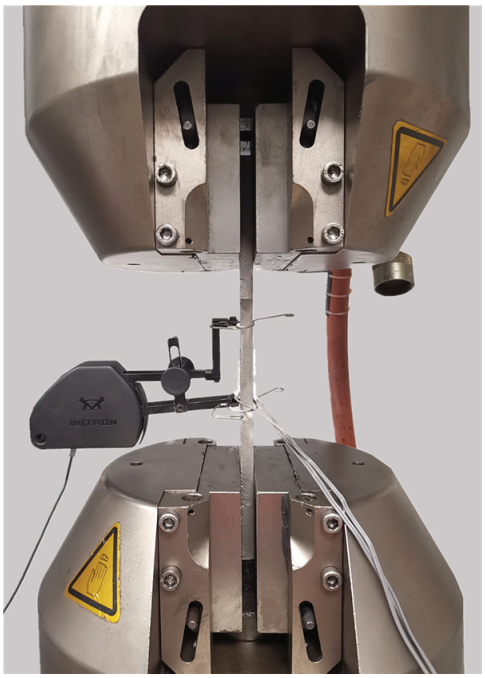

Figure 5.3: Tensile coupon test setup

The coupons were labelled with respect to the nominal thickness of the plate from which they were extracted and whether they were extracted from the web or flange plate of a cross-section. An additional number (i.e. 1 or 2) was also used to label the coupons since two coupons were extracted from each web and flange plate. Thus, TC4.5-W-1 corresponds to one of the two tensile coupons extracted from a web plate with a nominal thickness of 4.5 mm.

The measured stress-strain curves from the eight tensile coupons are plotted in Fig. 5.4a–5.4d and the key material properties are reported in Table 5.3, where t is the coupon thickness, E is the Young's modulus, f_y is 0.2% proof stress, $f_{p1.0}$ is the 1% proof stress, $f_{2.0}$ is the stress at 2% total strain, f_u is the ultimate stress, ε_u is the ultimate strain and ε_f is the fracture strain measured over a 50 mm gauge length.

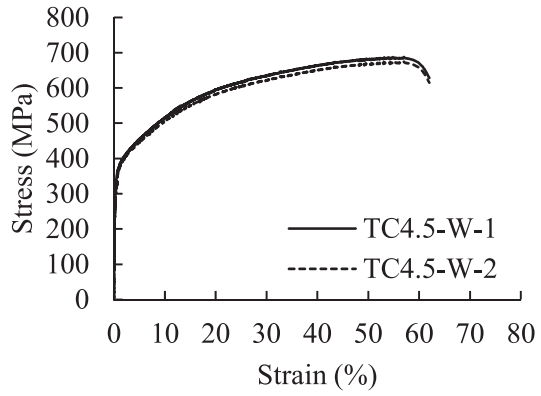

(a) Tensile coupon with 4.5 mm thickness (web)

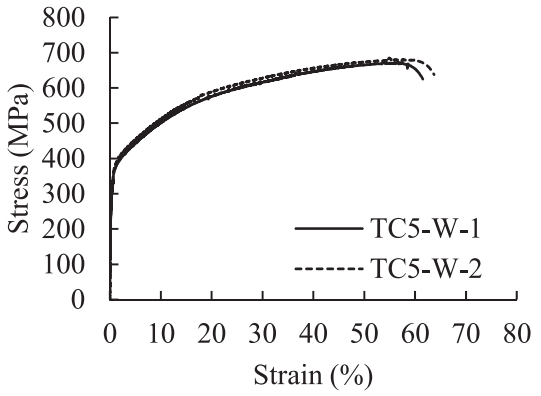

(b) Tensile coupon with 5 mm thickness (web)

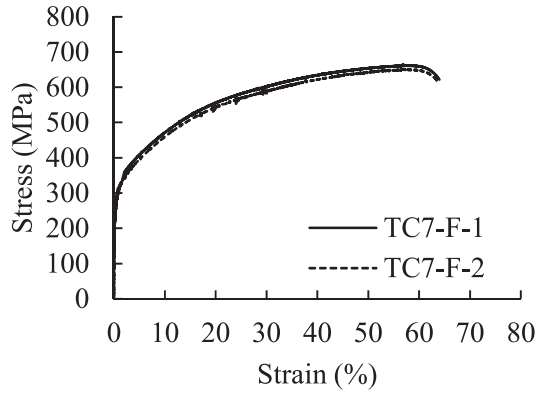

(c) Tensile coupon with 7 mm thickness (flange)

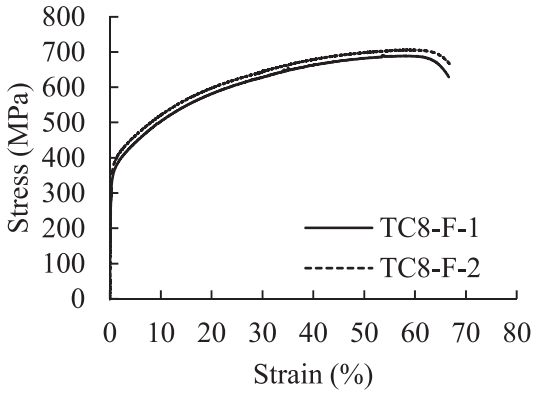

(d) Tensile coupon with 8 mm thickness (flange)

Figure 5.4: Tensile coupon test results at room temperature

The Ramberg-Osgood exponents n and m_{u} (Mirambell & Real, 2000; Rasmussen, 2003; Gardner & Yun, 2018; Arrayago *et al.*, 2015) in Table 5.3 were obtained by fitting the two-stage compound Ramberg–Osgood material model presented by Gardner (2019) and given by eq. (5.1) and eq. (5.2) to the stress-strain ($\sigma - \varepsilon$) curves obtained from the coupon tests. Note that in eq. (5.2),

Table 5.3: Key material properties obtained from tensile coupon tests

ID	t	E	f_y	$f_{p1.0}$	$f_{2.0}$	f_u	ε_u	ε_f	R-O coefficient	
	(mm)	(N/mm^2)	(N/mm^2)	(N/mm^2)	(N/mm^2)	(N/mm^2)	(%)	(%)	n	m_u
TC4.5-W-1	4.83	198200	324	386	405	688	57	70	4.7	2.8
TC4.5-W-2	4.87	194600	298	376	399	681	55	69	5.5	3.2
TC5-W-1	4.88	194800	297	377	396	674	54	69	5.4	2.8
TC5-W-2	4.85	197700	306	386	407	685	55	72	5.2	2.9
TC7-F-1	6.92	193700	263	320	356	665	57	74	5.7	2.8
TC7-F-2	6.93	198800	254	323	343	649	54	77	6.7	2.6
TC8-F-1	7.99	202700	324	375	395	691	54	78	5.9	2.5
TC8-F-2	8.01	202000	347	397	416	707	58	81	5.8	2.5

$E_{p0.2}$ and $\varepsilon_{p0.2}$ are the tangent modulus and total strain at the 0.2% proof stress, respectively.

$$\varepsilon = \frac{\sigma}{E} + 0.002\left(\frac{\sigma}{f_y}\right)^n \quad \text{for} \quad \sigma \leq f_y \tag{5.1}$$

$$\varepsilon = \frac{\sigma - f_y}{E_{p0.2}} + \left(\varepsilon_u - \varepsilon_{p0.2} - \frac{f_u - f_y}{E_{p0.2}}\right)\left(\frac{\sigma - f_y}{f_u - f_y}\right)^{m_u} + \varepsilon_{p0.2} \quad \text{for} \quad f_y < \sigma \leq f_u, \tag{5.2}$$

For the numerical simulation of the elevated temperature response of stainless steel elements, the modified two-stage compound Ramberg–Osgood material model presented in Section 3.2.1 can be used to represent their elevated temperature material stress-strain response. The elevated temperature material properties of stainless steel (i.e. $f_{p0.2,\theta}$, $f_{2,\theta}$, E_θ, $f_{u,\theta}$ and $\varepsilon_{u,\theta}$) can be estimated by multiplying the strength ($k_{p0.2,\theta}$, $k_{2,\theta}$), stiffness ($k_{E,\theta}$) and ductility ($k_{\varepsilon_{u,\theta}}$) reduction factors given in SCI (2017) (see Fig. 5.5) by the corresponding room temperature material properties, i.e. $f_{p0.2,\theta} = k_{p0.2,\theta} f_y$, $f_{2,\theta} = k_{2,\theta} f_y$, $E_\theta = k_{E,\theta} E$, $f_{u,\theta} = k_{u,\theta} f_u$ and $\varepsilon_{u,\theta} = k_{\varepsilon_{u,\theta}} \varepsilon_u$. The full elevated temperature stress-strain curves can be generated using eqs. (3.1) and (3.2) in conjunction with the measured room temperature properties and the reduction factors from SCI (2017), as shown for the 8 mm thick material examined herein in Fig. 5.6.

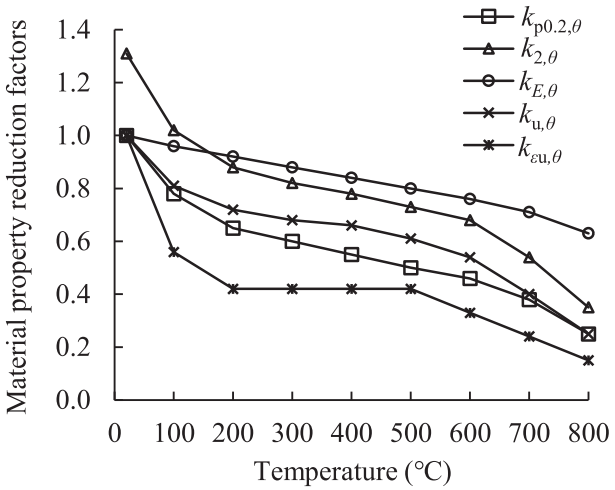

Figure 5.5: Strength ($k_{p0.2,\theta}$, $k_{2,\theta}$), stiffness ($k_{E,\theta}$) and ductility ($k_{\varepsilon_{u,\theta}}$) reduction factors of grade 1.4301 austenitic stainless steel at elevated temperatures from SCI (2017)

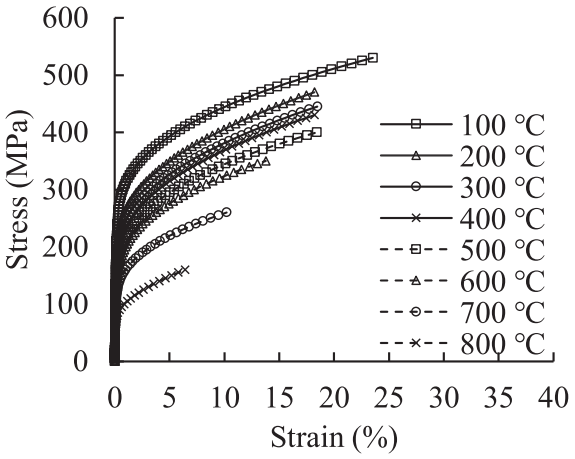

Figure 5.6: Stress-strain response of stainless steel at elevated temperatures determined using eqs. (3.1) and (3.2), based on the measured room temperature material properties and the elevated temperature reduction factors from SCI (2017), shown, as an example, for the 8 mm thick material

5.3 Geometry and imperfection measurements

Prior to conducting the column tests, the geometric properties of the ten tested specimens were measured; the measurements are summarised in Table 5.4, where L is the buckling length of the columns between the two centres of the knuckle bearings used in the tests, as shown in Fig. 5.7. The column specimens were labelled considering their cross-section profiles: LC1 corresponds to the column specimens with the I-248×124×5×8 cross-section, while LC2 corresponds to the column specimens with the I-198×99×4.5×7 cross-section. An additional number was also utilised in the labelling of the column specimens to signify the four different nominal axial load ratios $n_r = 0.6, 0.5, 0.4$ and 0.3, which are equal to the ratio of the applied axial load $N_{Ed,test}$ to the room temperature minor axis flexural buckling resistances N_u determined from the room temperature column buckling tests (i.e. $n_r = N_{Ed,test}/N_u$). The column specimens tested at room temperature were denoted LC1-20C for the column with the I-248×124×5×8 cross-section and LC2-20C for the column with the I-198×99×4.5×7 cross-section.

Table 5.4: Geometric properties of tested stainless steel I-section column specimens

ID	Cross-section	L (mm)	h (mm)	b (mm)	t_w (mm)	t_f (mm)
LC1-20C	I-248×124×5×8	2502.25	248.27	124.43	4.90	8.03
LC1-0.6	I-248×124×5×8	2502.20	248.46	124.44	4.91	8.05
LC1-0.5	I-248×124×5×8	2502.60	248.23	124.45	4.90	8.06
LC1-0.4	I-248×124×5×8	2501.75	248.45	124.45	4.96	8.05
LC1-0.3	I-248×124×5×8	2502.50	248.31	124.52	5.00	8.03
LC2-20C	I-198×99×4.5×7	2751.75	198.12	99.47	4.88	6.94
LC2-0.6	I-198×99×4.5×7	2752.20	198.22	99.45	4.67	6.92
LC2-0.5	I-198×99×4.5×7	2752.25	198.04	99.44	4.92	6.89
LC2-0.4	I-198×99×4.5×7	2752.50	198.32	99.47	4.95	6.95
LC2-0.3	I-198×99×4.5×7	2752.60	198.21	99.49	4.77	7.02

Initial local geometric imperfections of four columns (LC1-20C, LC1-0.6, LC2-20C and LC2-0.6) and initial global geometric imperfections of all tested columns were measured following the procedure recommended by Schafer & Peköz (1998). For the local imperfection measurements, the columns were first secured to the bed of a CNC milling machine, and then an LVDT, which

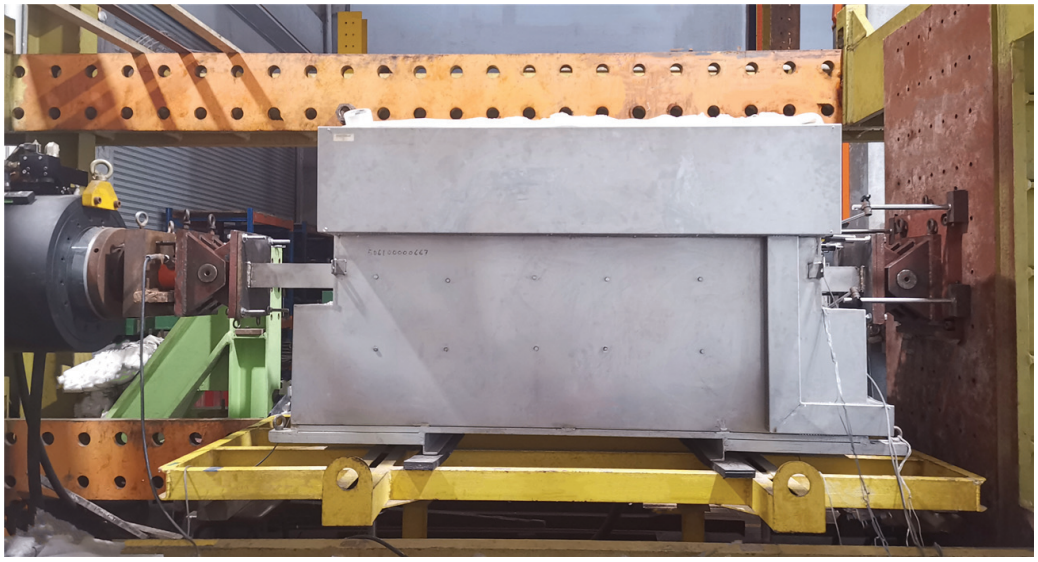

(a) Photo of test setup at room temperature

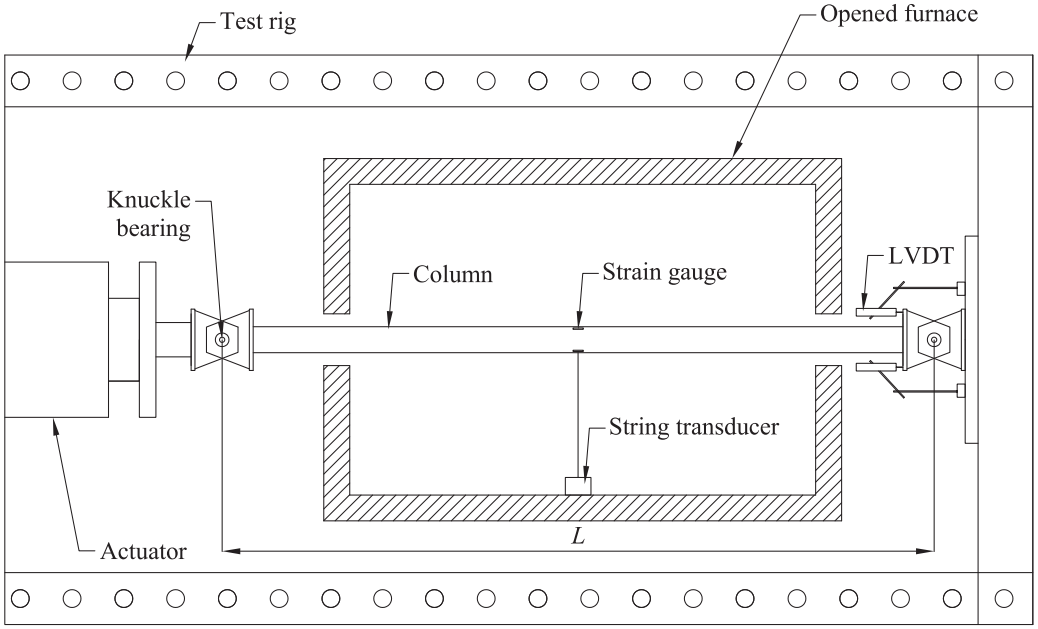

(b) Schematic drawing of room temperature column test setup

Figure 5.7: Column test setup at room temperature

was attached to the movable frame of the CNC milling machine, was moved along a 600 mm length away from the ends of the specimens to record displacements at 1 mm intervals, as shown in Fig. 5.8; lines of measurements were taken at the nine different locations illustrated in Fig. 5.9.

Figure 5.8: Imperfection measurement setup

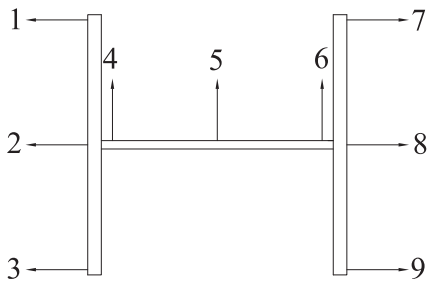

Figure 5.9: Imperfection measurement locations

Fig. 5.10 shows a typical measured local geometric imperfection distribution. The measured web local imperfection magnitudes w_{w} and the measured flange local imperfection magnitudes w_{f}, which are provided in Table 5.5, were defined as the maximum deviations from a straight line

fitted to the local imperfection measurements along the specimen lengths least squares regression. As can be seen from Table 5.5, both the measured web w_w and flange local imperfections w_f were significantly lower than the manufacturing tolerance of 1/100 of the web height and 1/100 of the flange width set out in EN 1090-2 (CEN, 2018).

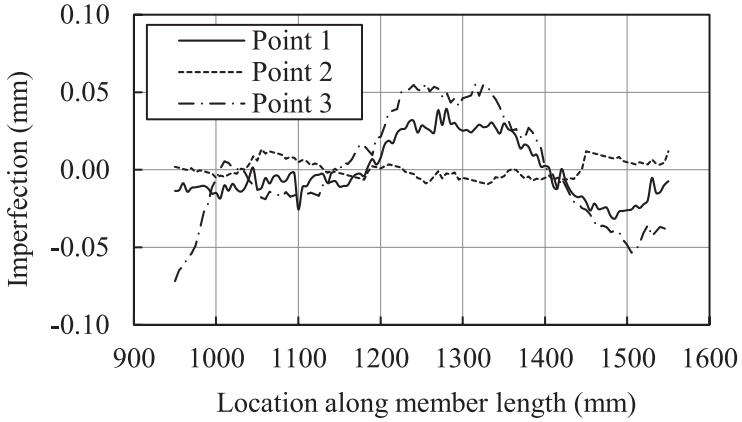

Figure 5.10: Typical measured local imperfection distributions; shown for the top flange of specimen LC2-20C

Table 5.5: Geometric imperfections of tested stainless steel I-section column specimens

ID	Cross-section	w_f (mm)	w_w (mm)	w_0 (mm)	v_0 (mm)
LC1-20C	I-248×124×5×8	0.08	0.07	0.08	0.32
LC1-0.6	I-248×124×5×8	0.05	0.06	0.06	0.15
LC1-0.5	I-248×124×5×8	-	-	-	0.35
LC1-0.4	I-248×124×5×8	-	-	-	0.23
LC1-0.3	I-248×124×5×8	-	-	-	0.30
LC2-20C	I-198×99×4.5×7	0.07	0.05	0.07	0.47
LC2-0.6	I-198×99×4.5×7	0.04	0.04	0.04	0.39
LC2-0.5	I-198×99×4.5×7	-	-	-	0.35
LC2-0.4	I-198×99×4.5×7	-	-	-	0.39
LC2-0.3	I-198×99×4.5×7	-	-	-	0.44

In the measurement of the initial global geometric imperfection magnitudes, the LVDT was moved to record deviations at Location 5 of the cross-sections (see Fig. 5.9) along the full lengths L_c of the specimens with the exception of two 100 mm lengths at the ends of the columns due to the limited range of the movable frame of the CNC milling machine. Fig. 5.11 shows a typ-

ical measured initial global geometric imperfection distribution where the maximum deviation from a straight line connecting the ends of the measured length of the column was taken as the maximum global geometric imperfection v_0. The measured global geometric imperfections for each specimen are provided in Table 5.4, where it can be seen that the average of the measured global geometric imperfection magnitudes was around 1/7000 of the specimen lengths L_c (i.e. $L_c/7000$), which is significantly lower than the manufacturing tolerance of $L_c/1000$ set out in EN 1090-2 (CEN, 2018).

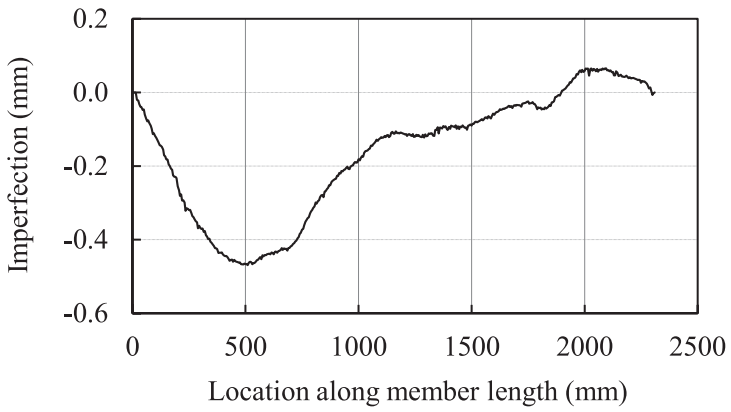

Figure 5.11: Typical measured initial global imperfection distributions; shown for specimen LC2-20C

5.4 Column tests at room temperature

To provide a benchmark against which to assess the influence of fire conditions on the structural response of the examined stainless steel I-section columns, two corresponding room temperature minor axis flexural buckling tests were performed. The columns were tested with pinned end conditions in a horizontal self-reacting test rig, which was also utilised in the fire tests. The nominal geometries of the two specimens were identical to those of the columns tested in fire: (i) a column with an I-248×124×5×8 cross-section and a buckling length L of 2.5 m and (ii) a column with an I-198×99×4.5×7 cross-section and a buckling length L of 2.75 m.

5.4.1 Test setup and testing procedures

Fig. 5.7 shows the overall experimental apparatus, which consisted of a 5000 kN capacity horizontal self-reacting test rig with hydraulic actuator to apply the axial load, knuckle bearings at the ends of the column to provide pin-ended support conditions about the minor axis, four LVDTs placed at four corners of the right hand end plate to measure the end rotations and one string transducer attached to the mid-height of the column to measure the mid-height lateral deformations. The furnace was retained in situ but left open during the room temperature testing. Fig. 5.12 shows the details of the loading system at the left hand end of the column, where a load cell, placed between the actuator and the left hand knuckle bearing, was used for measuring the applied loading. Before testing, a laser leveller was utilised to verify the alignment of the actuator, the load cell, the pins of the two knuckle bearings and the column.

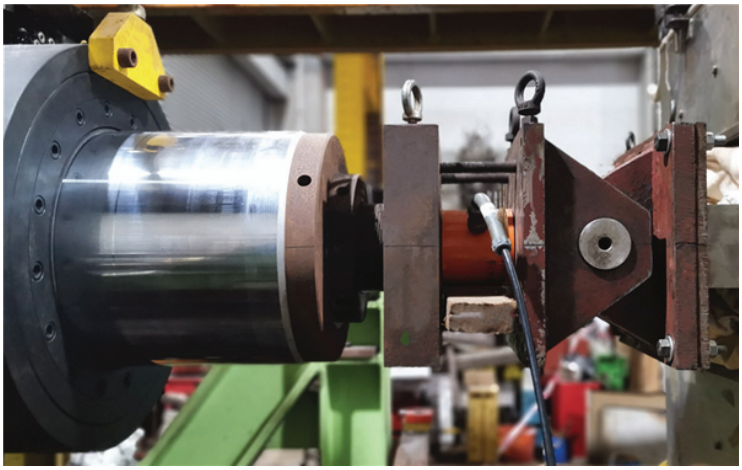

Figure 5.12: Details of loading system at column head

Member bow imperfections v_0 were measured using the setup shown in Fig. 5.9 prior to testing and found to have an average magnitude of about $L/7000$; additional loading eccentricities e_0 were introduced by eccentrically welding the specimens to their end plates, as shown in Fig. 7.2, such that the total (downward) global imperfection $(v_0 + e_0)$ was approximately $L/1000$. The actual measured total global imperfection amplitudes were back-calculated using four strain gauges affixed to the specimens at mid-height at a distance of d_s =10 mm from the outer edges

of the four flanges, following the method described by Zhao *et al.* (2015a). The calculation of the actual total global imperfection amplitude ($v_0 + e_0$) was performed using eqs. (5.3)–(5.5):

$$v_0 + e_0 = \frac{EI_z(\varepsilon_{max} - \varepsilon_{min})}{N(b_f - 2d_s)} - \delta, \tag{5.3}$$

in which

$$\varepsilon_{max} = (\varepsilon_1 + \varepsilon_2)/2, \tag{5.4}$$

$$\varepsilon_{min} = (\varepsilon_3 + \varepsilon_4)/2, \tag{5.5}$$

where $\varepsilon_1, \varepsilon_2, \varepsilon_3$ and ε_4 are the strain gauge readings, E is the modulus of elasticity, I_z is the minor axis second moment of area, N is the applied load and δ is the mid-height lateral deflection. The locations of the four strain gauges are illustrated in Fig. 5.14.

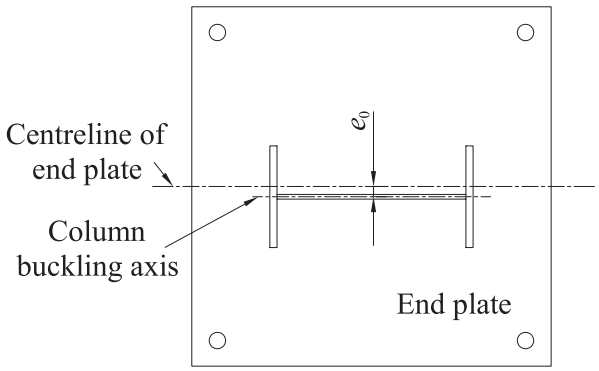

Figure 5.13: Positioning of specimens and end-plates

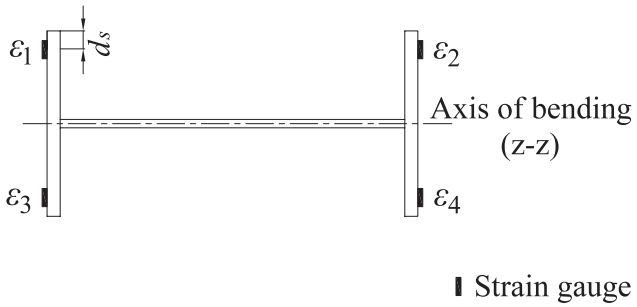

Figure 5.14: Strain gauge arrangement adopted at the mid-height of the specimens

Table 5.6 summarises the measured total test global imperfection values, which comprised two parts: (i) the initial global imperfection v_0 and (ii) the additional loading eccentricity e_0 introduced in each test. In the two room temperature column tests, a displacement-controlled loading scheme was utilised and the axial loading was applied at a rate of 0.3 mm/min. All the data, including the applied load, the mid-height deflection, the strains measured by the four strain gauges and the displacements of the four LVDTs, were recorded by a data logger at 1 s intervals.

Table 5.6: Key experimental results of column tests at room temperature

ID	Total global imperfection $v_0 + e_0$ (mm)	Ultimate load N_u (kN)	Lateral displacement at N_u (mm)	End rotation at N_u (rad)
LC1-20C	2.42	398	8.8	0.72
LC2-20C	1.03	223	7.0	0.32

5.4.2 Test results

As anticipated, both of the tested stainless steel columns (LC1-20C and LC2-20C) failed by minor axis flexural buckling; a typical failure mode, that of LC2-20C, is shown in Fig. 5.15. The load versus mid-height lateral displacement curves for the tested columns are plotted in Fig. 5.16. The key results from the tests – the minor axis flexural buckling loads N_u and the lateral mid-height displacements and end-rotations at failure – are summarised in Table 5.6.

Figure 5.15: Typical failure mode from room temperature tests, showing flexural buckling about the minor axis, illustrated for specimen LC2-20C

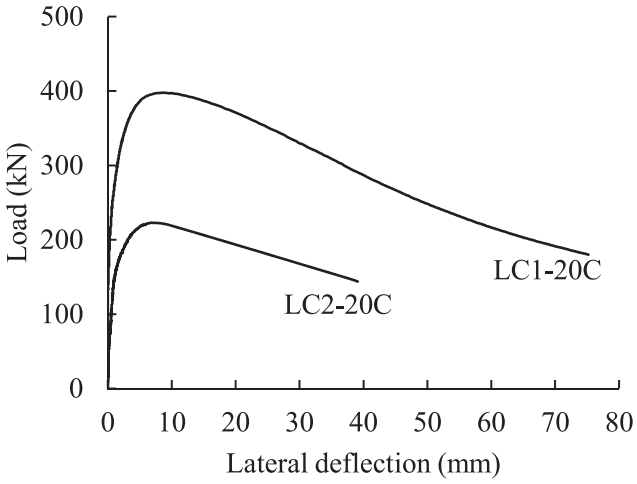

Figure 5.16: Load-mid-height lateral deflection curves for column tests at room temperature

5.5 Column fire tests

A total of eight fire tests were carried out on pin-ended stainless steel I-section columns. Of these eight tested columns, four had an I-248×124×5×8 cross-section with a buckling length of 2.5 m and the other four had an I-198×99×4.5×7 cross-section with a buckling length of 2.75 m. An anisothermal testing method was employed in all fire tests. Four different load ratios n_r equal to the ratio of the applied axial load $N_{Ed,test}$ to the minor axis flexural buckling capacities N_u (i.e. $n_r = N_{Ed,test}/N_u$) obtained from the room temperature tests, namely n_r =0.3, 0.4, 0.5 and 0.6, were considered to achieve a broad range of failure temperatures.

5.5.1 Test setup

Fig. 5.17 shows the column fire test setup, which consisted of a 5000 kN capacity horizontal self-reacting test rig with an actuator, an electric furnace, an LVDT with a bespoke displacement measurement system to measure the lateral deflection of the column at mid-height and four strain gauges to determine the total test eccentricity. Note that a length of 115 mm for the LC1 specimens and a length of 240 mm for the LC2 specimens were left outside the furnace at the two ends, which remained unheated during the testing; this was because the knuckle bearings connected to the end plates of the columns had to be placed outside the furnace and required space to rotate. Before the testing, the left hand and right hand openings of the furnace were heavily insulated around the columns by heat resistant fabrics and rockwool to avoid any heat loss.

The electric furnace shown in Fig. 5.18 was used for the column fire tests. During testing, the air temperature of the furnace, which was measured through two thermocouples, was increased in accordance with the ISO-834 (1999) standard fire curve as shown in Fig. 5.19. One of the thermocouples was connected to the furnace heating control system and the other thermocouple was embedded into a furnace wall (see Fig. 5.20).

(a) Photo of test setup at elevated temperature

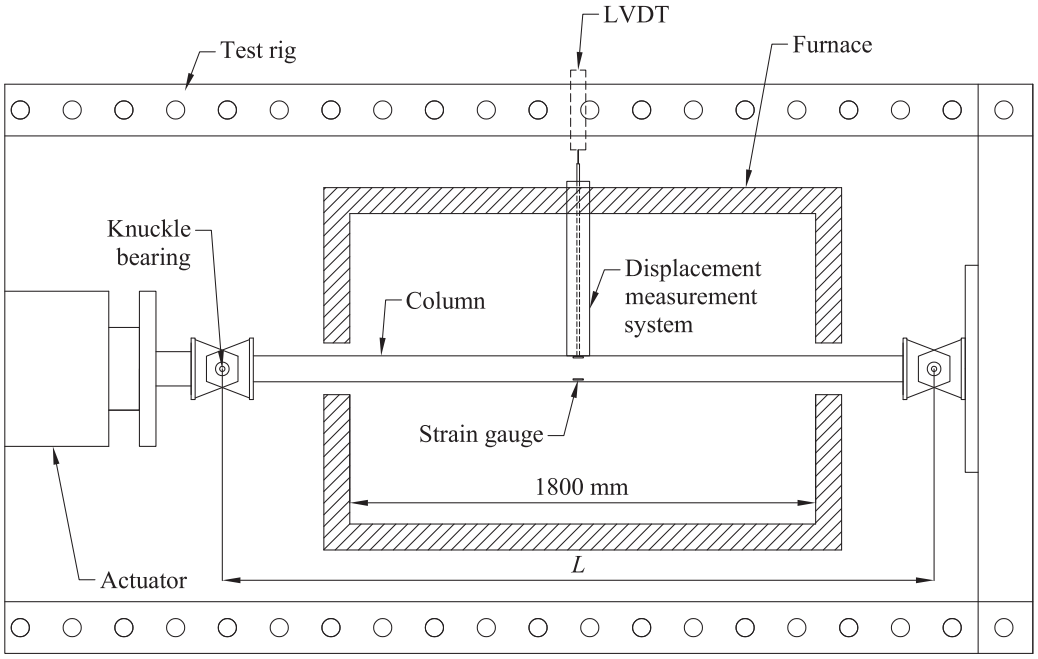

(b) Schematic drawing of elevated temperature column test setup

Figure 5.17: Column test setup at elevated temperature

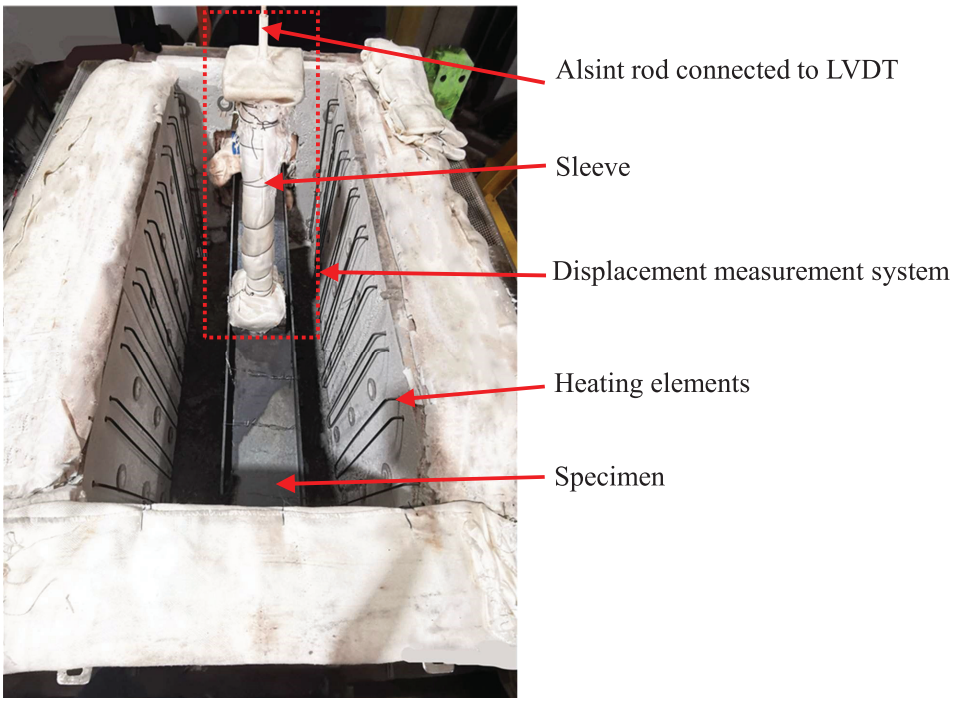

Figure 5.18: Inside of furnace used in fire tests

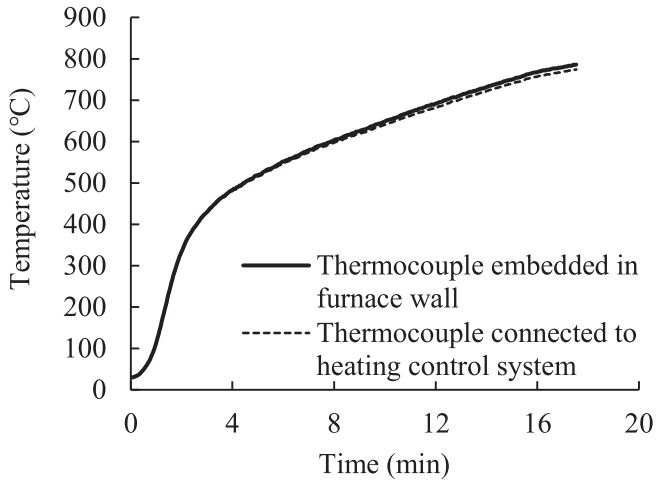

Figure 5.19: Furnace temperature measured by two thermocouples

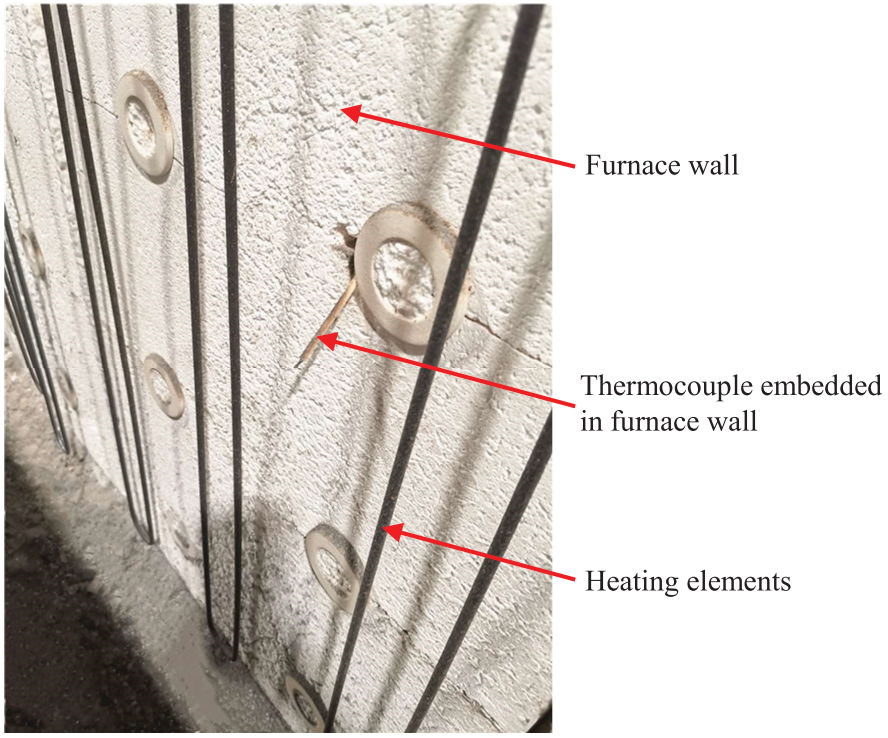

Figure 5.20: Thermocouple embedded in furnace wall

In addition to these two thermocouples, there were seven thermocouples attached to the columns at a series of points along their lengths to capture the surface temperature distribution; the locations of the thermocouples are illustrated in Fig. 5.21, where thermocouple 1 and 7 were used for measuring the temperature of the two parts of the specimens outside the furnace.

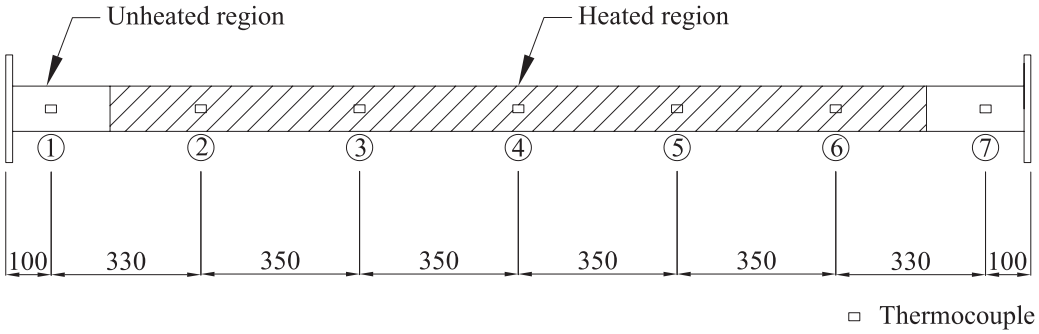

(a) Columns with I-248×124×5×8 cross-section

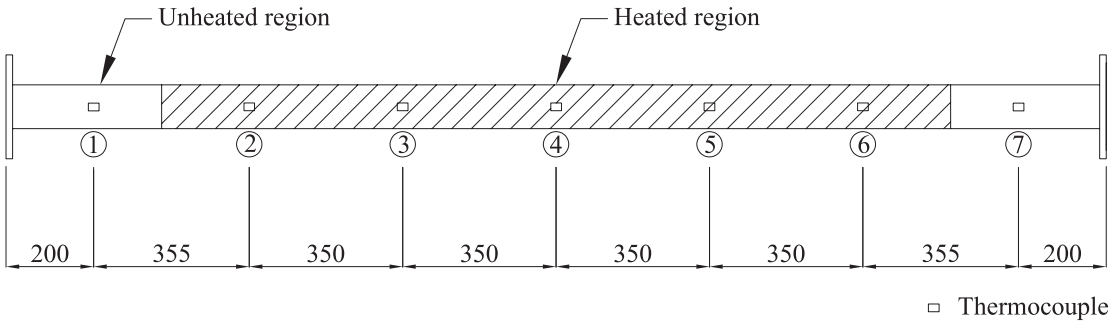

(b) Columns with I-198×99×4.5×7 cross-section

Figure 5.21: Locations of seven thermocouples on column specimens (dimensions in mm)

Fig. 5.22 shows the LVDT used to measure the mid-height lateral deflection of the column specimens; the LVDT was installed above the furnace and covered with heat resistant fabric. The uncovered extension rod of the LVDT was connected to the bespoke displacement measurement system shown in Fig. 5.18 using an Alsint 99.7 rod. Alsint 99.7 has a high yield strength (300 MPa) and a low coefficient of thermal expansion (7.8×10^{-6} K^{-1}). The Alsint 99.7 rod, one end of which was connected to the extension rod of the LVDT and the other end of which was attached to the surface of the column, was able to move vertically with the extension rod of the LVDT to measure the lateral deflection of the columns at the mid-height.

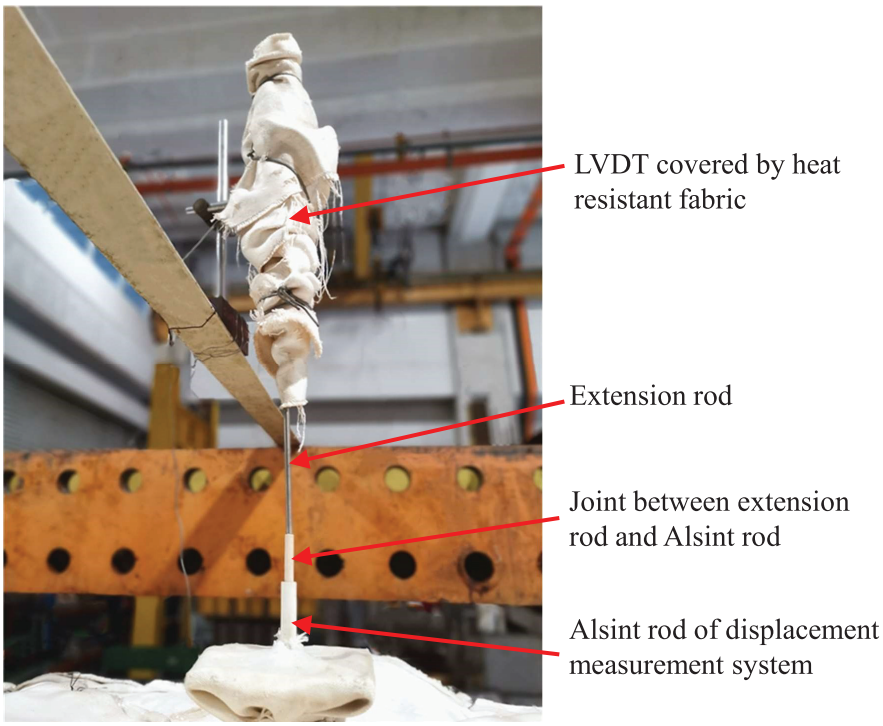

Figure 5.22: LVDT covered by heat resistant fabric used to measure mid-height lateral deflection of columns

5.5.2 Testing procedure

In the fire tests, the axial load $N_{\mathrm{Ed,test}}$ was first applied to the specimens through the horizontal self-reacting test rig under displacement control at a rate of 0.3 mm/min. Once the predefined axial load ratio $n_{\mathrm{r}} = N_{\mathrm{Ed,test}}/N_{\mathrm{u}}$ equal to ratio of the applied axial load $N_{\mathrm{Ed,test}}$ to the room temperature minor axis flexural buckling capacity N_{u} of the specimen, testing was switched to load control and the load was held constant for fifteen minutes. Note that the room temperature minor axis flexural buckling capacities N_{u} were taken as the ultimate loads obtained for the LC1-20C and LC2-20C columns from the room temperature tests, which are described in Section 5.4. The air temperature in the furnace was then increased following the ISO-834 (1999) standard fire curve until the axial load applied to the column $N_{\mathrm{Ed,test}}$ could no longer be sustained. During the

heating process, the column was allowed to expand in order to keep the predefined axial load ratio constant. The applied axial compression values $N_{\mathrm{Ed,test}}$, load ratios n_{r} and measured total eccentricities of the eight tested stainless steel columns are reported in Table 5.7.

Table 5.7: Measured imperfections, pre-applied axial loads and load ratios of columns subjected to fire testing

ID	Cross-section	Total global imperfection $v_0 + e_0$ (mm)	Pre-applied load $N_{\mathrm{Ed,test}}$ (kN)	Load ratio n_{r}
LC1-0.6	I-248×124×5×8	2.47	248	0.62
LC1-0.5	I-248×124×5×8	2.38	203	0.51
LC1-0.4	I-248×124×5×8	2.04	160	0.40
LC1-0.3	I-248×124×5×8	2.29	119	0.30
LC2-0.6	I-198×99×4.5×7	2.74	137	0.61
LC2-0.5	I-198×99×4.5×7	2.37	110	0.49
LC2-0.4	I-198×99×4.5×7	2.71	97	0.43
LC2-0.3	I-198×99×4.5×7	2.52	68	0.30

5.5.3 Test results

All the tested columns failed by minor axis flexural buckling. Fig. 5.23 shows the typical failure modes of the columns with different axial load ratios n_{r}, where surface colour changes associated with the different failure temperatures are clearly evident. In this subsection, additional details with respect to the temperature distributions in the tested specimens and the behaviour of the tested stainless steel columns observed during the experiments are presented.

Figure 5.23: Typical minor flexural buckling failure modes of specimens LC2-0.6, LC2-0.5, LC2-0.4, LC2-0.3 from top to bottom

Temperature distributions

The measured furnace air temperature versus time relationships in the eight column tests are shown in Fig. 5.24a–5.24b together with the ISO-834 (1999) standard fire curve. As can be seen from the figures, the air temperature in the furnace generally followed the trend of the ISO-834 (1999) standard fire curve though lagged somewhat behind, particularly at the beginning of the experiments.

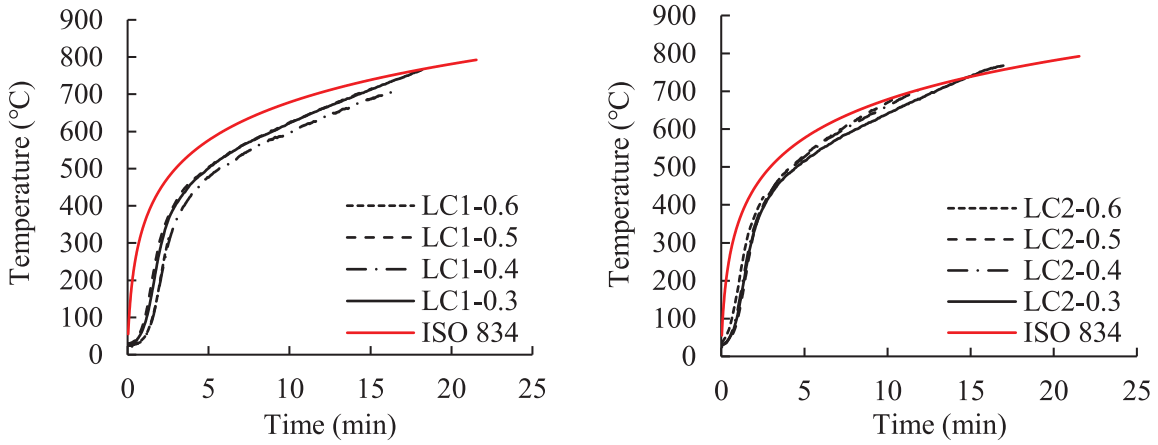

(a) Columns with I-248×124×5×8 cross-section (b) Columns with I-198×99×4.5×7 cross-section

Figure 5.24: Comparison of measured furnace temperature-time relationship with ISO-834 (1999) standard fire curve

Fig. 5.25 shows the temperatures measured by the seven thermocouples attached to the surface of specimen LC2-0.3. In the figure, the temperature values measured by thermocouples 2–6 in the heated region increased following a similar trend with time. The temperatures of the two parts of the column outside the furnace were measured by thermocouple 1 and thermocouple 7, which remained at room temperature throughout the testing.

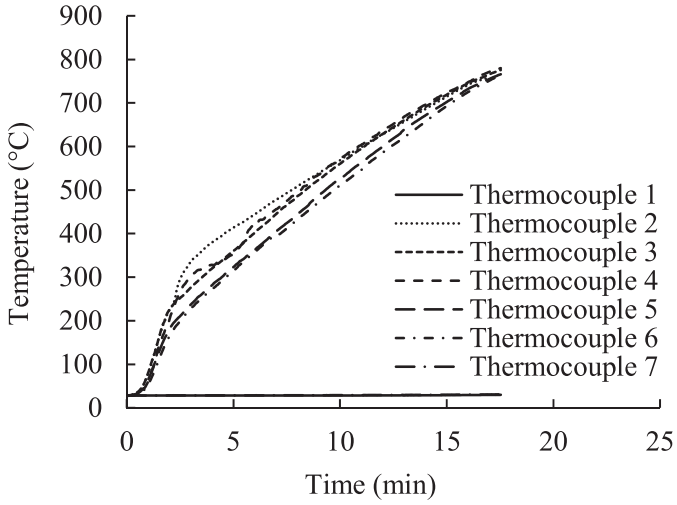

Figure 5.25: Temperature rise of column surface, shown for LC2-0.3

Fig. 5.26a–5.26b show the average measured column surface temperature-time relationships for all the fire tests, where the column surface temperatures are taken as the mean of the temperature values measured by the five thermocouples attached to the column surfaces in the heated regions.

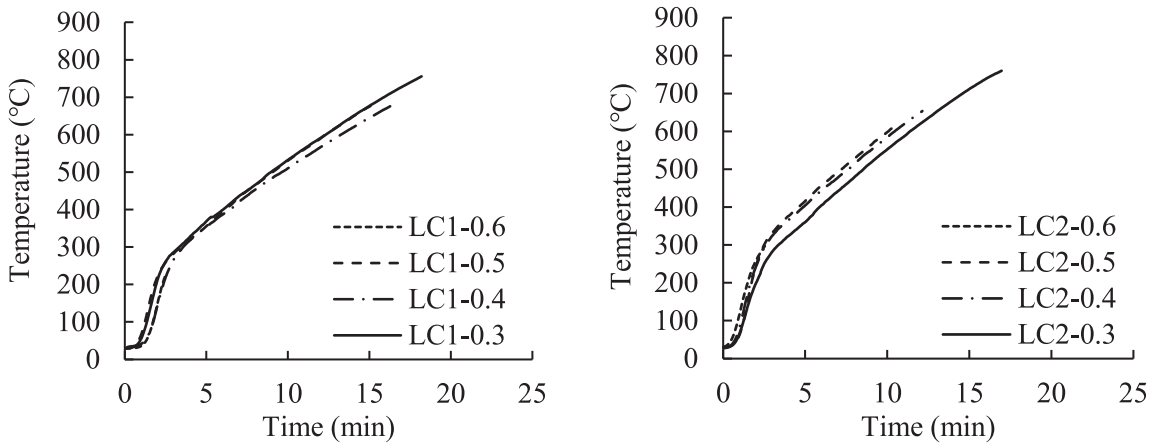

(a) Columns with I-248×124×5×8 cross-section (b) Columns with I-198×99×4.5×7 cross-section

Figure 5.26: Average measured column surface temperature-time relationships for eight fire test specimens

Table 5.8 provides a summary of the key experimental results for the eight stainless steel I-section column tests in fire, including the critical failure temperature $\theta_{\mathrm{cr,test}}$ and the fire resistance in terms of the time duration $t_{\mathrm{fi,test}}$ for which the columns were able to resist the pre-applied loads $N_{\mathrm{Ed,test}}$. The fire resistance $t_{\mathrm{fi,test}}$ and critical temperature $\theta_{\mathrm{cr,test}}$ of a specimen was assumed to be reached when one of the two failure criteria provided in European Standard EN 1363-1 (CEN, 2012) was reached: (i) the maximum allowable axial contraction magnitude of $C = h/100$ mm or (ii) the maximum allowable axial contraction rate of $dC/dt = 3h/1000$ mm/min, where h is the initial column height in mm.

Behaviour of columns

In Fig. 5.27, the recorded axial deformation versus temperature paths for the eight stainless steel column tests in fire are shown. It can be seen that the columns initially shortened due to the

Table 5.8: Measured fire resistances from column tests

ID	Fire resistance $t_{fi,test}$ (min)	Critical temperature $\theta_{cr,test}$ (°C)
LC1-0.6	9.27	488
LC1-0.5	15.07	676
LC1-0.4	20.57	770
LC1-0.3	24.43	799
LC2-0.6	2.53	297
LC2-0.5	10.30	609
LC2-0.4	12.13	654
LC2-0.3	16.97	760

applied axial loading $N_{Ed,test}$, and then started to expand with increasing temperature. When the column temperatures were below about 300 °C, it is seen from Fig. 5.27 that the measured axial expansion rates of the columns were smaller than those measured for high temperature levels. This was mainly because the column temperature increased rapidly to 300 °C and the position of the actuator, which was manually controlled to maintain a constant axial load, lagged slightly behind where it ought to have been. After 300 °C, the column temperature increased more slowly and all the columns expanded linearly with increasing temperature levels and behaved similarly prior to their failure.

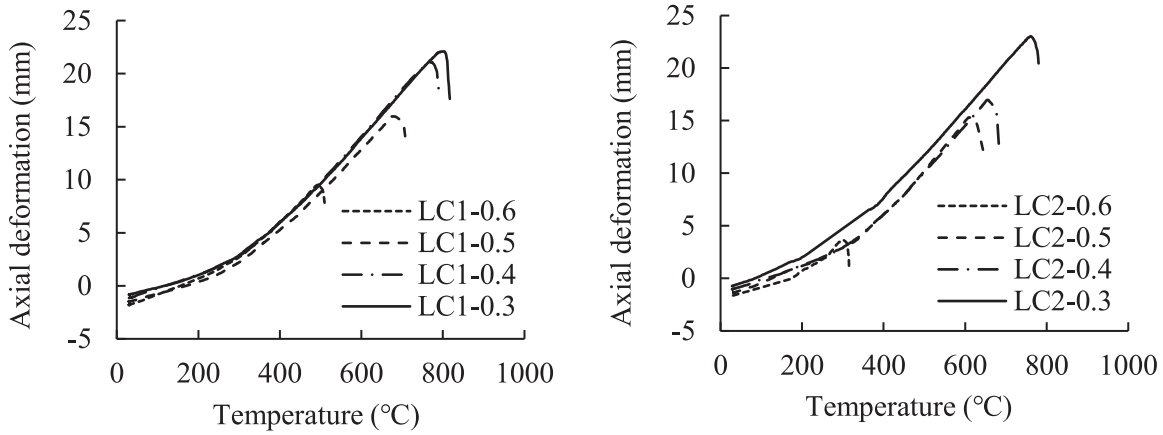

(a) Columns with I-248×124×5×8 cross-section (b) Columns with I-198×99×4.5×7 cross-section

Figure 5.27: Axial deformation versus column temperature paths obtained from eight fire tests, with positive deformations corresponding to expansion of the columns

Fig. 5.28 shows the recorded lateral mid-height deflection versus average surface temperature curves for the eight tested stainless steel I-section columns in fire. Note that the thermal expansion of the Alsint 99.7 rod, although small, was non-negligible (up to about 2 mm at 750 °C) and was hence calculated and removed from the measured mid-height lateral deflections of column specimens. As can be seen in the figure, the columns exhibited small lateral deflections under the initial axial loading; the lateral deflections of the columns then displayed small fluctuations owing to possible thermal bowing under increasing temperature. Finally, as the columns approached failure, the column stiffness reduced rapidly and there were significant increases in mid-height lateral deflections signifying flexural buckling about minor axis.

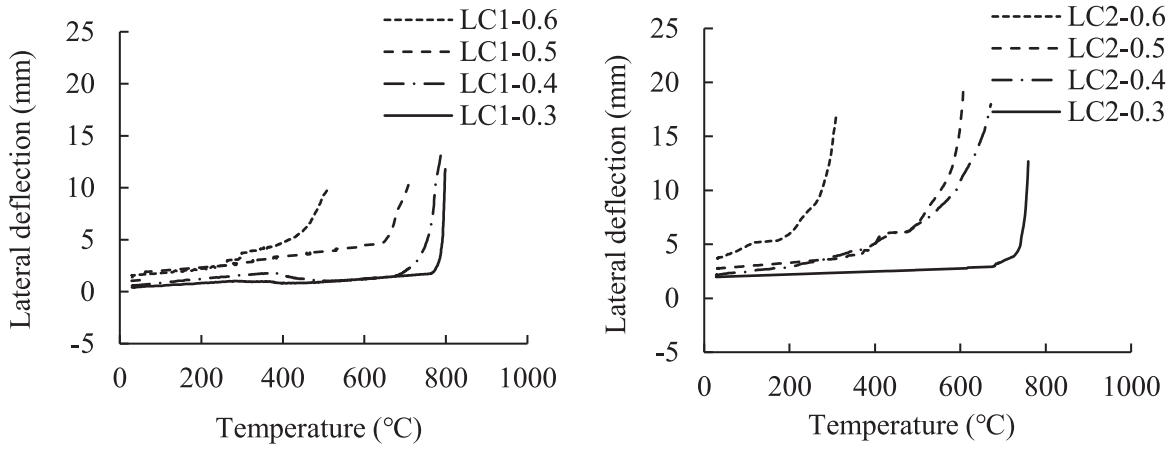

(a) Columns with I-248×124×5×8 cross-section (b) Columns with I-198×99×4.5×7 cross-section

Figure 5.28: Mid-height lateral deflection versus column temperature paths obtained from eight column fire tests, with positive lateral deflections corresponding to downward deflections of the columns

5.6 Conclusions

An experimental study on grade 1.4301 austenitic stainless steel I-section columns in fire has been presented in this chapter. Material tests on tensile coupons extracted from the web and flange plates of the stainless steel column specimens were performed at room temperature; the corresponding elevated temperature material properties were inferred on the basis of the strength

and stiffness reduction factors set out in SCI (2017). Prior to the fire tests, two columns with the same geometrical properties as those subjected to fire testing were tested at room temperature to obtain their benchmark room temperature minor axis flexural buckling load N_{u}. Following the room temperature member tests, eight anisothermal stainless steel column fire tests were conducted, in which two cross-sections and two column buckling lengths were considered. Four axial load ratios n_{r}, equal to 0.3, 0.4, 0.5 and 0.6, were adopted to achieve a range of failure temperature values. The experimental study carried out in this chapter fills an important gap in knowledge on the behaviour of stainless steel I-section columns in fire.

Chapter 6

FE modelling and design of I-section columns

6.1 Introduction

With the aim of establishing a consistent design approach for stainless steel structural columns in fire, a new design method for the flexural buckling assessment of stainless steel columns at elevated temperatures is proposed in this chapter. Finite element models able to replicate the physical response of stainless steel elements at elevated temperatures are developed. Extensive parametric studies to furnish fundamental structural performance data are then performed. A broad range of elevated temperature levels, cross-section geometries, slendernesses and different stainless steel grades are taken into consideration. The accuracy and reliability of the proposed new design method, which is compatible with the existing methods provided for carbon steel columns in EN 1993-1-2 (CEN, 2005), are verified against the results from the nonlinear finite element modelling for all the considered cases.

6.2 Finite element modelling

In this section, finite element models able to mimic the response of stainless steel columns in fire are developed and validated against a series of experimental studies from the literature. The validated finite element models are employed in the following sections for the development and assessment of the proposed new design method.

6.2.1 Development of finite element models

The finite element models were created by means of the finite element analysis software ABAQUS (2014). The shell element S4R was utilised to mesh all the finite element models; the number of elements was chosen in the same fashion as described in Section 4.2.1. Unless otherwise indicated, all the investigated columns had simply-supported end conditions, which were established by means of coupling constraints at the column ends.

Both local and global geometric imperfections were incorporated into the finite element models, of which the local imperfections were as defined in Fig. 4.2 and the global imperfections were assumed to take the shape of a half-sine wave along the longitudinal axis and scaled to 1/1000 of the member length as shown in Fig. 6.1. The two-stage compound Ramberg-Osgood material model defined in Section 3.2.1 was utilized to represent the elevated temperature material stress-strain response. The residual stress pattern put forward by Yuan *et al.* (2014) was adopted to define the residual stresses in the finite element models, details of which have been given in Section 4.2.1. The finite element models were analysed isothermally following the procedures presented in Section 4.2.1. A finite element model of a typical column is shown in Fig. 6.2.

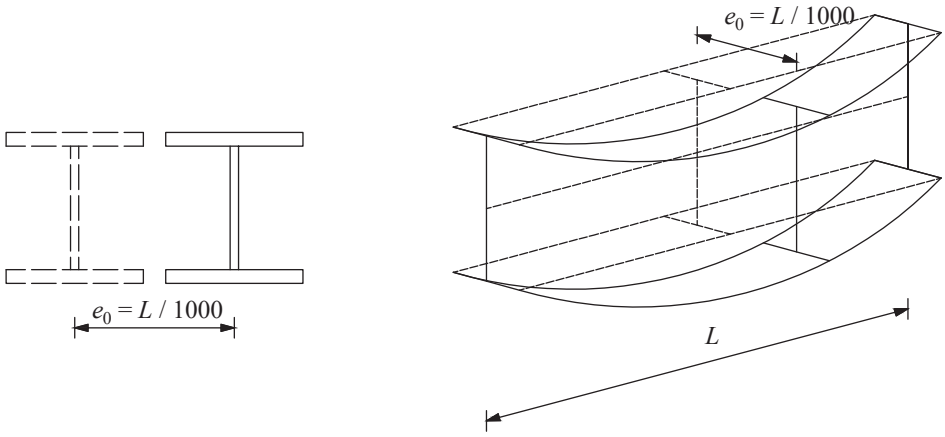

Figure 6.1: Global imperfections applied to the finite element models

Figure 6.2: Finite element model of a typical stainless steel column

6.2.2 Validation of finite element models

The finite element modelling approach was validated against the column fire tests reported in Chapter 5. The two-stage compound Ramberg-Osgood material model in Section 3.2.1 was used to define the material response of the specimens in fire, using the elevated temperature material properties determined by multiplying the strength and stiffness reduction factors given in SCI (2017) by the corresponding room temperature material properties of the specimens obtained from tensile coupon tests. The measured geometric imperfection amplitudes were included in the finite element modelling. Since the disparity in the predictions from the isothermal and anisothermal analysis methods due to creep effects is insignificant especially at high strains (Gardner *et al.*, 2010; Afshan, 2013), the validated models were analysed isothermally so as to be consistent with the finite element modelling approach in this study. In the isothermal analysis method, the models were heated up to a specific temperature level and then loaded to failure; hence, the peak loads were directly taken as the ultimate load carrying capacities. Table 6.1 summarises the obtained numerical results, where it can be seen that the average ratio of the experimental to numerical load carrying capacities is almost equal to unity, indicating that the finite element models developed in this chapter are capable of replicating the flexural buckling response of stainless steel I-section columns at elevated temperatures.

The finite element modelling approach was also validated against experiments carried out on carbon steel I-section members. Pauli *et al.* (2012) carried out a series of tests on pin-ended columns made of grade S 355 carbon steel with a European HEA 100 cross-section undergoing major and minor axis flexural buckling at a range of elevated temperature levels; the results of these tests are utilised herein for the validation of the finite element models in this chapter. The experiments were conducted isothermally, whereby the columns were first heated to a specified temperature level and then loaded until failure. The measured geometrical properties, elevated temperature material properties and mean values of local and global geometrical imperfections of the specimens reported by Pauli *et al.* (2012) were incorporated into the finite element models created herein. In Fig. 6.3, the load versus end-shortening paths of the specimens undergoing

Table 6.1: Comparison of ultimate load carrying capacities $N_{u,test}$ of simply-supported stainless steel columns in fire determined from the tests reported in Chapter 5 and finite element models $N_{u,FE}$ created in this chapter

ID	Failure temperature °C	$N_{u,test}$	$N_{u,FE}$ (kN)	$N_{u,FE}/N_{u,test}$
LC1-0.6	488	248	241	0.97
LC1-0.5	676	203	201	0.99
LC1-0.4	770	160	159	0.99
LC1-0.3	799	119	142	1.19
LC2-0.6	297	137	119	0.87
LC2-0.5	609	110	97	0.88
LC2-0.4	653	97	91	0.94
LC2-0.3	760	68	73	1.07
Average				0.99
COV				0.107

major and minor axis buckling at elevated temperature levels of 400 °C, 550 °C and 700 °C, as well as at room temperature, obtained from the experiments and the finite element modelling approach adopted in this study are compared. As can be seen from the figure, the correlation between the experimental and numerical load-displacement paths is good. Additionally, the ultimate axial load carrying capacities of the specimens determined by Pauli *et al.* (2012) $N_{u,test}$ and those obtained from the finite element developed herein $N_{u,FE}$ are also compared Table 6.2.

6.3 EN 1993-1-2 rules for flexural buckling assessment of stainless steel columns in fire

As previously indicated, in spite of the different material response of stainless steel relative to carbon steel at elevated temperatures, EN 1993-1-2 (CEN, 2005) provides the same form of column buckling design rules for both carbon steel and stainless steel columns in fire. Adopting the traditional Perry-Robertson concept (Ayrton & Perry, 1886; Robertson, 1925) used in EN 1993-1-1 (CEN, 2005) for room temperature design, the European structural fire design code EN 1993-1-2 (CEN, 2005) provides the following expressions for the assessment of the flexural

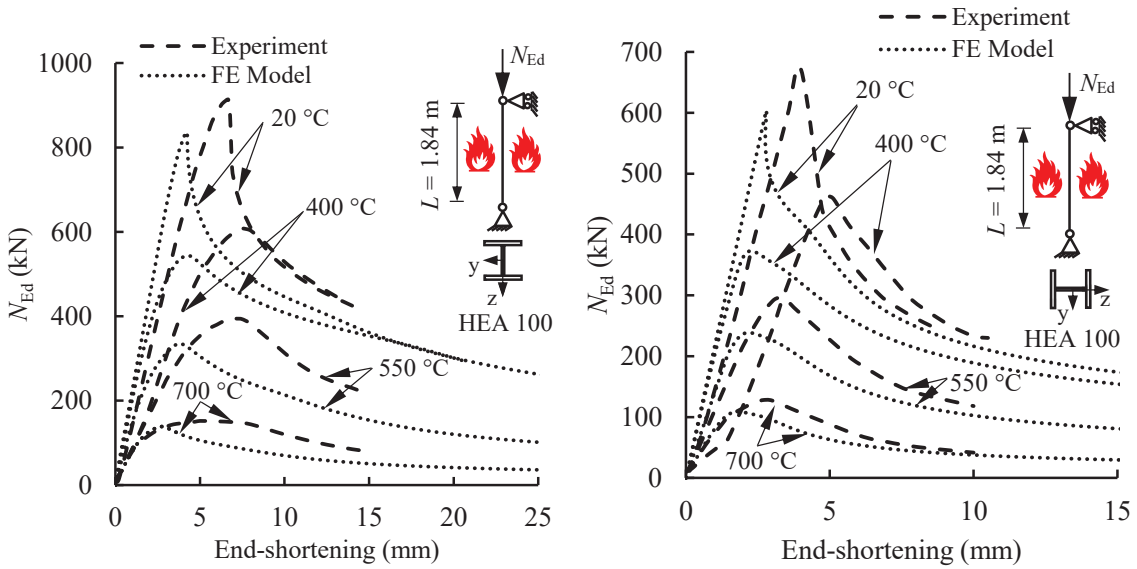

(a) Major axis flexural buckling

(b) Minor axis flexural buckling

Figure 6.3: Comparison between the load versus end-shortening paths obtained from experiments (Pauli *et al.*, 2012) and finite element models for carbon steel I-section columns undergoing flexural buckling in fire

Table 6.2: Comparison of ultimate load carrying capacities $N_{u,test}$ of simply-supported HEA 100 carbon steel columns in fire determined by Pauli *et al.* (2012) and finite element models $N_{u,FE}$ created in this chapter

Test	Specimen	Buckling axis	L(m)	θ (^{o}C)	$N_{u,test}$ (kN)	$N_{u,FE}$ (kN)	$N_{u,FE}/N_{u,test}$
HEA100_M_20C_z0	M01	z-z	0.85	20	857	803	0.94
HEA100_M_400C_z0	M02	z-z	0.85	400	646	588	0.91
HEA100_M_550C_z0	M03	z-z	0.85	550	405	351	0.87
HEA100_SL_20C_y0	L04	y-y	1.84	20	914	836	0.91
HEA100_SL_20C_y0	L15	y-y	1.84	20	859	836	0.97
HEA100_SL_20C_z0	L13	z-z	1.84	20	671	604	0.90
HEA100_SL_20C_z0	L10	z-z	1.84	20	512	604	1.18
HEA100_SL_400C_y0	L08	y-y	1.84	400	608	543	0.89
HEA100_SL_400C_z0	L16	z-z	1.84	400	466	373	0.80
HEA100_SL_550C_y0	L07	y-y	1.84	550	395	335	0.85
HEA100_SL_550C_z0	L11	z-z	1.84	550	297	239	0.80
HEA100_SL_700C_y0	L01	y-y	1.84	700	152	139	0.91
HEA100_SL_700C_z0	L12	z-z	1.84	700	128	109	0.85
						Average	0.91
						COV	0.106

buckling resistance of stainless steel columns at a uniform elevated temperature θ:

$$N_{\mathrm{b,fi,t,Rd}} = \frac{\chi_{\mathrm{fi}} A k_{2,\theta} f_{\mathrm{y}}}{\gamma_{\mathrm{M,fi}}} \quad \text{for Class 1, 2 or 3 sections,} \tag{6.1}$$

$$N_{\mathrm{b,fi,t,Rd}} = \frac{\chi_{\mathrm{fi}} A_{\mathrm{eff}} k_{\mathrm{p0.2},\theta} f_{\mathrm{y}}}{\gamma_{\mathrm{M,fi}}} \quad \text{for Class 4 sections,} \tag{6.2}$$

where $N_{\mathrm{b,fi,t,Rd}}$ is the design buckling resistance at time t of a compression member, $\gamma_{\mathrm{M,fi}}$ is the partial safety factor for fire design taken equal to 1.0, f_{y} is the 0.2% proof strength at room temperature, A is the cross-sectional area for Class 1, 2 and 3 sections based on the cross-section classification rules provided in EN 1993-1-4 (CEN, 2015), A_{eff} is the effective cross-sectional area for Class 4 sections calculated adopting the room temperature effective width calculation rules given in (CEN, 2015) with $\varepsilon = 0.85\sqrt{(235/f_{\mathrm{y}})/(E/210000)}$ and χ_{fi} is the elevated temperature column buckling reduction factor calculated as:

$$\chi_{\mathrm{fi}} = \frac{1}{\phi_\theta + \sqrt{\phi_\theta^2 - \overline{\lambda}_\theta^2}} \qquad \text{where} \qquad \phi_\theta = 0.5\left[1 + \eta_\theta + \overline{\lambda}_\theta^2\right], \tag{6.3}$$

in which η_θ is the generalised imperfection factor expressed as:

$$\eta_\theta = \alpha\overline{\lambda}_\theta \qquad \text{with} \qquad \alpha = 0.65\sqrt{235/f_{\mathrm{y}}}. \tag{6.4}$$

Note that the generalised imperfection factor η_θ is the primary parameter determining the shape of a buckling curve. In eq. (6.3) and eq. (6.4), $\overline{\lambda}_\theta$ is the non-dimensional slenderness at temperature θ calculated using the following expression:

$$\overline{\lambda}_\theta = \sqrt{\frac{A f_{\mathrm{y}}}{N_{\mathrm{cr}}}}\sqrt{\frac{k_{2,\theta}}{k_{E,\theta}}} = \overline{\lambda}\sqrt{\frac{k_{2,\theta}}{k_{E,\theta}}} \quad \text{for Class 1, 2 and 3 sections,} \tag{6.5}$$

$$\overline{\lambda}_\theta = \sqrt{\frac{A_{\mathrm{eff}} f_{\mathrm{y}}}{N_{\mathrm{cr}}}}\sqrt{\frac{k_{2,\theta}}{k_{E,\theta}}} = \overline{\lambda}\sqrt{\frac{k_{2,\theta}}{k_{E,\theta}}} \quad \text{for Class 4 sections,} \tag{6.6}$$

where N_{cr} and $\overline{\lambda}$ are the elastic critical buckling load and non-dimensional slenderness at room temperature, respectively.

In Fig. 6.4, the existing EN 1993-1-2 (CEN, 2005) rules for the flexural buckling assessment of stainless steel columns are compared against the ultimate strengths predicted by the Geometrically and Materially Nonlinear Analyses with imperfections (GMNIA) of the shell finite element models of welded columns with cross-sections having the shape of an HEM 100 profile without the presence of the fillets, considering austenitic, duplex and ferritic stainless steel grades and various temperature levels and non-dimensional slenderness values. Note that the GMNIA results are assumed as the benchmark data. As can be seen from Fig. 6.4, the current EN 1993-1-2 (CEN, 2005) rules provide a single buckling curve leading to flexural buckling strength predictions on the unsafe side for the majority of columns regardless of the stainless steel grade, indicating that improvements to the current design rules are necessary. It is important to note that the overpredictions of resistance of EN 1993-1-2 increase with increasing temperature level. Similar observations were also made by Lopes *et al.* (2010a).

6.4 Development of new flexural buckling rules for stainless steel columns in fire

In this section, flexural buckling curves for the design of stainless steel columns at elevated temperatures are developed. A new set of buckling curves, based on the elevated temperature strength at 2% total strain $f_{2,\theta}$, are calibrated against results from nonlinear shell finite element modelling considering a wide range of slenderness values, cross-section geometries and elevated temperature values for the three primary stainless steel grades (i.e. austenitic, duplex and ferritic). Use of the elevated temperature strength at 2% total strain $f_{2,\theta}$ in the new proposal maintain the consistency with the existing design rules for carbon steel columns provided in EN 1993-1-2 (CEN, 2005).

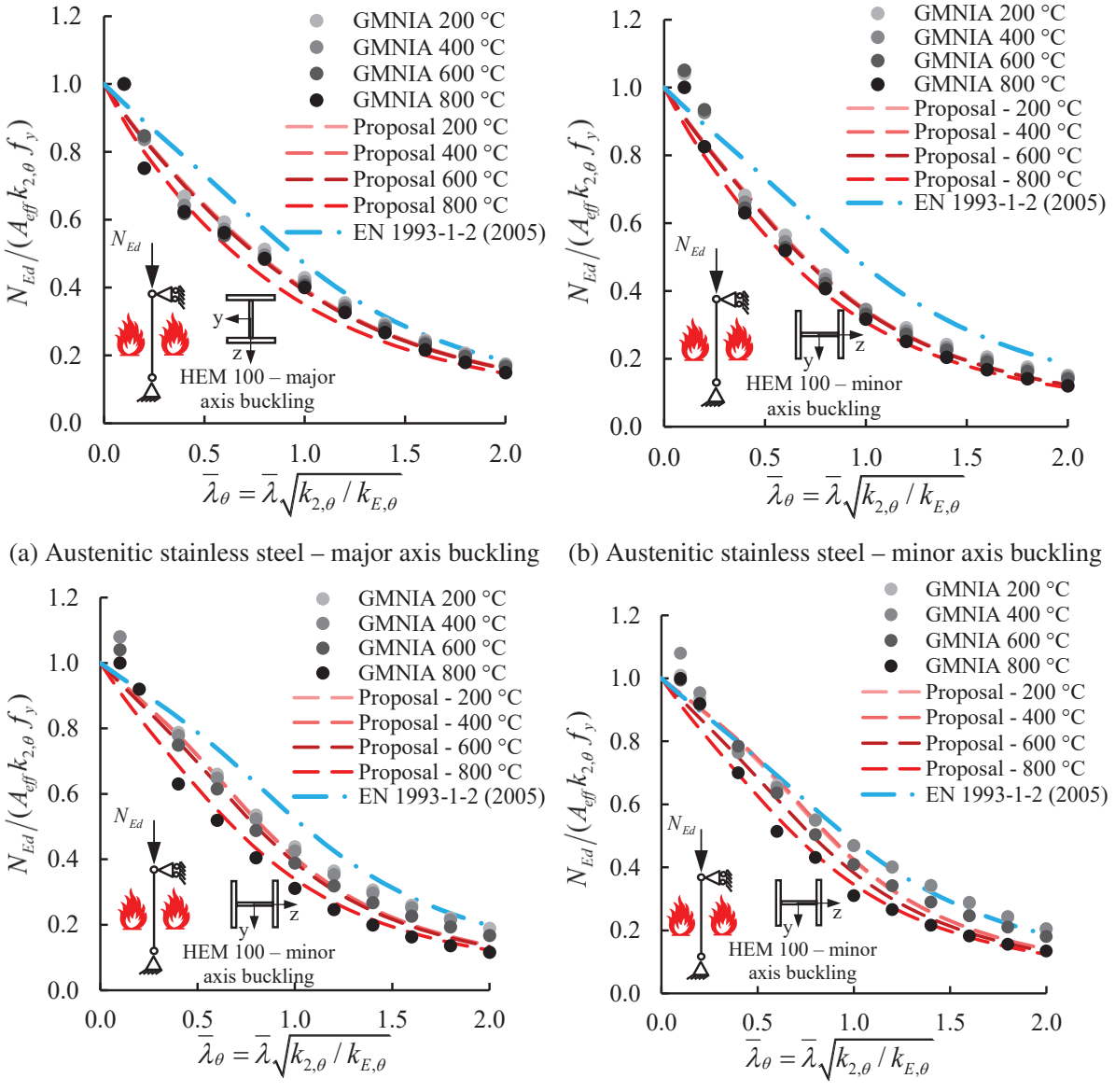

(a) Austenitic stainless steel – major axis buckling

(b) Austenitic stainless steel – minor axis buckling

(c) Duplex stainless steel – minor axis buckling

(d) Ferritic stainless steel – minor axis buckling

Figure 6.4: Accuracy of strength predictions from EN 1993-1-2 and the new design proposal relative to FE results for the flexural buckling of stainless steel columns in fire

6.4.1 New proposal for the definition of the generalised imperfection factor η_θ

The European structural fire design code EN 1993-1-2 (CEN, 2005) adopts the Perry-Robertson concept (Ayrton & Perry, 1886; Robertson, 1925) for the fire design of columns, which is based on the second-order elastic analysis of a pin-ended column with a half-sine wave imperfection along its length scaled to a magnitude of $\overline{e}_0$ at mid-height as shown in Fig. 6.5.

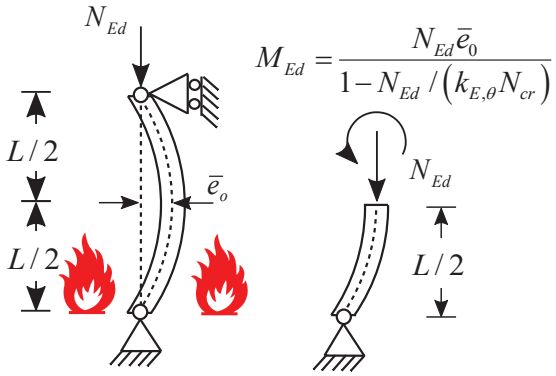

Figure 6.5: Imperfect pin-ended column used in the derivation of column buckling equations in EN 1993-1-2 (CEN, 2005) following the Perry-Robertson concept

According to this concept, failure of a column is signified by first yield occurring at the extreme compressive fibre of the mid-height cross-section on the concave side of the member. The imperfection magnitude $\overline{e}_0$, which is directly proportional to the column length, is calibrated such that it considers fully the adverse influence of the development and spread of plasticity, residual stresses and geometrical imperfections on the ultimate load carrying capacity of a column; $\overline{e}_0$ is thus also referred to as an 'equivalent imperfection' in the literature.

The derivation of the column buckling equations in EN 1993-1-2 (CEN, 2005) is based on the attainment of first yield (though taken as the strength at 2% strain) at the mid-height section of a steel column in fire shown in Fig. 6.5 and using the equation below:

$$\frac{N_{\mathrm{Ed}}}{Ak_{2,\theta}f_{\mathrm{y}}}+\frac{N_{\mathrm{Ed}}\overline{e}_0}{W_{\mathrm{el}}k_{2,\theta}f_{\mathrm{y}}}\frac{1}{1-N_{\mathrm{Ed}}/\left(k_{E,\theta}N_{\mathrm{cr}}\right)}=1.0, \tag{6.7}$$

where W_{el} is the elastic section modulus and N_{cr} is the elastic buckling load relevant to the axis of buckling. Defining the column buckling reduction factor in fire χ_{fi} and elevated temperature non-dimensional column buckling slenderness $\overline{\lambda}_\theta$ as:

$$\chi_{\text{fi}} = \frac{N_{\text{Ed}}}{A k_{2,\theta} f_{\text{y}}} \quad \text{and} \quad \overline{\lambda}_\theta = \sqrt{\frac{A f_{\text{y}}}{N_{\text{cr}}}} \sqrt{\frac{k_{2,\theta}}{k_{E,\theta}}}, \tag{6.8}$$

eq. (6.7) can be expressed as follows:

$$\chi_{\text{fi}} + \chi_{\text{fi}} \frac{1}{1 - \chi_{\text{fi}} \overline{\lambda}_\theta^2} \eta_\theta = 1.0, \tag{6.9}$$

where the generalised imperfection factor η_θ is equal to:

$$\eta_\theta = \frac{A \overline{e}_0}{W_{\text{el}}}. \tag{6.10}$$

Solving eq. (6.8) for χ_{fi} gives the expression below provided in EN 1993-1-2 (CEN, 2005) for the determination of the column buckling reduction factor in fire χ_{fi}, which is also given by eq. (6.3):

$$\chi_{\text{fi}} = \frac{1}{\phi_\theta + \sqrt{\phi_\theta^2 - \overline{\lambda}_\theta^2}} \quad \text{where} \quad \phi_\theta = 0.5 \left[1 + \eta_\theta + \overline{\lambda}_\theta^2 \right] \tag{6.11}$$

In the development of the EN 1993-1-2 (CEN, 2005) column buckling rules, considering the actual elastic-plastic response of an imperfect steel column, the calibration of the Perry-Robertson equation was carried out such that the expression for the generalised imperfection factor η_θ given by eq. (6.10) was replaced by the expression given below

$$\eta_\theta = \alpha \overline{\lambda}_\theta. \tag{6.12}$$

Using eq. (6.10) and eq. (6.12), the equivalent imperfection $\bar{e}_0$ of the column can be expressed as

$$\bar{e}_0 = \alpha \frac{W_{\text{el}}}{A} \bar{\lambda}_\theta = \alpha \frac{W_{\text{el}}}{A} \bar{\lambda} \sqrt{\frac{k_{2,\theta}}{k_{E,\theta}}}. \tag{6.13}$$

Considering a column with a welded section having cross-section properties the same as an HEB 300 section and buckling about the minor axis, the ratio of the equivalent imperfection $\bar{e}_0$ to the column length L, i.e. $\bar{e}_0/L$, calculated according to EN 1993-1-2 (CEN, 2005) as given by eq. (6.13), is shown for a range of elevated temperature values in Fig. 6.6 for austenitic stainless steel and carbon steel columns.

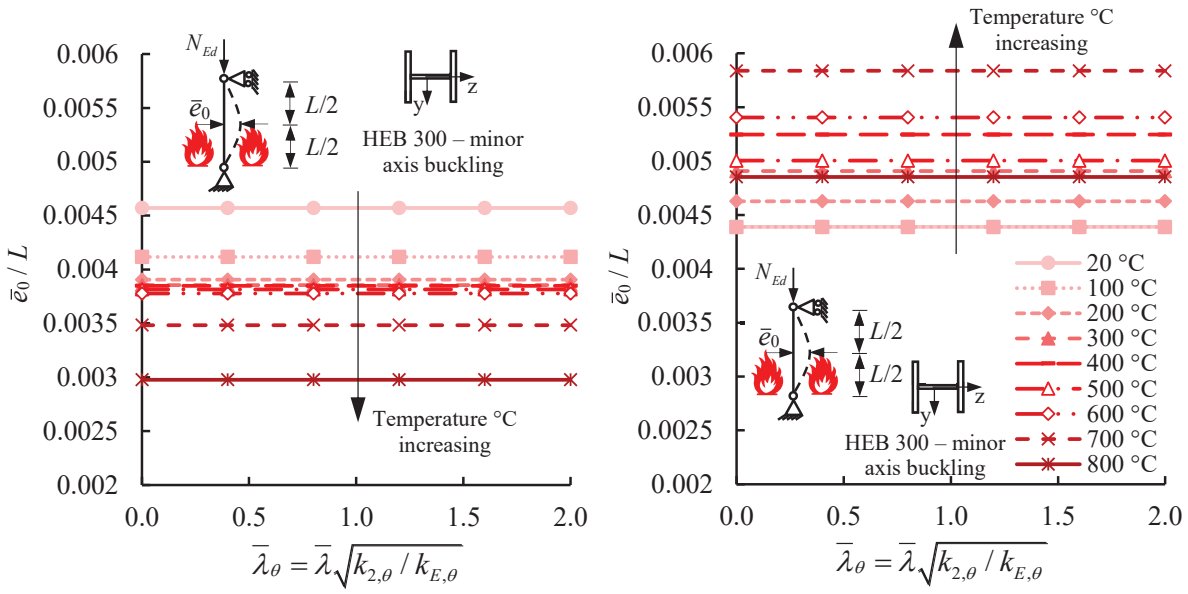

(a) Austenitic stainless steel

(b) Carbon steel

Figure 6.6: Equivalent imperfections $\bar{e}_0$ relative to column lengths L (i.e. $\bar{e}_0/L$) for austenitic stainless steel and carbon steel columns at different temperatures as adopted in EN 1993-1-2 (CEN, 2005)

As can be seen from the figure, the $\bar{e}_0/L$ ratios change with the elevated temperature level – Fig. 6.6 (a) shows that for austenitic stainless steel, the higher the temperature, the lower the $\bar{e}_0/L$ ratio; the same trend is also observed for duplex and ferritic stainless steel grades. On the other hand, for the case of carbon steel, the $\bar{e}_0/L$ ratios assume greater values with increasing temperature, as can be seen from Fig. 6.6 (b). Clearly, imperfection magnitudes changing with

temperature (reducing in size for stainless steel and increasing in size for carbon steel at higher temperatures) does not reflect the physical reality of the situation; this shortcoming is addressed below.

The dependency of $\overline{e}_0/L$ on temperature results from the equivalent imperfection $\overline{e}_0$ being a function of $\xi_\theta = \sqrt{k_{2,\theta}/k_{E,\theta}}$, as can be seen from eq. (6.13). Fig. 6.7 shows that $\xi_\theta = \sqrt{k_{2,\theta}/k_{E,\theta}}$ decreases with increasing temperature for stainless steels, indicating that the strength reduction is more severe than the stiffness reduction at elevated temperatures, while the opposite is the case for carbon steel.

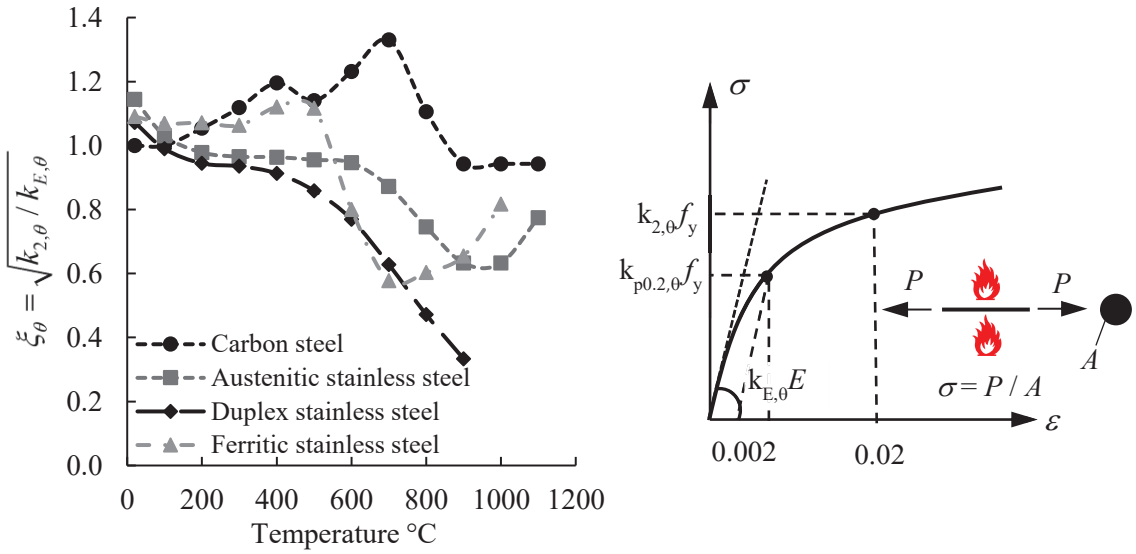

Figure 6.7: Variation of the square root of the elevated temperature strength-to-stiffness ratio factor ξ_θ with temperature for different steel types

Thus, whereas the ratio of the equivalent imperfection to the column length $\overline{e}_0/L$ decreases with increasing temperature for stainless steel, it increases at higher temperature levels for carbon steel, leading to a situation where the EN 1993-1-2 (CEN, 2005) design predictions become unconservative for stainless steel columns as shown in Fig. 6.4, but are acceptable for carbon steel columns as illustrated by Franssen *et al.* (1998).

Since the equivalent imperfection $\overline{e}_0$ should not logically be dependent upon temperature, this

study recommends the following expression of the generalised imperfection factor:

$$\eta_{\theta}^{*} = \alpha \overline{\lambda}_{\theta} / \xi_{\theta} \tag{6.14}$$

whereby $\overline{e}_0$ can be expressed as:

$$\overline{e}_0 = \alpha \frac{W_{\mathrm{el}}}{A} \overline{\lambda}_{\theta} / \xi_{\theta} = \alpha \frac{W_{\mathrm{el}}}{A} \overline{\lambda} \sqrt{\frac{k_{2,\theta}}{k_{E,\theta}}} / \sqrt{\frac{k_{2,\theta}}{k_{E,\theta}}} = \alpha \frac{W_{\mathrm{el}}}{A} \overline{\lambda}, \tag{6.15}$$

thus leading to a constant value of $\overline{e}_0/L$ regardless of the temperature level as shown below:

$$\overline{e}_0/L = \alpha \frac{W_{\mathrm{el}}}{A} \overline{\lambda}/L = \alpha \frac{W_{\mathrm{el}}}{A} \left(\frac{L}{i} \sqrt{\frac{f_{\mathrm{y}}}{\pi^2 E}} \right) /L = \alpha \frac{W_{\mathrm{el}}}{A} \left(\frac{1}{i} \sqrt{\frac{f_{\mathrm{y}}}{\pi^2 E}} \right), \tag{6.16}$$

where i is the radius of gyration for the axis about which the buckling occurs. Adopting the newly proposed generalised imperfection factor η_{θ}^{*} given by eq. (6.14), new flexural buckling curves are developed in the next subsection.

6.4.2 New design rules for flexural buckling assessment of stainless steel columns in fire

Similar to the cross-section design rules developed in Chapter 3, the elevated temperature strength at 2% total strain $f_{2,\theta}$ was adopted in the development of the new proposals for the flexural buckling design of stainless steel columns in fire. The new proposals are based on the Perry-Robertson concept (Ayrton & Perry, 1886; Robertson, 1925) and are thus compatible with the existing design rules in EN 1993-1-2 (CEN, 2005). The accuracy of the new proposals is assessed against GMNIA results and the existing EN 1993-1-2 (CEN, 2005) rules considering a wide range of cases in Section 6.4.4.

Adopting the elevated temperature strength at 2% total strain $f_{2,\theta} = k_{2,\theta} f_{\mathrm{y}}$, the following equations are proposed for the flexural buckling assessment of stainless steel columns in fire in this

study:

$$N_{\mathrm{b,fi,t,Rd}} = \frac{\chi_{\mathrm{fi}} A k_{2,\theta} f_{\mathrm{y}}}{\gamma_{M,fi}} \quad \text{for non-slender sections,} \tag{6.17}$$

$$N_{\mathrm{b,fi,t,Rd}} = \frac{\chi_{\mathrm{fi}} A_{\mathrm{eff}} k_{2,\theta} f_{\mathrm{y}}}{\gamma_{M,fi}} \quad \text{for slender sections,} \tag{6.18}$$

in which

$$\chi_{\mathrm{fi}} = \frac{1}{\phi_\theta + \sqrt{\phi_\theta^2 + \beta \overline{\lambda}_\theta^2}} \qquad \text{where} \qquad \phi_\theta = 0.5\left[1 + \alpha \overline{\lambda}_\theta / \xi_\theta + \beta \overline{\lambda}_\theta^2\right] \tag{6.19}$$

where α is the imperfection factor, β is the auxiliary coefficient, $\xi_\theta = \sqrt{k_{2,\theta}/k_{E,\theta}}$ is the elevated temperature strength-to-stiffness ratio reduction factor and $\overline{\lambda}_\theta$ is the elevated temperature non-dimensional slenderness calculated as:

$$\overline{\lambda}_\theta = \overline{\lambda}\xi_\theta = \sqrt{\frac{A f_{\mathrm{y}}}{N_{\mathrm{cr}}}}\sqrt{\frac{k_{2,\theta}}{k_{E,\theta}}} \quad \text{for non-slender sections} \tag{6.20}$$

$$\overline{\lambda}_\theta = \overline{\lambda}\xi_\theta = \sqrt{\frac{A_{\mathrm{eff}} f_{\mathrm{y}}}{N_{\mathrm{cr}}}}\sqrt{\frac{k_{2,\theta}}{k_{E,\theta}}} \quad \text{for slender sections.} \tag{6.21}$$

Note that A_{eff} is determined using the expressions provided in Section 3.4, classifying a column cross-section as either 'non-slender' or 'slender' on the basis of the given procedure.

6.4.3 Calibration of the proposed design rules

Expressing eq. (6.19) in terms of the generalised imperfection factor $\eta_\theta^* = \alpha \overline{\lambda}_\theta / \xi_\theta$, and taking the ratio of the ultimate strength determined by the GMNIA to the ultimate axial resistance of the cross-section as χ_{FE}, (i.e. $\chi_{\mathrm{FE}} = N_{\mathrm{Ed,max,FE}}/(A k_{2,\theta} f_{\mathrm{y}})$ or $\chi_{\mathrm{FE}} = N_{\mathrm{Ed,max,FE}} \,/\, (A_{\mathrm{eff}} k_{2,\theta} f_{\mathrm{y}})$ depending on whether the cross-section is slender or non-slender, the numerical generalised im-

perfection factors $\eta^*_{\theta,FE}$ can be determined by:

$$\eta^*_{\theta,FE} = \left(\frac{1}{\chi_{\text{FE}}} - 1\right)\left(1 - \beta\chi_{\text{FE}}\overline{\lambda}^2_{\theta}\right). \tag{6.22}$$

In this study, η^*_{θ} given in eq. (6.14), with $\xi_{\theta} = \sqrt{k_{2,\theta}/k_{E,\theta}}$, was calibrated against the $\eta^*_{\theta,FE}$ values obtained from GMNIA through eq. (6.22), as shown in Fig. 6.8 for a series of austenitic stainless steel columns undergoing major axis buckling at various temperature levels. In the figure, the considered range of elevated temperature non-dimensional slenderness of the columns $\overline{\lambda}_{\theta}$ may be seen to be between 0.1 and 2.0, while for the cross-sections, seven welded I-section profiles with the same properties as those of European HE and IPE sections, whose proportions ranged between the values given in Table 6.3, were considered. As can be seen from Fig. 6.8, incorporation of the elevated temperature strength-to-stiffness ratio reduction factor ξ_{θ} within η^*_{θ} captures the requirement for larger generalised imperfection factor values $\eta^*_{\theta,FE}$ for higher temperature levels.

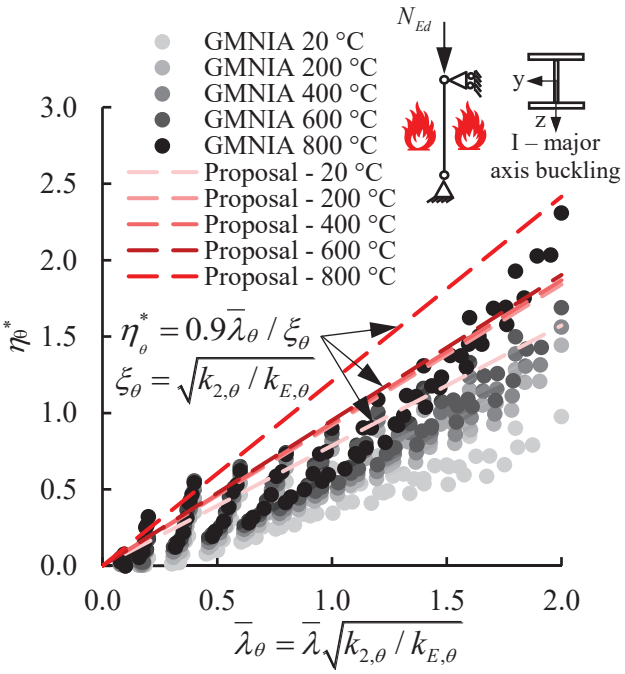

Figure 6.8: Calibration of generalised imperfection factors $\eta_{\theta}*$ for austenitic stainless steel columns buckling about the major axis in fire

Table 6.3: Range of the proportions of the cross-sections considered in the calibration

	h/b	b/t_f	h/t_w
Maximum	2.00	28.57	42.25
Minimum	0.93	5.30	10.00

The same calibration procedure was also followed for austenitic columns undergoing minor axis buckling, as well as duplex and ferritic stainless steel columns buckling about both axes. Seven cross-section profiles were considered for each of the austenitic and ferritic stainless steel grades, while six cross-section profiles were considered in duplex stainless steel. The proportions of the sections ranged between the values provided in Table 6.3, which shows that a wide range of cross-section properties were considered. The selected profiles were classified as Class 1, Class 3 and Class 4 cross-sections according to classification rules provided in EN 1993-1-4 (CEN, 2015), thereby allowing the response of columns having stocky, intermediate and slender cross-sections to be explored. It should also be noted that due to the adoption of $f_{2,\theta}$ in the new cross-section instability assessment rules introduced in Chapter 3, the considered Class 3 cross-sections according to EN 1993-1-2 (CEN, 2005) fall into the 'slender' category, for which the effective cross-section areas A_{eff} were used in the calculations. The calibrated values of the imperfection factor α and auxiliary coefficient β for the new design rules are shown in Table 6.4. In the following subsection, the accuracy of the new proposals is assessed.

Table 6.4: Calibrated values of imperfection factor α and auxiliary coefficient β for the new proposal

	Austenitic		Duplex		Ferritic	
Axis of buckling	α	β	α	β	α	β
Major	0.90	1.00	0.55	1.00	0.55	1.00
Minor	0.90	1.50	0.55	1.50	0.55	1.50

6.4.4 Assessment of the accuracy and reliability of new proposals

In this subsection, the accuracy and reliability of the new design proposals are assessed against the results obtained from nonlinear finite element modelling. The new proposals are also compared against EN 1993-1-2 (CEN, 2005) and the design method recommended by Lopes *et al.* (2010a) for the flexural buckling assessment of stainless steel columns at elevated temperatures.

The accuracy of the new proposals is shown in Fig. 6.9 and Fig. 6.10 for a series of stainless steel columns experiencing flexural buckling about the major and minor axes, respectively. Note that the room temperature results (i.e. those for 20°C) were included in the figures for reference only. In Fig. 6.9 and Fig. 6.10, seven cross-sections were considered for both the austenitic and ferritic stainless steel grades, while six cross-sections were considered for the duplex grade; the cross-section proportions ranged between the values given in Table 6.3. As can be seen from both figures, the new proposals lead to generally safe-sided and accurate ultimate strength predictions for stainless steel columns for over the wide considered range of elevated temperature levels, non-dimensional slendernesses, cross-section proportions, axes of buckling and stainless steel grades. The use of ξ_θ in the definition of the generalised imperfection factor η_θ^* results in multiple buckling curves that generally lie lower with increasing temperature. Very accurate results were achieved for non-slender cross-sections, as shown previously in Fig. 6.4 for an HEM 100 section, while accurate but somewhat more conservative estimations were observed in Fig. 6.9 and Fig. 6.10 for cross-sections falling into the 'slender' category.

The accuracy of the new proposals is also illustrated in Table 6.5 for 2200 columns for elevated temperature levels ranging between 200°C and 800°C in increments of 200°C, considering the array of cross-sections previously described with the range of proportions shown in Table 6.3. In the table, ε_{av}, ε_{COV}, ε_{max} and ε_{min} are the average, coefficient of variation, maximum and minimum values of the ratios of the ultimate strength predictions obtained through GMNIA $N_{Ed,max,FE}$ and the proposed design method $N_{Ed,max,prop}$, respectively. Table 6.3 shows that the new proposals lead to generally safe-sided ultimate strength predictions for all the considered

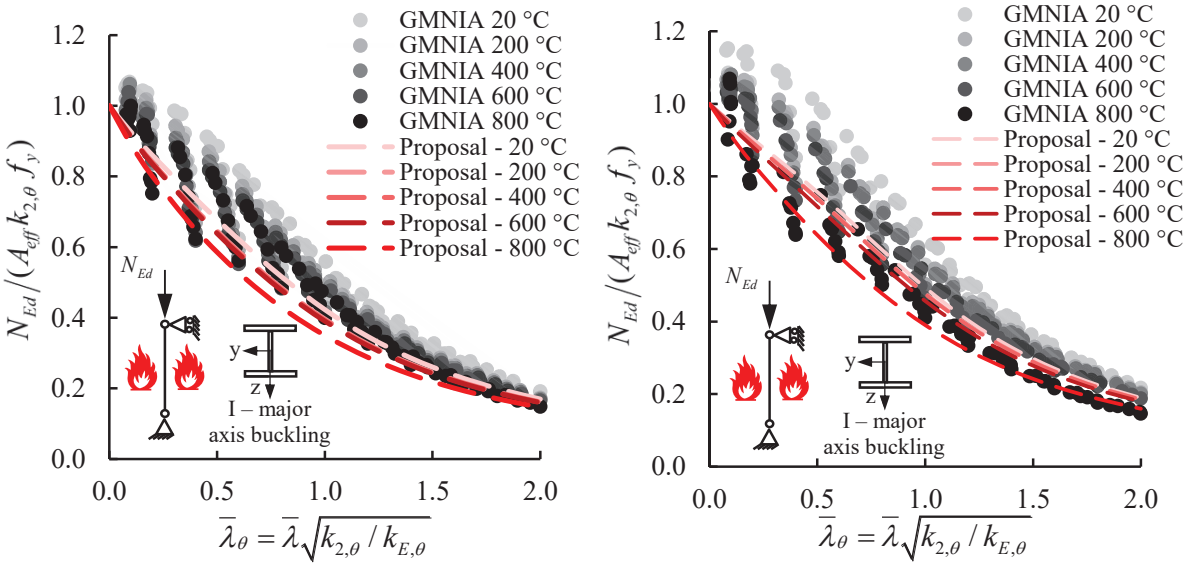

(a) Austenitic stainless steel columns

(b) Duplex stainless steel columns

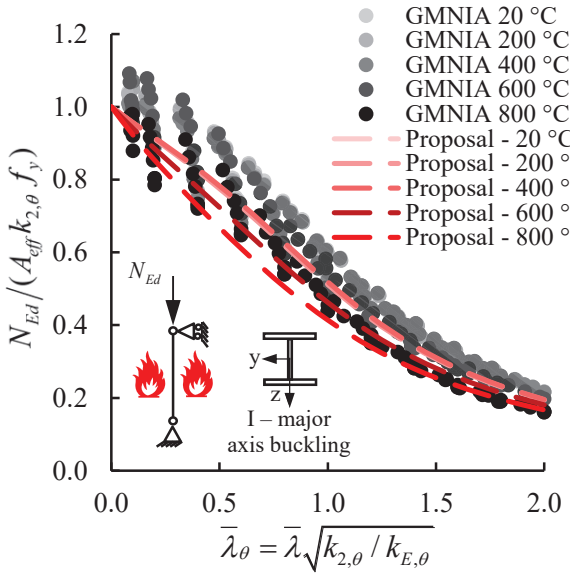

(c) Ferritic stainless steel columns

Figure 6.9: Accuracy of the new design proposals for the major axis flexural buckling assessment of stainless steel columns in fire

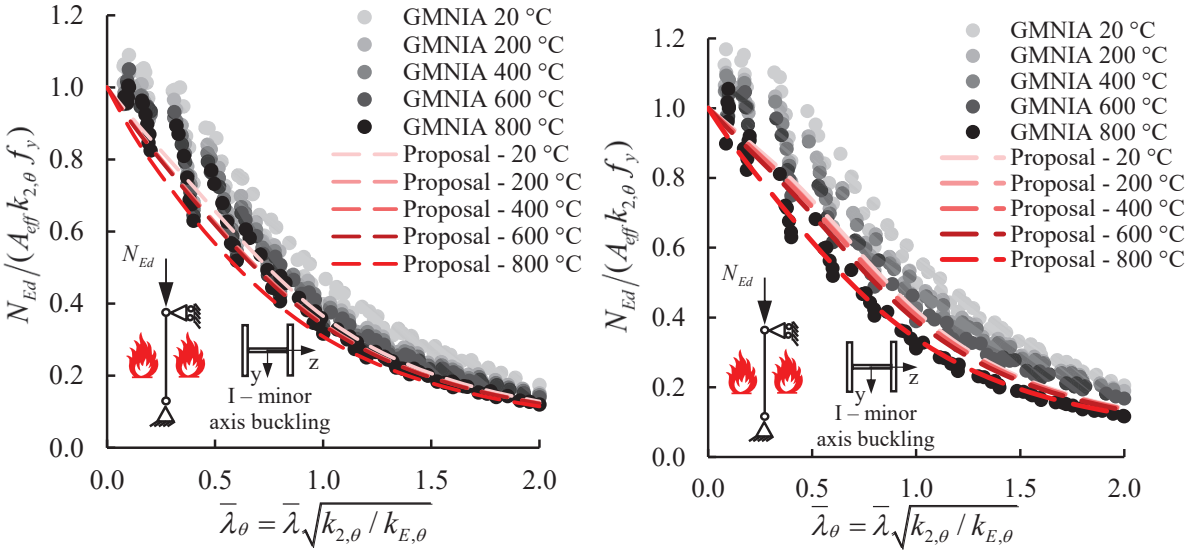

(a) Austenitic stainless steel columns

(b) Duplex stainless steel columns

(c) Ferritic stainless steel columns

Figure 6.10: Accuracy of the new design proposals for the minor axis flexural buckling assessment of stainless steel columns in fire

wide range of stainless steel columns. Additionally, the accuracy of the current rules provided in EN 1993-1-2 and the design proposal made by Lopes *et al.* (2010a) is also investigated in Table 6.5. As can be seen from the table, EN 1993-1-2 (CEN, 2005) leads to very unsafe strength predictions for stainless steel columns in fire. The proposals of Lopes *et al.* (2010a), in which the elevated temperature strength at 2% strength $f_{2,\theta}$ was adopted as in the present study, also lead to generally safe-sided strength predictions. However, they are somewhat overly-conservative and also less consistent than the column design rules developed in this study.

Table 6.5: Accuracy of the new proposals, EN 1993-1-2 (CEN, 2005) and Lopes *et al.* (2010a) relative to the FE results for the flexural buckling assessment of stainless steel columns in fire

			Major axis buckling				Minor axis buckling			
	Grade	N	ε_{av}	ε_{COV}	ε_{max}	ε_{min}	ε_{av}	ε_{COV}	ε_{max}	ε_{min}
New proposals	Austenitic	770	1.17	0.080	1.41	0.88	1.16	0.079	1.42	0.94
	Duplex	660	1.12	0.075	1.33	0.91	1.17	0.127	1.51	0.92
	Ferritic	770	1.10	0.065	1.27	0.90	1.16	0.126	1.47	0.87
EN 1993-1-2	Austenitic	770	0.98	0.105	1.23	0.77	0.87	0.151	1.20	0.64
	Duplex	660	1.00	0.125	1.40	0.74	0.91	0.173	1.26	0.57
	Ferritic	770	1.10	0.156	1.76	0.78	1.00	0.148	1.74	0.65
Lopes *et al.* (2010a)	Austenitic	770	1.41	0.115	1.90	1.03	1.34	0.089	1.67	1.05
	Duplex	660	1.19	0.068	1.49	0.98	1.22	0.108	1.53	0.99
	Ferritic	770	1.56	0.135	2.21	1.09	1.54	0.133	1.82	1.06

In Table 6.6, the reliability of the new column buckling design proposals is assessed considering the three reliability criteria put forward by Kruppa (1999) for the design of steel members in fire. It can be seen that the new proposals satisfy all three reliability criteria set out by Kruppa (1999), as does the method of Lopes *et al.* (2010a). On the other hand, EN 1993-1-2 generally fails to fulfill the three reliability criteria for the design of stainless steel columns in fire.

Finally, the accuracy of the new proposal is assessed against that of EN 1993-1-2 (CEN, 2005) and the method of Lopes *et al.* (2010a) in Fig. 6.11 for all the considered 2200 stainless steel columns buckling about the major and minor axis in this study. As can be seen from the figure, the new proposals lead to significantly enhanced accuracy relative to the existing methods for the flexural buckling assessment of stainless steel columns in fire.

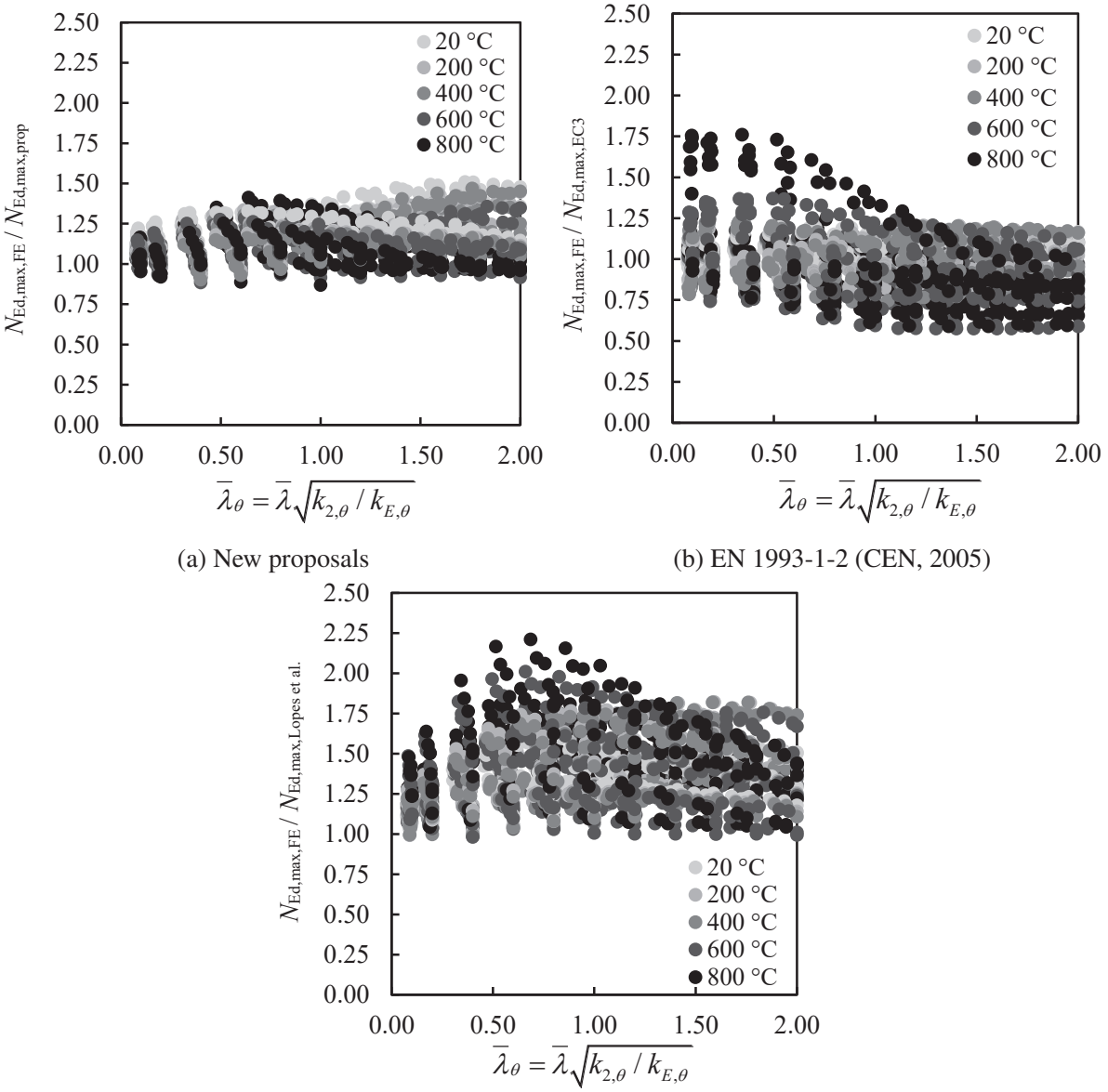

(a) New proposals

(b) EN 1993-1-2 (CEN, 2005)

(c) Lopes *et al.* (2010a)

Figure 6.11: Comparison of the accuracy of the new proposal against EN 1993-1-2 (CEN, 2005) and the method of Lopes *et al.* (2010a) for all stainless steel columns considered in this study

Table 6.6: Assessment of the reliability of the new proposal, EN 1993-1-2 (CEN, 2005) and Lopes *et al.* (2010a) on the basis of the three reliability criteria set out by Kruppa (1999). Note that the numbers denoted by * violates the corresponding criterion.

		Major axis buckling			Minor axis buckling		
	Grade	Crit. 1	Crit. 2	Crit. 3	Crit. 1	Crit. 2	Crit. 3
New Proposals	Austenitic	0.0	3.9	-13.6	0.0	2.4	-13.3
	Duplex	0.0	8.2	-10.5	0.0	16.2	-13.3
	Ferritic	0.0	11	-8.4	0.0	12.5	-12.8
EN 1993-1-2	Austenitic	16.1*	57.0*	3.2*	56.2*	80.2*	16.9*
	Duplex	15.8*	45.8*	1.8*	35.6*	73.1*	14.3*
	Ferritic	4.6*	28.0*	-5.7	8.3*	52.5*	1.6*
Lopes *et al.* (2010a)	Austenitic	0.0	0.0	-28.2	0.0	0.0	-25.0
	Duplex	0.0	1.2	-15.8	0.0	1.3	-17.4
	Ferritic	0.0	0.0	-34.7	0.0	0.0	-33.9

6.5 Conclusions

In this chapter, new proposals for the design of stainless steel I-section columns in fire, compatible with the existing design methods for carbon steel columns given in EN 1993-1-2 (CEN, 2005) have been developed. Shell finite element models of stainless steel welded I-section columns able to replicate their behaviour at elevated temperatures were created and validated against existing experimental results from the literature. Using the validated finite element models, the accuracy of the rules given in EN 1993-1-2 (CEN, 2005) for the flexural buckling assessment of stainless steel columns in fire was examined. It was shown that the current EN 1993-1-2 rules (CEN, 2005) lead to significant overpredictions of member resistance, which was ascribed to the dependency of the generalised imperfection factor used in these equations on the temperature level. A new expression for the generalised imperfection factor independent of the temperature level in accordance with the Perry-Robertson concept (Ayrton & Perry, 1886; Robertson, 1925) adopted in EN 1993-1-2 (CEN, 2005) was put forward. Using the new expression for the generalised imperfection factor and adopting the elevated temperature strength at 2% total strain $f_{2,\theta}$ as the basic design strength to maintain the consistency with the carbon steel column design rules in EN 1993-1-2 (CEN, 2005), new flexural buckling assessment rules for

stainless steel columns in fire were calibrated considering a range of elevated temperature levels, cross-section geometries, slendernesses and stainless steel grades. The reliability of the new proposals was assessed against the fire design reliability criteria set out by Kruppa (1999), which were shown to be satisfied. The new proposals made herein are expected to be incorporated into the upcoming version of EN 1993-1-2.

Chapter 7

Testing of I-section beam-columns

7.1 Introduction

Six full-scale fire tests have been carried out on grade 1.4301 austenitic stainless steel laser-welded I-section beam-columns; the testing procedure and results are described in this chapter. Two loading eccentricity values of 10 mm and 30 mm were utilised in the fire tests to achieve different combinations of axial compression and uniform minor axis bending. In addition to the fire tests, two full-scale room temperature tests on beam-columns with the same geometric properties and from the same batch of material as those of the specimens subjected to fire testing were also carried out. In the fire tests, the anisothermal testing method, which mimics a real fire situation, was adopted. In addition to the full-scale beam-column tests, the results of initial geometric imperfection measurements on the specimens are also reported. Note that the results of complementary room temperature tensile coupon tests have been presented in Section 5.2.

7.2 Geometry and imperfection measurements

The geometric properties of the eight beam-column specimens were measured before conducting the tests; the measured results are reported in Table 7.1. The tested specimens were labelled with respect to the initial loading eccentricity e_0, where BC-Z10 corresponds to the specimen with the initial loading eccentricity of 10 mm while BC-Z30 corresponds to the specimen with the initial loading eccentricity of 30 mm. The Z indicates that bending was induced about the minor axis, which was the case in all tests. An additional number was also utilised to signify the three different nominal axial load ratios $n_r = 0.6, 0.5$ and 0.4 applied to the specimens, which are equal to the ratios of the applied axial loading $N_{Ed,test}$ to the room temperature minor axis flexural buckling resistances N_u, determined from the room temperature beam-column tests with the corresponding loading eccentricities (i.e. $n_r = N_{Ed,test}/N_u$). Thus, BC-Z30-0.5 corresponds to the beam-column specimen with the initial loading eccentricity value of 30 mm and axial load ratio of 0.5. The beam-column specimens tested at room temperature were denoted BC-Z10-20C for the specimen with the initial loading eccentricity of 10 mm and BC-Z30-20C for the specimen with the initial loading eccentricity of 30 mm.

Table 7.1: Geometric properties and imperfections of tested stainless steel I-section beam-column specimens

ID	L (mm)	h (mm)	b (mm)	t_w (mm)	t_f (mm)	w_f (mm)	w_w (mm)	w_0 (mm)	v_0 (mm)
BC-Z10-20C	2751.50	198.08	99.41	4.95	6.93	0.03	0.06	0.06	0.38
BC-Z10-0.6	2752.75	198.32	99.23	5.02	6.93	0.08	0.05	0.08	0.23
BC-Z10-0.5	2752.25	198.26	99.53	4.96	6.93	-	-	-	0.17
BC-Z10-0.4	2751.25	198.04	99.55	4.77	6.94	-	-	-	0.32
BC-Z30-20C	2751.25	198.31	99.48	4.84	6.96	0.05	0.05	0.05	0.27
BC-Z30-0.6	2751.50	198.28	99.43	4.88	6.91	0.04	0.06	0.06	0.39
BC-Z30-0.5	2753.25	198.24	99.64	4.87	6.92	-	-	-	0.43
BC-Z30-0.4	2752.25	197.96	99.45	4.82	6.86	-	-	-	0.21

Initial local geometric imperfections of four beam-column specimens (BC-Z10-20C, BC-Z10-0.6, BC-Z30-20C and BC-Z30-0.6) and initial global geometric imperfections of all beam-column specimens were measured in line with the procedure reported in Section 5.3. A typ-

ical measured local geometric imperfection distribution is shown in Fig. 7.1 (a). The measured web local geometric imperfection magnitudes w_w and flange local geometric imperfection magnitudes w_f are summarised in Table 7.1, where it is found that the measured web w_w and flange w_f local geometric imperfection magnitudes are significantly lower than the manufacturing tolerance of 1/100 of the web height and 1/100 of the flange width set out in EN 1090-2 (CEN, 2018). Fig. 7.1 (b) shows a typical measured initial global geometric imperfection distribution. The measured global geometric imperfections v_0 are summarized in Table 7.1, where it can be seen that the measured global geometric imperfections v_0 are significantly lower than the manufacturing tolerance of $L_s/1000$ set out in EN 1090-2 (CEN, 2018).

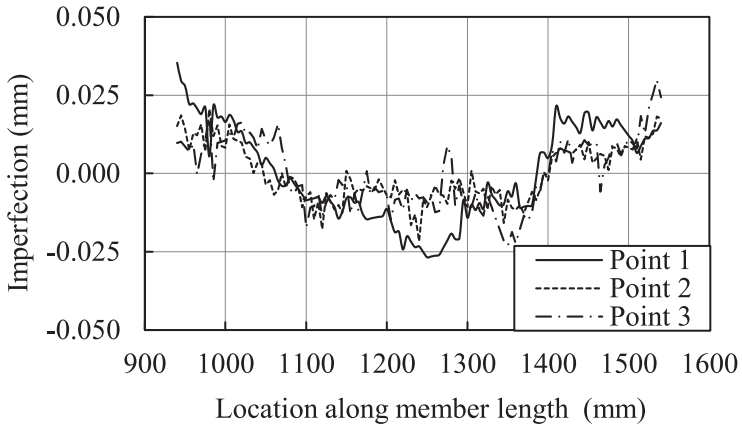

(a) Local geometric imperfection distributions for top flange

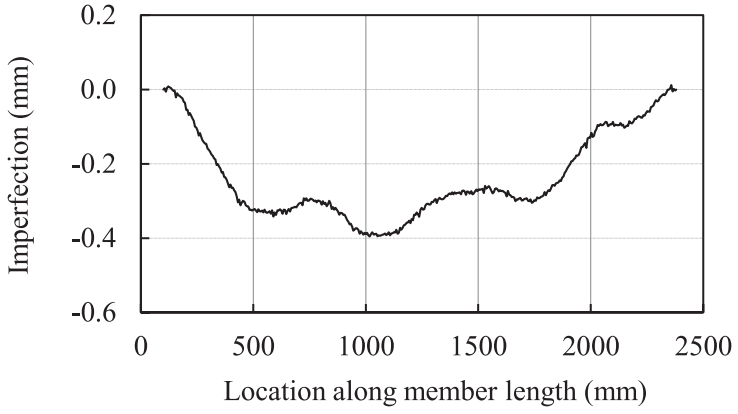

(b) Initial global geometric imperfection distribution

Figure 7.1: Typical measured imperfection distributions; shown for specimen BC-Z10-20C

7.3 Beam-column tests at room temperature

To obtain reference resistances for the fire tests to be benchmarked against, two corresponding specimens were tested under combined axial compression and minor axis bending at room temperature. The specimens had the same nominal cross-section size of I-198×99×4.5×7 and the same nominal buckling length L of 2.75 m. Two values of initial loading eccentricities e_0 equal to 10 mm and 30 mm were considered to achieve different bending moment-to-axial load ratios. As shown in Fig. 7.2, the initial loading eccentricity e_0 was introduced by eccentrically welding the specimens to the end plates; the distance between the centrelines of the end plate and the specimen was equal to the initial loading eccentricity e_0.

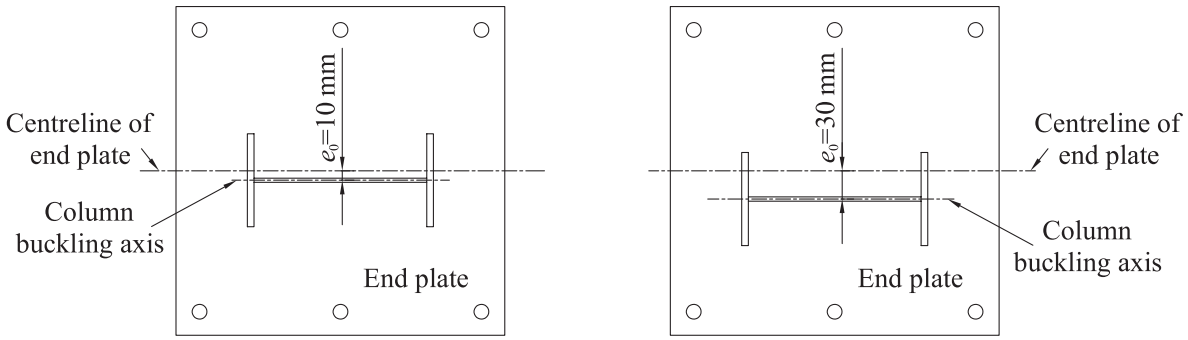

Figure 7.2: Positioning of specimens and end-plates

The test setup and testing procedures of the room temperature beam-column tests are the same as those of the room temperature column tests reported in Section 5.4.1. Note that in the beam-column tests, the total test eccentricity comprised the initial loading eccentricity e_0 and the global imperfection of the test specimens v_0. The measured total test eccentricities are summarised in Table 7.2.

Table 7.2: Key experimental results of beam-column tests performed at room temperature

ID	Total eccentricity $v_0 + e_0$ (mm)	Ultimate load N_u (kN)	Lateral displacement at N_u (mm)	Ultimate first order bending moment M_u (kNm)
BC-Z10-20C	10.98	145	26.9	1.59
BC-Z30-20C	30.36	99	38.3	3.01

The two tested beam-column specimens (BC-Z10-20C and BC-Z30-20C) failed by flexural buckling about the minor axis, which was accentuated by the presence of the applied minor axis bending moment. A typical failure mode of the tested beam-columns, that of BC-Z30-20C, is shown in Fig. 7.3. The load versus mid-height lateral displacement curves for the two beam-column tests are plotted in Fig. 7.4. The key results from these two beam-column tests are summarised in Table 7.2, where M_{u} is the first order ultimate bending moment, calculated as:

$$M_{\mathrm{u}} = N_{\mathrm{u}}(v_0 + e_0). \tag{7.1}$$

Figure 7.3: Typical failure mode from room temperature tests, showing flexural buckling about the minor axis, illustrated for specimen BC-Z30-20C

7.4 Beam-column fire tests

Six fire tests on pin-ended stainless steel I-section beam-columns under combined axial compression and bending about the minor axis were carried out in this study. The cross-section of the six beam-column specimens was an I-198×99×4.5×7 profile and the buckling length of members was equal to 2.75 m, mirroring two beam-columns tested at room temperature. Of the six

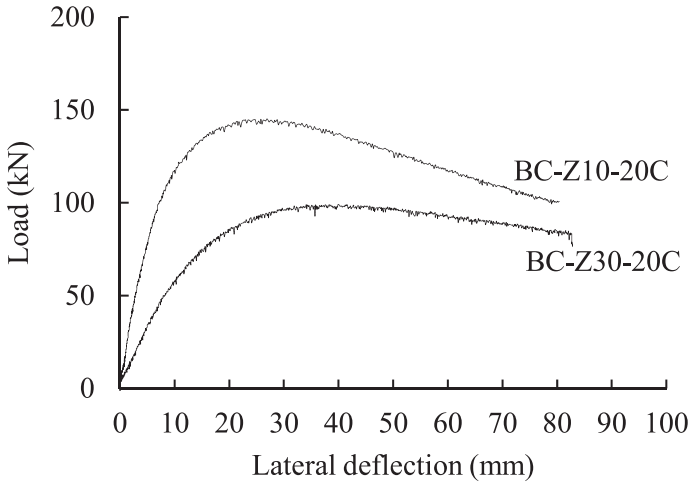

Figure 7.4: Load-lateral deflection curves for beam-column tests at room temperature

beam-column fire tests, three tests were conducted with an initial nominal loading eccentricity e_0 of 10 mm and three were carried out with an initial nominal loading eccentricity e_0 of 30 mm. An anisothermal testing method was employed in all the beam-column fire tests. Three different load ratios n_r, equal to 0.6, 0.5 and 0.4, were adopted to achieve a range of failure temperatures.

The test setup and testing procedures of the beam-column fire tests are the same as those of the column fire tests reported in Section 5.5. The pre-applied compressive load $N_{Ed,test}$, load ratios n_r and the measured total eccentricity $(v_0 + e_0)$ of the six beam-column tests are reported in Table 7.3.

Table 7.3: Pre-applied loads and load ratios of specimens under compression and bending about the minor axis subjected to fire testing

ID	Total eccentricity $v_0 + e_0$ (mm)	Pre-applied load (kN)	Load ratio n_r -
BC-Z10-0.6	10.53	89	0.61
BC-Z10-0.5	9.89	76	0.52
BC-Z10-0.4	10.21	60	0.42
BC-Z30-0.6	30.35	60	0.60
BC-Z30-0.5	30.72	51	0.51
BC-Z30-0.4	30.07	44	0.44

As anticipated, all the tested beam-column specimens failed by flexural buckling about the minor axis accentuated by the presence of minor axis bending. Fig. 7.5 shows the failure modes of the beam-column specimens with the 10 mm nominal eccentricity for the three different load ratios n_r. The specimens with the 30 mm nominal eccentricity exhibited similar failure modes. In this subsection, additional details are presented regarding the temperature distributions and the behaviour of the specimens observed during the testing.

(a) BC-Z10-0.6

(b) BC-Z10-0.5

(c) BC-Z10-0.4

Figure 7.5: Failure modes of the beam-column fire test specimens with the 10 mm nominal eccentricity

Temperature distributions

The measured air temperature versus time relationships for the six beam-column fire tests are shown in Fig. 7.6, together with the ISO-834 (1999) standard fire curve. As can be seen from the figures, the air temperature in the furnace generally followed the trend of the ISO-834 (1999) standard fire curve though lagged somewhat behind, particularly at the beginning of the experiments.

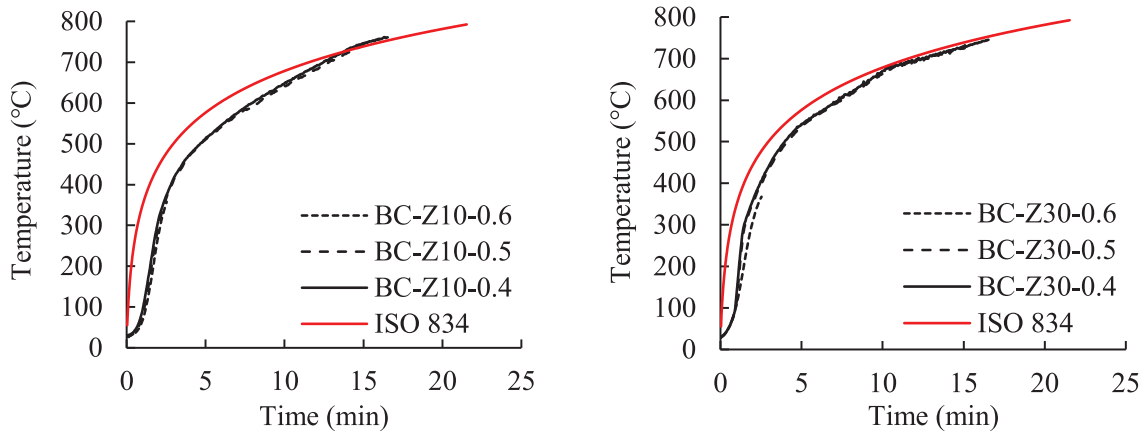

(a) Specimen with e_0 equal to 10 mm

(b) Specimen with e_0 equal to 30 mm

Figure 7.6: Comparison of the measured furnace temperature-time relationships with the ISO-834 standard fire curve

Fig. 7.7 shows the temperatures measured by the seven thermocouples attached to the surface of specimen BC-Z10-0.4. In this figure, the temperatures measured by thermocouples 2–6 in the heated region can be seen to have increased following a similar trend with time. The temperatures of the two unheated parts outside the furnace were measured by thermocouple 1 and thermocouple 7 found to remain at room temperature throughout the testing. Fig. 7.8 show the average measured surface temperature-time relationships for all six fire test specimens, where the surface temperatures are taken as the mean temperature values measured by the five thermocouples attached to the specimens in the heated regions.

The key experimental results from the six beam-column fire tests are summarised in Table 7.4,

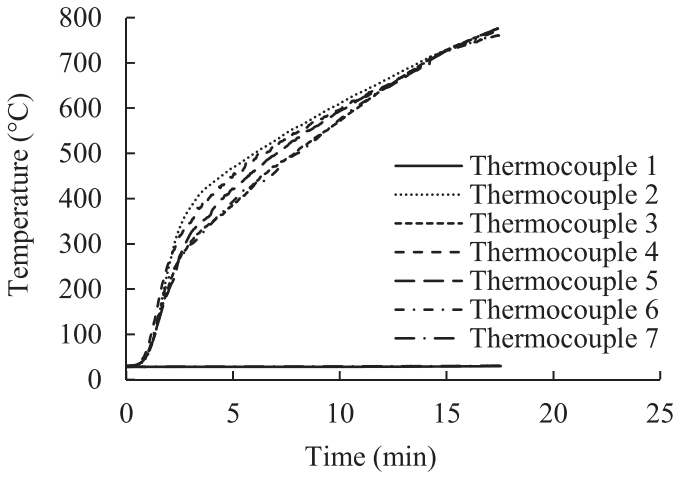

Figure 7.7: Specimen surface temperature versus time paths measured by thermocouples along specimen length, shown for BC-Z10-0.4

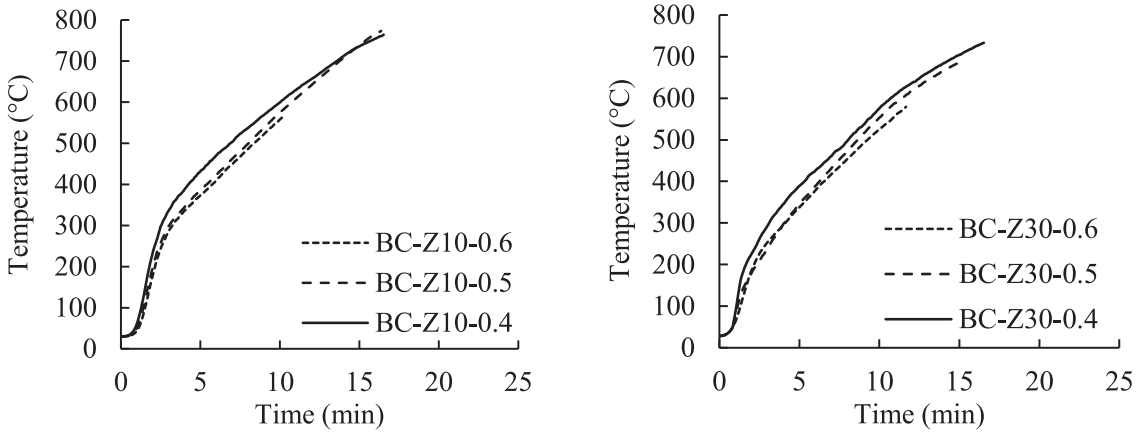

(a) Specimen with e_0 equal to 10 mm

(b) Specimen with e_0 equal to 30 mm

Figure 7.8: Average measured specimen surface temperature-time paths for six fire test specimens

including the critical failure temperature θ_{cr} and the fire resistance in terms of duration $t_{fi,test}$ for which the specimens were able to resist the pre-applied loads $N_{Ed,test}$.

Table 7.4: Measured fire resistances from beam-column tests

ID	Fire resistance $t_{fi,test}$ (min)	θ_{cr} (°C)
BC-Z10-0.6	9.53	540
BC-Z10-0.5	15.40	749
BC-Z10-0.4	16.97	771
BC-Z30-0.6	11.30	567
BC-Z30-0.5	12.77	637
BC-Z30-0.4	16.77	737

Behaviour of specimens

The axial deformation versus temperature paths for the tested six stainless steel beam-column specimens are shown in Fig. 7.9. It can be seen that the beam-column specimens shortened initially due to the pre-applied load ($N_{Ed,test}$ and, due to the eccentricity, $M_{Ed,test}$), and then started to expand with increasing temperatures. When the beam-column specimen temperatures were below about 300 °C, it can be seen in Fig. 7.9 that the measured axial expansion rates of the specimens were smaller than those measured for high temperature levels. This was mainly because the specimen temperatures increased rapidly to 300 °C and the position of the actuator, which was manually controlled to maintain a constant axial loading, lagged slightly behind where it ought to have been. After reaching 300 °C, the specimen temperature increased more slowly and all the specimens expanded linearly with increasing temperature values until failure.

Fig. 7.10 shows the mid-height lateral deflection versus average surface temperature paths for the six fire test specimens. As shown in Fig. 7.10, there was a small mid-height lateral deflection under the initial applied load; the mid-height lateral deflections of the specimens then displayed small fluctuations owing to possible thermal bowing under increasing temperature. Finally, as the beam-column specimens approached failure, their stiffness reduced rapidly and there were significant increases in mid-height lateral deflections, signifying flexural buckling about the minor

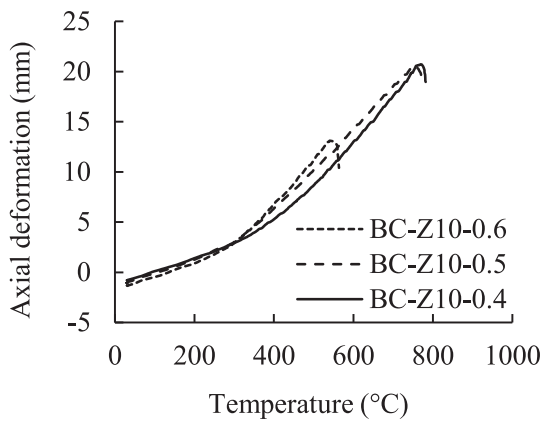

(a) Specimen with e_0 equal to 10 mm

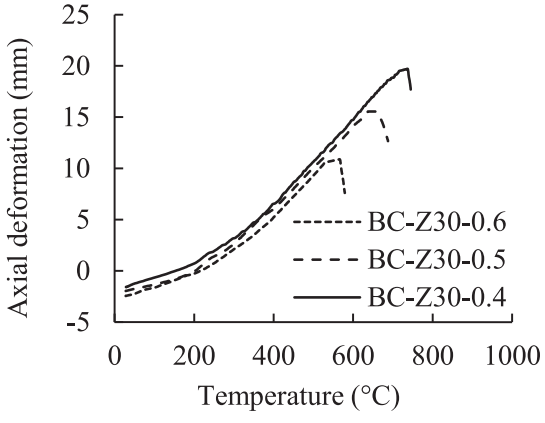

(b) Specimen with e_0 equal to 30 mm

Figure 7.9: Axial deformation versus specimen temperature paths obtained from six fire tests, with positive deformations corresponding to expansion of the specimens

axis.

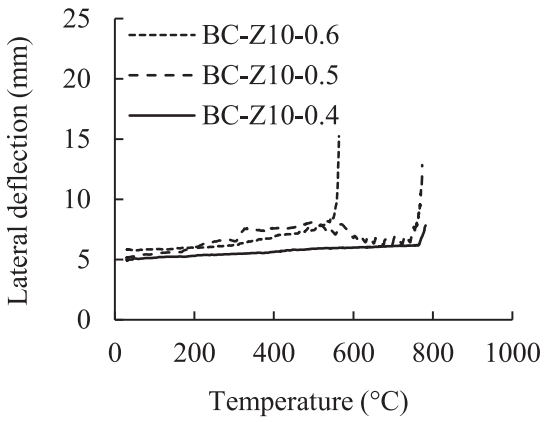

(a) Specimen with e_0 equal to 10 mm

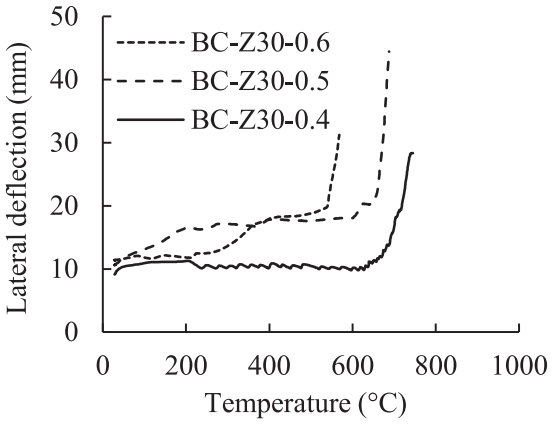

(b) Specimen with e_0 equal to 30 mm

Figure 7.10: Lateral deflection versus specimen temperature paths obtained from six beam-column fire tests

7.5 Conclusions

An experimental study of grade 1.4301 austenitic stainless steel laser-welded I-section beam-columns in fire has been presented. Before the fire tests, two beam-column specimens with the same geometrical properties as those subjected to fire testing were tested at room temperature to obtain benchmark room temperature failure loads N_{u}. Six anisothermal fire tests were then conducted on stainless steel I-section beam-columns. In the fire tests, two initial loading eccentricity values e_0, equal to 10 mm and 30 mm, and three load ratios n_{r}, equal to 0.4, 0.5 and 0.6, were employed to achieve a range of bending moment-to-axial load ratios and a range of failure temperatures.

Chapter 8

FE modelling and design of I-section beam-columns

8.1 Introduction

In this chapter, shell finite element models able to replicate the behaviour of stainless steel beam-columns at elevated temperatures are created and validated. Through the validated finite element models, extensive structural performance data, covering austenitic, duplex and ferritic stainless steel grades, a wide range of cross-section geometries, slenderness and elevated temperature levels, are generated for the assessment of the accuracy of the existing EN 1993-1-2 (CEN, 2005) design rules and the development of new fire design rules of stainless steel beam-columns. New beam-column equations, which are consistent with the beam-column provisions set out in the newly revised European standard prEN 1993-1-1 (CEN, 2020) for the room temperature design of steel members, are put forward. The accuracy and reliability of the new proposals are verified against the generated numerical structural performance data and compared to those of the existing beam-column design rules of EN 1993-1-2 (CEN, 2005).

8.2 Finite element modelling

In this section, finite element models able to mimic the structural response of stainless steel beam-columns in fire are developed and validated against experimental results. The finite element models are then utilised to perform extensive numerical parametric studies, the results of which are used for (i) the assessment of the accuracy of the current EN 1993-1-2 (CEN, 2005) beam-column design rules and (ii) the establishment of a new fire design method for stainless steel I-section beam-columns.

8.2.1 Development of finite element models

The finite element modelling approach for the stainless steel I-section beam-columns at elevated temperatures is the same as that for the columns reported in Section 6.2.1, except for the boundary conditions and applied forces. The boundary conditions applied to the finite element models of the beam-columns under major axis bending plus axial compression and those subjected to minor axis bending plus axial compression are illustrated in Fig. 8.1. As can be seen from the figure, the displacements and rotations of the end cross-sections were linked to two reference points, referred to as RP1 and RP2, through rigid body kinematic coupling constraints. The horizontal and vertical translations (U1 ans U2) and rotation about axis 3 (UR3) of the two reference points, as well as the longitudinal translation (U3) of reference point 2 (i.e. RP2), were restrained. For the models of the beam-columns under major axis bending plus axial compression (see Fig. 8.1(a)), the horizontal translations (U1) at the web-flange junctions were also restrained along the member lengths to ensure in-plane buckling of the beam-columns. The forces were applied as concentrated axial loads and bending moments to the two reference points, as shown in Fig. 8.1.

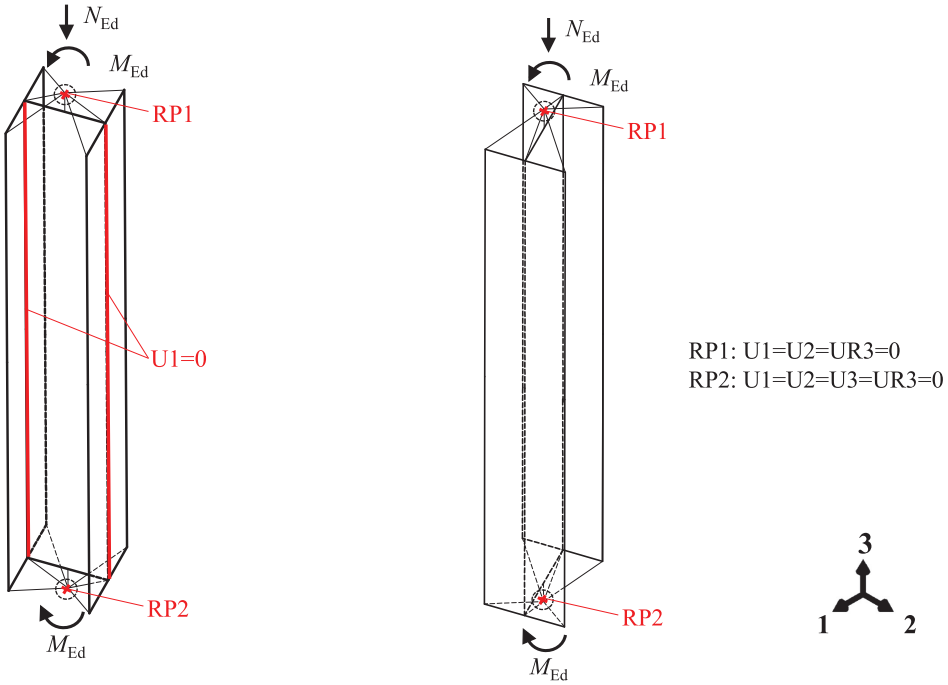

(a) Beam-columns under major axis bending plus axial compression

(b) Beam-columns under minor axis bending plus axial compression

Figure 8.1: Boundary conditions applied to beam-column finite element models

8.2.2 Validation of finite element models

The six fire tests carried out on austenitic stainless steel I-section beam-columns in Chapter 7 were utilised to validate the adopted finite element modelling approach. The measured geometric properties and imperfections of the six beam-columns were employed in the validation study. Sixteen elements were utilised across the width of each web and flange plate of the modelled I-sections; the element number along the member length was then determined by adopting an element aspect ratio of unity. The two-stage R-O material model in Section 3.2.1 was used to define the elevated temperature stress-strain response of the specimens, using the elevated temperature material properties determined by multiplying the strength and stiffness reduction factors given in SCI (2017) by the room temperature material properties obtained from the tensile coupon tests reported in Section 5.2. The three analysis steps described in Section 4.2.1 were adopted in the validation of the finite element modelling approach, taking the target temperatures θ equal to the critical temperature θ_{cr} values measured in the fire tests. The numerically determined failure loads $N_{Ed,FE}$ are compared against those obtained from the fire tests $N_{Ed,test}$ in Table 8.1, where it can be seen that the ratios of the failure loads determined using the finite element models $N_{Ed,FE}$ to those observed in the tests $N_{Ed,test}$ are generally close to unity, thus verifying that the finite element models created in this study are able to accurately predict the ultimate resistances of stainless steel beam-columns in fire. Excellent agreement is also obtained in comparisons between the experimental and FE failure modes, typical examples of which are shown in Fig. 8.2.

8.2.3 Parametric studies

Numerical parametric studies were conducted to establish comprehensive data for the structural response of stainless steel I-section beam-columns at elevated temperatures. The range of the parameters explored in the numerical studies are summarised in Table 8.2, where it can be seen that three stainless steel grades: (i) grade 1.4301 austenitic stainless steel, (ii) grade 1.4462

Table 8.1: Comparison of ultimate capacities of stainless steel beam-columns obtained from physical experiments reported in Chapter 7 and from FE analyses

ID	Cross-section	θ_{cr} (°C)	$N_{Ed,test}$ (kN)	$N_{Ed,FE}$ (kN)	$N_{Ed,FE}/N_{Ed,test}$
BC1-Z10-0.6	198×99×4.5×7	540	89	87	0.98
BC1-Z10-0.5	198×99×4.5×7	749	76	66	0.86
BC1-Z10-0.4	198×99×4.5×7	771	60	61	1.02
BC1-Z30-0.6	198×99×4.5×7	567	60	57	0.97
BC1-Z30-0.5	198×99×4.5×7	637	51	53	1.05
BC1-Z30-0.4	198×99×4.5×7	737	44	44	1.01
Average					0.98
COV					0.067

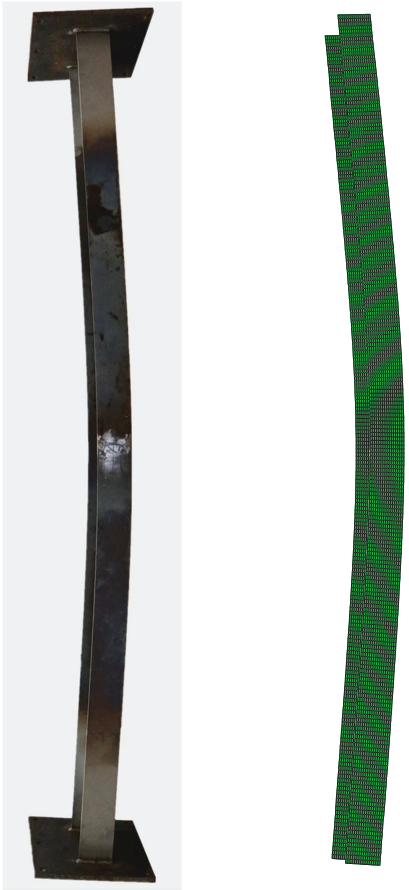

Figure 8.2: Experimental and numerical failure modes for specimen BC-Z10-0.4

duplex stainless steel and (iii) grade 1.4003 ferritic stainless steel were considered and, for each grade, six cross-section profiles, covering all four cross-section classes according to EN 1993-1-4 (CEN, 2015), were modelled. The considered elevated temperature levels varied from 200 °C to 800 °C in increments of 200 °C, while the considered elevated temperature non-dimensional slendernesses $\overline{\lambda}_\theta$ of the beam-columns equal to the square root of the ratio of the axial yield load Af_y to the elastic critical flexural buckling load N_{cr} multiplied by the square root of the ratio of the strength and stiffness reduction factors $\sqrt{k_{2,\theta}/k_{E,\theta}}$ (i.e. $\overline{\lambda}_\theta = \sqrt{Af_y/N_{cr}}\sqrt{k_{2,\theta}/k_{E,\theta}}$) were 0.5, 1 and 1.5 (i.e. $\overline{\lambda}_\theta = 0.5, 1.0$ and 1.5). Note that for the beam-columns under combined major axis bending and compression, the non-dimensional slendernesses were taken as the major axis flexural buckling slendernesses $\overline{\lambda}_{y,\theta}$ determined using the major axis elastic flexural buckling loads $N_{cr,y}$ ($\overline{\lambda}_\theta = \overline{\lambda}_{y,\theta} = \sqrt{Af_y/N_{cr,y}}\sqrt{k_{2,\theta}/k_{E,\theta}}$), while for those under minor axis bending plus axial compression, the non-dimensional slendernesses $\overline{\lambda}_\theta$ were taken as the minor axis flexural buckling slendernesses $\overline{\lambda}_{z,\theta}$ determined using the minor axis elastic flexural buckling loads $N_{cr,z}$ ($\overline{\lambda}_\theta = \overline{\lambda}_{z,\theta} = \sqrt{Af_y/N_{cr,z}}\sqrt{k_{2,\theta}/k_{E,\theta}}$). In the numerical parametric studies, a parameter referred to as the radial angle ϕ was used to describe the combination of axial compression and bending moment applied to a beam-column; the radial angle ϕ is calculated as:

$$\phi = \tan^{-1}\left(\frac{N_{Ed}/N_{Rd}}{M_{Ed}/M_{Rd}}\right), \tag{8.1}$$

where N_{Rd} and M_{Rd} are the axial compression resistance and bending moment resistance calculated using the considered design method. The definition of the radial angle ϕ within a beam-column interaction curve is illustrated in Fig. 8.3. As can be seen from the figure, when the radial angle ϕ increases from 0° to 90°, the applied loading changes from pure bending ($\phi = 0°$) to combined axial compression and bending ($0° < \phi < 90°$), and then to pure compression ($\phi = 90°$). In the numerical parametric studies, six different radial angles ϕ, varying from 0° to 90°, were considered for each beam-column at each elevated temperature level θ, as shown in Table 8.2. Fig. 8.4 shows typical failure modes of stainless steel beam-columns under major axis bending plus axial compression and under minor axis bending plus axial compression.

Table 8.2: Summary of parameters considered in numerical parametric studies carried out in this chapter

Loading condition	Stainless steel family	Cross-section	Temperature	Slenderness $\overline{\lambda}_\theta$	ϕ
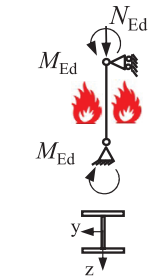 Major axis bending	Austenitic	HEM 200 HEAA 200 HEAA 300 IPE 100 IPE 200 IPE 300			
	Duplex	HEM 140 HEB 300 HEAA 200 IPE 80 IPE 100 IPE 180	200°C 400°C 600°C 800°C	0.5 1 1.5	0° 10° 30° 50° 70° 90°
Minor axis bending	Ferritic	HEM 200 HEAA 180 HEAA 300 IPE 100 IPE 180 IPE 300			

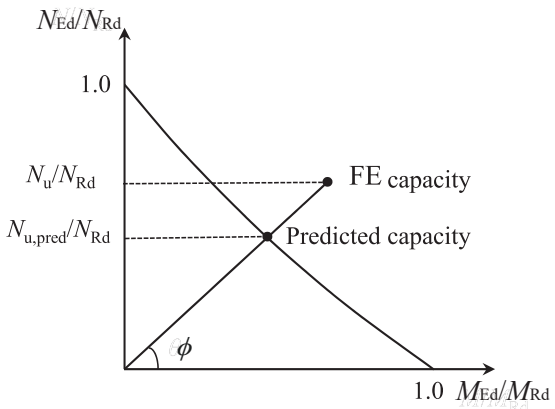

Figure 8.3: Definition of radial angle ϕ on axial load-moment interaction curve

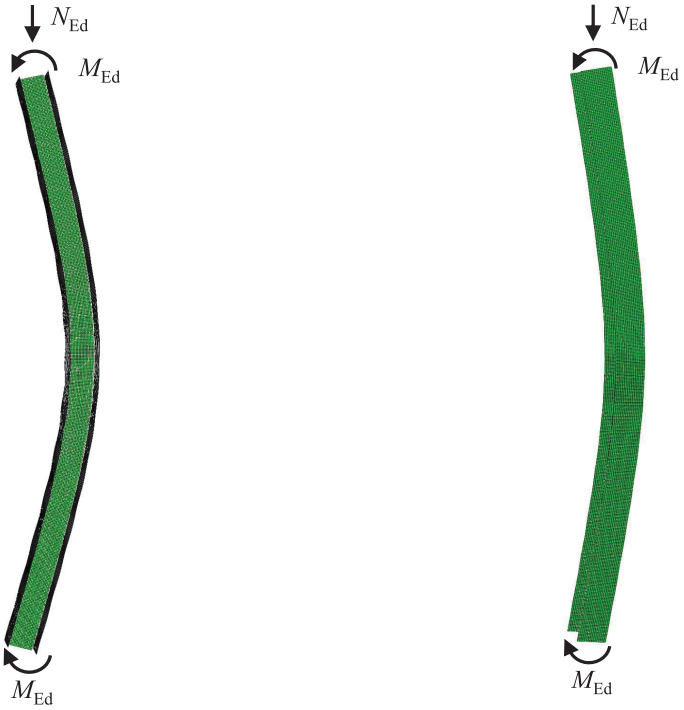

(a) Beam-columns under major axis bending plus axial compression

(b) Beam-columns under minor axis bending plus axial compression

Figure 8.4: Typical failure modes of stainless steel beam-columns under different loading conditions

8.3 Assessment of existing EN 1993-1-2 design rules for stainless steel beam-columns in fire

According to EN 1993-1-2 (CEN, 2005), a stainless steel member subjected to combined axial compression and bending in fire should satisfy eqs. (8.2)–(8.3) when it has a Class 1 or Class 2 cross-section:

$$\frac{N_{\mathrm{fi,Ed}}}{\chi_{\mathrm{min,fi}} A k_{\mathrm{y},\theta} \dfrac{f_{\mathrm{y}}}{\gamma_{\mathrm{M,fi}}}} + \frac{k_{\mathrm{y}} M_{\mathrm{y,fi,Ed}}}{W_{\mathrm{pl,y}} k_{\mathrm{y},\theta} \dfrac{f_{\mathrm{y}}}{\gamma_{\mathrm{M,fi}}}} + \frac{k_{\mathrm{z}} M_{\mathrm{z,fi,Ed}}}{W_{\mathrm{pl,z}} k_{\mathrm{y},\theta} \dfrac{f_{\mathrm{y}}}{\gamma_{\mathrm{M,fi}}}} \leq 1, \tag{8.2}$$

$$\frac{N_{\mathrm{fi,Ed}}}{\chi_{\mathrm{z,fi}} A k_{\mathrm{y},\theta} \dfrac{f_{\mathrm{y}}}{\gamma_{\mathrm{M,fi}}}} + \frac{k_{\mathrm{LT}} M_{\mathrm{y,fi,Ed}}}{\chi_{\mathrm{LT,fi}} W_{\mathrm{pl,y}} k_{\mathrm{y},\theta} \dfrac{f_{\mathrm{y}}}{\gamma_{\mathrm{M,fi}}}} + \frac{k_{\mathrm{z}} M_{\mathrm{z,fi,Ed}}}{W_{\mathrm{pl,z}} k_{\mathrm{y},\theta} \dfrac{f_{\mathrm{y}}}{\gamma_{\mathrm{M,fi}}}} \leq 1, \tag{8.3}$$

eqs. (8.4)–(8.5) when it has a Class 3 cross-section:

$$\frac{N_{\mathrm{fi,Ed}}}{\chi_{\mathrm{min,fi}} A k_{\mathrm{y},\theta} \dfrac{f_{\mathrm{y}}}{\gamma_{\mathrm{M,fi}}}} + \frac{k_{\mathrm{y}} M_{\mathrm{y,fi,Ed}}}{W_{\mathrm{el,y}} k_{\mathrm{y},\theta} \dfrac{f_{\mathrm{y}}}{\gamma_{\mathrm{M,fi}}}} + \frac{k_{\mathrm{z}} M_{\mathrm{z,fi,Ed}}}{W_{\mathrm{el,z}} k_{\mathrm{y},\theta} \dfrac{f_{\mathrm{y}}}{\gamma_{\mathrm{M,fi}}}} \leq 1, \tag{8.4}$$

$$\frac{N_{\mathrm{fi,Ed}}}{\chi_{\mathrm{z,fi}} A k_{\mathrm{y},\theta} \dfrac{f_{\mathrm{y}}}{\gamma_{\mathrm{M,fi}}}} + \frac{k_{\mathrm{LT}} M_{\mathrm{y,fi,Ed}}}{\chi_{\mathrm{LT,fi}} W_{\mathrm{el,y}} k_{\mathrm{y},\theta} \dfrac{f_{\mathrm{y}}}{\gamma_{\mathrm{M,fi}}}} + \frac{k_{\mathrm{z}} M_{\mathrm{z,fi,Ed}}}{W_{\mathrm{el,z}} k_{\mathrm{y},\theta} \dfrac{f_{\mathrm{y}}}{\gamma_{\mathrm{M,fi}}}} \leq 1, \tag{8.5}$$

and eqs. (8.6)–(8.7) when it has a Class 4 cross-section:

$$\frac{N_{\mathrm{fi,Ed}}}{\chi_{\mathrm{min,fi}} A_{\mathrm{eff}} k_{\mathrm{y},\theta} \dfrac{f_{\mathrm{y}}}{\gamma_{\mathrm{M,fi}}}} + \frac{k_{\mathrm{y}} M_{\mathrm{y,fi,Ed}}}{W_{\mathrm{eff,y}} k_{\mathrm{y},\theta} \dfrac{f_{\mathrm{y}}}{\gamma_{\mathrm{M,fi}}}} + \frac{k_{\mathrm{z}} M_{\mathrm{z,fi,Ed}}}{W_{\mathrm{eff,z}} k_{\mathrm{y},\theta} \dfrac{f_{\mathrm{y}}}{\gamma_{\mathrm{M,fi}}}} \leq 1, \tag{8.6}$$

$$\frac{N_{\mathrm{fi,Ed}}}{\chi_{\mathrm{z,fi}} A_{\mathrm{eff}} k_{\mathrm{y},\theta} \dfrac{f_{\mathrm{y}}}{\gamma_{\mathrm{M,fi}}}} + \frac{k_{\mathrm{LT}} M_{\mathrm{y,fi,Ed}}}{\chi_{\mathrm{LT,fi}} W_{\mathrm{eff,y}} k_{\mathrm{y},\theta} \dfrac{f_{\mathrm{y}}}{\gamma_{\mathrm{M,fi}}}} + \frac{k_{\mathrm{z}} M_{\mathrm{z,fi,Ed}}}{W_{\mathrm{eff,z}} k_{\mathrm{y},\theta} \dfrac{f_{\mathrm{y}}}{\gamma_{\mathrm{M,fi}}}} \leq 1. \tag{8.7}$$

In eqs. (8.2)–(8.7), $N_{\mathrm{fi,Ed}}$ is the design axial force, $M_{\mathrm{y,fi,Ed}}$ and $M_{\mathrm{z,fi,Ed}}$ are the maximum major axis and minor axis first order bending moments along the length of the beam-column, $\chi_{\mathrm{min,fi}}$ is the lowest of the buckling reduction factors determined for flexural buckling about the major and minor axes, torsional buckling and torsional-flexural buckling, $\chi_{\mathrm{z,fi}}$ is the lowest of the buckling reduction factors determined for flexural buckling about the minor axis, torsional buckling and torsional-flexural buckling and $\chi_{\mathrm{LT,fi}}$ is the reduction factor for lateral-torsional buckling. For the geometric properties, A and A_{eff} are the gross cross-sectional area and the effective area, $W_{\mathrm{pl,y}}$, $W_{\mathrm{el,y}}$ and $W_{\mathrm{eff,y}}$ are the plastic, elastic and effective section moduli about the major axis and $W_{\mathrm{pl,z}}$, $W_{\mathrm{el,z}}$ and $W_{\mathrm{eff,z}}$ are the plastic, elastic and effective section moduli about the minor axis; for the material properties, $k_{\mathrm{y},\theta}$ is the yield strength reduction factor taken as $k_{2,\theta}$ for members with Class 1, 2 or 3 cross-sections and $k_{\mathrm{p0.2},\theta}$ for members with Class 4 cross-sections and f_{y} is the yield strength (i.e. the 0.2% proof strength) at room temperature. Finally, $\gamma_{\mathrm{M,fi}}$ is the partial safety factor for fire design taken as 1.0 and k_{y}, k_{z} and k_{LT} are interaction coefficients calculated as:

$$k_{\mathrm{y}} = 1 - \frac{\mu_{\mathrm{y}} N_{\mathrm{fi,Ed}}}{\chi_{\mathrm{y,fi}} A k_{\mathrm{y},\theta} \dfrac{f_{\mathrm{y}}}{\gamma_{\mathrm{M,fi}}}} \leq 3 \tag{8.8}$$

with $\mu_{\mathrm{y}} = (2\beta_{\mathrm{M,y}} - 5)\bar{\lambda}_{\mathrm{y},\theta} + 0.44\beta_{\mathrm{M,y}} + 0.29 \leq 0.8$,

$$k_{\mathrm{z}} = 1 - \frac{\mu_{\mathrm{z}} N_{\mathrm{fi,Ed}}}{\chi_{\mathrm{z,fi}} A k_{\mathrm{y},\theta} \dfrac{f_{\mathrm{y}}}{\gamma_{\mathrm{M,fi}}}} \leq 3 \tag{8.9}$$

with $\mu_{\mathrm{z}} = (1.2\beta_{\mathrm{M,z}} - 3)\bar{\lambda}_{\mathrm{z},\theta} + 0.71\beta_{\mathrm{M,z}} - 0.29 \leq 0.8$,

$$k_{\mathrm{LT}} = 1 - \frac{\mu_{\mathrm{LT}} N_{\mathrm{fi,Ed}}}{\chi_{\mathrm{z,fi}} A k_{\mathrm{y},\theta} \dfrac{f_{\mathrm{y}}}{\gamma_{\mathrm{M,fi}}}} \leq 1 \tag{8.10}$$

with $\mu_{LT} = 0.15\bar{\lambda}_{z,\theta}\beta_{M,LT} - 0.15 \leq 0.9$, where $\beta_{M,y}$ and $\beta_{M,z}$ are equivalent uniform moment factors. Note that $k_{2,\theta}$ is the elevated temperature reduction factor for the strength at 2% total strain, which is equal to the ratio of the elevated temperature strength at 2% total strain $f_{2,\theta}$ to the room temperature yield strength (i.e. $k_{2,\theta} = f_{2,\theta}/f_y$), while $k_{p0.2,\theta}$ is the elevated temperature 0.2% proof strength reduction factor equal to the ratio of the elevated temperature 0.2% proof strength $f_{p0.2,\theta}$ to the room temperature yield strength (i.e. $k_{p0.2,\theta} = f_{p0.2,\theta}/f_y$).

Using the column and beam buckling design curves for the determination of $\chi_{min,fi}$, $\chi_{z,fi}$ and $\chi_{LT,fi}$ and the effective width rules for the determination of the effective section properties A_{eff}, $W_{eff,y}$ and $W_{eff,z}$ given in EN 1993-1-2 (CEN, 2005), the accuracy of the existing beam-column design rules of EN 1993-1-2 (CEN, 2005) is assessed against the results from the nonlinear finite element modelling, considering the wide range of parameters set out in Table 8.2. Figs. 8.5–8.7 show the assessment of the accuracy of the current EN 1993-1-2 (CEN, 2005) beam-column design equations against the GMNIA results for beam-columns subjected to uniform major axis bending plus compression and having the same cross-section properties as those of a European HEAA 200 cross-section for the austenitic stainless steel members, an HEB 300 cross-section for the duplex stainless steel members and an HEAA 180 cross-section for the ferritic stainless steel members. It can be seen from Figs. 8.5–8.7 that the current EN 1993-1-2 (CEN, 2005) rules lead to somewhat inaccurate ultimate strength predictions for stainless steel I-section beam-columns in fire that lie generally on the unsafe side. Similar results are found for the cases where the beam-columns were subjected to minor axis bending plus axial compression (see Figs. 8.8–8.10), thus indicating the need to develop a new fire design approach for stainless steel beam-columns.

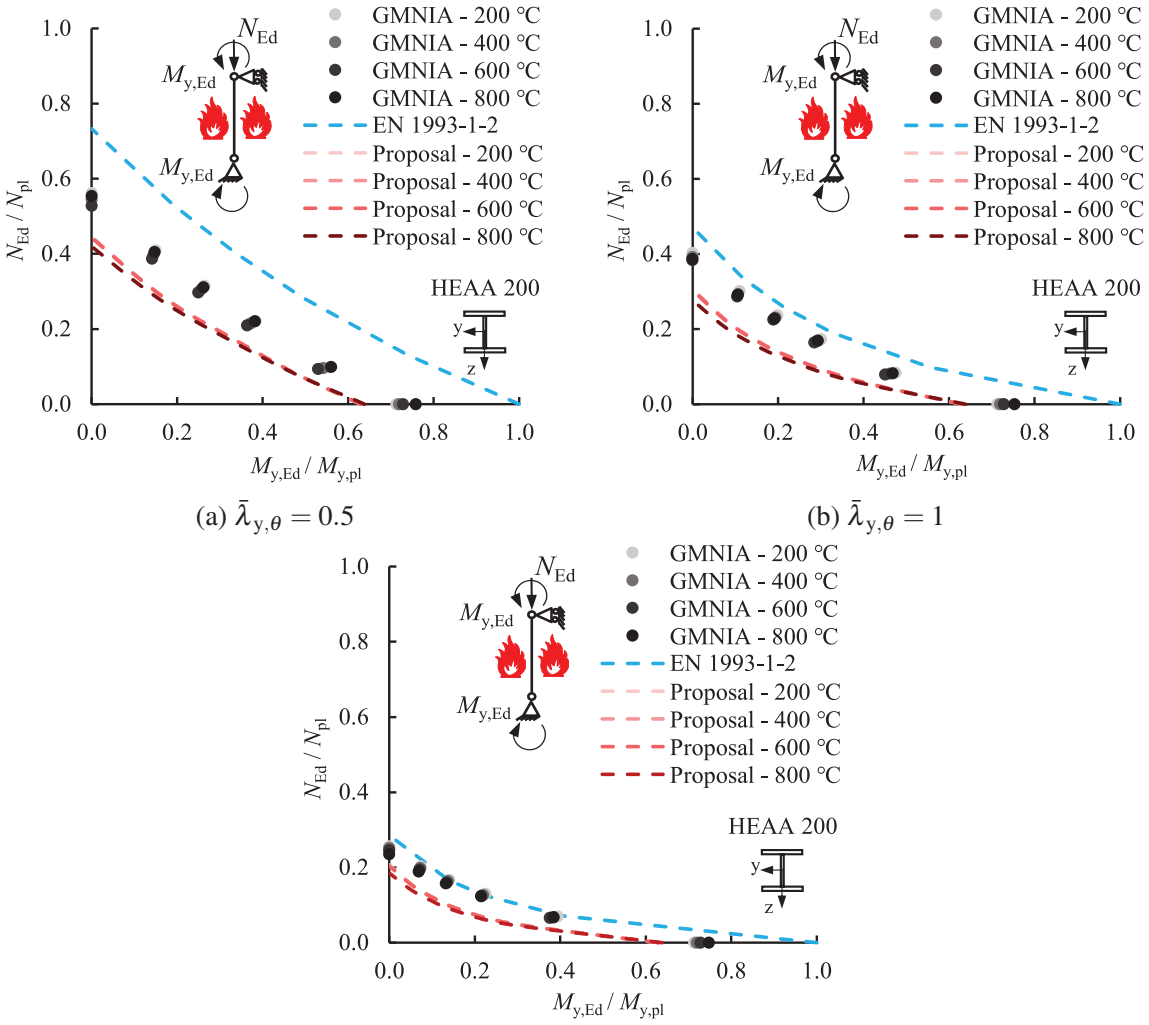

(a) $\bar{\lambda}_{y,\theta} = 0.5$

(b) $\bar{\lambda}_{y,\theta} = 1$

(c) $\bar{\lambda}_{y,\theta} = 1.5$

Figure 8.5: Assessment of EN 1993-1-2 (CEN, 2005) and new proposals for austenitic stainless steel beam-columns under major axis bending plus axial compression

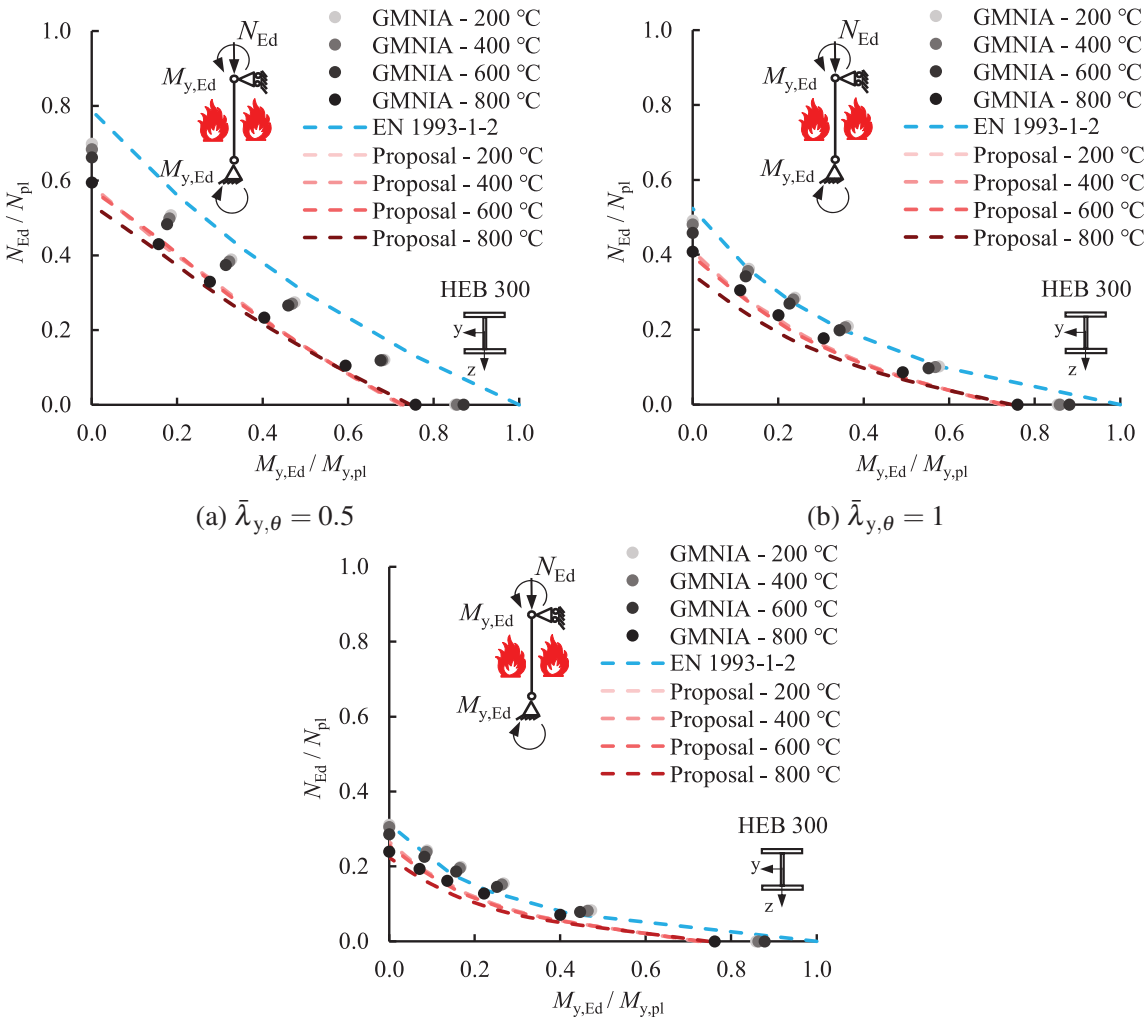

(a) $\bar{\lambda}_{y,\theta} = 0.5$

(b) $\bar{\lambda}_{y,\theta} = 1$

(c) $\bar{\lambda}_{y,\theta} = 1.5$

Figure 8.6: Assessment of EN 1993-1-2 (CEN, 2005) and new proposals for duplex stainless steel beam-columns under major axis bending plus axial compression

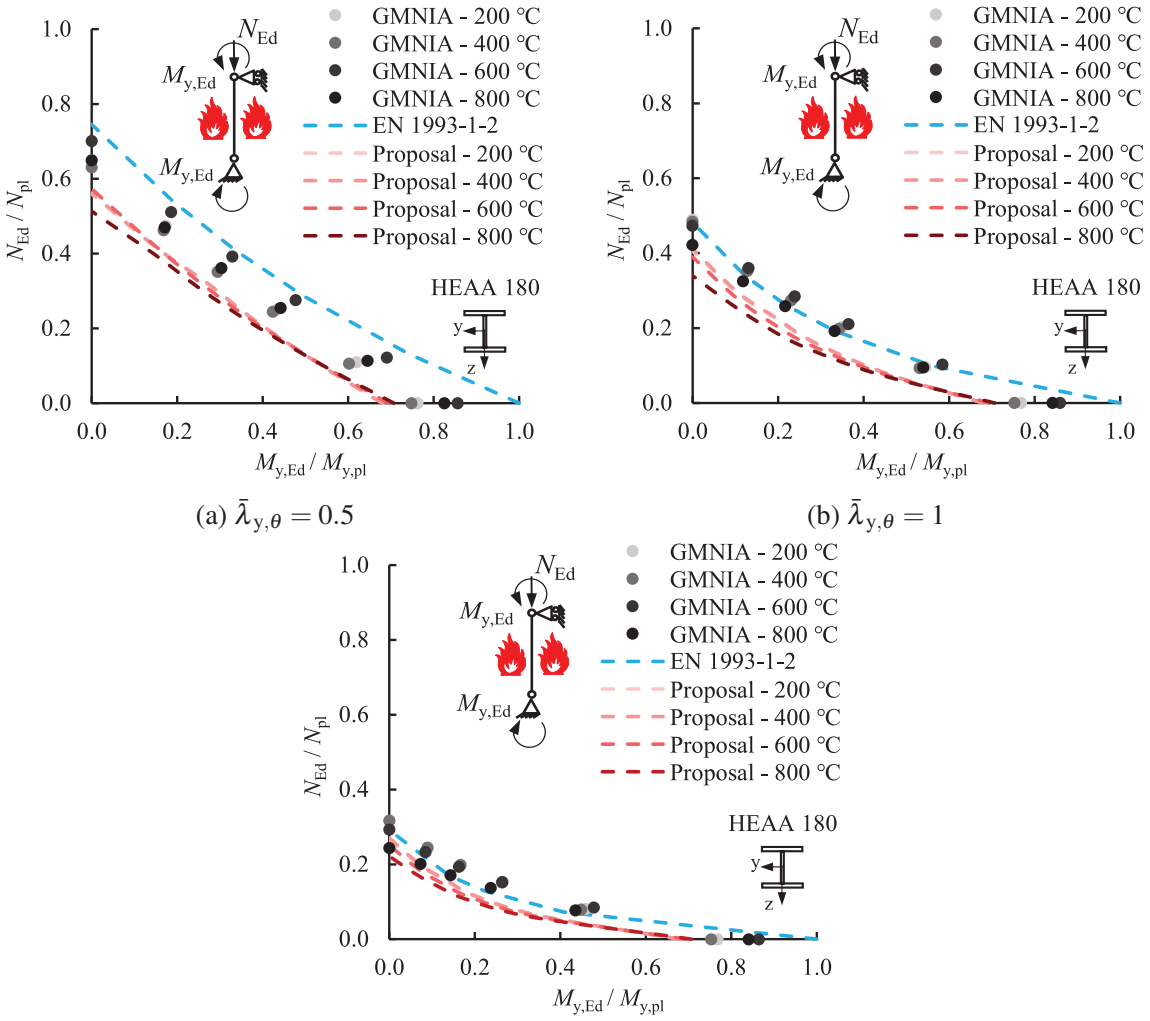

(a) $\bar{\lambda}_{y,\theta} = 0.5$

(b) $\bar{\lambda}_{y,\theta} = 1$

(c) $\bar{\lambda}_{y,\theta} = 1.5$

Figure 8.7: Assessment of EN 1993-1-2 (CEN, 2005) and new proposals for ferritic stainless steel beam-columns under major axis bending plus axial compression

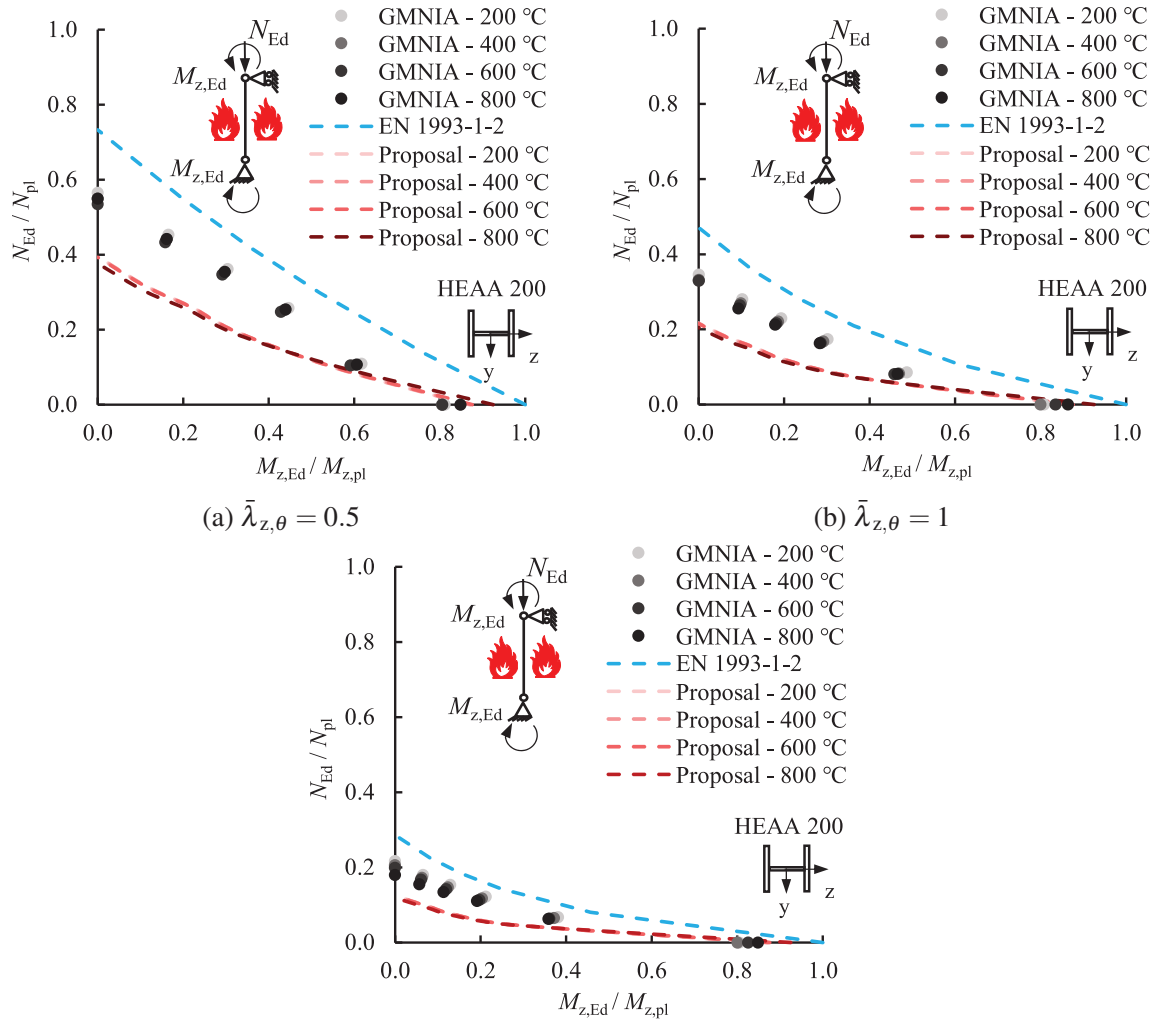

(a) $\bar{\lambda}_{z,\theta} = 0.5$ (b) $\bar{\lambda}_{z,\theta} = 1$

(c) $\bar{\lambda}_{z,\theta} = 1.5$

Figure 8.8: Assessment of EN 1993-1-2 (CEN, 2005) and new proposals for austenitic stainless steel beam-columns under minor axis bending plus axial compression

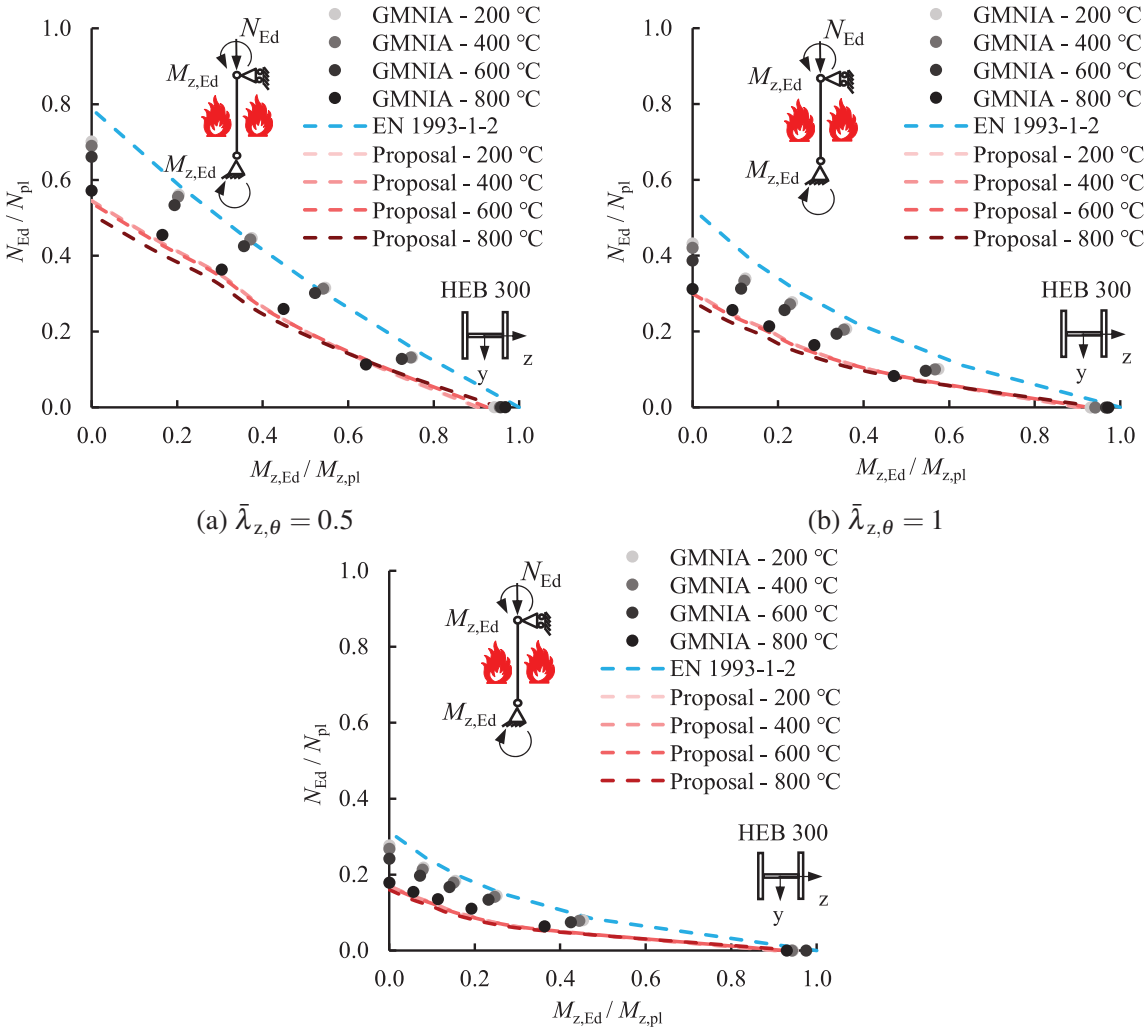

(a) $\bar{\lambda}_{z,\theta} = 0.5$

(b) $\bar{\lambda}_{z,\theta} = 1$

(c) $\bar{\lambda}_{z,\theta} = 1.5$

Figure 8.9: Assessment of EN 1993-1-2 (CEN, 2005) and new proposals for duplex stainless steel beam-columns under minor axis bending plus axial compression

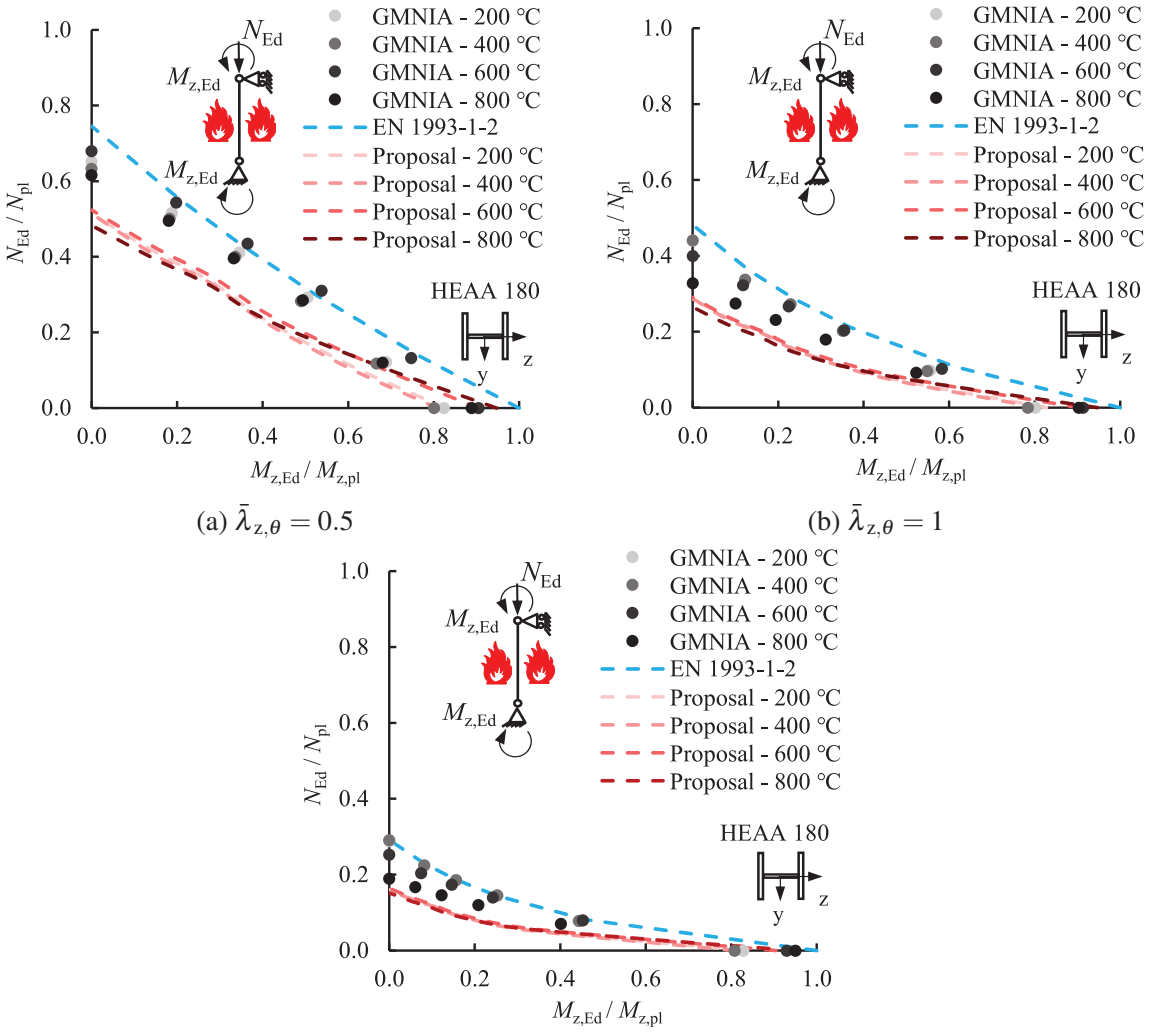

(a) $\bar{\lambda}_{z,\theta} = 0.5$

(b) $\bar{\lambda}_{z,\theta} = 1$

(c) $\bar{\lambda}_{z,\theta} = 1.5$

Figure 8.10: Assessment of EN 1993-1-2 (CEN, 2005) and new proposals for ferritic stainless steel beam-columns under minor axis bending plus axial compression

8.4 Development of new proposals for the design of stainless steel beam-columns in fire

The development of the new fire design rules for stainless steel beam-columns is described in this section. In the development of the proposed design rules, the format used in the beam-column design approach of the upcoming version of the European standard for room temperature structural steel design prEN 1993-1-1 (CEN, 2020) was adopted with the aim of increasing consistency between to two standards. In addition to this, the elevated temperature strength at 2% total strain $f_{2,\theta} = k_{2,\theta} f_y$ was adopted in the new proposals for the design of stainless steel beam-columns in fire with cross-sections falling into all the cross-section classses to ensure consistency with the recently revised fire design rules for carbon steel beam-columns proposed by Couto *et al.* (2016), which will appear in the next version of EN 1993-1-2.

8.4.1 New proposals for the design of stainless steel beam-columns in fire

In the new beam-column design rules proposed in this study, the design buckling resistance of members with non-slender cross-sections subjected to combined axial compression and bending in fire should thus satisfy eqs. (8.11)–(8.12):

$$\frac{N_{\mathrm{fi,Ed}}}{\chi_{\mathrm{y,fi}} A k_{2,\theta} \dfrac{f_{\mathrm{y}}}{\gamma_{\mathrm{M,fi}}}} + k_{\mathrm{yy}} \frac{M_{\mathrm{y,fi,Ed}}}{W_{\mathrm{pl,y}} k_{2,\theta} \dfrac{f_{\mathrm{y}}}{\gamma_{\mathrm{M,fi}}}} + k_{\mathrm{yz}} \frac{M_{\mathrm{z,fi,Ed}}}{W_{\mathrm{pl,z}} k_{2,\theta} \dfrac{f_{\mathrm{y}}}{\gamma_{\mathrm{M,fi}}}} \leq 1, \tag{8.11}$$

$$\frac{N_{\mathrm{fi,Ed}}}{\chi_{\mathrm{z,fi}} A k_{2,\theta} \dfrac{f_{\mathrm{y}}}{\gamma_{\mathrm{M,fi}}}} + k_{\mathrm{zy}} \frac{M_{\mathrm{y,fi,Ed}}}{\chi_{\mathrm{LT,fi}} W_{\mathrm{pl,y}} k_{2,\theta} \dfrac{f_{\mathrm{y}}}{\gamma_{\mathrm{M,fi}}}} + k_{\mathrm{zz}} \frac{M_{\mathrm{z,fi,Ed}}}{W_{\mathrm{pl,z}} k_{2,\theta} \dfrac{f_{\mathrm{y}}}{\gamma_{\mathrm{M,fi}}}} \leq 1. \tag{8.12}$$

For members with slender cross-sections, eqs. (8.13)–(8.14) should be satisfied:

$$\frac{N_{\mathrm{fi,Ed}}}{\chi_{\mathrm{y,fi}} A_{\mathrm{eff}} k_{2,\theta} \dfrac{f_{\mathrm{y}}}{\gamma_{\mathrm{M,fi}}}} + k_{\mathrm{yy}} \frac{M_{\mathrm{y,fi,Ed}} + \triangle M_{\mathrm{y,fi,Ed}}}{W_{\mathrm{eff,y}} k_{2,\theta} \dfrac{f_{\mathrm{y}}}{\gamma_{\mathrm{M,fi}}}} + k_{\mathrm{yz}} \frac{M_{\mathrm{z,fi,Ed}} + \triangle M_{\mathrm{z,fi,Ed}}}{W_{\mathrm{eff,z}} k_{2,\theta} \dfrac{f_{\mathrm{y}}}{\gamma_{\mathrm{M,fi}}}} \leq 1, \tag{8.13}$$

$$\frac{N_{\mathrm{fi,Ed}}}{\chi_{\mathrm{z,fi}} A_{\mathrm{eff}} k_{2,\theta} \dfrac{f_{\mathrm{y}}}{\gamma_{\mathrm{M,fi}}}} + k_{\mathrm{zy}} \frac{M_{\mathrm{y,fi,Ed}} + \triangle M_{\mathrm{y,fi,Ed}}}{\chi_{\mathrm{LT,fi}} W_{\mathrm{eff,y}} k_{2,\theta} \dfrac{f_{\mathrm{y}}}{\gamma_{\mathrm{M,fi}}}} + k_{\mathrm{zz}} \frac{M_{\mathrm{z,fi,Ed}} + \triangle M_{\mathrm{z,fi,Ed}}}{W_{\mathrm{eff,z}} k_{2,\theta} \dfrac{f_{\mathrm{y}}}{\gamma_{\mathrm{M,fi}}}} \leq 1, \tag{8.14}$$

where $\triangle M_{\mathrm{y,fi,Ed}}$ and $\triangle M_{\mathrm{z,fi,Ed}}$ are the moments due to the shift of the centroid of the effective cross-section relative to that of the gross cross-section, $\chi_{\mathrm{y,fi}}$ is the buckling reduction factor considering flexural buckling about the major axis and $\chi_{\mathrm{z,fi}}$ is the minimum of the buckling reduction factors for minor axis flexural buckling, torsional or torsional-flexural buckling; the determination of $\chi_{\mathrm{y,fi}}$ and $\chi_{\mathrm{z,fi}}$ using the newly derived column buckling curves for stainless steel members in fire is described in Chapter 6. Additionally, $\chi_{\mathrm{LT,fi}}$ is the reduction factor for lateral-torsional buckling, which may be taken as $\chi_{\mathrm{LT,fi}} = 1.0$ for beam-columns that are not susceptible (either due to the cross-section shape or the provision of sufficiently closely spaced lateral restraints) to flexural-torsional buckling. It should be emphasised that in the proposed method considered currently the effective section properties A_{eff}, $W_{\mathrm{eff,y}}$ and $W_{\mathrm{eff,z}}$ of the stainless steel beam-columns should be determined on the basis of the new effective width rules established in Chapter 3 and 4 for stainless steel cross-sections in fire.

In eqs. (8.11)–(8.14), k_{yy}, k_{yz}, k_{zy} and k_{zz} are the interaction factors for the design of members with doubly symmetric cross-sections. The interaction factor k_{yy} is calculated as:

$$k_{\mathrm{yy}} = C_{\mathrm{my}} \left[1 + D_{1,\mathrm{y}} \left(\bar{\lambda}_{\mathrm{y},\theta} - D_{2,\mathrm{y}}\right) n_{\mathrm{y}}\right] \quad \text{for } \bar{\lambda}_{\mathrm{y},\theta} < D_{3,\mathrm{y}}, \tag{8.15}$$

$$k_{\mathrm{yy}} = C_{\mathrm{my}} \left[1 + D_{1,\mathrm{y}} \left(D_{1,\mathrm{y}} - D_{3,\mathrm{y}}\right) n_{\mathrm{y}}\right] \quad \text{for } \bar{\lambda}_{\mathrm{y},\theta} \geq D_{3,\mathrm{y}}, \tag{8.16}$$

and the interaction factor k_{zz} is determined as:

$$k_{\mathrm{zz}} = C_{\mathrm{mz}} \left[1 + D_{1,\mathrm{z}} \left(\bar{\lambda}_{\mathrm{z},\theta} - D_{2,\mathrm{z}}\right) n_{\mathrm{z}}\right] \quad \text{for } \bar{\lambda}_{\mathrm{z},\theta} < D_{3,\mathrm{z}}, \tag{8.17}$$

$$k_{\mathrm{zz}} = C_{\mathrm{mz}} \left[1 + D_{1,\mathrm{z}} \left(D_{3,\mathrm{z}} - D_{2,\mathrm{z}}\right) n_{\mathrm{z}}\right] \quad \text{for } \bar{\lambda}_{\mathrm{z},\theta} \geq D_{3,\mathrm{z}}, \tag{8.18}$$

in which the parameters n_y and n_z are calculated using the following equations:

$$n_y = \frac{N_{fi,Ed}}{\chi_{y,fi} A k_{2,\theta} \frac{f_y}{\gamma_{M,fi}}} \quad \text{and} \quad n_z = \frac{N_{fi,Ed}}{\chi_{z,fi} A k_{2,\theta} \frac{f_y}{\gamma_{M,fi}}} \text{ for non-slender sections,} \tag{8.19}$$

$$n_y = \frac{N_{fi,Ed}}{\chi_{y,fi} A_{eff} k_{2,\theta} \frac{f_y}{\gamma_{M,fi}}} \quad \text{and} \quad n_z = \frac{N_{fi,Ed}}{\chi_{z,fi} A_{eff} k_{2,\theta} \frac{f_y}{\gamma_{M,fi}}} \text{ for slender sections.} \tag{8.20}$$

The interaction factors k_{yz} and k_{zy} are determined using the following equations in accordance with prEN 1993-1-1 (CEN, 2020):

$$k_{yz} = k_{zz} \tag{8.21}$$

$$k_{zy} = 0.8 k_{yy}. \tag{8.22}$$

In eqs. (8.15)–(8.16) and eqs. (8.17)–(8.18), D_y and D_z are stainless steel grade–dependent auxiliary coefficients used in the determination of the interaction factors. Following the approach described by Boissonnade *et al.* (2006), these coefficients were determined through the calibration of the proposed interaction factors (i.e. k_{yy} and k_{zz}) against those obtained from the GMNIA of the stainless steel beam-column finite element models. The interaction factors from the GMNIA of the finite element models k_{FE} were determined considering a re-arrangement of the interaction formulae given by eq. (8.11)–(8.12) and eq. (8.13)–(8.14) as:

$$k_{FE} = (1 - n) \frac{M_{fi,\theta,Rd}}{M_{fi,Ed}} \quad \text{where} \quad n = \frac{N_{fi,Ed}}{N_{b,fi,\theta,Rd}}. \tag{8.23}$$

In eq. (8.23), $N_{b,fi,\theta,Rd}$ is the flexural buckling resistance and $M_{fi,\theta,Rd}$ is the bending moment resistance of the beam-column about the axis of applied bending $M_{fi,Ed}$. The calibration of k_{yy} and k_{zz} of the new proposals (i.e. $k_{yy,prop}$ and $k_{zz,prop}$) against the k_{FE} values determined through the GMNIA of austenitic, duplex and ferritic stainless steel beam-columns with a European HEM 100 cross-section is shown in Figs. 8.11–8.16. Note that in Figs. 8.11–8.16, the flexural buckling resistances of the beam-columns $N_{b,fi,\theta,Rd}$ obtained from GMNIA are used. The calibrated values

of the auxiliary coefficients D_y and D_z are provided in Table 8.3. Note that in eqs. (8.15)–(8.18), C_{my} and C_{mz} are the equivalent uniform moment factors defined in prEN 1993-1-1 (CEN, 2020), which are equal to unity for beam-columns under uniform bending moment.

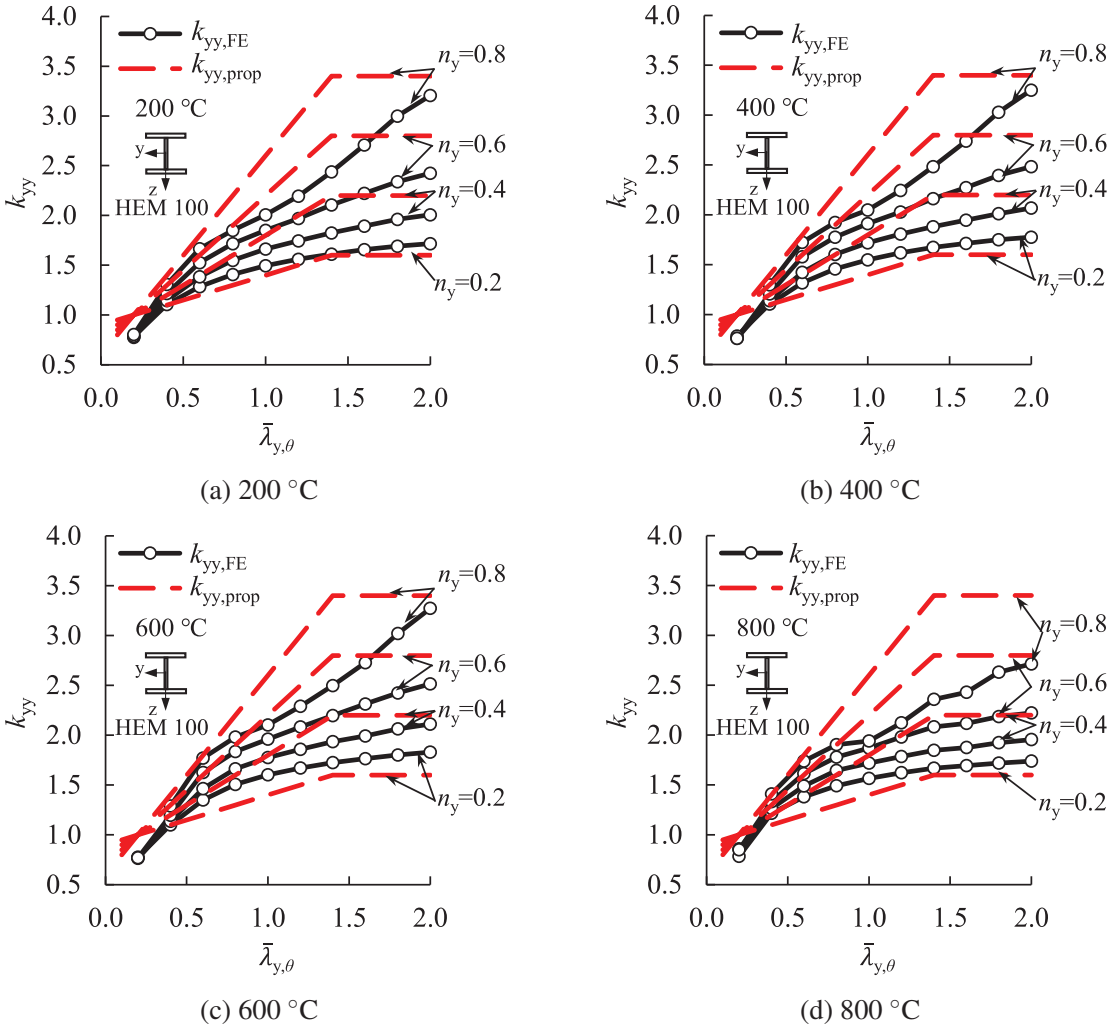

(a) 200 °C (b) 400 °C

(c) 600 °C (d) 800 °C

Figure 8.11: Calibration of interaction factors k_{yy} for austenitic stainless steel beam-columns in fire

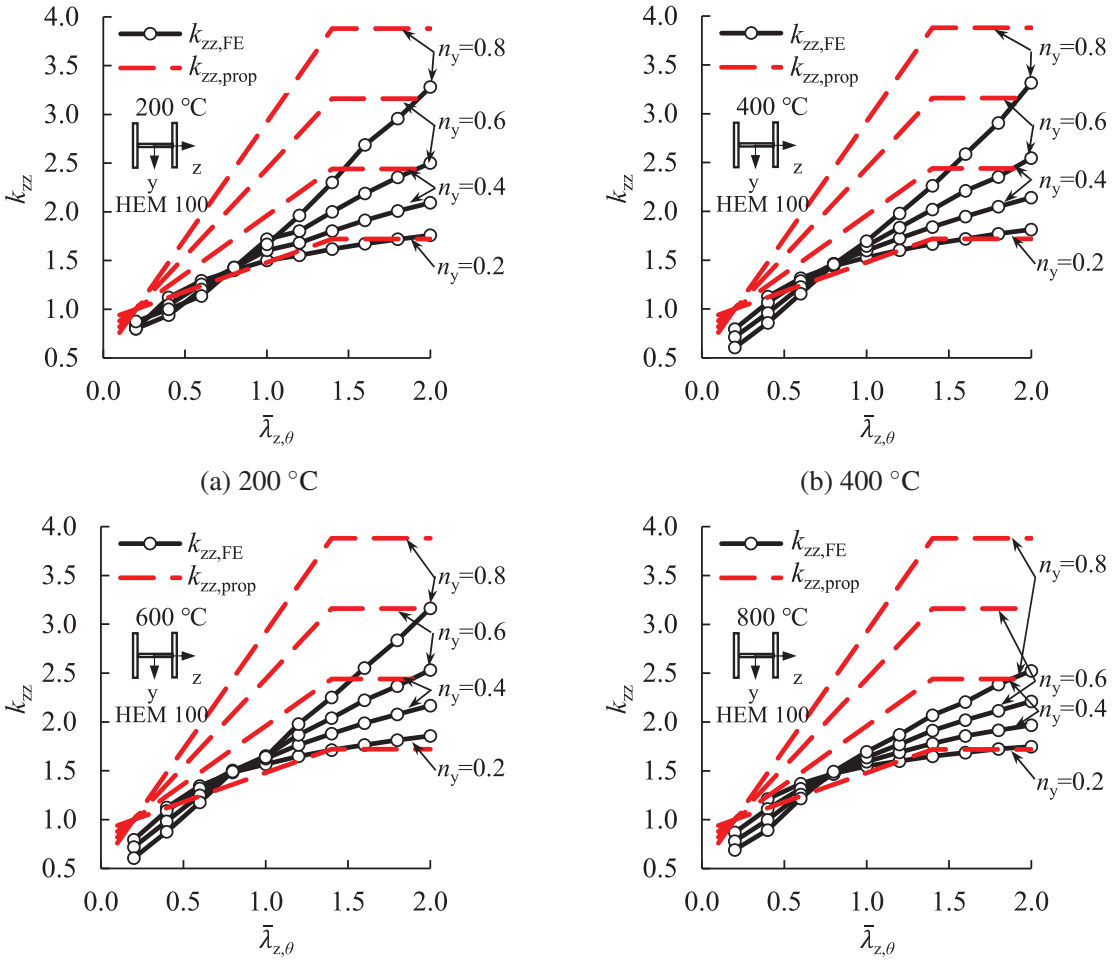

(a) 200 °C (b) 400 °C

(c) 600 °C (d) 800 °C

Figure 8.12: Calibration of interaction factors k_{zz} for austenitic stainless steel beam-columns in fire

Table 8.3: Proposed values of auxiliary coefficients D_y and D_z

Coefficient	Austenitic	Duplex and Ferritic
$D_{1,y}$	2.5	2.0
$D_{2,y}$	0.2	0.3
$D_{3,y}$	1.4	1.6
$D_{1,z}$	3.0	2.5
$D_{2,z}$	0.2	0.4
$D_{3,z}$	1.4	1.8

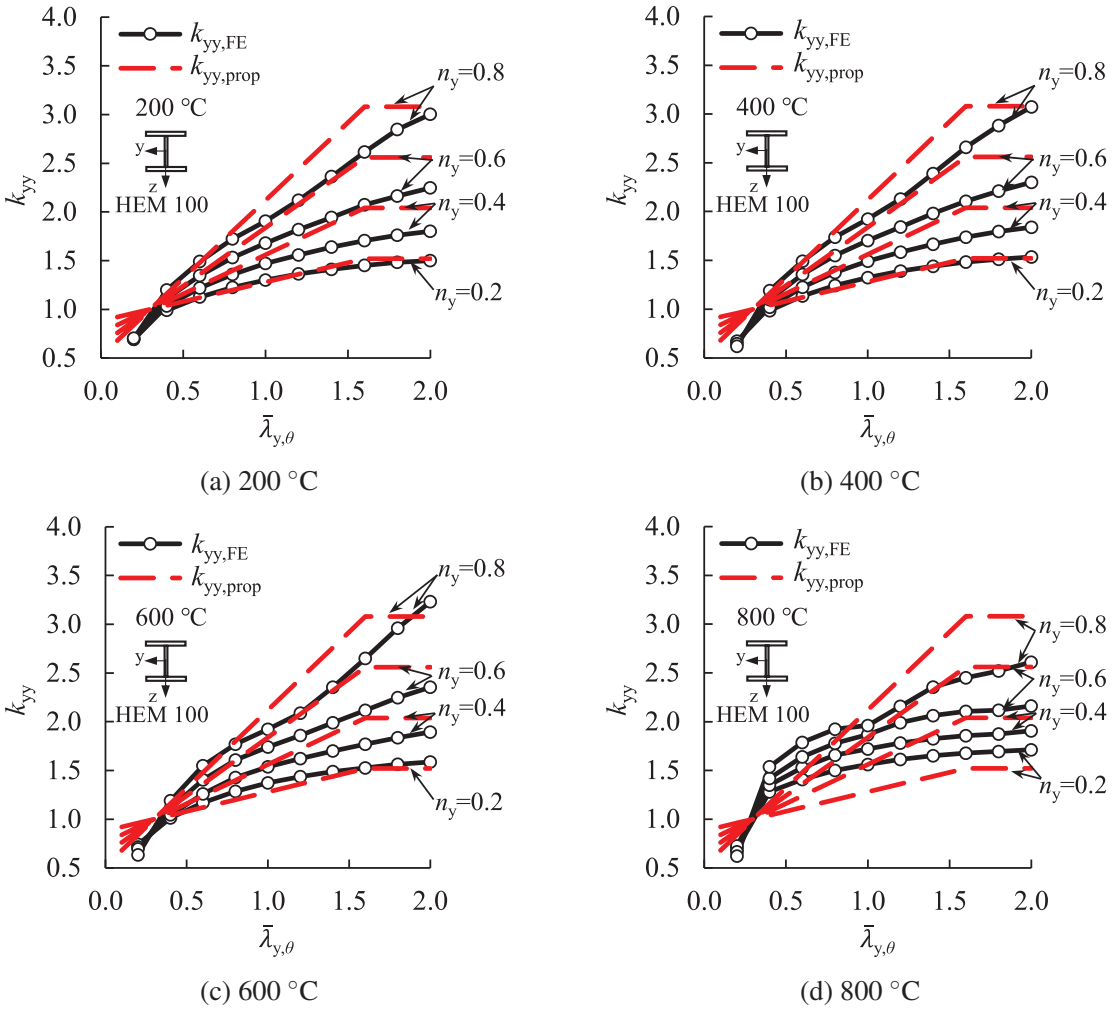

(a) 200 °C (b) 400 °C

(c) 600 °C (d) 800 °C

Figure 8.13: Calibration of interaction factors k_{yy} for duplex stainless steel beam-columns in fire

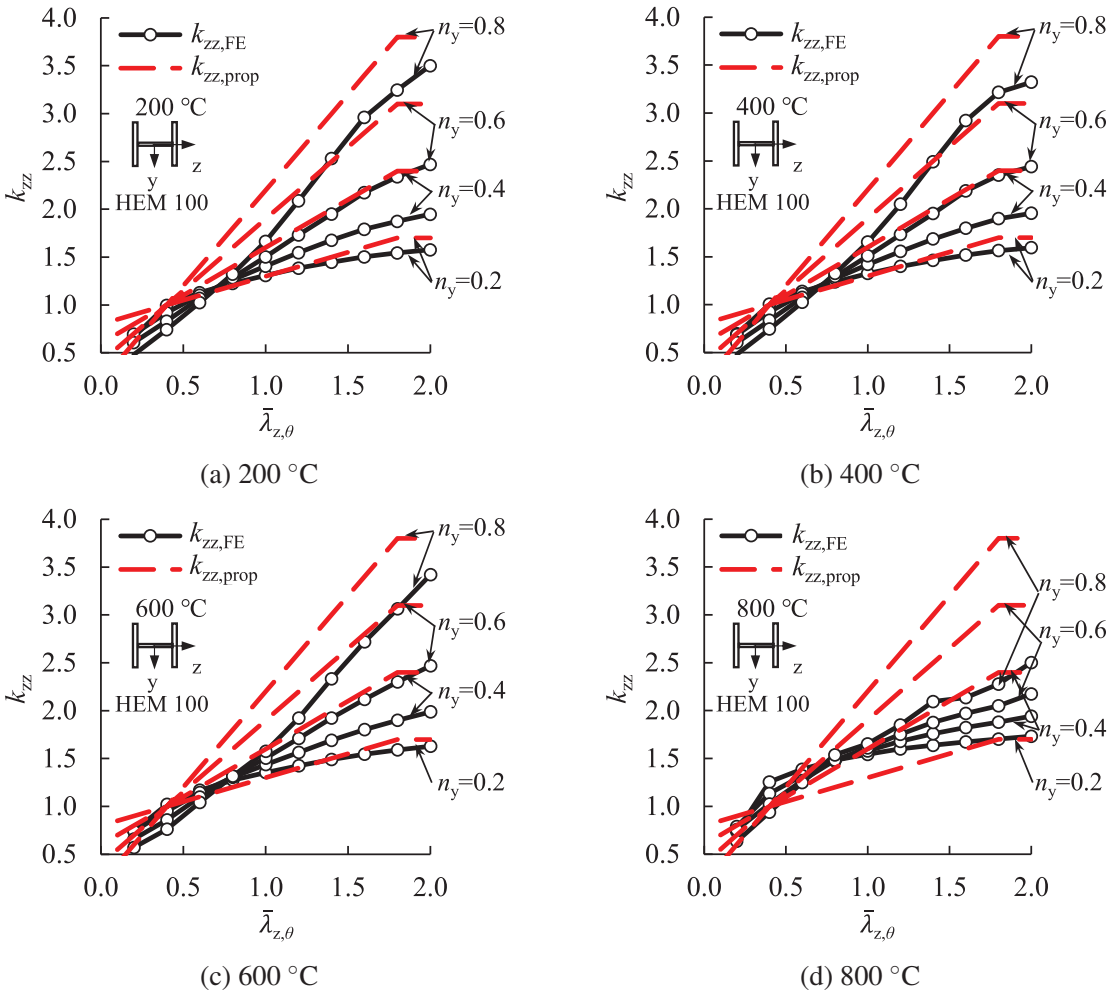

Figure 8.14: Calibration of interaction factors k_{zz} for duplex stainless steel beam-columns in fire

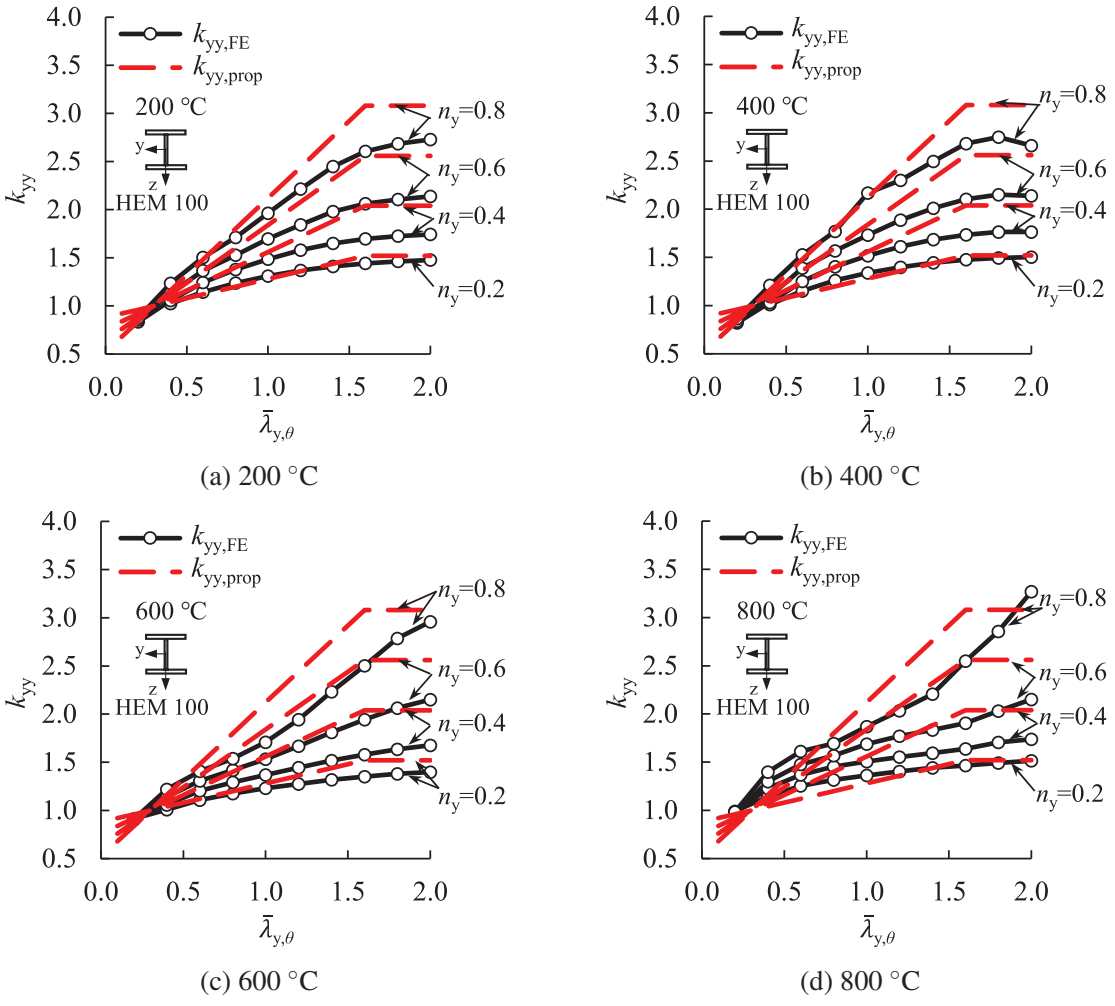

Figure 8.15: Calibration of interaction factors k_{yy} for ferritic stainless steel beam-columns in fire

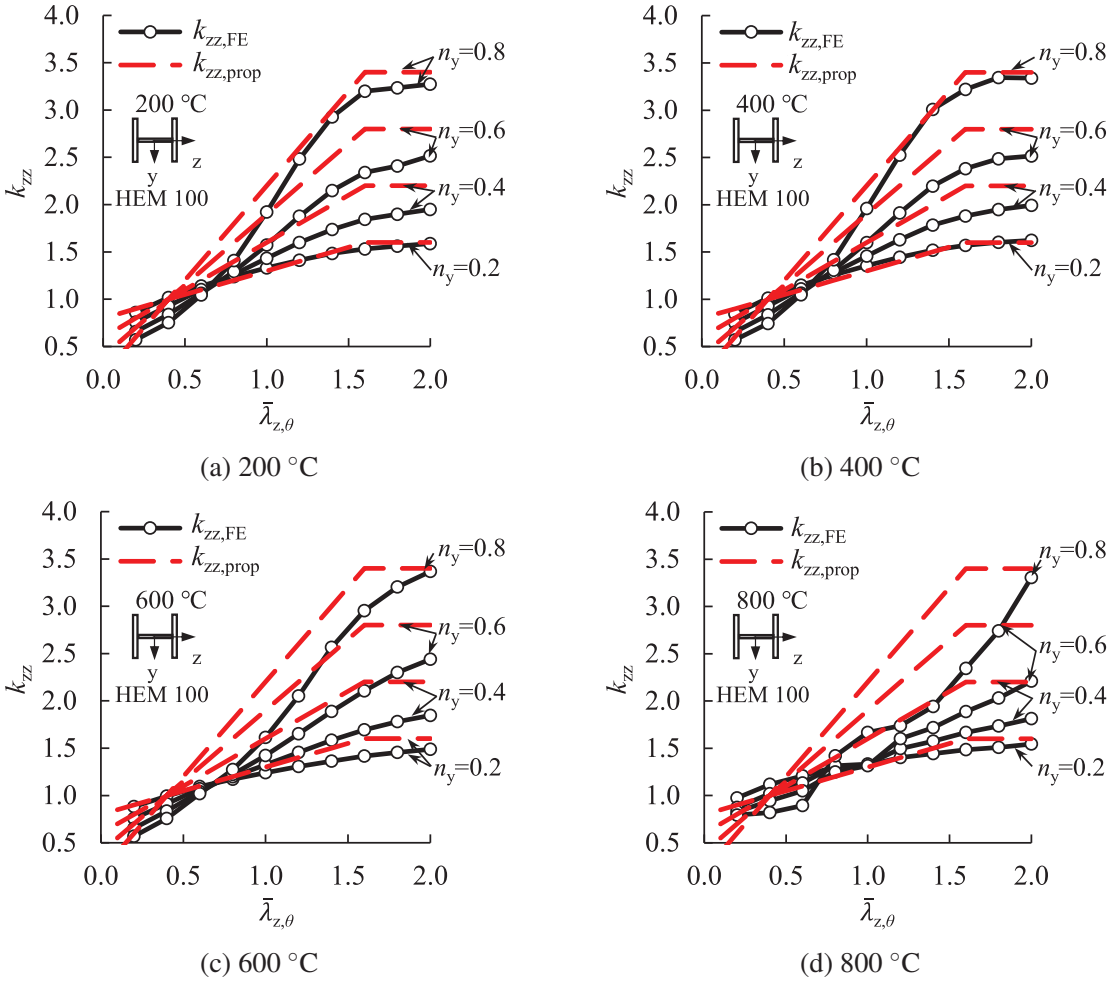

(a) 200 °C (b) 400 °C

(c) 600 °C (d) 800 °C

Figure 8.16: Calibration of interaction factors k_{zz} for ferritic stainless steel beam-columns in fire

8.4.2 Assessment of accuracy and reliability of new proposals

In this subsection, the accuracy of the new stainless steel beam-column fire design proposals is assessed against the numerical data from the nonlinear finite element modelling, considering the broad range of cases summarised in Table 8.2. Figs. 8.5–8.10 show the accuracy of the new proposals against the GMNIA results for I-section beam-columns equivalent to a European HEAA 200 profile for the austenitic stainless steel members, an HEB 300 section for the duplex stainless steel members and an HEAA 180 section for the ferritic stainless steel members; the level of the accuracy of the current EN 1993-1-2 (CEN, 2005) beam-column design rules is also illustrated in the figures. As can be seen from Figs. 8.5–8.10, the new proposals lead to significantly more accurate and safe-sided ultimate strength predictions for stainless steel beam-columns in fire relative to the current EN 1993-1-2 (CEN, 2005) beam-column design rules.

The accuracy of the new proposals is also assessed by comparing the numerical failure loads N_{u} to the predicted resistances $N_{\mathrm{u,pred}}$ for different radial angles ϕ, considering the broad range of parameters provided in Table 8.2. As shown in Fig. 8.3, if the ratio of N_{u} to $N_{\mathrm{u,pred}}$ is greater than or equal to unity (i.e. $N_{\mathrm{u}}/N_{\mathrm{u,pred}} \geq 1.0$), the predicted design resistance $N_{\mathrm{u,pred}}$ is on the safe side. The predicted resistances $N_{\mathrm{u,pred}}$ are obtained by assuming that the beam-columns are subjected to proportional loading in accordance with the procedure reported in (Zhao *et al.*, 2015b; Bu & Gardner, 2019; Yang *et al.*, 2019). The accuracy of the new proposals is assessed in Fig. 8.17 for the stainless steel beam-columns under major axis bending plus axial compression and in Fig. 8.18 for the stainless steel beam-columns under minor axis bending plus axial compression; an assessment of the EN 1993-1-2 (CEN, 2005) beam-column design rules is also provided for comparison in Figs. 8.17–8.18. As can be seen from the figures, the new proposals lead to significantly enhanced accuracy with a lower level of scatter relative to the existing EN 1993-1-2 (CEN, 2005) rules for the design of stainless steel I-section beam-columns in fire.

A statistical appraisal of the accuracy of the new proposals is provided in Table 8.4. In the table, $\varepsilon_{\mathrm{av}}$, $\varepsilon_{\mathrm{COV}}$, $\varepsilon_{\mathrm{max}}$ and $\varepsilon_{\mathrm{min}}$ are the mean value, coefficient of variation (COV), maximum value and

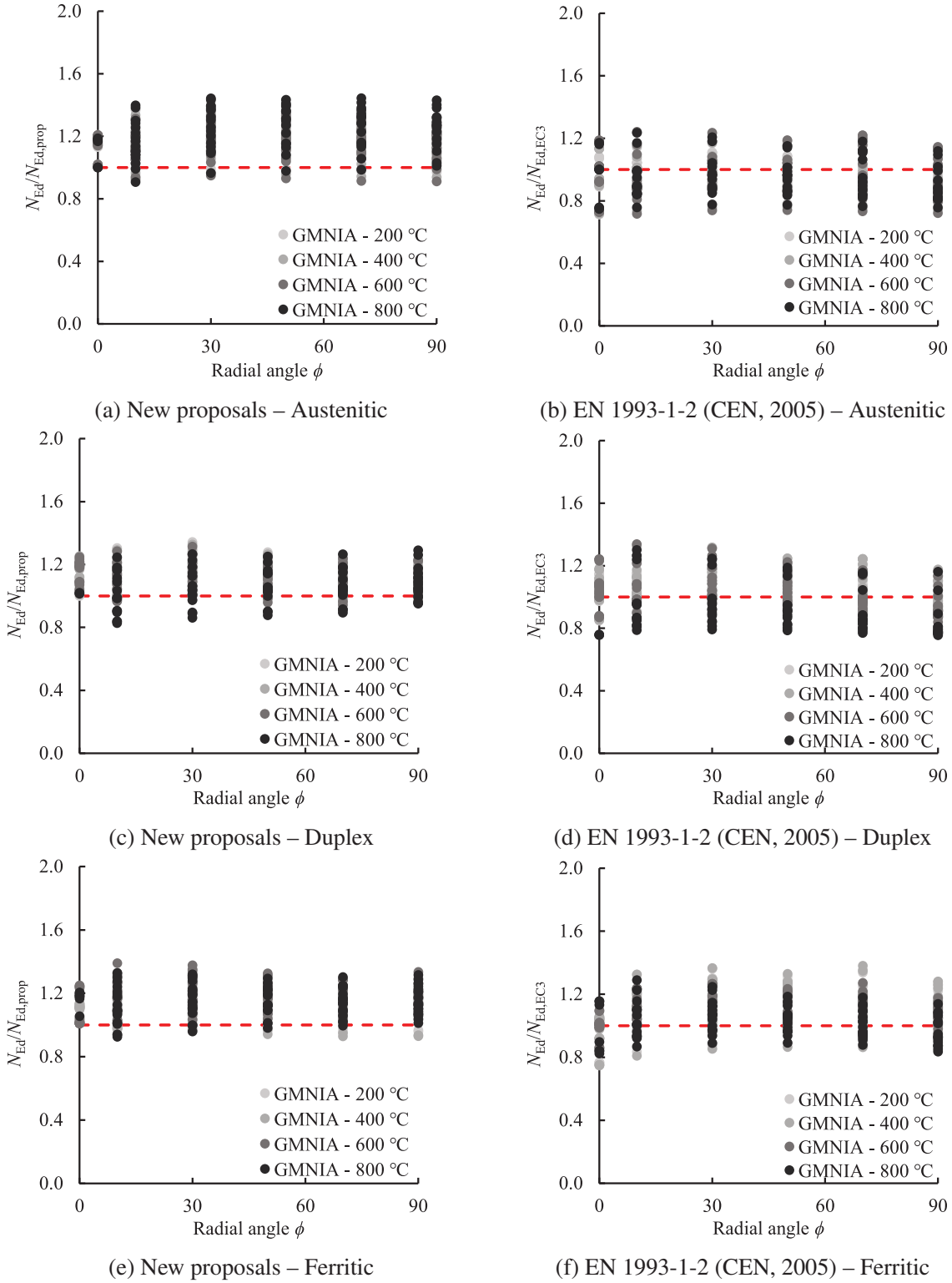

(a) New proposals – Austenitic

(b) EN 1993-1-2 (CEN, 2005) – Austenitic

(c) New proposals – Duplex

(d) EN 1993-1-2 (CEN, 2005) – Duplex

(e) New proposals – Ferritic

(f) EN 1993-1-2 (CEN, 2005) – Ferritic

Figure 8.17: Comparison of accuracy of new proposals against FE results relative to EN 1993-1-2 (CEN, 2005) for stainless steel beam-columns under major axis bending plus axial compression in fire

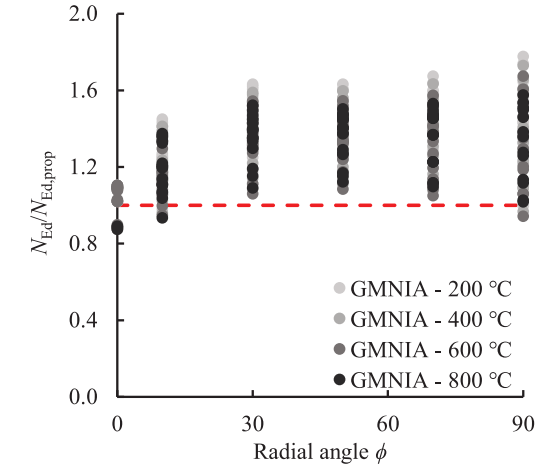

(a) New proposals – Austenitic

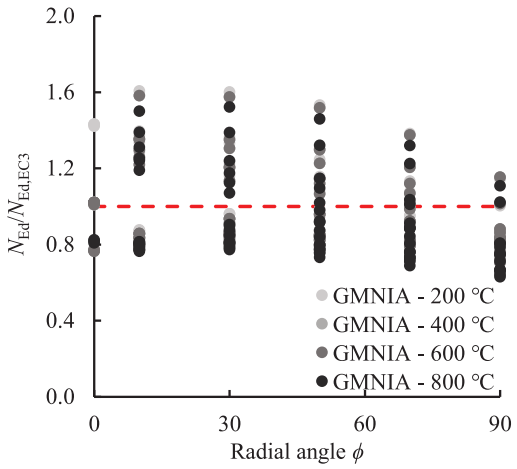

(b) EN 1993-1-2 (CEN, 2005) – Austenitic

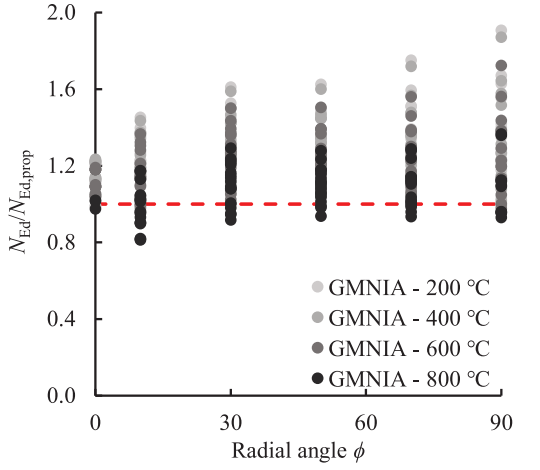

(c) New proposals – Duplex

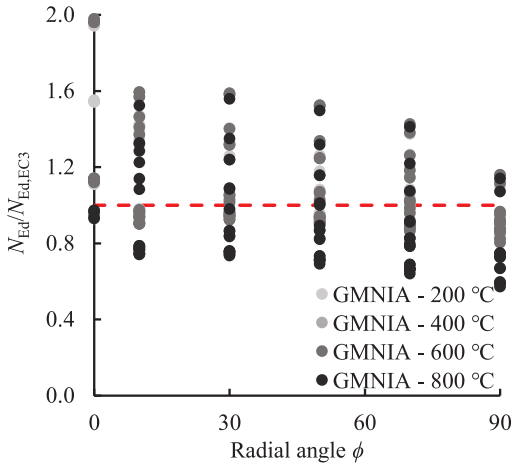

(d) EN 1993-1-2 (CEN, 2005) – Duplex

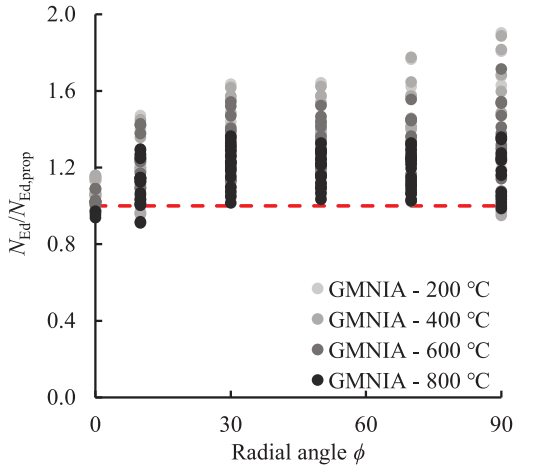

(e) New proposals – Ferritic

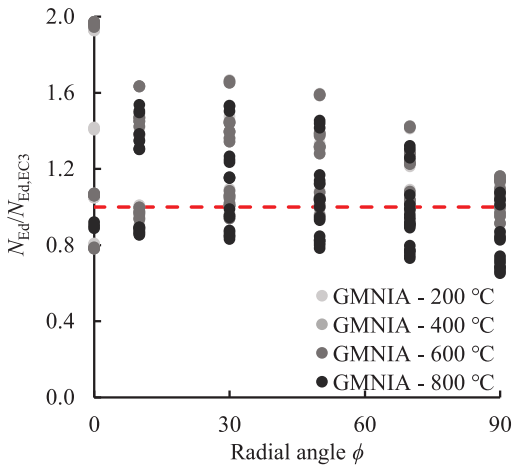

(f) EN 1993-1-2 (CEN, 2005) – Ferritic

Figure 8.18: Comparison of accuracy of new proposals against FE results relative to EN 1993-1-2 (CEN, 2005) for stainless steel beam-columns under minor axis bending plus axial compression in fire

minimum value, respectively, of the ratios of the ultimate resistances obtained from the finite element modelling to the corresponding predictions from the design methods i.e. $\varepsilon = N_{\mathrm{u}}/N_{\mathrm{u,pred}}$. As can be seen from Table 8.4, the new proposals lead to accurate and safe-sided ultimate strength predictions for all the considered stainless steel beam-columns with low $\varepsilon_{\mathrm{COV}}$ values, while the current EN 1993-1-2 (CEN, 2005) design rules generally result in unsafe strength predictions with high $\varepsilon_{\mathrm{COV}}$ values, thus demonstrating the increased level of accuracy achieved through the new design proposals.

Table 8.4: Assessment of new proposals against FE results relative to EN 1993-1-2 (CEN, 2005) for stainless steel beam-columns in fire

Loading condition	Design method	Grade	$\varepsilon_{\mathrm{av}}$	$\varepsilon_{\mathrm{COV}}$	$\varepsilon_{\mathrm{max}}$	$\varepsilon_{\mathrm{min}}$
Major axis bending plus axial compression	New proposal	Austenitic	1.19	0.10	1.44	0.91
		Duplex	1.12	0.09	1.34	0.83
		Ferritic	1.15	0.08	1.39	0.93
	EN 1993-1-2	Austenitic	0.96	0.13	1.24	0.71
		Duplex	1.02	0.12	1.34	0.76
		Ferritic	1.08	0.11	1.38	0.75
Minor axis bending plus axial compression	New proposal	Austenitic	1.30	0.15	1.78	0.87
		Duplex	1.20	0.14	1.91	0.81
		Ferritic	1.23	0.15	1.90	0.90
	EN 1993-1-2	Austenitic	0.97	0.27	2.06	0.63
		Duplex	1.04	0.26	1.98	0.57
		Ferritic	1.17	0.25	1.97	0.65

Finally, in Table 8.5, the reliability of the new proposals is assessed on the basis of the three fire design reliability criteria put forward by Kruppa (1999). The reliability of the EN 1993-1-2 (CEN, 2005) beam-column design rules is also assessed in Table 8.5. Note that in the table, a number denoted by '*' indicates the cases for which the reliability criteria are not satisfied. As can be seen from Table 8.5, the new beam-column design proposals generally satisfy the reliability criteria of Kruppa (1999), confirming their suitability for inclusion in the upcoming revision to EN 1993-1-2, while the current EN 1993-1-2 (CEN, 2005) beam-column design rules fail to satisfy the criteria in a high number of cases.

Table 8.5: Reliability assessment of new proposals against FE results relative to EN 1993-1-2 (CEN, 2005) for stainless steel beam-columns in fire

Loading condition	Design method	Grade	Criterion 1	Criterion 2	Criterion 3
Major axis bending plus axial compression	New proposal	Austenitic	0.00	6.98	-0.15
		Duplex	0.01*	11.82	-10.03
		Ferritic	0.00	6.73	-12.05
	EN 1993-1-2	Austenitic	21.20*	62.34*	0.05*
		Duplex	13.14*	44.04*	-0.79
		Ferritic	5.05*	23.56*	-0.06
Minor axis bending plus axial compression	New proposal	Austenitic	0.00	5.81	-21.04
		Duplex	0.74*	11.08	-15.28
		Ferritic	0.00	7.78	-16.76
	EN 1993-1-2	Austenitic	51.26*	65.66*	8.62*
		Duplex	22.66*	58.87*	1.33*
		Ferritic	9.43*	34.67*	-9.55

8.5 Conclusions

A new design method for stainless steel beam-columns in fire has been developed in this chapter. Finite element models able to replicate the structural behaviour of stainless steel I-section beam-columns at elevated temperatures were created and validated against experimental data. Parametric studies were subsequently performed by carrying out the Geometrically and Materially Nonlinear Analyses with Imperfections (GMNIA) using the validated finite element models, in which a wide range of stainelss steel grades, cross-section geometries, elevated temperature levels and slendernesses were considered. Using the obtained GMNIA results, the shortcomings of the current EN 1993-1-2 (CEN, 2005) were revealed, highlighting the need for the development of improved fire design rules for stainless steel beam-columns. New beam-column design rules were derived, adopting the format used in the beam-column design equations of the upcoming European standard for room temperature structural steel design prEN1993-1-1 (CEN, 2020) to achieve consistency between room temperature and fire design rules for beam-columns. The accuracy of the proposed beam-column design rules was assessed against the GMNIA results. It was shown that the new beam-column design rules provided more consistent and safe-sided resistance predictions than the existing EN 1993-1-2 (CEN, 2005) design rules, and generally

satisfied the fire design reliability criteria of Kruppa (1999), confirming their suitability for inclusion in the upcoming revision to EN 1993-1-2.

Chapter 9

Conclusions and suggestions for future research

The key research findings and principal conclusions reached in this thesis are summarised in this chapter. Recommendations for future research, building on that carried out in this thesis, are also presented thereafter.

9.1 Conclusions

Fire resistant design is a key aspect of structural engineering. Metallic structures can be vulnerable to the effects of fire, especially if unprotected, owing to their rapid temperature development, which leads to the degradation of the strength and stiffness of the material. Stainless steel exhibits better strength and stiffness retention at elevated temperatures and is hence better suited to use in structures at risk of exposure to fire relative to carbon steel. With the increasing use of stainless steel structural members in construction and the offshore industry, the need for comprehensive and efficient fire design rules is clear. In this thesis, experimental and numerical studies into the behaviour of stainless steel structures at elevated temperatures were conducted.

New design methods for stainless steel structures in fire were also proposed and assessed in this thesis; incorporation of the proposed design methods into future revisions of EN 1993-1-2 is recommended.

The local buckling response of stainless steel plates at elevated temperatures was investigated in Chapter 3. Since the existing design provisions of EN 1993-1-2 (CEN, 2005) lead to inaccurate ultimate strength predictions in fire, a new effective width-based design approach able to reflect the variation in strength and stiffness of stainless steel at different temperature levels in the determination of the local plate slenderness and thereby the ultimate resistances of stainless steel plates in fire was put forward. It was found that the new effective width-based method leads to more accurate and reliable ultimate strength predictions relative to the current design rules of EN 1993-1-2 (CEN, 2005) as assessed against results obtained from finite element models of stainless steel plates of different grades for a range of elevated temperature levels, loading conditions, boundary conditions and local slendernesses. A new cross-section classification approach was also introduced in Chapter 3 for stainless steel cross-sections in fire, in which two classes, referred to as 'non-slender' and 'slender', were adopted.

The cross-section behaviour of stainless steel I-sections in fire was investigated in Chapter 4. Finite element models of stainless steel I-sections were created and validated against a series of test results from the literature. Parametric studies were then carried out to generate extensive structural performance data covering different cross-section geometries, stainless steel grades, elevated temperature levels and loading conditions. The design methods proposed in Chapter 3 were subsequently assessed against the numerical data, from which the design methods of Chapter 3 were shown to provide enhanced accuracy in the ultimate strength predictions of stainless steel I-sections under compression and major axis bending in fire relative to the current EN 1993-1-2 (CEN, 2005) design rules. The plastic effective width method of Bambach & Rasmussen (2004), in conjunction with the modified plate slenderness proposed in Chapter 3, was recommended for the design of stainless steel I-sections under minor axis bending in fire thus allowing for the inelastic behaviour of the outstand flanges under stress gradients within stainless steel I-sections.

The flexural buckling behaviour of stainless steel columns in fire was investigated in Chapters 5 and 6. In Chapter 5, an experimental study on grade 1.4301 austenitic stainless steel I-section columns in fire was presented, in which eight anisothermal fire tests, covering two cross-section profiles, two column buckling lengths and four axial load ratios n_r equal to 0.3, 0.4, 0.5 and 0.6, were conducted. The obtained experimental results were then utilised to validate the finite element models of stainless steel columns in fire in Chapter 6. Based upon the validated models, new design methods for the flexural buckling assessment of stainless steel I-section columns in fire, compatible with the existing design methods for carbon steel columns given in EN 1993-1-2 (CEN, 2005), were developed and calibrated. The accuracy and reliability of the new proposals were assessed against the numerical data, which showed that the new proposals provide accurate and safe ultimate strength predictions for stainless steel columns in fire.

The behaviour and design of stainless steel beam-columns in fire were investigated in Chapters 7 and 8. Chapter 7 presented an experimental study on the structural behaviour stainless steel beam-columns at elevated temperatures, in which six fire tests were conducted anisothermally on grade 1.4301 austenitic stainless steel I-section beam-columns. Two initial loading eccentricity values e_0 equal to 10 mm and 30 mm and three load ratios n_r equal to 0.4, 0.5 and 0.6 were taken into account to achieve a spectrum of bending moment-to-axial load ratios and failure temperatures. In Chapter 8, shell finite element models, capable of replicating the response of stainless steel I-section beam-columns at elevated temperatures, were created, validated and utilized to generate extensive numerical structural performance data. Improved fire design rules for stainless steel beam-columns were subsequently proposed and assessed against numerical data. It was observed that the new proposals lead to accurate and safe estimations of the ultimate strength of stainless steel beam-columns in fire. The proposed design rules established in this thesis are due to be incorporated into the next revision of EN 1993-1-2.

9.2 Suggestions for future research

Although the research findings of this thesis have provided insights into the behaviour and design of stainless steel structures in fire, to comprehensively understand their behaviour at elevated temperatures, more research studies are still required and therefore suggestions for possible future research are given in this section.

Chapter 2 of this thesis has given the design methods for the local buckling assessment of internal elements and outstand flanges; however, the local buckling of stainless steel circular hollow sections and elliptical hollow sections in fire has not yet been studied, although they are widely used for exposed structural elements owing to their efficiency and aesthetic appearance. Therefore, to fill this gap, new proposals for local buckling assessment of circular hollow sections and elliptical hollow sections in fire should be established with systematic consideration of the full range of contributing parameters in future research studies.

To understand better the structural behaviour of stainless steel components in fire, more cross-section and member level tests are required. More specifically, at the cross-section level, since there are only six stub column tests on rectangular hollow sections (Uppfeldt *et al.*, 2008) and four beam tests on rectangular hollow sections and I-sections (Gardner & Baddoo, 2006), it is recommended that experimental studies on (i) rectangular hollow sections under combined loading, (ii) I-sections under compression and combined loading and (iii) circular/elliptical hollow sections, angle sections and channel sections under compression, bending and combined loading should be carried out. At the member level, major axis flexural buckling tests of stainless steel I-section columns and beam-columns are suggested since no such experiments have been performed to date. Additionally, the structural behaviour of stainless steel columns and beam-columns with circular/elliptical hollow sections, angle sections and channel sections in fire also requires further experimental investigations.

Finally, the suitability of column design methods and beam-column design methods proposed in this study for the prediction of ultimate strength of stainless steel components with circu-

lar/elliptical hollow sections, angle sections and channel sections should be assessed in future research. Extension of the continuous strength method from room temperature to elevated temperature design is also recommended.

References

ABAQUS. 2014. *ABAQUS/Standard user's manual volumes I-III and ABAQUS CAE manual*. Dassault Systemes Simulia Corporation.

Abdella, K. 2009. Explicit full-range stress–strain relations for stainless steel at high temperatures. *Journal of Constructional Steel Research*, **65**(4), 794–800.

Afshan, S., Gardner, L., & Baddoo, N. 2013. Buckling response of ferritic stainless steel columns at elevated temperatures. *Research and Applications in Structural Engineering, Mechanics and Computation*, 1471–1476.

Afshan, S., Zhao, O., & Gardner, L. 2019. Standardised material properties for numerical parametric studies of stainless steel structures and buckling curves for tubular columns. *Journal of Constructional Steel Research*, **152**, 2–11.

Afshan, Sheida. 2013. *Structural behaviour of cold-formed stainless steel tubular members*. Ph.D. thesis, Imperial College London UK.

Ala-Outinen, T. 1999. Fire resistance of stainless steel structures. *Proceedings of Second European Conference on Steel Structures (Eurosteel 1999)*, 165–168.

Ala-Outinen, T., & Oksanen, T. 1997. *Stainless steel compression members exposed to fire*. VTT Technical Research Centre of Finland.

Albrifkani, S., & Wang, Y. 2020. Behaviour of axially and rotationally restrained reinforced concrete beams in fire. *Engineering Structures*, **213**, 110572.

Arrayago, I., Real, E., & Gardner, L. 2015. Description of stress-strain curves for stainless steel alloys. *Materials & Design*, **87**, 540–552.

Ashraf, M., Gardner, L., & Nethercot, D. A. 2006. Finite element modelling of structural stainless steel cross-sections. *Thin-Walled Structures*, **44**(10), 1048–1062.

Ayrton, W., & Perry, J. 1886. On struts. *The Engineer*, **62**, 464–465.

Baddoo, N. 2013. 100 years of stainless steel: A review of structural applications and the development of design rules. *SESOC Journal*, **26**(2), 17–27.

Baddoo, N., Burgan, R., & Ogden, R. 1997. *Architects' guide to stainless steel*. The Steel Construction Institute.

Bambach, M. R., & Rasmussen, K. J. R. 2004. Effective widths of unstiffened elements with stress gradient. *Journal of Structural Engineering*, **130**(10), 1611–1619.

Bihina, G., Zhao, B., & Bouchaïr, A. 2013. Behaviour of composite steel–concrete cellular beams in fire. *Engineering Structures*, **56**, 2217–2228.

Boissonnade, N, Greiner, R, Jaspart, Jean-Pierre, & Lindner, J. 2006. Rules for Member Stability in EN 1993-1-1: Background documentation and design guidelines. ECCS European Convention for Constructional Steelwork.

Bu, Y., & Gardner, L. 2019. Laser-welded stainless steel I-section beam-columns: Testing, simulation and design. *Engineering Structures*, **179**, 23–36.

Cai, Y., & Young, B. 2014. Behavior of cold-formed stainless steel single shear bolted connections at elevated temperatures. *Thin-Walled Structures*, **75**, 63–75.

Cai, Y., & Young, B. 2016. Bearing factors of cold-formed stainless steel double shear bolted connections at elevated temperatures. *Thin-Walled Structures*, **98**, 212–229.

Cai, Y., & Young, B. 2018. Fire resistance of stainless steel single shear bolted connections. *Thin-Walled Structures*, **130**, 332–346.

Cai, Y., & Young, B. 2019. Structural behaviour of cold-formed stainless steel bolted connections at post-fire condition. *Journal of Constructional Steel Research*, **152**, 312–321.

CEN. 1997. *Welding: Electrons and laser beam welded joints – Guidance on quality levels for imperfections – Part 1: Steel. EN ISO 13919-1*.

CEN. 2005. *Eurocode 3: Design of steel structures - Part 1-2: General rules - Structural fire design. EN 1993-1-2*.

CEN. 2006. *Eurocode 3: Design of steel structures - Part 1-5: General rules - Supplementary rules for plated structures. EN 1993-1-5*.

CEN. 2012. *Fire resistance tests – Part 1: General requirements. EN 1363-1*.

CEN. 2015. *Eurocode 3: Design of steel structures - Part 1-4: General rules - Supplementary rules for stainless steels. EN 1993-1-4*.

CEN. 2018. *Execution of steel structures and aluminium structures. Part 2: Technical requirements for steel structures. EN 1090-2*.

CEN. 2020. *Eurocode 3 Design of steel structures-Part 1-1: General rules and rules for buildings. prEN 1993-1-1*.

Chen, J., & Young, B. 2006. Stress–strain curves for stainless steel at elevated temperatures. *Engineering Structures*, **28**(2), 229–239.

Chen, J., & Young, B. 2007. Cold-formed steel lipped channel columns at elevated temperatures. *Engineering Structures*, **29**(10), 2445–2456.

Couto, C., Vila-Real, P., Lopes, N., & Zhao, B. 2014. Effective width method to account for the local buckling of steel thin plates at elevated temperatures. *Thin-Walled Structures*, **84**, 134–149.

Couto, C, Sanzel, A, Vila-Real, P, Lopes, N, & Zhao, B. 2016. Beam-columns with thin wall cross-sections in case of fire. 9th International Conference Structures in Fire.

Ding, J., & Wang, Y. 2007. Experimental study of structural fire behaviour of steel beam to concrete filled tubular column assemblies with different types of joints. *Engineering Structures*, **29**(12), 3485–3502.

Ding, R., Fan, S., Chen, G., Li, C., Du, E., & Liu, C. 2019. Fire resistance design method for restrained stainless steel H-section columns under axial compression. *Fire Safety Journal*, **108**, 102837.

Dwaikat, M., Kodur, V., Quiel, S., & Garlock, M. 2011. Experimental behavior of steel beam–columns subjected to fire-induced thermal gradients. *Journal of Constructional Steel Research*, **67**(1), 30–38.

ENV. 1995. *Eurocode 3: Design of steel structures - Part 1.2: General rules - Structural fire design. ENV 1993-1-2*.

ENV. 2001. *Eurocode 3: Design of steel structures - Part 1.2: General rules - Structural fire design (together with United Kingdom National Application Document). DD ENV 1993-1-2*.

Fan, S., Ding, X., Sun, W., Zhang, L., & Liu, M. 2016. Experimental investigation on fire resistance of stainless steel columns with square hollow section. *Thin-Walled Structures*, **98**, 196–211.

Fan, S., Liu, M., Sun, W., Guo, Y., & Han, Y. 2018. Experimental investigation of eccentrically compressed stainless steel columns with constraints in fire. *Fire Safety Journal*, **99**, 49–62.

Fan, S., Ding, R., Zheng, J., Xie, F., & Wu, Q. 2020. Refined model for the stress-strain curve of austenitic stainless steel materials at elevated temperatures. *Journal of Materials in Civil Engineering*, **32**(4), 04020032.

Feng, M., Wang, Y., & Davies, J. M. 2003. Structural behaviour of cold-formed thin-walled short steel channel columns at elevated temperatures. Part 1: experiments. *Thin-Walled Structures*, **41**(6), 543–570.

Feng, M., Wang, Y., & Davies, J. M. 2004. A numerical imperfection sensitivity study of cold-formed thin-walled tubular steel columns at uniform elevated temperatures. *Thin-Walled Structures*, **42**(4), 533–555.

Fieber, A., Gardner, L., & Macorini, L. 2019. Formulae for determining elastic local buckling half-wavelengths of structural steel cross-sections. *Journal of Constructional Steel Research*, **159**, 493–506.

Franssen, J. M., Talamona, D., Kruppa, J., & Cajot, L. G. 1998. Stability of steel columns in case of fire: experimental evaluation. *Journal of Structural Engineering*, **124**(2), 158–163.

Gardner, L. 2005. The use of stainless steel in structures. *Structural Engineering and Materials*, **7**(2), 45–55.

Gardner, L. 2007. Stainless steel structures in fire. *Proceedings of the Institution of Civil Engineers-Structures and Buildings*, **160**(3), 129–138.

Gardner, L. 2008. Aesthetics, economics and design of stainless steel structures. *Advanced Steel Construction*, **4**(2), 113–122.

Gardner, L. 2019. Stability and design of stainless steel structures – Review and outlook. *Thin-Walled Structures*, **141**, 208–216.

Gardner, L., & Baddoo, N. 2006. Fire testing and design of stainless steel structures. *Journal of Constructional Steel Research*, **62**(6), 532–543.

Gardner, L., & Nethercot, D. A. 2004. Numerical Modeling of Stainless Steel Structural Components – A Consistent Approach. *Journal of Structural Engineering*, **130**(10), 1586–1601.

Gardner, L., & Ng, K. T. 2006. Temperature development in structural stainless steel sections exposed to fire. *Fire Safety Journal*, **41**(3), 185–203.

Gardner, L., & Theofanous, M. 2008. Discrete and continuous treatment of local buckling in stainless steel elements. *Journal of Constructional Steel Research*, **64**(11), 1207–1216.

Gardner, L., & Yun, X. 2018. Description of stress-strain curves for cold-formed steels. *Construction and Building Materials*, **189**, 527–538.

Gardner, L., Insausti, A., Ng, K. T., & Ashraf, M. 2010. Elevated temperature material properties of stainless steel alloys. *Journal of Constructional Steel Research*, **66**(5), 634–647.

Gardner, L., Bu, Y., Francis, P., Baddoo, N., Cashell, K. A., & McCann, F. 2016a. Elevated temperature material properties of stainless steel reinforcing bar. *Construction and Building Materials*, **114**, 977–997.

Gardner, L., Bu, Y., & Theofanous, M. 2016b. Laser-welded stainless steel I-sections: Residual stress measurements and column buckling tests. *Engineering Structures*, **127**, 536–548.

Gardner, L., Fieber, A., & Macorini, L. 2019. Formulae for calculating elastic local buckling stresses of full structural cross-sections. *Structures*, **17**, 2–20.

Gedge, G. 2008. Structural uses of stainless steel-buildings and civil engineering. *Journal of Constructional Steel Research*, **64**(11), 1194–1198.

Han, L. 2001. Fire performance of concrete filled steel tubular beam-columns. *Journal of Constructional Steel Research*, **57**(6), 697–711.

Han, L., Zhao, X., Yang, Y., & Feng, J. 2003. Experimental study and calculation of fire resistance of concrete-filled hollow steel columns. *Journal of Structural Engineering*, **129**(3), 346–356.

Han, L., Huo, J., & Wang, Y. 2005. Compressive and flexural behaviour of concrete filled steel tubes after exposure to standard fire. *Journal of Constructional Steel Research*, **61**(7), 882–901.

He, A., Liang, Y., & Zhao, O. 2019. Experimental and numerical studies of austenitic stainless steel CHS stub columns after exposed to elevated temperatures. *Journal of Constructional Steel Research*, **154**, 293–305.

He, A., Li, H., Lan, X., Liang, Y., & Zhao, O. 2020. Flexural buckling behaviour and residual strengths of stainless steel CHS columns after exposure to fire. *Thin-Walled Structures*, **152**, 106715.

Hradil, P., Talja, A., Real, E., Mirambell, E., & Rossi, B. 2013. Generalized multistage mechanical model for nonlinear metallic materials. *Thin-Walled Structures*, **63**, 63–69.

Huang, Y., & Young, B. 2012. Material properties of cold-formed lean duplex stainless steel sections. *Thin-Walled Structures*, **54**, 72–81.

Huang, Y., & Young, B. 2014a. The art of coupon tests. *Journal of Constructional Steel Research*, **96**, 159–175.

Huang, Y., & Young, B. 2014b. Stress–strain relationship of cold-formed lean duplex stainless steel at elevated temperatures. *Journal of Constructional Steel Research*, **92**, 103–113.

ISO-834. 1999. *Fire resistance tests – elements of building construction*. International Organization for Standardization, Geneva, Switzerland.

Jandera, M., Gardner, L., & Machacek, J. 2008. Residual stresses in cold-rolled stainless steel hollow sections. *Journal of Constructional Steel Research*, **64**(11), 1255–1263.

Knobloch, M., Fontana, M., & Frangi, A. 2008. Steel beam-columns subjected to fire. *Steel Construction*, **1**(1), 51–58.

Kruppa, J. 1999. Eurocodes-Fire parts: Proposal for a methodology to check the accuracy of assessment methods. CEN TC 250. *Horizontal Group Fire, Document*.

Lan, X., Huang, Y., Chan, T., & Young, B. 2018. Static strength of stainless steel K- and N-joints at elevated temperatures. *Thin-Walled Structures*, **122**, 501–509.

Li, G., & Guo, S. 2008. Experiment on restrained steel beams subjected to heating and cooling. *Journal of Constructional Steel Research*, **64**(3), 268–274.

Li, G., Wang, P., & Wang, Y. 2010. Behaviour and design of restrained steel column in fire, Part 1: Fire test. *Journal of Constructional Steel Research*, **66**(8-9), 1138–1147.

Liang, Y., Manninen, T., Zhao, O., Walport, F., & Gardner, L. 2019. Elevated temperature material properties of a new high-chromium austenitic stainless steel. *Journal of Constructional Steel Research*, **152**, 261–273.

Liu, F., Gardner, L., & Yang, H. 2014. Post-fire behaviour of reinforced concrete stub columns confined by circular steel tubes. *Journal of Constructional Steel Research*, **102**, 82–103.

Liu, M., Fan, S., Sun, W., Ding, R., & Zhu, T. 2018. Fire-resistant design of eccentrically compressed stainless steel columns with constraints. *Fire Safety Journal*, **100**, 1–19.

Liu, M., Fan, S., Ding, R., Chen, G., Du, E., & Wang, K. 2019. Experimental investigation on the fire resistance of restrained stainless steel H-section columns. *Journal of Constructional Steel Research*, **163**, 105770.

Liu, T., Fahad, M. K., & Davies, J. M. 2002. Experimental investigation of behaviour of axially restrained steel beams in fire. *Journal of Constructional Steel Research*, **58**(9), 1211–1230.

Lopes, N., Vila-Real, P., Da Silva, L., & Franssen, J. 2010a. Axially loaded stainless steel columns in case of fire. *Journal of Structural Fire Engineering*, **1**(1), 43–59.

Lopes, N., Vila-Real, P., Da Silva, L., & Franssen, J. 2010b. Numerical modelling of thin-walled stainless steel structural elements in case of fire. *Fire Technology*, **46**(1), 91–108.

Lopes, N., Vila-Real, P., Da Silva, L., & Franssen, J. 2012. Numerical analysis of stainless steel beam-columns in case of fire. *Fire Safety Journal*, **50**, 35–50.

Lopes, N., Manuel, M., Da Silva, L., & Vila-Real, P. 2019. Parametric study on austenitic stainless steel beam-columns with hollow sections under fire. *Journal of Constructional Steel Research*, **152**, 274–283.

Maraveas, C., Wang, Y., & Swailes, T. 2016. Elevated temperature behaviour and fire resistance of cast iron columns. *Fire Safety Journal*, **82**, 37–48.

Mirambell, E., & Real, E. 2000. On the calculation of deflections in structural stainless steel beams: an experimental and numerical investigation. *Journal of Constructional Steel Research*, **54**(1), 109–133.

Mohammed, A., & Afshan, S. 2019. Numerical modelling and fire design of stainless steel hollow section columns. *Thin-Walled Structures*, **144**, 106243.

Ng, K. T., & Gardner, L. 2007. Buckling of stainless steel columns and beams in fire. *Engineering Structures*, **29**(5), 717–730.

Ozyurt, E., Wang, Y., & Tan, K. 2014. Elevated temperature resistance of welded tubular joints under axial load in the brace member. *Engineering Structures*, **59**, 574–586.

Pauli, J., Somaini, D., Knobloch, M., & Fontana, M. 2012. *Experiments on steel columns under fire conditions*. IBK test report no. 340; Institute of Structural Engineering (IBK), ETH Zurich.

Pauli, Jacqueline. 2012. The Behaviour of Steel Columns in Fire: Material-Cross-sectional Capacity-Column Buckling. *IBK Bericht*, **343**.

Pournaghshband, A., Afshan, S., & Theofanous, M. 2019a. Elevated temperature performance of restrained stainless steel beams. *Structures*, **22**, 278–290.

Pournaghshband, A., Afshan, S., & Foster, A. S. J. 2019b. Structural fire performance of axially and rotationally restrained stainless steel columns. *Thin-Walled Structures*, **137**, 561–572.

Ramberg, W., & Osgood, W. R. 1943. *Description of stress-strain curves by three parameters*. Technical note no. 902, National Advisory Committee on Aeronautics (NACA).

Ranby, A. 1998. Structural fire design of thin walled steel sections. *Journal of Constructional Steel Research*, **1**(46), 303–304.

Rasmussen, K. 2003. Full-range stress–strain curves for stainless steel alloys. *Journal of Constructional Steel Research*, **59**(1), 47–61.

Robertson, A. 1925. The strength of struts. *The Institution of Civil Engineers (ICE) – Selected Engineering Papers*, **1**(28), 1–55.

Saliba, N., & Gardner, L. 2013. Cross-section stability of lean duplex stainless steel welded I-sections. *Journal of Constructional Steel Research*, **80**, 1–14.

Schafer, B.W., & Peköz, T. 1998. Computational modeling of cold-formed steel: characterizing geometric imperfections and residual stresses. *Journal of Constructional Steel Research*, **47**(3), 193–210.

SCI. 2017. *Design Manual for Structural Stainless Steel, Fourth Edition*.

Tan, K., Toh, W., Huang, Z., & Phng, G. 2007. Structural responses of restrained steel columns at elevated temperatures. Part 1: Experiments. *Engineering Structures*, **29**(8), 1641–1652.

Tao, Z., & Han, L. 2007. Behaviour of fire-exposed concrete-filled steel tubular beam columns repaired with CFRP wraps. *Thin-Walled Structures*, **45**(1), 63–76.

Tao, Z., Ghannam, M., Song, T., & Han, L. 2016. Experimental and numerical investigation of concrete-filled stainless steel columns exposed to fire. *Journal of Constructional Steel Research*, **118**, 120–134.

Theofanous, M., Chan, T.M., & Gardner, L. 2009. Flexural behaviour of stainless steel oval hollow sections. *Thin-Walled Structures*, **47**(6-7), 776–787.

Timoshenko, S., & Gere, J. M. 1961. *Theory of Elastic Stability, McGrawhill Book Co*. Inc., New York.

Tondini, N., Rossi, B., & Franssen, J. 2013. Experimental investigation on ferritic stainless steel columns in fire. *Fire Safety Journal*, **62**, 238–248.

Trahair, N. S., Bradford, M. A., Nethercot, D., & Gardner, L. 2007. *The behaviour and design of steel structures to EC3*. CRC Press.

Ukomski, M., Turkowski, P., Roszkowski, P., & Papis, B. 2017. Fire resistance of unprotected steel beams - comparison between fire tests and calculation models. *Procedia Engineering*, **172**, 665–672.

Uppfeldt, B., Ala-Outinen, T., & Veljkovic, M. 2008. A design model for stainless steel box columns in fire. *Journal of Constructional Steel Research*, **64**(11), 1294–1301.

Wang, F., & Han, L. H. 2019. Analytical behavior of carbon steel-concrete-stainless steel double-skin tube (DST) used in submarine pipeline structure. *Marine Structures*, **63**, 99–116.

Wang, P., Wang, Y., & Li, G. 2010a. A new design method for calculating critical temperatures of restrained steel column in fire. *Fire Safety Journal*, **45**(6-8), 349–360.

Wang, Y., Davison, J. B., Burgess, I. W., Plank, R. J., Yu, H., Dai, X., & Bailey, C. 2010b. The safety of common steel beam/column connections in fire. *Structural Engineer*, **88**(21), 26–35.

Wang, Y., Burgess, I., František, & Gillie, M. 2012. *Performance-based fire engineering of structures*. CRC press.

Xing, Z., O., Zhao, Kucukler, M., & Gardner, L. 2020. Testing and design of slender stainless steel I-sections in minor axis bending in fire. *Engineering Structures*. Submitted for publication.

Yang, L., Zhao, M., Gardner, L., Ning, K., & Wang, J. 2019. Member stability of stainless steel welded I-section beam-columns. *Journal of Constructional Steel Research*, **155**, 33–45.

Young, B., & Ellobody, E. 2011. Performance of axially restrained concrete encased steel composite columns at elevated temperatures. *Engineering Structures*, **33**(1), 245–254.

Yuan, H., Wang, Y., Shi, Y., & Gardner, L. 2014. Residual stress distributions in welded stainless steel sections. *Thin-Walled Structures*, **79**, 38–51.

Zhao, B., & Blanguernon, A. 2004. *Member Tests in Fire and Structural Fire Design Guidance. Work package 6: Elevated Temperature Properties. ECSC project 'Structural design of cold-worked austenitic stainless steel'*. The Steel Construction Instititue, UK.

Zhao, O., Rossi, B., Gardner, L., & Young, B. 2015a. Behaviour of structural stainless steel cross-sections under combined loading – Part I: Experimental study. *Engineering Structures*, **89**, 236–246.

Zhao, O., Rossi, B., Gardner, L., & Young, B. 2015b. Behaviour of structural stainless steel cross-sections under combined loading – Part II: Numerical modelling and design approach. *Engineering Structures*, **89**, 247–259.

Zhou, F., & Young, B. 2007. Experimental and numerical investigations of cold-formed stainless steel tubular sections subjected to concentrated bearing load. *Journal of Constructional Steel Research*, **63**(11), 1452–1466.